CO_2 Capture and Storage from Power Plant Flue Gas Using Gas Hydrate-Based Technologies

Aliakbar Hassanpouryouzband

Submitted for the degree of Doctor of Philosophy

Heriot-Watt University

Institute of Petroleum Engineering

School of Energy, Geoscience, Infrastructure, and Society

August 2019

ABSTRACT

The climate system is changing globally, and there is substantial evidence that subsea permafrost and gas hydrate reservoirs are melting in high-latitude regions of the Earth, resulting in large volumes of CO_2 (from organic carbon deposits) and CH_4 (from gas hydrate reserves) venting into the atmosphere. As one of the main contributors to global climate change, power plants produce a substantial proportion of global anthropogenic CO_2 emissions. Here, we developed techniques to capture and storage CO_2 (CCS) present in power plant flue gases based on gas hydrate technologies. First, we experimentally measured the thermodynamic properties of different flue gases, followed by modelling and tuning the equations of states. Second, we proposed injection of flue gas into methane gas hydrate reservoirs as an option for economically sustainable production of natural gas as well as CCS. The optimum injection conditions were found and reaction kinetics was investigated in realistic conditions and well characterised systems. Third, kinetics of flue gas hydrate formation for both the geological storage of CO_2 and the secondary sealing of CH_4/CO_2 release in one simple process was investigated, followed be thoroughly investigation of hydrate formation kinetics using a highly accurate in house developed device. Finally, effect of the proposed methods on permeability and mechanical strength of the geological formations was investigated.

To my wonderful grandma, Gohar,

Without whose endless love, dedication and support this work would not have been possible.

I wish you were alive and well.

ACADEMIC REGISTRY
Research Thesis Submission

Name:	ALIAKBAR HASSANPOURYOUZBAND		
School:	Institute of GeoEnergy Engineering		
Version: *(i.e. First, Resubmission, Final)*	Final	Degree Sought:	PhD

Declaration

In accordance with the appropriate regulations I hereby submit my thesis and I declare that:

1. The thesis embodies the results of my own work and has been composed by myself
2. Where appropriate, I have made acknowledgement of the work of others
3. Where the thesis contains published outputs under Regulation 6 (9.1.2) these are accompanied by a critical review which accurately describes my contribution to the research and, for multi-author outputs, a signed declaration indicating the contribution of each author (complete Inclusion of Published Works Form – see below)
4. The thesis is the correct version for submission and is the same version as any electronic versions submitted*.
5. My thesis for the award referred to, deposited in the Heriot-Watt University Library, should be made available for loan or photocopying and be available via the Institutional Repository, subject to such conditions as the Librarian may require
6. I understand that as a student of the University I am required to abide by the Regulations of the University and to conform to its discipline.
7. Inclusion of published outputs under Regulation 6 (9.1.2) shall not constitute plagiarism.
8. I confirm that the thesis has been verified against plagiarism via an approved plagiarism detection application e.g. Turnitin.

* *Please note that it is the responsibility of the candidate to ensure that the correct version of the thesis is submitted.*

Signature of Candidate:		Date:	

Submission

Submitted By *(name in capitals)*:	
Signature of Individual Submitting:	
Date Submitted:	

For Completion in the Student Service Centre (SSC)

Received in the SSC by *(name in capitals)*:			
Method of Submission *(Handed in to SSC; posted through internal/external mail)*:			
E-thesis Submitted ***(mandatory for final theses)***			
Signature:		Date:	

TABLE OF CONTENTS

LISTS OF PUBLICATIONS BY THE CANDIDATE

1- **Hassanpouryouzband**, A., Yang, J., Tohidi, B., Chuvilin, E., Istomin, V., Bukhanov, B. and Cheremisin, A., 2018. CO2 capture by injection of flue gas or CO2–N2 mixtures into hydrate reservoirs: dependence of CO2 capture efficiency on gas hydrate reservoir conditions. Environmental science & technology, 52(7), pp.4324-4330.

2- **Hassanpouryouzband**, A., Yang, J., Tohidi, B., Chuvilin, E., Istomin, V., Bukhanov, B. and Cheremisin, A., 2018. Insights into CO2 Capture by Flue Gas Hydrate Formation: Gas Composition Evolution in Systems Containing Gas Hydrates and Gas Mixtures at Stable Pressures. ACS Sustainable Chemistry & Engineering, 6(5), pp.5732-5736.

3- **Hassanpouryouzband**, A., Vasheghani Farahani, M., Yang, J., Tohidi, B., Chuvilin, E., Istomin, V. and Bukhanov, B.A., 2019. Solubility of Flue Gas or Carbon Dioxide-Nitrogen Gas Mixtures in Water and Aqueous Solutions of Salts: Experimental Measurement and Thermodynamic Modelling. Industrial & Engineering Chemistry Research.

4- **Hassanpouryouzband**, A., Yang, J., Tohidi, B., Chuvilin, E.M., Istomin, V. and Bukhanov, B.A., 2019. Geological CO2 Capture and Storage with Flue Gas Hydrate Formation in Frozen and Unfrozen Sediments: Method Development, Real Time-Scale Kinetic Characteristics, Efficiency, and Clathrate Structural Transition. ACS Sustainable Chemistry & Engineering.

5- Yang, J., **Hassanpouryouzband**, A., Tohidi, B., Chuvilin, E., Istomin, V., Bukhanov, B. and Cheremisin, A., 2019. Gas Hydrates in Permafrost: Distinctive Effect of Gas Hydrates and Ice on the Geomechanical Properties of Simulated Hydrate-Bearing Permafrost Sediments. Journal of Geophysical Research: Solid Earth.

6- Okwananke, A., **Hassanpouyouzband, A.**, Farahani, M. V., Yang, J., Tohidi, B., Chuvilin, E., ... & Bukhanov, B, 2019. Methane recovery from gas hydrate-bearing

sediments: An experimental study on the gas permeation characteristics under varying pressure. Journal of Petroleum Science and Engineering.

7- **Hassanpouryouzband A.**, Okwananke, A., Yang, J., Tohidi, B., Chuvilin, E., Bukhanov, B., Istomin, V. and Cheremisin, A., 2017. CO2 Capture and Methane Recovery by Direct Injection of Flue Gas into Frozen Gas Hydrate-Bearing Sediments. In The ninth international conference on gas hydrate, Denver, American.

8- Okwananke, A., **Hassanpouryouzband**, A., Yang, J., Tohidi, B., Chuvilin, E., Bukhanov, B., Istomin, V. and Cheremisin, A., 2017. Comparative Study on Effect of Ice and Hydrate on the Geomechanical Properties of Sediments. In The ninth international conference on gas hydrate, Denver, American.

9- A., Yang, **Hassanpouryouzband**, A., Tohidi, B., Chuvilin, E., Bukhanov, B., Istomin, V. and Cheremisin, A., 2017. Experimental study of gas permeation through gas hydrate-bearing sediments. In The ninth international conference on gas hydrate, Denver, American.

10- **Hassanpouryouzband**, A., Yang, J., Joonaki, E., Tohidi, B., Chuvilin, E., Bukhanov, B. and Istomin, V., 2017, June. A Novel Method for CO2 Storage and Methane Recovery in Gas Hydrate Reservoirs through Injection of Flue Gas From Coal-fired Power Plants. In 79th EAGE Conference and Exhibition.

11- Chuvilin, E., Istomin, V., Ekimova, V., Bukhanov, B., **Hassanpouryouzband**, A., Yang, J. and Tohidi, B., GM18-134 Experimental Modeling of Methane Recovery by Flue Gas Injection Into Frozen Hydrate-bearing Reservoir.

12- Istomin, V., Chuvilin, E., Bukhanov, B., Tohidi, B., Yang, J., **Hassanpouryouzband**, A., Okwananke, A., 2019. Method for producing natural gas from gas hydrate reservoir. Russian Federation patent No. RU2693983C2.

Chapter 1 - INTRODUCTION

Gas hydrates are the center of research emphasis in sustainable chemistry because of their innovative applications in a wide range of scientific and industrial contexts. The early era of gas hydrates-related research was primarily dominated by the flow assurance. However, in recent years the upsurge of work in the field was stimulated by expanding its applications to energy recovery, CO_2 capture and storage, gas separation, water desalination, gas storage and transport, refrigeration, etc. More recently, emission of arctic methane from hydrate-bearing sediments has emerged as a greenhouse warming potential (GWP), which could be a major concern in the future.

Properties of gas hydrates under various conditions have countless practical consequences in science and technology, and it also affects natural cycles. One obvious example is the cycle of natural gas hydrate formation at high latitude regions of the earth during seasonal changes, which influences global phenomena such as climate change. On the other hand, controlling the properties of the clathrates using different methods and additives is of great importance to the mentioned sectors, particularly in the context of reducing the costs and controlling the kinetics of formation/dissociation, as the expenses required for the application of hydrate based methods impact the future of this technology. Even the multibillion-dollar oil industry is affected by the properties of gas hydrates formed from hydrocarbon gases, formation of which can plug the production facilities and transport pipelines, imposing billions of financial loses every year. Finally, fundamental understanding of properties of gas hydrates is undeniably involved in any hydrate-based technology, which forms the basis of the technologies.

Global energy demand is significantly increasing due to population and economic growth. The 2013 International Energy Outlook by the United States Department of Energy (US DOE) projected a global energy consumption rise by 56% from 524 quadrillion BTU (British Thermal Unit) in 2010 to 820 quadrillion BTU in 2040[1]. Growing non-OECD (Organization for Economic Co-operation and Development) economies, notably China and India are the major contributors to the growing energy consumption. Their combined consumption has been projected to reach 28% of world energy consumption by 2030[2].

As the world transits to a future where renewable is the energy mainstay, there has been tremendous progress in generating energy from non-fossil fuel sources. However, the

amount generated is insignificant in meeting the energy demand. About 80% of world energy supply will still be sourced from carbon-based fuels including natural gas, oil, and coal[3]. Combustion of these fuels will continue to emit CO_2, a greenhouse gas into the atmosphere increasing the atmospheric concentration of $CO_2$and its attendant global warming effect. Natural gas is the cleanest burning of these three fuel sources and its use is set to grow highest among others. Thus, in the medium to long term it could serve as a link between now and a future where low to zero carbon energy reigns.

Presently, about 80% of global natural gas consumption comes from conventional gas sources[4]. However, due to technological advances, contributions from unconventional sources including tight gas, shale gas, and coalbed methane have increased. To further increase the contribution from unconventional natural gas resources, there is need for development of natural gas hydrate reservoirs.

1.1 Natural gas hydrates

Natural gas hydrates are ice-like solids that form and stabilize under conditions of low temperature and high pressure. They consist of molecules of water interconnected by hydrogen bonds, forming an open lattice that large enough to encage small hydrocarbon molecules as guest molecules[5,6]. The most known guest molecules that form hydrate are light hydrocarbons from C1 to C5, CO2, N2 and H2S. These guest molecules are known to form three general structures of hydrates, namely structure I (sI), structure II (sII), and structure H (sH), which all structure contain various size of cavities and different types of guest molecules. Some cavities may remain empty during stable hydrate formation. Natural gas hydrates have nonstoichiometric nature, stabling by encaging guest molecules. Therefore, they differ from common stoichiometric hydrates such as CaSO4.2H2O[5]. They exist naturally in marine and permafrost sediments and have been stable for millions of years[7]. They are geographically evenly distributed. This has elicited active research and development activities into its development especially by conventional oil and gas-resource lean countries like Japan and South Korea. Estimates of natural gas hydrate resources shows that the amount of methane in natural Gas hydrate is several orders of magnitude greater than that in conventional and other unconventional gas sources combined. One of the early estimates was by Daniels et al.[8] at 3053×1015 m^3 based on assumptions that hydrates could occur wherever conditions for formation and stabilization exist. Soloviev[9] considered limiting factors such as availability of methane,

limited porosity, and percentage of organic matter to give a more conservative estimate of 0.2×1015 m^3 of methane. However, from improved understanding and information extracted in-situ from field trials, estimates of methane in natural gas hydrates reservoirs has decreased significantly over time. The most conservative in recent times is at 3×1015 m^3. Technically recoverable volumes of gas in gas hydrate reservoirs have been put at approximately 3×1013 m^3 by Boswell and Collet[10].

1.2 Techniques for methane recovery

From the foregoing, it is evident that natural gas hydrate is a potential and abundant future source of energy. It is therefore imperative to develop techniques to exploit and recover methane from it. This however presents itself a daunting challenge, firstly due to the harsh conditions in its natural habitat. In addition, it is markedly different from conventional and other unconventional natural gas sources. Conventional and other unconventional natural gas sources are trapped in place by geological structures (impermeable cap rock) and recovered by just sinking a well into the reservoir, and by creating additional conduit (hydraulic fracturing) in ultra-low permeability formations (tight gas and shale gas formations). Gas hydrates are solids in their natural state and does not need to be trapped, thus techniques to recover gas from them involves primarily in-situ dissociation and then creating a conduit (well) for gas flow. Three most commonly proposed recovery methods in literature are depressurization, thermal stimulation, and inhibitor injection.

1.3 Depressurization

Gas production by depressurization as the name implies involves lowering the reservoir pressure below the hydrate equilibrium pressure at the prevailing reservoir temperature[11–14]. This has been described as the most economical of the three methods as it does not incur additional cost either in form of energy or chemicals. However, it is reportedly a slow process.

1.1.2.2 Thermal stimulation

In thermal stimulation method, gas is recovered from natural gas hydrate by heating the reservoir to increase and shift the temperature away from the hydrate stability region leading to hydrate dissociation. Heat energy is supplied in the form of steam injection or hot water injection[15–19]. A major disadvantage of this technique is reduced efficiency due to the loss of heat energy during delivery from source to the reservoir. There is also the possible loss of heat to non-hydrate bearing zones and water handling issues due to

excessive water production. To mitigate these challenges, alternative heat transfer approaches has been suggested. Islam[20] proposed electromagnetic heating in which electromagnetic heat sources are introduced downhole to provide localized heating. This involves installation of electromagnetic heat generators along the length of vertical/horizontal wells in the hydrate bearing zone. In practical terms, this will incur additional cost not only in terms of installations, but also in terms of energy cost. Modelling and simulation studies also proposed in-situ combustion of methane from the methane hydrate reservoir[21]. They suggested the use of a mixture of liquid fuel and oxygen/CO_2 slurry as the combustion fluid downhole which will not be commercially viable considering the volume of liquid fuel and oxygen/CO_2 slurry needed for sustained methane production.

1.4 Inhibitor injection

Inhibitor injection works by altering the hydrate phase boundary to dissociate hydrate in-situ[22–26]. It does this by shifting the phase boundary to higher pressures and lower temperatures. As a gas recovery method from natural gas hydrate reservoirs, it is not well studied compared to depressurization and thermal stimulation. This is owing to the fact that it is economically unwise considering the volume and cost of chemical needed and its toxicity to the environment. Chemical inhibition studies have so far been limited to hydrate dissociation in pipelines and surface facilities. Chemical inhibitors are classified into two main categories: thermodynamic inhibitors and kinetic inhibitors. Thermodynamic inhibitors such as ethylene glycol (EG) and methylene glycol (MEG) alter the hydrate equilibrium condition, thereby dissociating hydrate. They are therefore more suitable for gas recovery in natural gas hydrate reservoir. On the other hand, kinetic inhibitors slow the rate of hydrate formation, hence they are of more interest in mitigating hydrate problems in pipelines and surface facilities.

1.5 Combination of processes

Combinations of two methods have also been proposed so that the effect of inherent deficiency in one method can be reduced by the other method. It has been reported that depressurization, apart from being a slow method, also has the possibility of ice formation when rapidly done[27] thereby causing a reduction or complete blockage of permeability which affects the volume of gas produced. In thermal stimulation, a significant proportion of the heat energy supplied is lost to ‘thief zones’ (none hydrate bearing zones). In addition, the hydrate-bearing zone must be of good porosity, about 15% or more for

effective heat stimulation. Chemical inhibition process is expensive owing to the cost of the chemicals and also requires a good porosity. Some of these combined approaches mimics production techniques applied in conventional reservoirs and are mostly a combination of thermal stimulation and depressurization. The huff and puff technique demonstrated by Li et al.[19] is a combination of thermal stimulation and depressurization involving cycles of injection of hot fluid (water or steam), soaking, and gas production. According to the authors gas to water ratio of 55 m^3 of methane (STP)/m^3 of water justifies the economic feasibility of the process. Steam Assisted Gravity Drainage (SAGD)[28] and Steam Assisted Antigravity Drainage (SAAD)[29] have also been tested for gas recovery in natural gas hydrates in sediments in a combination of thermal stimulation, depressurization, and brine injection. Both methods employ two horizontal wells; one injection and one production. In SAAD, the production well is above the injection well and was reported to produce more gas and less water in comparison to SAGD.

1.6 Gas injection

Gas injection, especially CO_2 into natural gas hydrate reservoir for methane recovery has received tremendous attention[30–32]. In this regard, natural gas hydrate reservoirs could serve as a CO_2 sink by sequestering CO_2 as CO_2 hydrate in CO_2-CH_4 exchange process[33]. Hydrate phase equilibria depends on the type of gas occupying the hydrate cage. Seo et al.[34] in their study reported that comparing equilibrium conditions of pure CO_2 and methane gases, pure CO_2 hydrates form at higher temperature for a given pressure, or at a lower pressure for a given temperature. Lee et al.[33] demonstrated this by carrying out quantitative experiments to investigate the kinetics of CO_2-CH_4 exchange by injecting liquid CO_2 into methane hydrate. From their results, they inferred the mechanism for methane production and identified the depth of the dissociation/exchange on hydrate particles[35]. The process has also been reported to be thermodynamically feasible[36] as the heat released during CO_2-hydrate formation (exothermic, -57.98 kJ/mol) is larger than the heat absorbed during methane hydrate dissociation (endothermic, 54.49 kJ/mol). Nitrogen injection has been also used to dissociate methane hydrate. Panter et al.[37] purged gas hydrate plug in pipeline by injecting nitrogen gas. In addition, Masuda et al.[38]flowed nitrogen through methane hydrate bearing limestone core. He observed that hydrate dissociated as the nitrogen gas passed through the core. Furthermore, mixtures of CO_2 and nitrogen has shown strong efficacy in dissociating methane hydrate[39–42]. Park et al.[43] quantified methane replacement using a mixture of CO_2 and nitrogen in comparison with

CO_2 only. With the use of Raman spectroscopy, they reported that 23% of methane in methane hydrate was replaced by nitrogen and 62% of methane in methane hydrates was replaced by CO_2, thus recovering about 85% of methane in the hydrate, a significant increase on 64% that could be recovered by pure CO_2.

1.7 Scientific and field trials

Following several exploratory expeditions, natural gas hydrates has been established to be abundantly and geographically widespread sparking unprecedented research effort into its exploitation and natural gas production from it. Based on increased knowledge from laboratory and simulation studies, a number of onshore and offshore field production trials have been conducted.

Recently, literature search was carried out to see if any new field trials of methane recovery from hydrate reservoirs worldwide. The search outcome did not show any new trials in plan or in progress in public accessible literature.

1.7.1 Messoyakha gas field

Messoyakha gas field in the Russian Arctic is the first reported gas hydrate field. Its production date of 1969 predates most of the active research in natural gas hydrates. The field consists of a free gas layer underlying the hydrate layer [44]. Depressurization technique is employed by producing gas from the free gas layer which reduces the reservoir pressure, causing the gas hydrate to dissociate and release more gas. Cumulative gas production to date from the field has been put at 12.9 BCM (billion cubic meters) of which 5.4 BCM was contributed from hydrate decomposition.

1.7.2 Mount Elbert, Alaska

BP Exploration has been active in natural gas hydrate production research in the Alaska North Slope. This area has a significant concentration of natural gas hydrate reserves in its permafrost with a total estimate of 2.4 TCM[45]. In 2007 in conjunction with US Department of Energy (U.S. DOE) and US geological Survey (USGS), they drilled a stratigraphic well to evaluate the potential of technical and commercial viability of gas resource from the Alaska North Slope gas hydrate accumulations. Results from their wireline Modular Dynamic Testing (MDT) analysis was in agreement with their pre-drill predictions[46].

1.7.3 Mallik Field, Canada

The Mallik field is situated in the Mackenzie delta, northwest Canada and it has seen active hydrate production testing since 2002[47]. Hydrate saturations in excess of 80% of pore volumes in some locations has been reported. This makes the Mallik field one of the most concentrated hydrate field in the world. There has been two production tests in this site so far.

The Mallik 2002 Gas Hydrate Production Research Well Program, a collaborative agreement between Japan National Oil Company (JNOC) and Geological Survey Canada (GSC) tested the feasibility of gas production from a natural gas hydrate reservoir at the Mallik 5L-38 well site by quantifying the pressure drawdown response of a hydrate reservoir. They employed both depressurization and thermal stimulation methods. Their test results confirm the possibility of gas production form especially sand dominated hydrate reservoirs[48].

Also, in 2007 and 2008, a consortium of researchers from Japan Oil, Gas and Metals National Corporation (JOGMEC), Natural Resources Canada (NRCan) conducted another production test at the Mallik 2L-38 well site using depressurization method[49]. The 2007 test lasted for only 60 hours due to excessive sand production. The 2008 test produced both water and gas at 10-20 m^3 water/day and 2000-3000 m^3 gas/day. It lasted for 6 days, the authors in their report opined that the initial high permeability conduits that caused initial high gas production rate collapsed with time as hydrate dissociated, consequently causing a decline in production.

1.7.4 Ignik Sikumi Field, Alaska

The Ignik Sikumi gas hydrate field is located in the Prudhoe Bay Unit, Alaska North Slope. In May 2012, researchers from ConocoPhillips in collaboration with JOGMEC and U.S. DOE the first field trial of CO_2-methane exchange mechanism for gas recovery from natural gas hydrate reservoir [51-52]. The obtained results are complex and hard to interpret[51]. They injected approximately 6000 m^3 of a gas mixture composed of 23% CO_2 and 77% N2 into the target hydrate bearing sediment. At the end of the test period, approximately 70% of the injected nitrogen was recovered while only 40 % of injected $CO_2$was recovered indicating that CO_2-methane exchange occurred, and CO_2 sequestered as CO_2-hydrate. Of the approximately 30000 m^3 of gas mixture produced, 24,210 m^3 was

methane. Methane component of the gas mixture produced reached over 90% and the test lasted for six weeks. However, this was a limited scale scientific field experiment and posed the unique challenge of maintaining rather than controlling the process[52].

1.7.5 MH-21 Nankai Trough, Japan

Following the successes achieved in onshore field production trials, the first offshore gas production gas production trial from natural gas hydrate reservoirs was conducted in March 2013 by JOGMEC in the eastern Nankai Trough, off the Pacific Coast of Japan[53]. They employed depressurization method by setting well bottom-hole pressure from 13.5 MPa to 4.5 MPa. The daily average gas production rate was 20,000 m^3/d and a cumulative gas production of 120,000 m^3. The test lasted for 6 days and was reportedly suspended due to bad weather and sand production.

1.7.6 Shenhu, South China Sea, China

In May 2017, China announced the success of the first country to produce methane gas from gas hydrate deposits beneath the South China Sea[54] (Zheng, 2017). China started its first test drilling at the Shenhu area in 2007. The Shenhu gas hydrate enrichment region is located in the northern slope of South China Sea, and tectonically belongs to the Baiyun sag of the Zhuer depression in the Pearl River Mouth Basin[54]. The water depth is from 1000 to 1700 m, the submarine temperature from 276.4 K to 276.8 K, the geothermal gradient in a range of 318-340 K/km, and seafloor pressure greater than 10 MPa. The well logging indicated that the gas hydrate beds have a thickness of 17.6 m, an average effective porosity of 30%, an average gas hydrate saturation of 46.2%, and an average permeability of 5.5 mD. The test drilling and production operation was conducted by China International Marine Containers Group and China National Petroleum Corporation. Simple depressurization was applied to decompose the gas hydrates. By May 17 2017, when the test production reached a steady output, 113,200 m^3 of natural gas was yielded over the previous seven days, with average daily production of just over 16,000 m^3 and methane content up to 99.5%. China expects commercial use of the resource before 2030. No further information is publicly available on the duration of gas production, the total volume of gas production, and encountered technical challenges.

1.8 Thesis structure

This thesis is focused almost exclusively on using gas hydrate-based technology for mitigating the CO_2 produced by power plants. The thesis is structured in 7 parts. In each part we introduce parts of our work that provided insights into different aspects of the gas hydrate-based technology for CO_2 capture from power plants.

In chapter 2, we introduce a new approach to accurately measure the solubility of three different types of simulated power plant flue gases, including coal-fired flue gas, gas-fired flue gas, and syngas, in water and aqueous solutions of NaCl. To mimic real operational conditions, the solubility measurements were carried out over a temperature range from 273.25 to 303.05 K and pressures up to 22 MPa with 5, 10 and 15 wt. % NaCl. The experimental data were presented in conjunction with thermodynamic predictions. To predict the solubility of CO_2 and N_2 in water and brine, we applied three different equations of state, including CPA-SRK72, VPT, and PC-SAFT, with adjusted binary interaction parameters (BIPs) using a wide range of available experimental data. We also performed a series of sensitivity analyses to identify the accuracy range of each EOS in terms of pressure, temperature and salinity.

In chapter 3, injection of flue gas or CO_2-N_2 mixtures into gas hydrate reservoirs has been investigated in bulk conditions. In this chapter a series of experiments were conducted to investigate the dependence of CO_2 capture efficiency on reservoir conditions. The CO_2 capture efficiency was investigated at different injection pressures from 2.6 to 23.8 MPa and hydrate reservoir temperatures from 273.2 to 283.2 K in the presence of two different saturations of methane hydrate (see Figure 1.1).

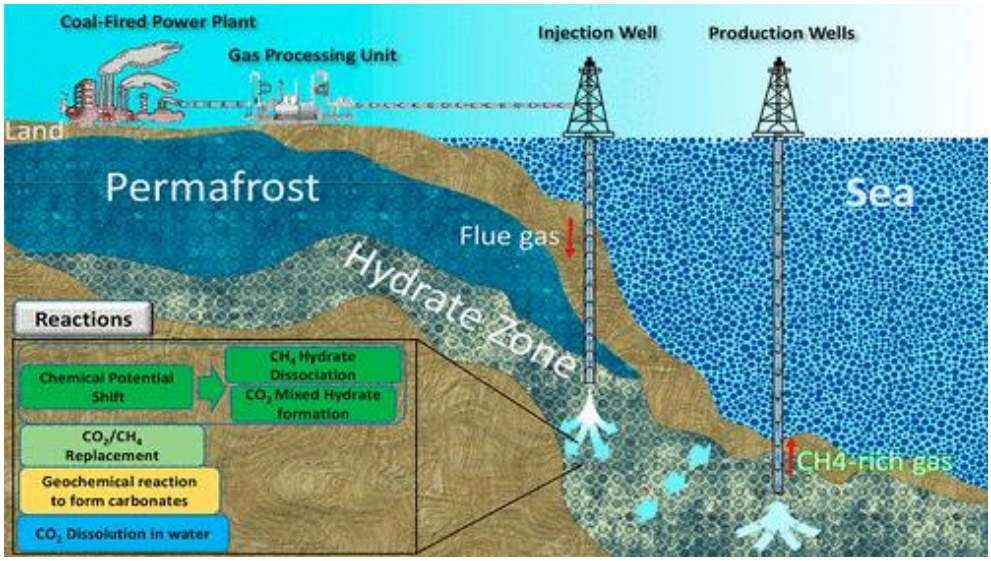

Figure 1.1 Table of content art for chapter 3

In chapter 4, Injection of flue gas into gas hydrates reservoirs was further investigated. We have carried out a series of real-time scale experiments under realistic conditions covering temperature 261.2-284.2 K and at the optimum pressures defined in our previous chapter, in order to characterize the kinetics of the process and evaluate the efficiency. (see Figure 1.2).

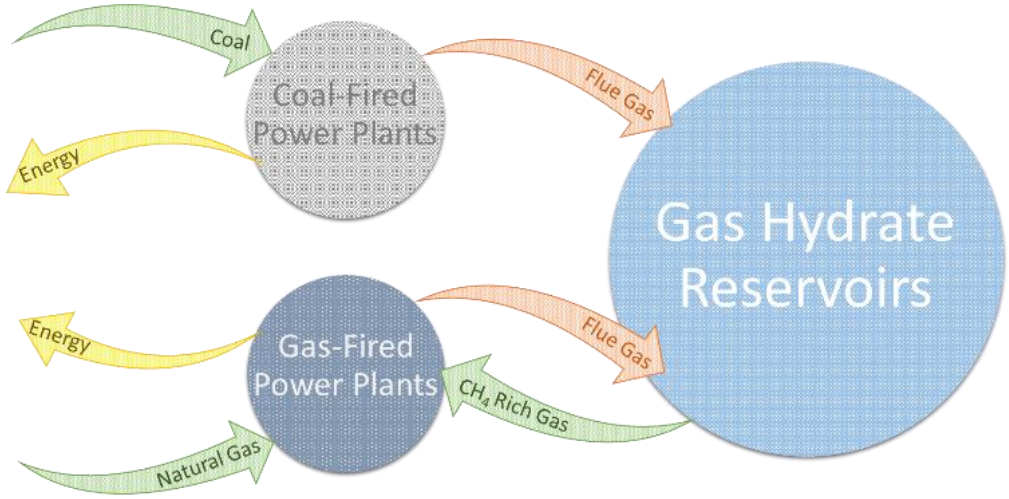

Figure 1.2 Table of content art for chapter 4

In chapter 5, we propose the formation of flue gas hydrates in permafrost regions and marine sediments for both the geological storage of CO_2 and the secondary sealing of CH_4/CO_2 release in one simple process, which could greatly reduce the cost of CO_2 capture and storage (CCS). The kinetics of flue gas hydrate formation inside frozen and unfrozen sediments were investigated under realistic conditions using a highly accurate method and a well-characterized system (see Figure 1.3).

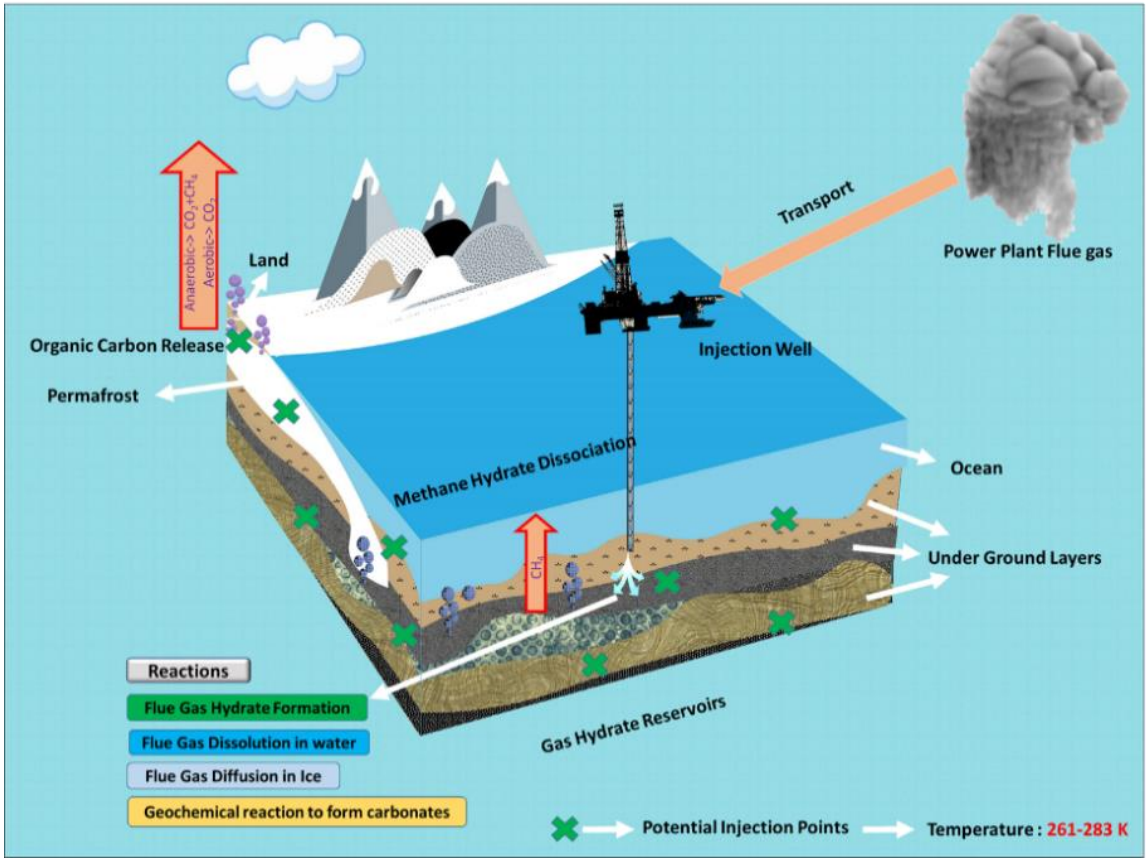

Figure 1.3Table of content art for chapter 5

In chapter 6, we present a highly accurate method to investigate the kinetics of flue gas hydrate formation. Preliminary results are detailed at three different temperatures. The results obtained from this study are important for optimizing CO_2 separation operations thus maximizing efficiency and reducing economic barriers. In addition, they are also useful in studying the kinetics of hydrate formation in other gas mixture systems.

In chapter 7, characteristics of gas permeation through gas hydrate-bearing sediments were explored under varying differential pressure for three types of sedimentary core samples, including 100 wt. % silica sand, 95 wt. % silica sand + 5 wt. % montmorillonite clay, and consolidated sandstone using a standard core-holder.

In chapter 8, the effect of gas hydrate and ice on the geomechanical properties of sediments were compared by triaxial compression tests for typical sediment conditions: unfrozen hydrate-free sediments at 273.4 K, hydrate-free sediments frozen at 263.1 K, unfrozen sediments containing about 22 vol% methane hydrate at 273.4 K, and hydrate-bearing sediments frozen at 263.1 K. The effect of hydrate saturation on the

geomechanical properties of simulated permafrost sediments was also investigated at predefined temperatures and confining pressures. Finally, a new physical model was developed, based on formation of hydrate networks or frame structures to interpret the observed strengthening in the shear strength and the ductile deformation.
It should be noted that the experiments in this chapter were conducted by Dr. Jinhai Yang, which is highly appreciated.

In chapter 9, we summarize the conclusions of previous sections and present recommendations for future works in our area of study.

1.9 References

(1) Yang, S. H. B.; Linga, P.; Chong, Z. R.; Babu, P.; Li, X.-S. Review of Natural Gas Hydrates as an Energy Resource: Prospects and Challenges. *Appl. Energy* **2015**, *162*, 1633–1652. DOI: 10.1016/j.apenergy.2014.12.061.

(2) Nago, A.; Nieto, A. Natural Gas Production from Methane Hydrate Deposits Using CO**2** Clathrate Sequestration: State-of-the-Art Review and New Technical Approaches. *J. Geol. Res.* **2011**, *2011*.

(3) Boot-Handford, M. E.; Abanades, J. C.; Anthony, E. J.; Blunt, M. J.; Brandani, S.; Mac Dowell, N.; Fernández, J. R.; Ferrari, M. C.; Gross, R.; Hallett, J. P.; et al. Carbon Capture and Storage Update. *Energy Environ. Sci.* **2014**, *7* (1), 130–189. DOI: 10.1039/c3ee42350f.

(4) Khatib, H. IEA World Energy Outlook 2011—A Comment. *Energy Policy* **2012**, *48*, 737–743.

(5) Sloan, E. D. Fundamental Principles and Applications of Natural Gas Hydrates. *Nature* **2003**, *426* (6964), 353–359. DOI: 10.1038/nature02135.

(6) Sloan, E. D.; Koh, C. A. *Clathrate Hydrates of Natural Gases - Chemical Industries/119*; CRC press, 2008.

(7) Kvenvolden, K. A.; McMenamin, M. A. Hydrates of Natural Gas: A Review of Their Geologic Occurrence. *Geolocial Surv. Circ.* **1980**, *825*, 1–11. DOI: 10.3133/cir825.

(8) Daniels, J. M.; Vidmar, P. J. Occurrence and Acoustical Significance of Natural Gas Hydrates in Marine Sediments. *J. Acoust. Soc. Am.* **1982**, *72* (5), 1564–1573.

(9) Soloviev, V. A. Global Estimation of Gas Content in Submarine Gas Hydrate Accumulations. *Russ. Geol. Geophys.* **2002**, *43* (7), 609–624.

(10) Boswell, R.; Collett, T. S. Current Perspectives on Gas Hydrate Resources. *Energy Environ. Sci.* **2011**, *4* (4), 1206–1215. DOI: 10.1039/c0ee00203h.

(11) Yousif, M. H.; Abass, H. H.; Selim, M. S.; Sloan, E. D. Experimental and Theoretical Investigation of Methane-Gas-Hydrate Dissociation in Porous Media. *SPE Reserv. Eng.* **1991**, *6* (01), 69–76.

(12) Xiong, L.; Li, X.; Wang, Y.; Xu, C. Experimental Study on Methane Hydrate

Dissociation by Depressurization in Porous Sediments. *Energies* **2012**, *5* (2), 518–530. DOI: 10.3390/en5020518.

(13) Circone, S.; Stern, L. A.; Kirby, S. H.; Pinkston, J. C.; Durham, W. B. Methane Hydrate Dissociation Rates at 0.1 MPa and Temperatures above 272 K. *Ann. N. Y. Acad. Sci.* **2000**, *912* (1), 544–555.

(14) Kono, H. O.; Narasimhan, S.; Song, F.; Smith, D. H. Synthesis of Methane Gas Hydrate in Porous Sediments and Its Dissociation by Depressurizing. *Powder Technol.* **2002**, *122* (2–3), 239–246.

(15) Kawamura, T.; Ohtake, M.; Sakamoto, Y.; Haneda, H.; Komai, T.; Higuchi, S. Experimental Study on Steam Injection Method Using Methane Hydrate Core Samples. In *Seventh ISOPE Ocean Mining Symposium*; International Society of Offshore and Polar Engineers, 2007.

(16) Zhao, J.; Cheng, C.; Song, Y.; Liu, W.; Liu, Y.; Xue, K.; Zhu, Z.; Yang, Z.; Wang, D.; Yang, M. Heat Transfer Analysis of Methane Hydrate Sediment Dissociation in a Closed Reactor by a Thermal Method. *Energies* **2012**, *5* (5), 1292–1308.

(17) Fitzgerald, G. C.; Castaldi, M. J. Thermal Stimulation Based Methane Production from Hydrate Bearing Quartz Sediment. *Ind. Eng. Chem. Res.* **2013**, *52* (19), 6571–6581. DOI: 10.1021/ie400025f.

(18) Pang, W. X.; Xu, W. Y.; Sun, C. Y.; Zhang, C. L.; Chen, G. J. Methane Hydrate Dissociation Experiment in a Middle-Sized Quiescent Reactor Using Thermal Method. *Fuel* **2009**, *88* (3), 497–503.

(19) Li, X.-S.; Yang, B.; Li, G.; Li, B.; Zhang, Y.; Chen, Z.-Y. Experimental Study on Gas Production from Methane Hydrate in Porous Media by Huff and Puff Method in Pilot-Scale Hydrate Simulator. *Fuel* **2012**, *94*, 486–494.

(20) Islam, M. R. A New Recovery Technique for Gas Production from Alaskan Gas Hydrates. *J. Pet. Sci. Eng.* **1994**, *11* (4), 267–281.

(21) Castaldi, M. J.; Zhou, Y.; Yegulalp, T. M. Down-Hole Combustion Method for Gas Production from Methane Hydrates. *J. Pet. Sci. Eng.* **2007**, *56* (1–3), 176–185. DOI: 10.1016/j.petrol.2006.03.031.

(22) Kawamura, T.; Sakamoto, Y.; Ohtake, M.; Yamamoto, Y.; Haneda, H.; Yoon, J.-H.; Komai, T. Dissociation Behavior of Hydrate Core Sample Using Thermodynamic Inhibitor. *Int. J. Offshore Polar Eng.* **2006**, *16* (01).

(23) He, Z.; Linga, P.; Jiang, J. CH4 Hydrate Formation between Silica and Graphite Surfaces: Insights from Microsecond Molecular Dynamics Simulations. *Langmuir* **2017**, *33* (43), 11956–11967. DOI: 10.1021/acs.langmuir.7b02711.

(24) Dong, F.; Zang, X.; Li, D.; Fan, S.; Liang, D. Experimental Investigation on Propane Hydrate Dissociation by High Concentration Methanol and Ethylene Glycol Solution Injection. *Energy & Fuels* **2009**, *23* (3), 1563–1567.

(25) Linga, P.; Haligva, C.; Nam, S. C.; Ripmeester, J. A.; Englezos, P. Gas Hydrate Formation in a Variable Volume Bed of Silica Sand Particles. *Energy and Fuels* **2009**, *23* (11), 5496–5507. DOI: 10.1021/ef900542m.

(26) Lee, J. Experimental Study on the Dissociation Behavior and Productivity of Gas Hydrate by Brine Injection Scheme in Porous Rock. *Energy & Fuels* **2009**, *24*

(1), 456–463.

(27) Bai, Y.; Li, Q. Simulation of Gas Production from Hydrate Reservoir by the Combination of Warm Water Flooding and Depressurization. *Sci. China Technol. Sci.* **2010**, *53* (9), 2469–2476.

(28) Li, X.-S.; Yang, B.; Duan, L.-P.; Li, G.; Huang, N.-S.; Zhang, Y. Experimental Study on Gas Production from Methane Hydrate in Porous Media by SAGD Method. *Appl. Energy* **2013**, *112*, 1233–1240.

(29) Li, G.; Li, X.-S.; Yang, B.; Duan, L.-P.; Huang, N.-S.; Zhang, Y.; Tang, L.-G. The Use of Dual Horizontal Wells in Gas Production from Hydrate Accumulations. *Appl. Energy* **2013**, *112*, 1303–1310.

(30) Lee, H.; Seo, Y.; Seo, Y.-T.; Moudrakovski, I. L.; Ripmeester, J. A. Recovering Methane from Solid Methane Hydrate with Carbon Dioxide. *Angew. Chemie Int. Ed.* **2003**, *42* (41), 5048–5051. DOI: 10.1002/anie.200351489.

(31) Baldwin, B. A.; Stevens, J.; Howard, J. J.; Graue, A.; Kvamme, B.; Aspenes, E.; Ersland, G.; Husebø, J.; Zornes, D. R. Using Magnetic Resonance Imaging to Monitor CH4 Hydrate Formation and Spontaneous Conversion of CH4 Hydrate to CO2 Hydrate in Porous Media. *Magn. Reson. Imaging* **2009**, *27* (5), 720–726.

(32) Graue, A.; Kvamme, B.; Baldwin, B.; Stevens, J.; Howard, J. J.; Aspenes, E.; Ersland, G.; Husebo, J.; Zornes, D. MRI Visualization of Spontaneous Methane Production from Hydrates in Sandstone Core Plugs When Exposed to CO2. *Spe J.* **2008**, *13* (02), 146–152.

(33) Ohgaki, K. A Proposal for Gas Storage on the Bottom of the Ocean Using Gas Hydrates. *Int. Chem. Eng.* **1994**, *34*, 417–419.

(34) Seo, Y.-T.; Lee, H. Multiple-Phase Hydrate Equilibria of the Ternary Carbon Dioxide, Methane, and Water Mixtures. *J. Phys. Chem. B* **2001**, *105* (41), 10084–10090.

(35) Lee, B. R.; Koh, C. A.; Sum, A. K. Quantitative Measurement and Mechanisms for CH4 Production from Hydrates with the Injection of Liquid CO2. *Phys. Chem. Chem. Phys.* **2014**, *16* (28), 14922–14927. DOI: 10.1039/c4cp01780c.

(36) Goel, N. In Situ Methane Hydrate Dissociation with Carbon Dioxide Sequestration: Current Knowledge and Issues. *J. Pet. Sci. Eng.* **2006**, *51* (3–4), 169–184.

(37) Panter, J. L.; Ballard, A. L.; Sum, A. K.; Sloan, E. D.; Koh, C. A. Hydrate Plug Dissociation via Nitrogen Purge: Experiments and Modeling. *Energy & Fuels* **2011**, *25* (6), 2572–2578.

(38) Masuda, Y.; Konno, Y.; Hasegawa, T.; Haneda, H.; Ouchi, H.; Kurihara, M. Prediction of Methane Hydrate Dissociation Behavior by Nitrogen Gas Injection. In *Proceedings of the 6th international conference on gas hydrates, vancouver, British Columbia, Canada*; 2008.

(39) Lee, Y.; Kim, Y.; Lee, J.; Lee, H.; Seo, Y. CH4 Recovery and CO2 Sequestration Using Flue Gas in Natural Gas Hydrates as Revealed by a Micro-Differential Scanning Calorimeter. *Appl. Energy* **2015**, *150*, 120–127.

(40) Garapati, N.; McGuire, P.; Anderson, B. J. Modeling the Injection of Carbon Dioxide and Nitrogen into a Methane Hydrate Reservoir and the Subsequent

Production of Methane Gas on the North Slope of Alaska. In *Unconventional Resources Technology Conference*; Society of Exploration Geophysicists, American Association of Petroleum …, 2013; pp 1942–1951.

(41) White, M.; Suk Lee, W. Guest Molecule Exchange Kinetics for the 2012 Ignik Sikumi Gas Hydrate Field Trial. In *Offshore Technology Conference*; Offshore Technology Conference, 2014.

(42) Kang, H.; Koh, D.; Kim, D.; Park, J.; Cha, M.; Lee, H. Recovery of Methane Intercalated in Natural Gas Hydrate Sediments Using a Carbon Dioxide and Flue Gas Mixture. In *Isope*; International Society of Offshore and Polar Engineers, 2012; Vol. 4, pp 67–71.

(43) Park, Y.; Cha, M.; Cha, J.-H.; Shin, K.; Lee, H.; Park, K.-P.; Huh, D.-G.; Lee, H.-Y.; Kim, S.-J.; Lee, J. Swapping Carbon Dioxide for Complex Gas Hydrate Structures. In *ICGH 6th International Conference on Gas Hydrates*; Citeseer, 2008.

(44) Collett, T. S.; Ginsburg, G. D. Gas Hydrates in the Messoyakha Gas Field of the West Siberian Basin-a Re-Examination of the Geologic Evidence. *Int. J. Offshore Polar Eng.* **1998**, *8* (01).

(45) Collett, T. S. Potential of Gas Hydrates Outlined. *Oil Gas J.* **1992**, *90* (25), 84–87.

(46) Anderson, B. J.; Kurihara, M.; White, M. D.; Moridis, G. J.; Wilson, S. J.; Pooladi-Darvish, M.; Gaddipati, M.; Masuda, Y.; Collett, T. S.; Hunter, R. B. Regional Long-Term Production Modeling from a Single Well Test, Mount Elbert Gas Hydrate Stratigraphic Test Well, Alaska North Slope. *Mar. Pet. Geol.* **2011**, *28* (2), 493–501.

(47) Hancock, S. H.; Collett, T. S.; Dallimore, S. R.; Satoh, T.; Inoue, T.; Huenges, E.; Henninges, J.; Weatherill, B. Overview of Thermal-Stimulation Production-Test Results for the JAPEX/JNOC/GSC et Al. Mallik 5L-38 Gas Hydrate Production Research Well. *Bull. Surv. Canada* **2005**, *585*, 135.

(48) Hancock, S. H.; Dallimore, S. R.; Collett, T. S.; Carle, D.; Weatherill, B.; Satoh, T.; Inoue, T. Overview of Pressure-Drawdown Production-Test Results for the JAPEX/JNOC/GSC et Al. Mallik 5L-38 Gas Hydrate Production Research Well. *Bull. Surv. Canada* **2005**, *585*, 134.

(49) Kurihara, M.; Ebinuma, T.; Ouchi, H.; Funatsu, K.; Ashford, D.; Wright, F.; Numasawa, M.; Dallimore, S.; NARITA, H.; Yamamoto, K.; et al. Analysis of Production Data for 2007/2008 Mallik Gas Hydrate Production Tests in Canada. In *International Oil and Gas Conference and Exhibition in China*; Society of Petroleum Engineers, 2010. DOI: 10.2523/132155-ms.

(50) Martin, K. L.; Howard, J.; Silpngarmlert, S.; Schoderbek, D.; Hester, K. North Slope Hydrate Fieldtrial: CO2/CH4 Exchange. In *Society of Petroleum Engineers - Arctic Technology Conference 2012*; Offshore Technology Conference, 2012; Vol. 1. DOI: 10.4043/23725-ms.

(51) Schicks, J. M., Strauch, B., Heeschen, K. U., Spangenberg, E., & Luzi-Helbing, M. From Microscale (400 µl) to Macroscale (425 L): Experimental Investigations of the CO2/N2-CH4 Exchange in Gas Hydrates Simulating the Iġnik Sikumi Field Trial. Journal of Geophysical Research: Solid Earth. **2018**, 123(5), 3608-3620.

(52) Boswell, R., Schoderbek, D., Collett, T. S., Ohtsuki, S., White, M., & Anderson, B. J. The Ignik Sikumi Field Experiment, Alaska North Slope: Design, Operations, and Implications for CO2–CH4 Exchange in Gas Hydrate Reservoirs. Energy & Fuels. **2016**, 31(1), 140-153.

(53) Boswell, R. Japan Completes First Offshore Methane Hydrate Production Test—methane Successfully Produced from Deepwater Hydrate Layers. *Cent. Nat. Gas Oil* **2013**, *412*, 386–7614.

(54) Li, J.; Ye, J.; Qin, X.; Qiu, H.; Wu, N.; Lu, H.; Xie, W.; Lu, J.; Peng, F.; Xu, Z. The First Offshore Natural Gas Hydrate Production Test in South China Sea. *China Geol.* **2018**, *1* (1), 5–16.

Chapter 2 - Solubility of Flue Gas in Water and Aqueous Solutions of Salts: Experimental Measurement and Thermodynamic Modelling

2.1 Introduction

Nowadays, fossil fuels, as the main sources of energy demanded in the world, are the major contributors to unprecedented anthropogenic CO_2 concentration in the atmosphere[1-2]. Use of the fossil fuels as a dominant energy resource is anticipated to be continued in the foreseeable future[3] despite the fact that the main portion of the greenhouse effect and global warming is unquestionably caused by the anthropogenic CO_2[4-5]. Hence, it is inevitable to develop efficient systems to capture and sequester the CO_2 away from the atmosphere to stabilize its atmospheric concentration and mitigate environmental problems[6]. Carbon capture and storage (CCS) refers to a process in which CO_2 is captured from large point sources (e.g. fossil fuel power plants) and stored into storage sites such as geological formations[7-10]. Localized reductions in CO_2 emission have been achieved by CCS pilots operating in the USA and Europe[11]. Regarding the high cost of conventional CCS technologies[12], it has been extensively attempted to enhance the efficiency of CCS processes by developing economical and viable CCS techniques[13]. However, there is still a number of technical and economic hindrances to be addressed[14].

Recently, injecting CO_2 into deep saline aquifers has been suggested as one of the potential CCS techniques. In this method, two mechanisms including solubility trapping and mineral trapping participate for long-term storage of the injected CO_2. The solubility trapping refers to dissolution of CO_2 into the formation water while the mineral trapping takes place by chemical transformation of the dissolved CO_2 to geologically and thermodynamically stable carbonate minerals. It is essential to conduct adequate theoretical and experimental studies on the two mechanisms to understand the interactions between the injected gas and formation water as well as the effect of other constituents and salinity of the formation water on CO_2 solubility[15-16].

More recently, direct injection of flue gas into methane hydrate-bearing sediments has been proposed as a cost-effective and advantageous technique for simultaneous recovery of methane and sequestration of CO_2 as gas hydrate from the flue gas[17-21]. The North Slope of Alaska hydrate field trial successfully demonstrated that it is technically feasible to produce methane and store CO_2 as hydrate by injection of CO_2-N_2 mixture into gas hydrate reservoirs[22-24]. In addition to the economic advantages, injection of the CO_2-N_2

in methane hydrate reservoirs results in a higher mobility in the sediments and subsequently higher methane recovery compared with those of pure CO_2[25-26]. Successful application of this method may persuade other CCS techniques to use the flue gas instead of pure CO_2 in order to reduce the CO_2 separation costs. To achieve this, it is necessary to understand physical and chemical interactions between water and CO_2 when other constituents of the flue gas such as N_2 coexist. Gas hydrates which are ice-like inclusion crystalline solids with water molecules encaged small gas molecules, stand in need of specific conditions in terms of pressure, temperature, and gas phase composition to be stable[27-28]. Accordingly, the presence of N_2 alters CO_2 solubility in water and consequently hydrate stability zone (HSZ) due to change in the flue gas composition after being contacted with water, which, in turn, alters the stable hydrate composition at various pressures and temperatures[27]. Therefore, since the presence of other constituents strongly affects the thermodynamic behavior of CO_2, their influence is required to be recognized and addressed in the CCS process design[29-30].

Given the remarkable influence of other constituents in gas stream on the CO_2 solubility in water and brine[31], such solubility data must be used for efficient design, development, and deployment of innovative CCS techniques, particularly the techniques in which the equilibrium liquid-phase composition is required to estimate the gas-liquid mass transfer rate. Furthermore, since there are limited experimental data available in the open literature for ternary and multicomponent systems with water[31], it is necessary to study these systems in terms of the fluid phase equilibria and solubility to assess thermodynamic models and improve their accuracy and reliability. Finally, calculating the solubility of different gases in the aqueous phase is a key factor for conducting molecular dynamics simulations in gas hydrate related researches[32-33].

CO_2 solubility in water and aqueous solutions of salts such as NaCl, KCl, and $CaCl_2$ has been well reported in literature[34-59]. Many efforts were made to study the solubility of N_2 in water and brine[60-71]. Furthermore, the phase equilibria and solubility of CO_2-N_2 contained mixtures have been studied by researchers (Table 2.1). As discussed, the flue gas storage in saline aquifers together with the gas hydrate-based CO_2 separation and storage are considered as the promising CCS techniques. Therefore, knowledge gaps regarding these techniques, including the solubility of gas mixtures in water and brine, is essential to be addressed before commercial implementation. However, to the best of our knowledge, little experimental data of CO_2 solubility in water and brine are available in literature for systems containing N_2 at the actual operational conditions of CCS techniques.

In this study, we introduce the application of a new well-characterized method for measuring the solubility of gas mixtures at liquid-gas systems, also applicable for liquid-liquid systems. The most critical advantages of this method are zero dead-volume for gas samples and higher speed of the measurements, increasing the accuracy and reducing the time required for collecting data. After the method was successfully evaluated using the existing solubility data, we accurately measured solubility of three different types of CO_2-N_2 mixtures in water and brine. The measurements were carried out over a wide range of pressures and temperatures covering the typical operational conditions of CCS techniques. Additionally, a thermodynamic model was utilized to predict the equilibrium compositions of both liquid and vapor phases at each experimental point. Three equations of state (EOS) including CPA-SRK72, VPT, and PC-SAFT were tuned by adjusting the BIPs and applied to calculate the fugacity values. Finally, the experimental data and the model predictions were compared with each other to evaluate the accuracy of the equations of state at different operating conditions.

*Table 2.1 Available VLE (Vapor Liquid Equilibria), density and solubility data in the literature for CO_2-N_2 contained mixtures**

No.	Year	Reference	System: CO_2 + N_2 + X	Property Type	Pressure		Temperature	
					Range (MPa)	Uncertainty	Range (K)	Uncertainty
1	1963	[72]	O_2	VLE	5.2-11	-	218-273	-
2	1965	[73]	O_2	VLE	5.2-11	0.10%	273.15	0.01 K
3	1971	[74]	CH_4	VLE	6.1-10.1	-	233-273	-
4	1978	[75]	CH_4	VLE	4.6-9.6	1.00%	270	0.02 K
5	1983	[76]	CH_4	VLE	6.0-12.2	0.001 MPa	220-240	0.02 K
6	1983	[77]	CF_2Cl_2	VLE	3.0-20	1.00%	223.15-273.15	0.05 K
7	1984	[78]	CH_3OH	Solubility	0.3-18.0	0.004 MPa	223-300	0.05 K
8	1986	[79]	n-C_{19}	VLE	5.8-8.2	0.70%	294.15-301.15	0.02 K
9	1988	[80]	C_2H_6	VLE	0.8-9.6	0.02 MPa	220-270	0.02 K
10	1989	[81]	n-C_4	VLE	3.4-27.6	1.00%	310.9-410.9	0.05 K
11	1989	[82]	Cyclohexane	VLE	6.9-27.6	0.01 MPa	366.5-410.9	0.05 K
12	1989	[83]	CH_4	VLE	2.0-12	-	220	-
13	1990	[84]	CH_4	VLE	6.2-10.3	0.1 MPa	230-250	0.02 K
14	1991	[85]	$CHClF_2$	VLE	1.6-5.2	0.50%	263.2-288.2	0.1 K
15	1992	[86]	CH_4	VLE	6-8.3	0.02 MPa	293	0.01 K
16	1996	[87]	CH_4	Density	19.9-100	2.00%	323.15-573.15	0.05 K
17	1999	[88]	C_3H_8	VLE	2.0-13	0.001 MPa	240-330	0.1 K
18	2012	[89]	H_2O H_2O + NaCl + KCl	VLE	8.0-16	0.13%	308.15-318.15	0.05 K
19	2015	[90]	H_2O	Solubility	8.0-18	0.0005 MPa	298.15-313.15	0.3 K
20	2015	[91]	H_2	VLE	2.1-8.7	0.07%	252-304	0.1 K
21	2017	[92]	O_2	VLE	4.0-15	0.06 MPa	233-273	0.06 K
22	2017	[93]	Ar	VLE Density	0-23	0.07%	268-303	0.1 K

* Available literature data for equilibrium phases under gas hydrate formation conditions can be found elsewhere [94-95].

2.2 Experimental Section

2.2.1 Materials and apparatus

Research-grade CO_2 and N_2 (purity 99.995 vol. %) were supplied by BOC Ltd. NaCl with a certified purity of 99.50 % was provided by Fisher Scientific. Deionized water generated by an integral water purification system (ELGA DV 25) was used throughout the experiments.

Figure 2.1 shows a schematic representation of the high-pressure apparatus used in this work. In this setup, a 316 stainless steel cylindrical autoclave (V_{Vessel}: 180 cm^3, Max. working pressure: 22 MPa), was utilized as the measurement vessel. An integral cooling jacket fitted around the measurement vessel is connected to a cryostat (Grant LTC) to achieve isothermal conditions. A calibrated Platinum-Resistance Thermometer (Pt 100, supplied by TC Ltd.) (PRT) with an accuracy of better than ±0.1 K was coated in the stainless steel to measure the vessel temperature. Regarding the temperature gradient in the cell, as the volume of the cell was considerably small compared to the surrounding cooling jacket, and the cooling rate was at maximum, the temperature gradient was neglected in all the measurements. The system pressure was measured using a precise calibrated Quartzdyne pressure transducer (QS30K–B, Quartzdyne Inc., USA) with an accuracy of ±0.005 MPa. A high-pressure magnetic stirrer (6180300B, Top Industrie SA, France) was located at the bottom of the vessel with a Rushton type impeller agitating the fluids to in order to attain a fast thermodynamic equilibrium. The pressure and temperature data were acquired using a data acquisition device and recorded on a PC with a LabVIEW software interface. Gas was injected into the measurement vessel via a tube connected to a source cell with volume of V_{Source} containing CO_2-N_2 gas mixture with the desired composition. Two temperature probes along with a pressure transducer were connected to the source cell to record the pressure and temperature of the cell.

The vessel was equipped with a movable capillary sampler (ROLSI^{TM}). The capillary sampler is usable for corrosive gases and able to operate from 233 to 373 K. Moreover, it has zero dead volume which makes it simple to take microliter samples from any desired phase by using an elevator joystick (to set the location of sampling) via a thin capillary tube (with internal diameter of 0.1 mm) connected through the top of the vessel. Since the volume of the taken sample is negligible compared with the volume of the vessel, the thermodynamic equilibrium inside the vessel does not be disturbed. The samples are heated in an expansion room to be fed through a heated line into the carrier gas stream of a gas chromatograph (Varian 3600, Agilent Technologies) for analysis. While in

application of this method, amount of the sampled gas is severely limited by the electromagnetic mechanism of the sampler. The sampler has an online connection to the GC, enabling solubility measurements to be automotive and time efficient.

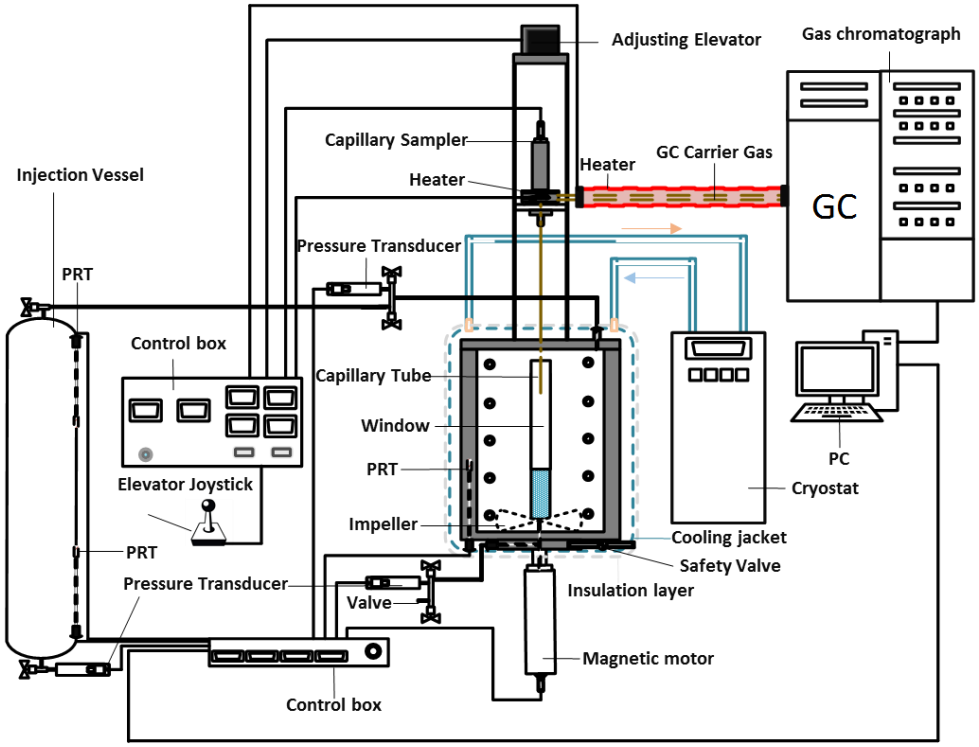

Figure 2.1 Schematic representation of the high-pressure experimental apparatus

2.2.2 Experimental procedure

Three typical types of simulated flue gases with different compositions (Table 2.2) were tested in this work. In the same line with our previous studies[20-21, 96], these gas mixtures were selected to simulate the main compositions of industrial flue gases and cover a wide range of CO_2-N_2 composition. For each type of flue gas, the corresponding CO_2-N_2 mixture was prepared in the source cell by injecting pure N_2 and CO_2 at a pre-determined molar ratio, mixing and leaving the mixture till the pressure and temperature of the cell become stable to ensure the homogeneity before commencing the experiment. In addition, three samples was taken and analyzed by the GC to confirm the desired gas composition.

Table 2.2 Compositions of flue gas types used in this study

Component	Composition (mole %)		
	Type 1: Coal-Fired Flue Gas	**Type 2: Gas-Fired Flue Gas**	**Type 3: Syngas**
N_2	85.4%	97.0%	39.0%
CO_2	14.6%	3.0%	61.0%

For a typical isothermal set of experiments, the measurement vessel was firstly washed, dried, sealed and vacuumed; then a certain amount of deionized water or brine prepared gravimetrically at a pre-specified salinity (m_L) with molecular weight of M_L and

gravimetric density of ρ_L was loaded from the bottom into the vessel. The cryostat was switched on to achieve the desired temperature. The system was left for at least 12 hours to ensure the stability of the system temperature at the determined value.

At a certain stage of pressure, the gas mixture with the known composition was introduced into the system and the mixture was left stirring until the variations in the system pressure became stable within ±0.0001 MPa. At each sampling point, three samples were taken from the vapor phase using the capillary sampler and analyzed with the GC. The pressure and temperature values of the measurement vessel and source cell were recorded twice: i) before injecting the flue gas into the system ($P_{1,Source}$ and $T_{1,Source}$), ii) after flue gas injection and thermodynamic equilibrium ($P_{2,Source}$ and $T_{2,Source}$). After taking the samples, the pressure and temperature of the measurement vessel were monitored (P_{Vessel} and T_{Vessel}) to make sure that the sample removal did not affect the pressure and temperature of the vessel. The recorded properties along with the GC data were used to determine the volume of the injected gas at the pressure stage, the amount of gas dissolved in the liquid phase and subsequently the solubility values. Figure 2.2 schematically illustrates the procedure followed for the CO_2 solubility (x_{CO2}) calculation. In this figure y_i, R, and n_i stand for mole fraction of i^{th} component in vapor phase, gas constant, and number of i^{th} component, respectively. As can be seen, CPA-SRK72[97] EOS [98-99] has been used for calculation of the compressibility factor (z) for the gas mixtures.

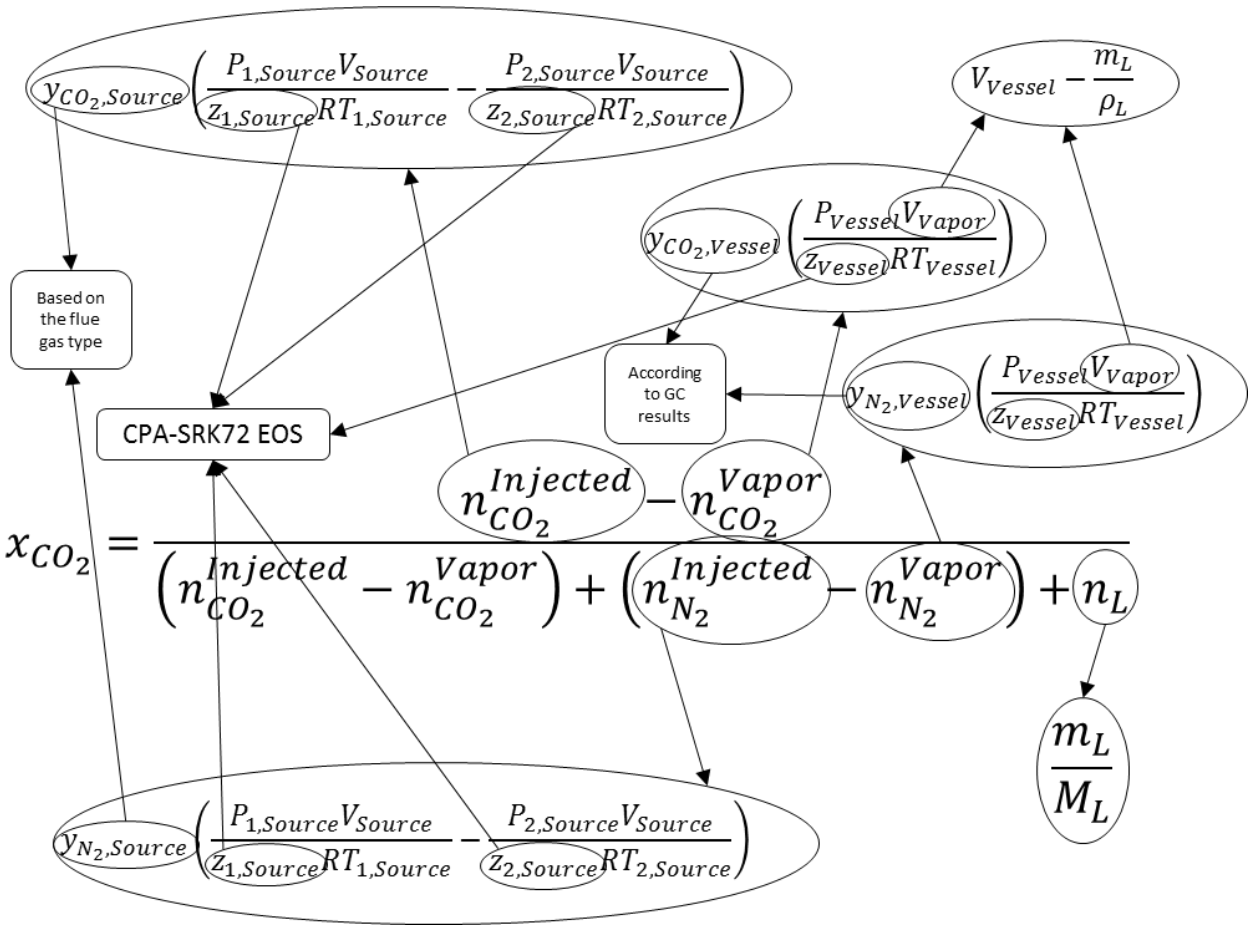

Figure 2.2 Schematic procedure of the solubility calculation for CO_2.

2.3 Thermodynamic modelling

A thermodynamic model was utilized based on the general criterion of thermodynamic equilibrium for isothermal systems i.e. equality of fugacity for each component in all phases[100]. To determine the fugacity of each component, three well-known equations of state including CPA-SRK72, VPT and PC-SAFT were applied. CPA-SRK72 EOS efficiently accounts for the physical interactions in mixtures containing associating compounds via combining the Cubic-Plus-Association (CPA) EOS with original Soave-Redlich-Kwong (SRK72) EOS[98-99]. Valderrama-Patel-Teja (VPT) EOS employs a non-density dependent (NDD) mixing rule for calculating the mixture parameters for asymmetric mixtures. This EOS is also successfully extended for prediction of thermodynamic properties for electrolyte solutions, particularly at high-pressure conditions[101]. PC-SAFT EOS, presented by Gross and Sadowski, has found several successful applications, especially for complex mixtures such as mixtures containing associating and polar molecules[102]. Here, we briefly discuss each EOS and refer the readers to relevant references for further studies.

2.3.1 CPA-SRK72 Equation of State

CPA-SRK72 has been recently applied successfully to describe the thermodynamic behavior of the CO_2-contained and water-contained mixtures [103]. In this EOS, the original SRK72 EOS [104] is combined with the Wertheim's first-order thermodynamic perturbation theory to describe the physical interactions as well as the effect of hydrogen bonding. The results obtained from this equation of state for multicomponent systems, in particular, for mixtures of strongly associating compounds, were very satisfactory[98, 99]. This EOS in terms of pressure can be written as:

$$P = P_{Physical\ Interaction} + P_{Association} \tag{1}$$

in which:

$$\begin{cases} P_{Physical\ Interaction} = \dfrac{RT}{\bar{V}-b} - \dfrac{a(T)}{\bar{V}(\bar{V}+b)} \\ P_{Associatiation} = -\dfrac{1}{2}\dfrac{RT}{\bar{V}}\left(1+\rho\dfrac{\partial \ln\left(g(\rho)\right)}{\partial\rho}\right)\sum_i x_i \sum_{A_i}\left(1-X_{A_i}\right) \end{cases} \tag{2}$$

In the physical interaction term, b is the co-volume parameter, $\bar{V}$ is the specific volume, and a(T) is the attraction parameter determined as:

$$a(T) = a_0\left[1+c_1\left(1-\sqrt{\frac{T}{T_c}}\right)\right]^2 \tag{3}$$

Here T_c is the critical temperature of the fluid, and a_0, c_1 are the constants known for each individual compound.

In the association term, ρ, g, x_i and X_{Ai} stand for fluid molar density, radial distribution function, mole fraction of the compound i and mole fraction of the compound i not bonded at site A, respectively. X_{Ai} can be obtained through Eq. (4):

$$X_{A_i} = \left(1+\rho\sum_j x_j \sum_{B_j} X_{B_j}\Delta^{A_iB_j}\right)^{-1} \tag{4}$$

Here, X_B is all other kind of association sites B. Δ^{AiBj} is called the association strength between the site A on the compound i and the site B on the compound j expressed as:

$$\Delta^{A_iB_j} = g(\rho)\left(\exp\left(\frac{\epsilon^{A_iB_j}}{RT}\right)-1\right)b_{ij}\beta^{A_iB_j} \tag{5}$$

In Eq. (5), ϵ^{AiBj} and β^{AiBj} are the association energy and association volume, respectively. A comprehensive discussion regarding this EOS can be found elsewhere [98-99].

In this work, CPA-SRK72 EOS employed the classical mixing rules to calculate the fugacity values. The simplified-hard sphere radial distribution function suggested by Kontogeorgis et al. was also used in the association term calculations [105]. A four-site (4C)

association scheme was adopted for water as a highly hydrogen-bonded substance. Table 2.3 summarizes the CPA-SRK72 EOS pure compound parameters.

Table 2.3 CPA-SRK72 EOS parameters for water (SI units)

a_0	B	c_1	ϵ	β	Reference
0.12277	1.4515×10^{-5}	0.67359	16655	69.2×10^{-3}	[105]

2.3.2 VPT Equation of State

VPT (Valderrama modification of Patel and Teja) equation of state is a three-parameter EOS similar to the PT (Patel and Teja) which is well proven and has been applied efficiently for predicting the volumetric properties of fluids[106]. In VPT equations the empirical parameters of PT equations regarding critical compressibility factor and acentric factor were formulated and no adjustable parameters required in terms of the mentioned properties. In terms of pressure, this EOS can be expressed by:

$$P = \frac{RT}{\bar{V} - b} - \frac{a(T)}{\bar{V}(\bar{V} + b) + c(\bar{V} - b)} \tag{6}$$

in which:

$$a(T) = a_c \left[1 + m\left(1 - \sqrt{\frac{T}{T_c}}\right)\right]^2 \tag{7}$$

Here m is a constant known for each individual compound and a_c is the force constant in the critical point. VPT is able to predict the properties of both polar and non-polar fluids with a remarkable accuracy by using a non-density dependent (NDD) mixing rule developed by Avlonitis et al. to calculate the mixture parameters for asymmetric mixtures [107]. In the NND mixing rule, the attraction parameter a(T) is separated into classical mixing rule part a^m and asymmetric contribution part a^A [100]:

$$a = a^m + a^A \tag{8}$$

where:

$$a^m = \sum_i \sum_j x_i x_j \sqrt{a_i a_j}\left(1 - k_{ij}\right) \tag{9}$$

$$a^A = \sum_p x_p^2 \sum_i x_i a_{pi} l_{pi} \tag{10}$$

In Equation (9), k_{ij} is the classical binary interaction parameter. Parameters a_{pi} and l_{pi} are determined as:

$$a_{pi} = \sqrt{a_p a_i} \tag{11}$$

$$l_{pi} = l_{pi}^0 - l_{pi}^1 (T - 273.15) \tag{12}$$

In the above equations, the subscript p stands for polar components and l_{pi} is the temperature dependent binary interaction parameter between the polar component and the others. More details about VPT EOS can be found in the literature [100]. Critical properties and acentric factor of pure compounds used in this EOS are provided in Table 2.4.

Table 2.4 Critical properties and acentric factor of water, CO_2, and N_2

Component	P_c (MPa)	T_c (K)	Z_c	ω	Reference
Water	22.055	647.13	0.2294	0.3449	[100]
CO_2	7.382	304.19	0.2744	0.2276	[100]
N_2	3.394	126.10	0.2917	0.0403	[100]

2.3.3 PC-SAFT Equation of State

PC-SAFT is a modified SAFT EOS widely used to predict the phase behavior of the complex systems. This EOS considers molecules as chains composed of spherical segments. The PC-SAFT EoS has been one of the most reliable equations of state that was proposed for non-associating fluids by applying the perturbation theory for dispersive interactions within the PC-SAFT model. A simple approximate solution for a given molecular model is typically described using perturbation theories. Originally, the PC-SAFT assumed the hard-sphere fluid as a reference fluid and was developed for spherical molecules. In this methodology, the total intermolecular forces are divided into reference and perturbation terms. The hard chain fluid with high attractive intermolecular forces is assumed as the reference fluid in the model. There are three specific parameters for non-associating compounds including the segment number in the chain (m), the spherical segment diameter (σ) and the dispersion interaction energy between the segments (ε/k) and also two additional parameters for associating compounds including the association energy (ε^{AB}) and the association volume (κ^{AB}) which are set through fitting experimental data at certain experimental conditions [102]. To calculate the effective hard sphere diameter, a pair potential function for the segment of a chain is employed as [108]:

$$u(r) = \begin{cases} \infty & r < \sigma - s_1 \\ 3\varepsilon & \sigma - s_1 \le r < \sigma \\ -\varepsilon & \sigma < r < \alpha\sigma \\ 0 & \alpha\sigma \le r \end{cases} \quad (13)$$

where α and s_1 are two constants and r denotes the radial distance between two segments. In terms of the reduced Helmholtz energy (A), PC-SAFT can be written as:

$$\frac{A^{Res}}{NkT} = \frac{A^{HC}}{NkT} + \frac{A^{Disp}}{NkT} \quad (14)$$

in which N and k are the total number of molecules and Boltzmann constant, respectively. More details regarding PC-SAFT EOS can be found elsewhere [109-110]. PC-SAFT parameters for water, CO_2, and N_2 used in this study are listed in Table 2.5.

Table 2.5 PC-SAFT parameters for water, CO_2, and N_2

Component	MW (kg/kmol)	M	σ(Å)	ε/k (K)	ε^{AB}(K)	κ^{AB}	Reference
Water	18.02	2.00	2.3533	207.84	1506.4	0.1550	[111]
CO_2	44.01	2.0729	2.7852	169.21	-	-	[110]
N_2	28.01	1.2053	3.3130	90.96	-	-	[110]

2.3.4 Modeling of the aqueous solution of NaCl

The impact of NaCl on the equilibrium compositions was incorporated in the model by using the method introduced by Aasberg-Petersen et al. [112]. In this method, an electrostatic contribution is added to the fugacity coefficient of components in the aqueous phase to take the shift in the equilibrium conditions into account:

$$\ln(\phi_i) = \ln\left(\phi_i^{EOS}\right) + \ln(\gamma_i^{EL}) \qquad (15)$$

in which φ_i^{EOS} is the fugacity coefficient of non-electrolyte component i computed by an EOS. γ_i^{EL} is the Debye-Hückel activity coefficient calculated by:

$$\ln(\gamma_i^{EL}) = \frac{2Ah_{is}M_m}{B^3} f\left(BI^{1/2}\right) \qquad (16)$$

In Eq. (16), his is the adjustable interaction coefficient between the salt and non-electrolytic components and Mm is the molecular weight of the salt-free mixture. More detailed discussion regarding this method could be found elsewhere 113. Table 2.6 presents the formulas used to calculate H_2O-NaCl, CO_2-NaCl and N_2-NaCl interaction coefficients in this study. We measured the solubility of CO_2 in brine and performed a regression against the solubility data to obtain the CO_2-NaCl interaction coefficients. Moreover, $h_{N2\text{-}NaCl}$ was regressed against the solubility data of N_2 in brine reported by Mao and Duan 114.

Table 2.6 Interaction coefficients between NaCl and water, CO_2, and N_2

Component	Formula	Reference
H_2O	$h_{H_2O-NaCl} = -\frac{3879.89}{W} - 6.09W^2 - \frac{45.95}{W^2} - 8137.28T + 10.43$	[113]
CO_2	$h_{CO_2-NaCl} = 47.665 - 0.432T + 1.463 \times 10^{-3}T^2 - 2.163 \times 10^{-6}T^3$	This Work
N_2	$h_{N_2-NaCl} = 32.849 - 0.238T + 5.751 \times 10^{-4}T^2 - 4.510 \times 10^{-7}T^3$	[114], This Work

2.3.5 Binary interaction parameters (BIPs)

2.3.5.1 CPA-SRK72

The temperature dependent BIPs were taken equal to those of the work of Haghighi et al. [115] represented by Eq. (17). Coefficients A and B are also summarized in Table 2.7.

$$k_{ij} = A + \frac{B}{T} \qquad (17)$$

Table 2.7 Optimized BIPs between water and the other gas components used for CPA-SRK72

Component	A	B	Reference
CO_2	0.1099	-53.7586	[115]
N_2	0.9909	-379.9691	[115]

2.3.5.2 VPT

The parameters of the experimental BIPs reported by Chapoy et al. [116] aresummarized in Table 2.8.

Table 2.8 BIPs between water and the other gas components used for VPT

Component	$k_{Water-j}$	l_{H2O}^0	l_{H2O}^1	Reference
CO_2	0.19	2.78	23.5	[116]
N_2	0.49	2.68	36.8	[116]

2.3.5.3 PC-SAFT

We adjusted the temperature dependent BIPs using the solubility data measured for water-N_2 and water-CO_2 binary systems through a simplex algorithm through using the objective function expressed by Eq. (18):

$$OBJ = \sum_{i=1}^{N} \left(\frac{x_i^{Pre.} - x_i^{Exp.}}{x_i^{Exp.}} \right)^2 \quad (18)$$

In this equation, N and x_i are the total number of data points and the solubility of CO_2 or N_2 in water at specified temperature and pressure, respectively. We fitted the BIPs to a quadratic polynomial function presented by:

$$k_{ij} = A_0 + A_1 T + A_2 T^2 \quad (19)$$

Constants A_0, A_1 and A_2 are reported in Table 2.9.

Table 2.9 Constants of the temperature dependent BIP polynomial function

Binary System	A_0	A_1	A_2
Water-CO_2	-1.67617	1.27089×10^{-2}	-3.07478×10^{-5}
Water-N_2	-1.09318	5.41529×10^{-3}	-6.39052×10^{-6}

2.4 Results and discussion

In this section, the results of the experimental measurements are presented and compared with the predictions made by the thermodynamic model described in the previous section. The operating conditions were set at 273.25, 283.15 and 303.15 K (0.1, 10.0 and 30.0 °C) and pressures up to 22 MPa to cover the typical operational conditions outside the flue gas hydrate stability zone [21]. Due to the negligible concentration of water in the vapor phase, the mole fractions of CO_2 and N_2 in the vapor phase at the experimental conditions are reported on the water-free basis [20,57].

2.4.1 Solubility of CO_2 and N_2 in water

Changes in composition of vapor phase after gas dissolution in water leads to significantly different HSZs when compared with initial composition[20]. As discussed before, for the hydrate-based gas separation and storage, gas composition is essential to obtain optimized conditions. However, the presence of mixed gas with different partial solubility for each component of the gas makes it difficult to accurately predict HSZ. Accordingly, partial solubility of each component is essential property that needs to be determined via solubility curves for different components. The flue gas solubility was measured at three different isotherms of 273.25, 283.15 and 303.05 K and plotted in Figures 3-5. As can be seen, the experimental and predicted equilibrium compositions of the liquid and vapor phases for CO_2-N_2-Water ternary systems show the typical PT features of gas solubility: higher solubility at higher pressures and lower temperatures. Notably higher solubility for CO_2 than N_2 at all PT conditions was observed. Since CO_2 molecule has a slight negative charge near the oxygen and a slight positive charge near the carbon, it is expected to be more soluble than N_2 because water molecules are attracted to these polar areas.

Pure N_2 is known to require considerably higher pressure to form hydrate compared to CO_2 which can form single guest structure I hydrate at low pressure. This leads to the HSZ shifting to higher pressures after gas dissolution, which can be calculated using the measured gas composition after the gas dissolution. As also seen, CO_2 concentration change in the vapor phase can be up to more than 40% in some cases, which can change HSZ up to more than 6 MPa[20]. This becomes even clearer at lower temperature. Therefore, it can be concluded that partial solubility effect on the HSZ plays a major role in determining the equilibrium pressures. Considering the presence of gas mixtures in the system, it was important to calculate relative mole percent of each gas and water in the system for modelling approach, as otherwise no quantitative comparison was achieved. These quantities together with measured solubility data are provided in the Appendix A.

Interestingly, partial solubility of CO_2 in water at all PT conditions is considerably higher when compared to that of pure CO_2 at the same temperature and partial pressures. Accordingly, the presence of N_2 will increase overall pressure of the system if the amount of CO_2 is limited. This will consequently increase the amount of dissolved CO_2 in water. Furthermore, the experimental results have also been compared with the predictions made by CPA-SRK72, VPT and PC-SAFT for all the experimental data points in Figures 3-5. The comparisons demonstrate that the predictions made by the equations of state are in good agreement with the measured experimental data.

Table 2.10 summarizes the average relative deviation (ARD) of the equations of state used in this study from the experimental data (Figures 3-5) calculated as:

$$ARD\ (\%) = \frac{100}{N}\sum_{i}^{N}\left(\frac{\theta_{j,Pre.} - \theta_{j,Exp.}}{\theta_{j,Exp.}}\right) \qquad (20)$$

in which θ_j is the equilibrium composition of component j (CO_2 or N_2) in the liquid or vapor phase and N is the total number of measurements at a specific isotherm condition. By comparing the AADs in the table, one can find that VPT EOS is able to predict the equilibrium compositions of CO_2 and N_2 more accurately compared to the other two equations of state, particularly in lower temperatures and for the gas types 1 and 2 in which the concentration of CO_2 is remarkably lower than N_2. In other words, as the temperature of the system or the concentration of CO_2 in the gas mixture increases, the accuracy of VPT in determination of the equilibrium compositions of CO_2 and N_2 decreases. Besides, deviations of the statistical thermodynamics-based equations of state from the experimental measurements decrease when the temperature is raised. In particular, in terms of the equilibrium mole fraction of CO_2 in liquid and vapor phases for the gas of Type 3, CPA-SRK72 and PC-SAFT predictions are more accurate in comparison with VPT. It is also observed that PC-SAFT presents lower deviations at 303.05 K for all types of the gases. Meanwhile, it has some difficulties representing the mole fraction of N_2 in the liquid phase.

The measured values of solubility data in deionized water are summarized in Figure 2.6 to analyze the effect of temperature and gas composition on the solubility of CO_2 in water in the presence of N_2. CO_2 concentration change depends greatly on the initial composition of the gas feed. For the systems with higher initial CO_2 content, the CO_2 concentration change after dissolution is more than those with less initial CO_2 content, which is expected as the solubility of CO_2 increases with respect to the increase in its partial pressure the vapor phase. This implies more HSZ change with more initial CO_2 concentration in the gas phase. Therefore, it is observed that the mole fraction of CO_2

dissolved in the liquid phase is higher for the gas of Type 3. Accordingly, lower CO_2 concentration in the liquid and vapor phases is anticipated when the gas of Type 2 was injected into the system. Moreover, it is shown that the solubility of CO_2-N_2 mixtures is strongly influenced by the pressure when the CO_2 concentration in the gas mixture is remarkable. For instance, a rapid increase in the solubility of CO_2 in water is observed for the gas of Type 3 at pressures less than 10 MPa. Furthermore, for all gas types, the mole fractions of CO_2 and N_2 in the liquid phase decrease with increasing the temperature. As a consequence, CO_2 concentration in the vapor phase shows an ascending behavior with respect to the temperature. It can also be known that for the gas of Type 2 in which N_2 is the dominant component, temperature and pressure changes have a minor effect on the solubility values.

Table 2.10 ARD of EOS predictions from the experimental results for CO_2-N_2-water system

Feed Type	Equation of State	ARD (%)											
		Liquid Phase						Vapor Phase					
		CO_2			N_2			CO_2			N_2		
		273.25	283.15	303.05	273.25	283.15	303.05	273.25	283.15	303.05	273.25	283.15	303.05
Type 1	CPA-SRK72	7.87	8.08	4.34	6.43	4.33	4.45	5.26	5.74	1.37	1.23	0.90	0.20
	VPT	1.92	2.04	5.67	0.65	0.34	5.50	1.18	1.08	2.76	0.09	0.12	0.24
	PC-SAFT	4.51	6.90	3.47	12.43	9.34	11.65	4.38	4.14	0.44	0.38	0.44	0.15
Type 2	CPA-SRK72	6.86	7.75	7.89	4.73	0.77	0.74	8.26	5.74	5.61	0.29	0.16	0.16
	VPT	3.50	6.50	6.21	0.89	0.21	0.24	1.72	3.49	3.61	0.03	0.06	0.06
	PC-SAFT	6.50	3.51	3.05	10.79	12.01	10.59	5.38	1.95	1.75	0.13	0.07	0.06
Type 3	CPA-SRK72	5.56	5.38	3.84	3.34	1.69	5.64	4.45	1.74	1.15	2.76	0.69	0.57
	VPT	4.95	8.39	3.19	1.61	6.36	3.35	4.82	3.54	0.76	1.41	1.38	0.26
	PC-SAFT	2.01	6.72	2.91	9.20	11.12	10.00	1.80	2.78	0.71	0.60	1.12	0.46

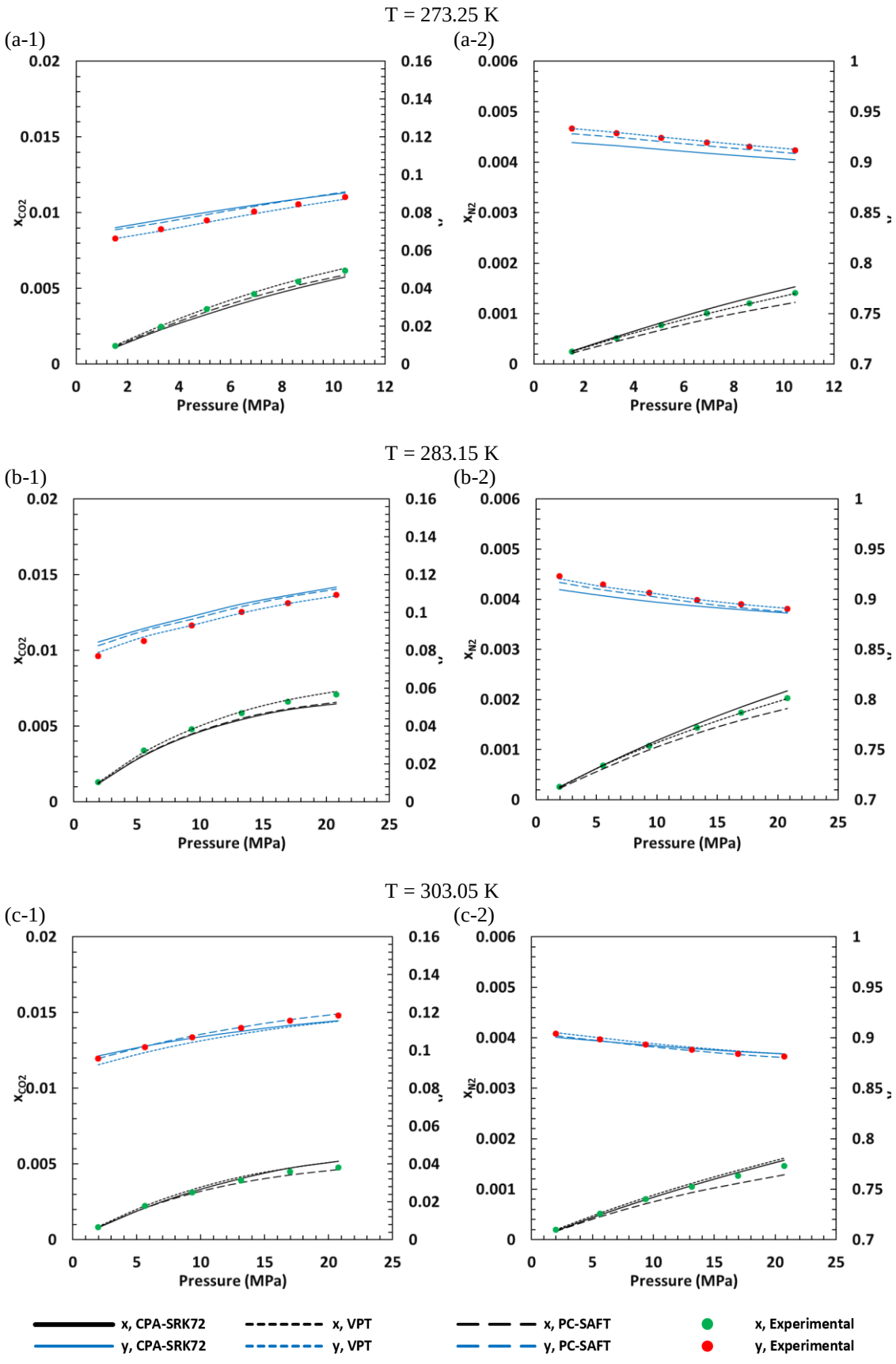

Figure 2.3 Experimental and predicted equilibrium compositions of liquid (x, black) and vapor phases (y, blue) of N_2+CO_2+water system for the gas of Type 1: a to c correspond to the temperatures 273.25, 283.15 and 303.05 K; 1 and 2 correspond to CO_2 and N_2, respectively. As observed, predictions of VPT are more accurate than CPA-SRK72 and PC-SAFT for this gas type, particularly at lower temperatures. However, its accuracy decreases at higher temperaures.

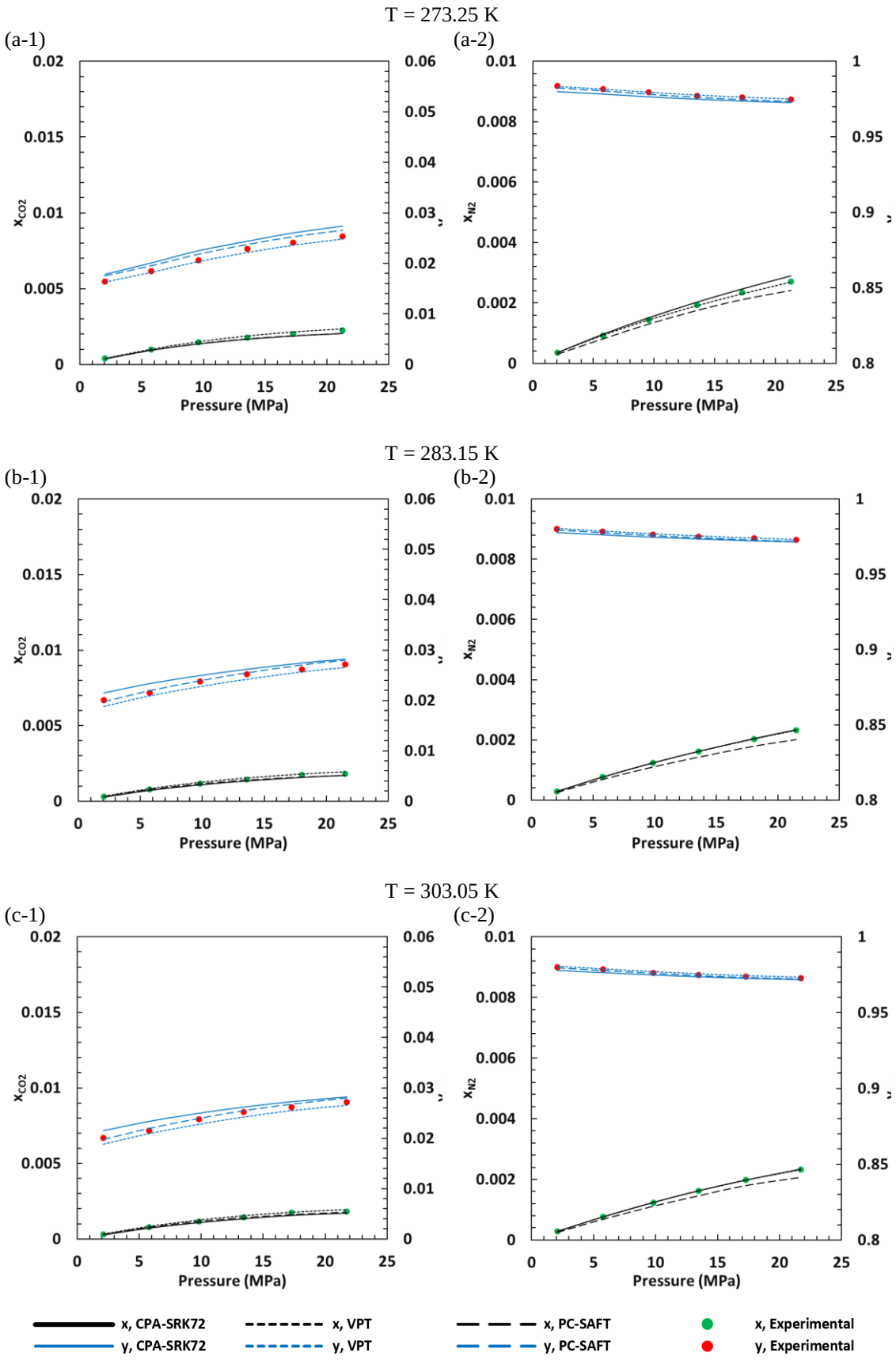

Figure 2.4 Experimental and predicted equilibrium compositions of liquid (x, black) and vapor phases (y, blue) of N_2+CO_2+water system for the gas of Type 2: a to c correspond to the temperatures 273.25, 283.15 and 303.05 K; 1 and 2 correspond to CO_2 and N_2, respectively. As can be seen, VPT predictions for this gas type are more accurate than the other two equations of state, particularly at lower temperatures.

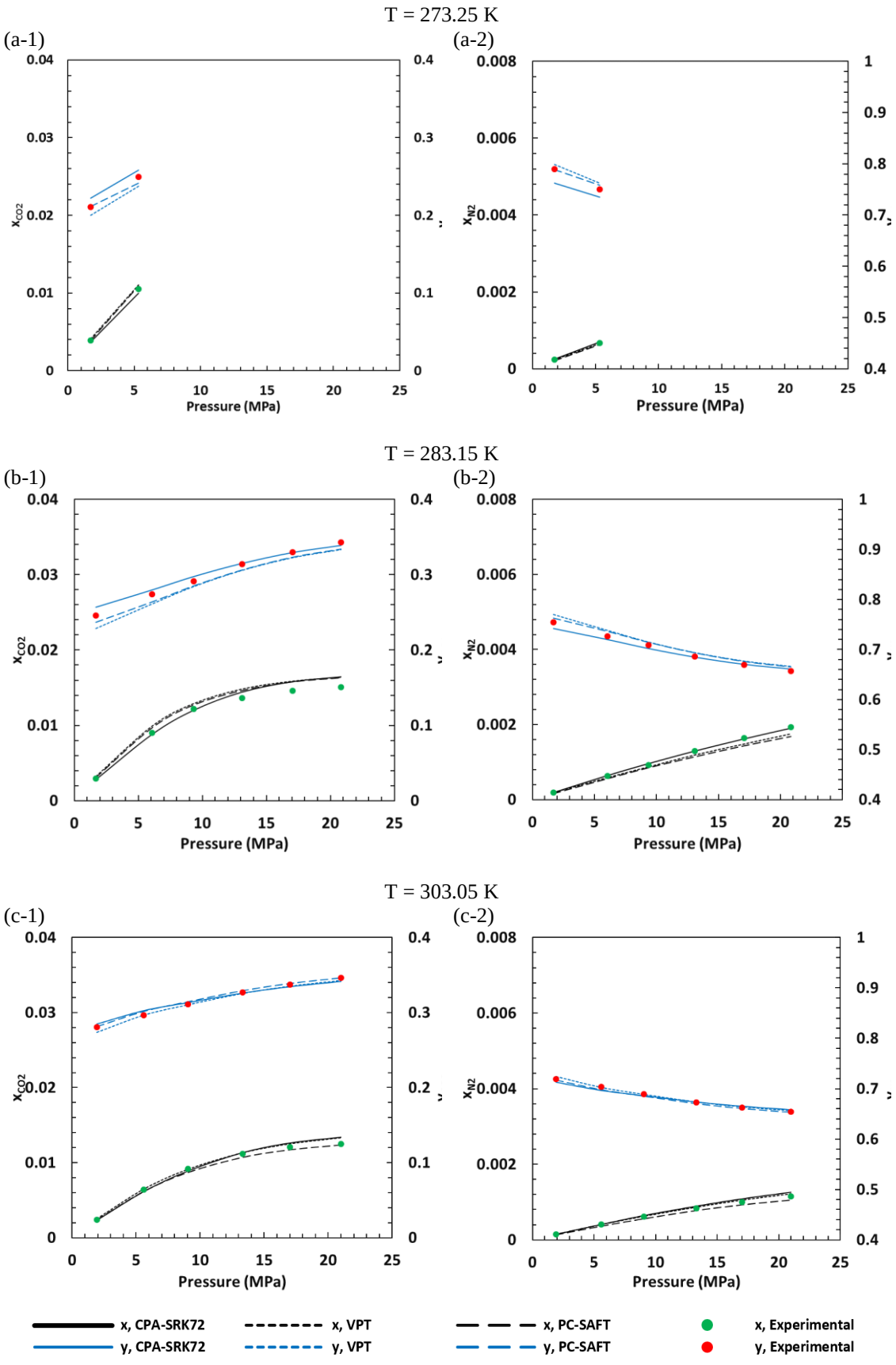

Figure 2.5 Experimental and predicted equilibrium compositions of liquid (x, black) and vapor phases (y, blue) of N_2+CO_2+water system for the gas of Type 3: a to c correspond to the temperatures 273.25, 283.15 and 303.05 K; 1 and 2 correspond to CO_2 and N_2, respectively. As observed, the statistical thermodynamics-based equations of state are more accurate compared with VPT in predicting the equilibrium mole fractions of CO_2 for this gas type.

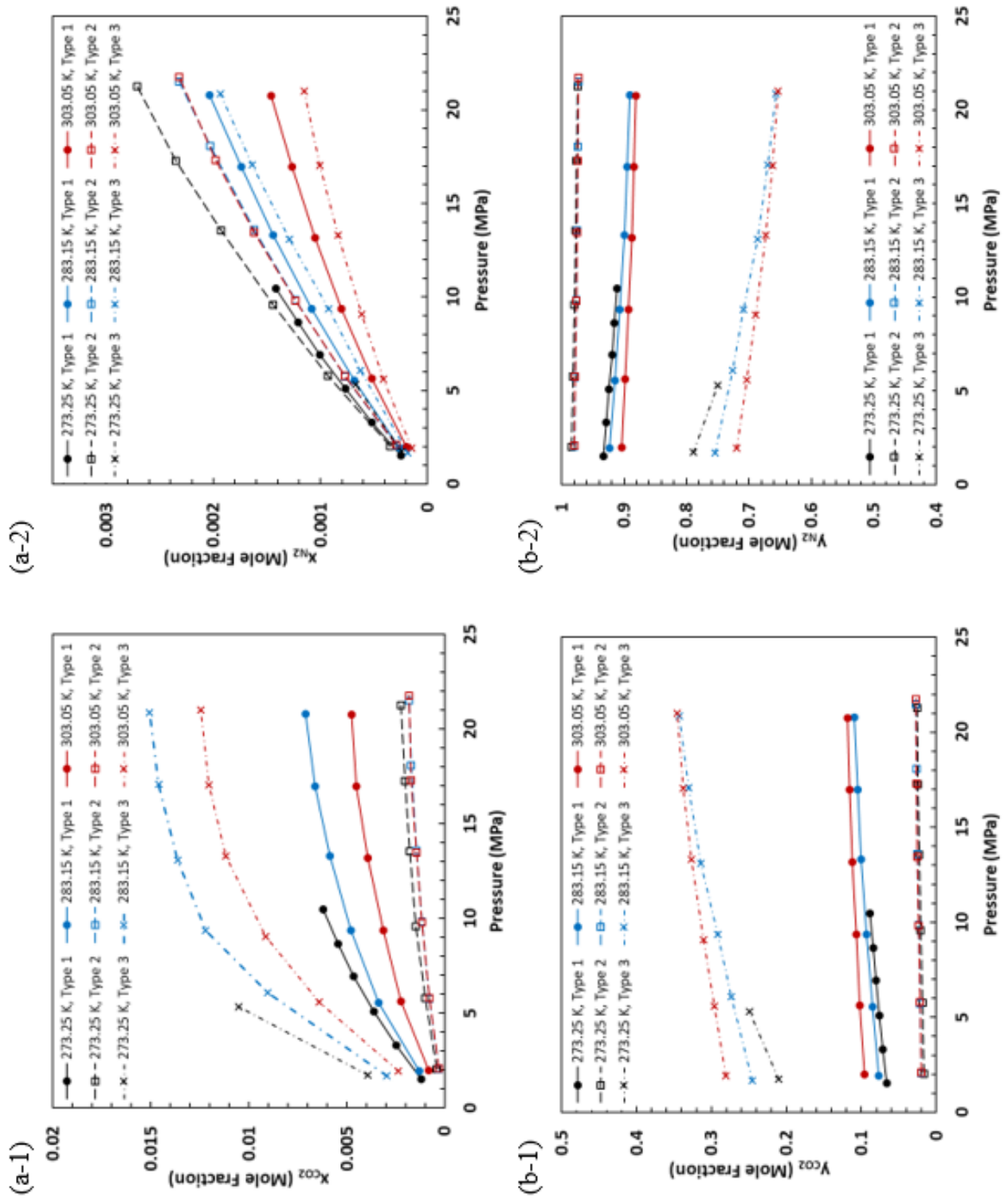

Figure 2.6 Experimentally determined equilibrium compositions of liquid (x) and vapor phases (y) of N_2+CO_2+water system: a and b correspond to liquid and vapor; 1 and 2 correspond to CO_2 and N_2, respectively.

2.4.2 Solubility of CO_2 and N_2 in brine

The equilibrium compositions of liquid and vapor phases were also measured for CO_2-N_2-aqueous solutions with 5, 10 and 15 wt. % NaCl at three different isotherms of 273.25, 283.15, and 303.05 K and pressures up to 22 MPa. Similar trend of partial solubility for each type of gas was also observed in brine. In comparison with the solubility in water solubility of flue gas reduced by increasing the salinity. Hence, the solubility obtained for higher salinities was slightly lower than that for lower salinities. The measured solubility data have been also compared against the predictions of CPA-SRK72, VPT and PC-SAFT equations of state. The experimental results are tabulated in Appendix A and plotted in Figures 7-9 along with the model predictions showing a reasonable agreement between the measured and predicted solubility values. Given that the magnetic mixer allowed considerably high surface contact of the components and improved mass transfer between vapor and liquid phases within the system, final equilibrium point could be achieved in time-effective manner. The measured solubility data can be used as a key parameter for modelling studies of kinetic characteristics of flue gas dissolution inside formation water-saturated mesoporous media.

The average relative deviation (ARD) of the equations of state from the experimental results (see Figures 7-9) has been calculated using Eq. (20) and presented in Table 2.11. As observed in this table, while predictions made by VPT are more accurate at lower temperatures and NaCl concentrations, performance of CPA-SRK72 and PC-SAFT at higher temperatures and concentrations of NaCl is more acceptable. Indeed, VPT is able to reliably predict the mole fractions of CO_2 and N_2 in diluted solutions and its predictions become less accurate when the concentration of NaCl in the aqueous phase increases whereas the accuracy of CPA-SRK72 is remarkable at elevated temperatures and NaCl concentrations. Similar to the previous part, deviation of PC-SAFT in predicting the mole fraction of N_2 from the experimental results is still much higher than VPT and CPA-SRK72.

The experimental solubility values of all gas mixtures at different salinities of brines (see Figures 7-9) are compared in Figure 2.10. As clearly observed, the solubility of CO_2 and N_2 in the aqueous solutions with different NaCl concentrations increases as the pressure increases at isothermal conditions. At high-pressure ranges, the solubility of CO_2 becomes less sensitive to the pressure. Moreover, by increasing the concentration of NaCl, the solubility of CO_2 and N_2 considerably decreases. Solubility of gases in aqueous solutions is usually impacted by inorganic salts since the hydration of salt ions makes

some water molecules unavailable to the gas molecules. This phenomenon is called salting-out effect [89]. More detailed discussion regarding the salting-out effect can be found elsewhere [117].

Table 2.11 ARD of EOS predictions from the experimental results for CO_2-N_2-aqueous solution of NaCl

NaCl Concentration (wt. %)	Equation of State	ARD (%)											
		Liquid Phase						Vapor Phase					
		CO_2			N_2			CO_2			N_2		
		273.25	283.15	303.05	273.25	283.15	303.05	273.25	283.15	303.05	273.25	283.15	303.05
0	CPA-SRK72	7.87	8.08	4.34	6.43	4.33	4.45	5.26	5.74	1.37	1.23	0.90	0.20
	VPT	1.92	2.04	5.67	0.65	0.34	5.50	1.18	1.08	2.76	0.09	0.12	0.24
	PC-SAFT	4.51	6.90	3.47	12.43	9.34	11.65	4.38	4.14	0.44	0.38	0.44	0.15
5	CPA-SRK72	5.22	3.23	2.99	6.24	0.90	6.45	4.33	1.79	2.19	0.72	0.20	0.35
	VPT	4.48	6.94	3.88	2.73	2.38	3.63	2.95	4.82	0.93	0.29	0.53	0.20
	PC-SAFT	1.07	5.76	1.74	11.98	11.60	11.17	0.55	2.48	3.12	0.06	0.25	0.48
10	CPA-SRK72	6.77	8.07	4.82	7.86	1.77	4.59	7.20	2.84	0.88	0.93	0.36	0.14
	VPT	1.10	4.86	8.55	0.32	0.72	6.55	0.42	2.32	1.95	0.04	0.26	0.17
	PC-SAFT	6.87	2.28	3.10	8.74	11.17	10.43	2.92	0.41	0.41	0.34	0.03	0.10
15	CPA-SRK72	6.35	3.17	3.76	2.19	0.26	3.14	3.58	1.44	0.40	0.44	0.21	0.07
	VPT	8.04	7.93	4.50	3.83	1.00	3.73	4.76	4.11	1.79	0.56	0.49	0.15
	PC-SAFT	3.28	4.93	6.98	11.39	11.79	10.93	1.10	1.43	1.35	0.11	0.15	0.17

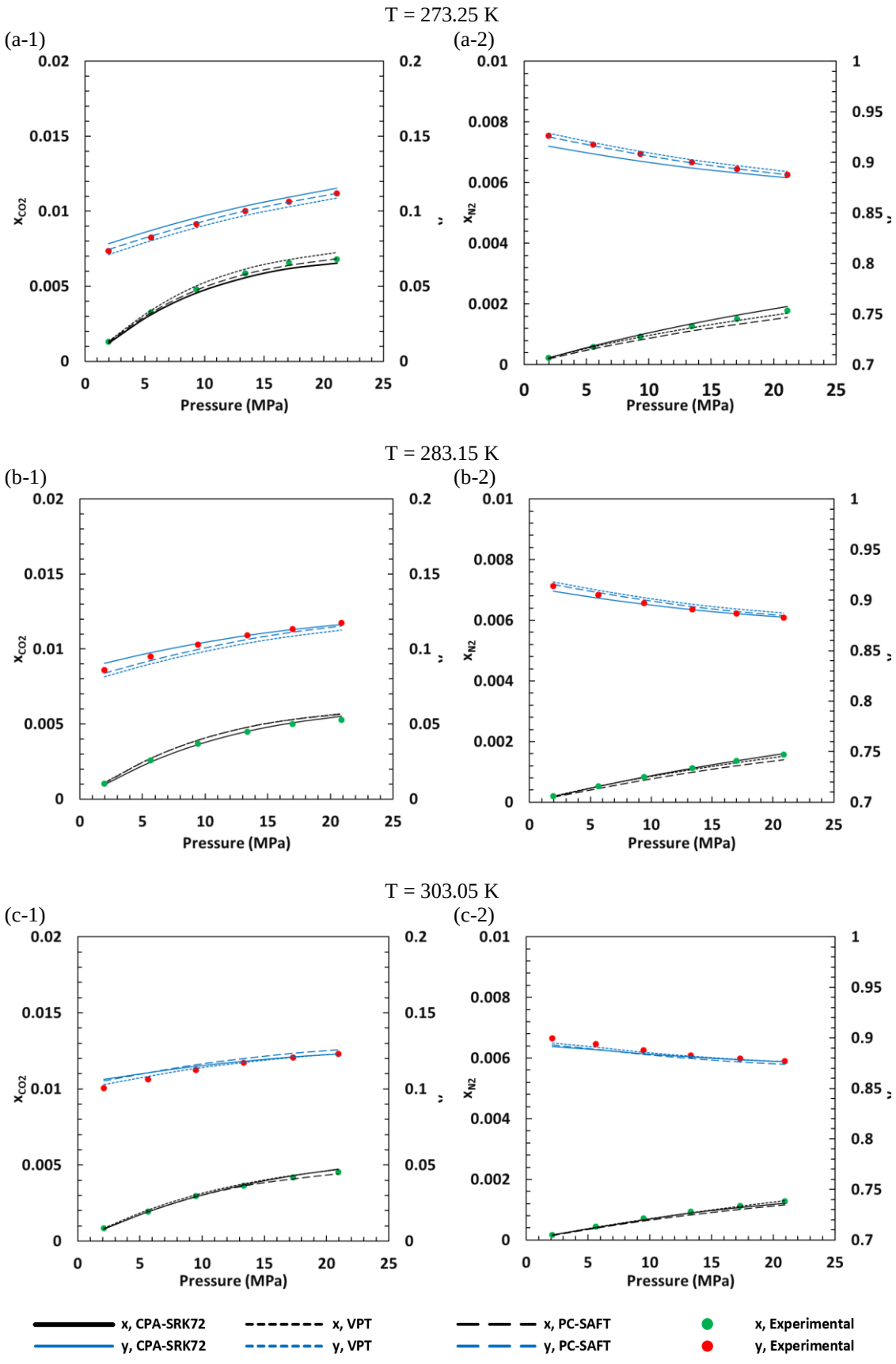

Figure 2.7 Experimental and predicted equilibrium compositions of the liquid (x, black) and vapor phases (y, blue) for the CO_2+N_2+aqueous Solution with 5 wt. % NaCl: a to c correspond to the temperatures 273.25, 283.15 and 303.05; 1 and 2 correspond to CO_2 and N_2, respectively. VPT predictions have more agreement with experimental data at lower temperatures. At higher temperatures, accuracy of VPT decreases while CPA-SRK72 and PC-SAFT become more accurate.

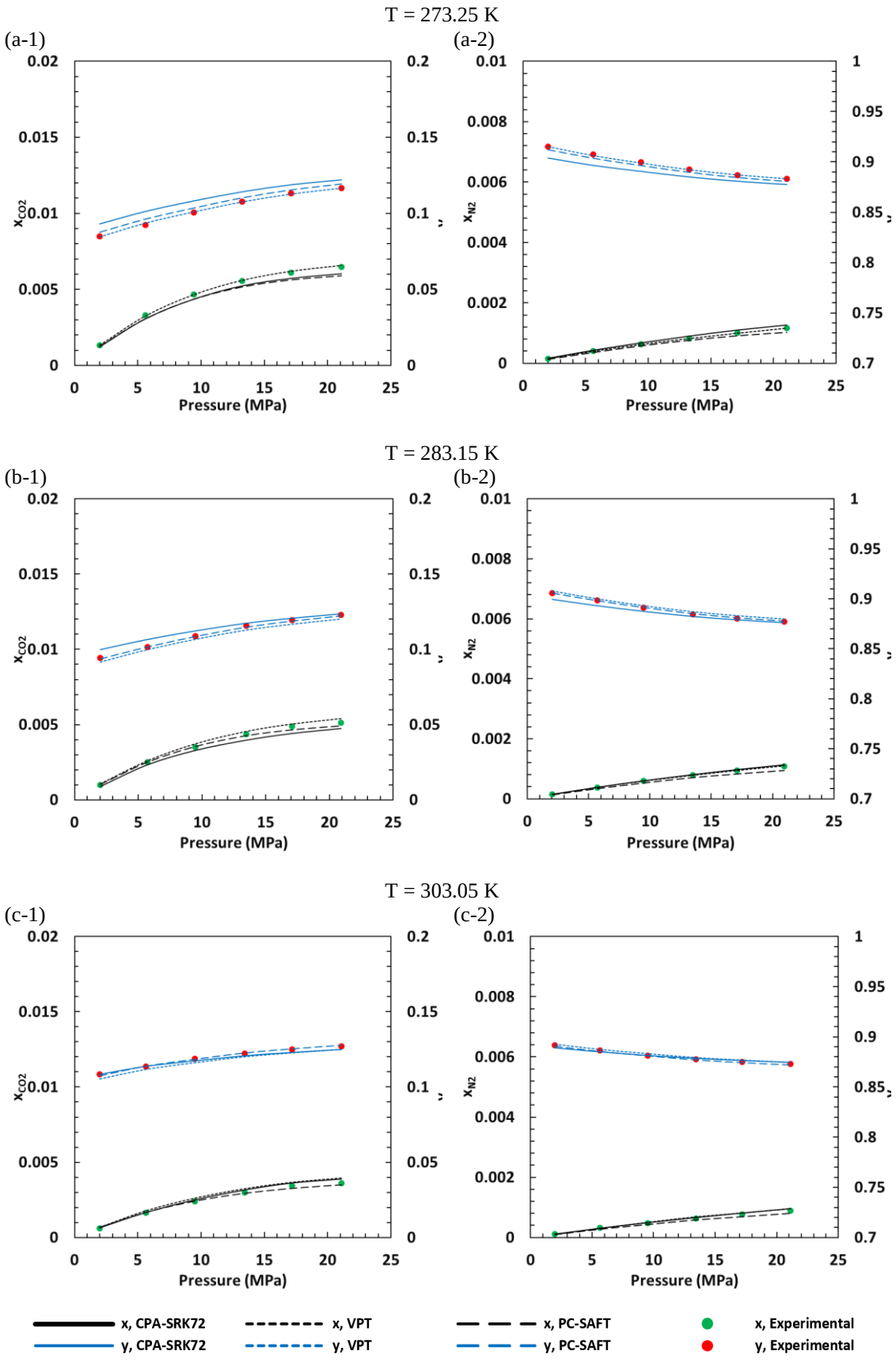

Figure 2.8 Experimental and predicted equilibrium compositions of the liquid (x, black) and vapor phases (y, blue) for the CO_2+N_2+aqueous Solution with 10 wt. % NaCl: a to c correspond to the temperatures 273.25, 283.15 and 303.05; 1 and 2 correspond to CO_2 and N_2, respectively. As observed, VPT is able to predict the equilibrium compositions of vapor and liquid phases more accrately compared with the the statistical thermodynamics-based equations of state.

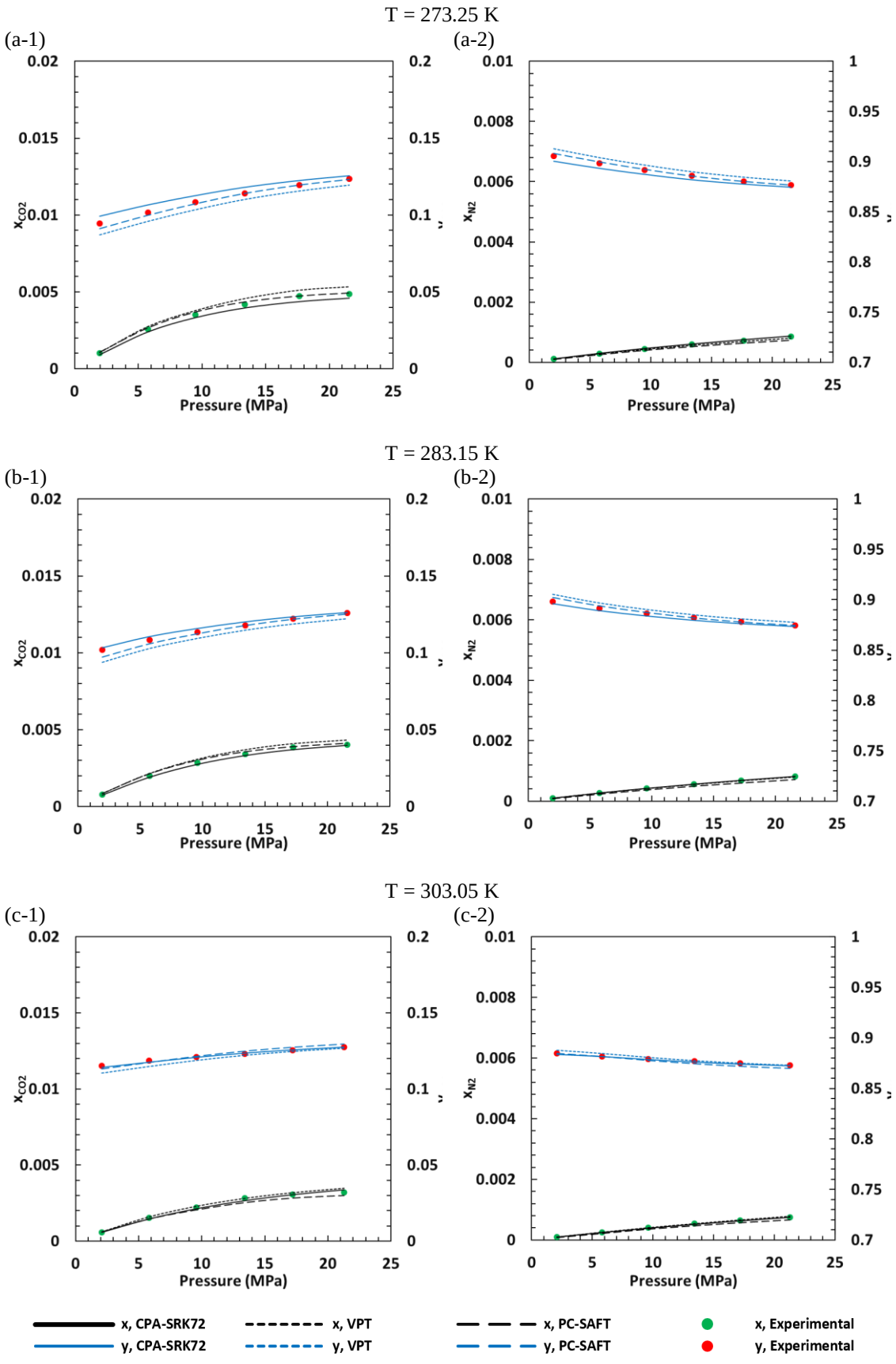

Figure 2.9 Experimental and predicted equilibrium compositions of the liquid (x, black) and vapor phases (y, blue) for the CO_2+N_2+aqueous Solution with 15 wt. % NaCl: a to c correspond to the temperatures 273.25, 283.15 and 303.05; 1 and 2 correspond to CO_2 and N_2, respectively. At this salinity, predictions of CPA-SRK72 and PC-SAFT equations of state are more accurate than VPT.

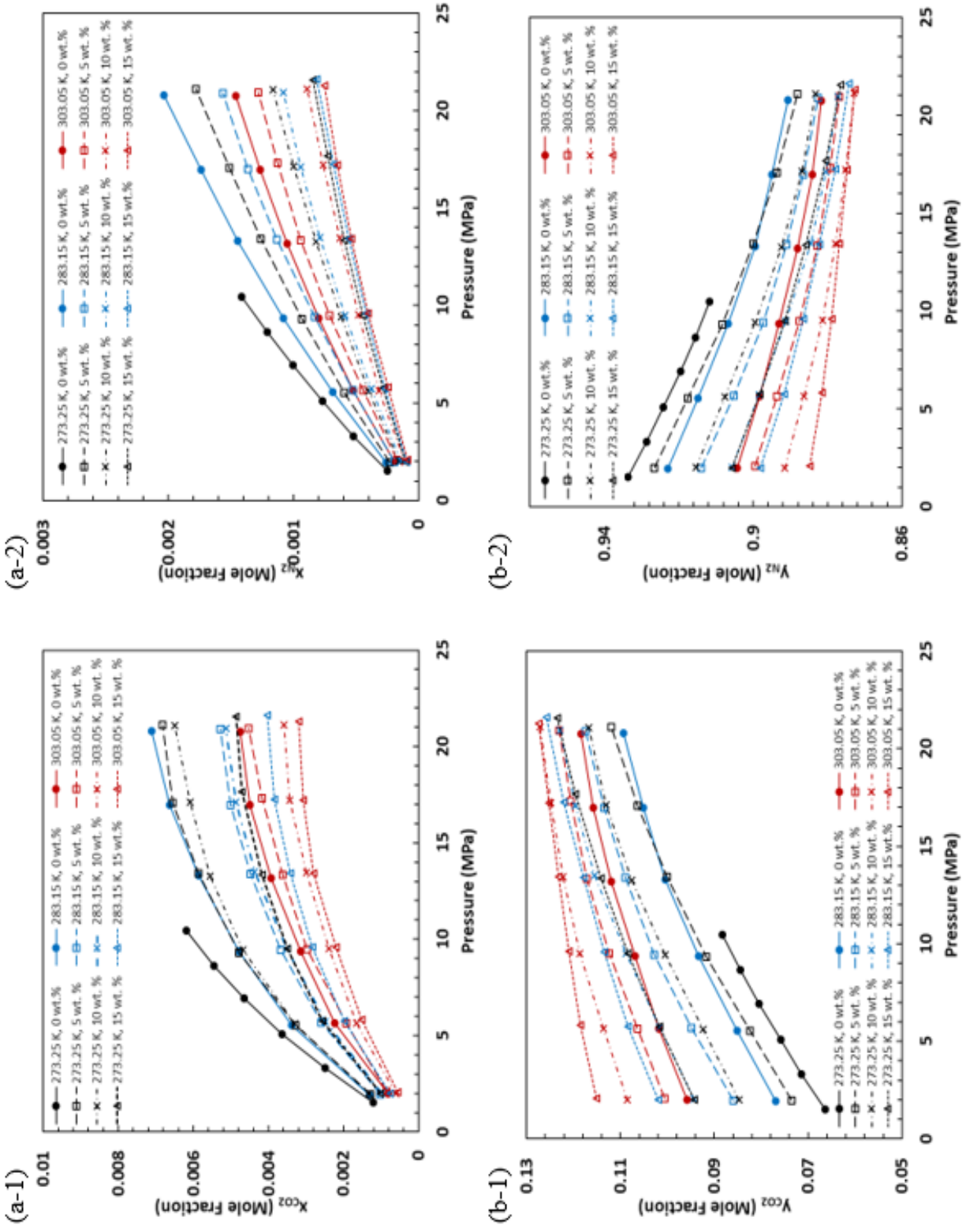

Figure 2.10 Experimentally determined equilibrium compositions of liquid (x) and vapor phases (y) of CO_2-N_2-aqueous solution of NaCl: a and b correspond to liquid and vapor; 1 and 2 correspond to CO_2 and N_2, respectively.

2.5 References

(1) House, K. Z.; Schrag, D. P.; Harvey, C. F.; Lackner, K. S. Permanent carbon dioxide storage in deep-sea sediments. *Proceedings of the National Academy of Sciences* **2006**, *103*, 12291-12295.

(2) Lackner, K. S. Carbonate chemistry for sequestering fossil carbon. *Annual review of energy and the environment* **2002**, *27*, 193-232.

(3) Chu, S.: Carbon capture and sequestration. American Association for the Advancement of Science, 2009.

(4) Smithson, P. A. IPCC, 2001: climate change 2001: the scientific basis. Contribution of Working Group 1 to the Third Assessment Report of the Intergovernmental Panel on Climate Change, edited by JT Houghton, Y. Ding, DJ Griggs, M. Noguer, PJ van der Linden, X. Dai, K. Maskell and CA Johnson (eds). Cambridge University Press, Cambridge, UK, and New York, USA, 2001. No. of pages: 881. Price£ 34.95, US $49.95, ISBN 0-521-01495-6 (paperback).£ 90.00, US $130.00, ISBN 0-521-80767-0 (hardback). *International Journal of Climatology* **2002**, *22*, 1144-1144.

(5) Hasib-ur-Rahman, M.; Siaj, M.; Larachi, F. CO2 capture in alkanolamine/room-temperature ionic liquid emulsions: A viable approach with carbamate crystallization and curbed corrosion behavior. *International Journal of Greenhouse Gas Control* **2012**, *6*, 246-252.

(6) Tohidi, B.; Yang, J.; Salehabadi, M.; Anderson, R.; Chapoy, A. CO2 hydrates could provide secondary safety factor in subsurface sequestration of CO2. *Environmental science & technology* **2010**, *44*, 1509-1514.

(7) Haghi, R. K.; Chapoy, A.; Peirera, L. M.; Yang, J.; Tohidi, B. pH of CO 2 saturated water and CO 2 saturated brines: Experimental measurements and modelling. *International Journal of Greenhouse Gas Control* **2017**, *66*, 190-203.

(8) Gunter, W. D.; Bachu, S.; Benson, S. The role of hydrogeological and geochemical trapping in sedimentary basins for secure geological storage of carbon dioxide. *Geological Society, London, Special Publications* **2004**, *233*, 129-145.

(9) Holloway, S. An overview of the underground disposal of carbon dioxide. *Energy Conversion and Management* **1997**, *38*, S193-S198.

(10) Myers, M.; Stalker, L.; Pejcic, B.; Ross, A. Tracers–Past, present and future applications in CO2 geosequestration. *Applied geochemistry* **2013**, *30*, 125-135.

(11) Publishing, O.; Staff, I. E. A.; Agency, I. E.: *CO2 Emissions from Fuel Combustion 2012*; Organisation for Economic Co-operation and Development, 2012.

(12) Hendriks, C.; Blok, K.; Turkenburg, W.: The recovery of carbon dioxide from power plants. In *Climate and Energy: The Feasibility of Controlling CO2 Emissions*; Springer, 1989; pp 125-142.

(13) Pires, J.; Martins, F.; Alvim-Ferraz, M.; Simões, M. Recent developments on carbon capture and storage: an overview. *Chemical Engineering Research and Design* **2011**, *89*, 1446-1460.

(14) Boot-Handford, M. E.; Abanades, J. C.; Anthony, E. J.; Blunt, M. J.; Brandani, S.; Mac Dowell, N.; Fernández, J. R.; Ferrari, M.-C.; Gross, R.; Hallett, J. P. Carbon capture and storage update. *Energy & Environmental Science* **2014**, *7*, 130-189.

(15) Gilfillan, S. M.; Lollar, B. S.; Holland, G.; Blagburn, D.; Stevens, S.; Schoell, M.; Cassidy, M.; Ding, Z.; Zhou, Z.; Lacrampe-Couloume, G. Solubility trapping in formation water as dominant CO 2 sink in natural gas fields. *Nature* **2009**, *458*, 614.

(16) Rosenqvist, J.; Kilpatrick, A. D.; Yardley, B. W. Solubility of carbon dioxide in aqueous fluids and mineral suspensions at 294 K and subcritical pressures. *Applied geochemistry* **2012**, *27*, 1610-1614.

(17) Kang, H.; Koh, D.-Y.; Lee, H. Nondestructive natural gas hydrate recovery driven by air and carbon dioxide. *Scientific reports* **2014**, *4*, 6616.

(18) Lee, Y.; Seo, Y.-j.; Ahn, T.; Lee, J.; Lee, J. Y.; Kim, S.-J.; Seo, Y. CH4–Flue gas replacement occurring in sH hydrates and its significance for CH4 recovery and CO2 sequestration. *Chemical Engineering Journal* **2017**, *308*, 50-58.

(19) Yang, J.; Okwananke, A.; Tohidi, B.; Chuvilin, E.; Maerle, K.; Istomin, V.; Bukhanov, B.; Cheremisin, A. Flue gas injection into gas hydrate reservoirs for methane recovery and carbon dioxide sequestration. *Energy conversion and management* **2017**, *136*, 431-438.

(20) Hassanpouryouzband, A.; Yang, J.; Tohidi, B.; Chuvilin, E.; Istomin, V.; Bukhanov, B.; Cheremisin, A. Insights into CO2 Capture by Flue Gas Hydrate Formation: Gas Composition Evolution in Systems Containing Gas Hydrates and Gas Mixtures at Stable Pressures. *ACS Sustainable Chemistry & Engineering* **2018**.

(21) Hassanpouryouzband, A.; Yang, J.; Tohidi, B.; Chuvilin, E. M.; Istomin, V.; Bukhanov, B. A.; Cheremisin, A. CO2 Capture by Injection of Flue Gas or CO2-N2 Mixtures into Hydrate Reservoirs: Dependence of CO2 Capture Efficiency on Gas Hydrate Reservoir Conditions. *Environmental science & technology* **2018**.

(22) Schoderbek, D.; Boswell, R. Iġnik Sikumi# 1, gas hydrate test well, successfully installed on the Alaska North Slope. *Natural Gas & Oil* **2011**, *304*, 285-4541.

(23) Schoderbek, D.; Martin, K. L.; Howard, J.; Silpngarmlert, S.; Hester, K. In *Tilte*2012; Offshore Technology Conference.

(24) Garapati, N.; McGuire, P.; Anderson, B. J. In *Tilte*2013; Unconventional Resources Technology Conference (URTEC).

(25) Shin, K.; Park, Y.; Cha, M.; Park, K.-P.; Huh, D.-G.; Lee, J.; Kim, S.-J.; Lee, H. Swapping phenomena occurring in deep-sea gas hydrates. *Energy & Fuels* **2008**, *22*, 3160-3163.

(26) Cha, M.; Shin, K.; Lee, H.; Moudrakovski, I. L.; Ripmeester, J. A.; Seo, Y. Kinetics of methane hydrate replacement with carbon dioxide and nitrogen gas mixture using in situ NMR spectroscopy. *Environmental science & technology* **2015**, *49*, 1964-1971.

(27) Sloan Jr, E. D.; Koh, C.: *Clathrate hydrates of natural gases*; CRC press, 2007.

(28) Mehrabian, H.; Bellucci, M. A.; Walsh, M. R.; Trout, B. L. Effect of Salt on Anti-Agglomerant Surface Adsorption in Natural Gas Hydrates. *The Journal of Physical Chemistry C* **2018**.

(29) Munkejord, S. T.; Hammer, M.; Løvseth, S. W. CO2 transport: Data and models–A review. *Applied Energy* **2016**, *169*, 499-523.

(30) Talman, S. Subsurface geochemical fate and effects of impurities contained in a CO2 stream injected into a deep saline aquifer: What is known. *International Journal of Greenhouse Gas Control* **2015**, *40*, 267-291.

(31) Hajiw, M.; Corvisier, J.; El Ahmar, E.; Coquelet, C. Impact of impurities on CO 2 storage in saline aquifers: Modelling of gases solubility in water. *International Journal of Greenhouse Gas Control* **2018**, *68*, 247-255.

(32) Walsh, M. R.; Koh, C. A.; Sloan, E. D.; Sum, A. K.; Wu, D. T. Microsecond simulations of spontaneous methane hydrate nucleation and growth. *Science* **2009**, *326*, 1095-1098.

(33) Alavi, S.; Ripmeester, J.; Klug, D. Molecular-dynamics study of structure II hydrogen clathrates. *The Journal of chemical physics* **2005**, *123*, 024507.

(34) Wiebe, R.; Gaddy, V. The solubility in water of carbon dioxide at 50, 75 and 100, at pressures to 700 atmospheres. *Journal of the American Chemical Society* **1939**, *61*, 315-318.

(35) Wiebe, R.; Gaddy, V. The solubility of carbon dioxide in water at various temperatures from 12 to 40 and at pressures to 500 atmospheres. Critical phenomena. *Journal of the American Chemical Society* **1940**, *62*, 815-817.

(36) Wiebe, R. The Binary System Carbon Dioxide-Water under Pressure. *Chemical reviews* **1941**, *29*, 475-481.

(37) Malinin, S.; Saveleva, N. Experimental investigations of CO2 solubility in NaCl and CaCl2 solutions at temperatures of 25, 50 and 75 degrees and elevated CO2 pressure. *Geokhimiya* **1972**, 643-&.

(38) Zawisza, A.; Malesinska, B. Solubility of carbon dioxide in liquid water and of water in gaseous carbon dioxide in the range 0.2-5 MPa and at temperatures up to 473 K. *Journal of Chemical and Engineering Data* **1981**, *26*, 388-391.

(39) Briones, J.; Mullins, J.; Thies, M.; Kim, B.-U. Ternary phase equilibria for acetic acid-water mixtures with supercritical carbon dioxide. *Fluid Phase Equilibria* **1987**, *36*, 235-246.

(40) D'souza, R.; Patrick, J. R.; Teja, A. S. High pressure phase equilibria in the carbon dioxide-n-Hexadecane and carbon dioxide—water systems. *The Canadian Journal of Chemical Engineering* **1988**, *66*, 319-323.

(41) Nighswander, J. A.; Kalogerakis, N.; Mehrotra, A. K. Solubilities of carbon dioxide in water and 1 wt.% sodium chloride solution at pressures up to 10 MPa and temperatures from 80 to 200. degree. C. *Journal of Chemical and Engineering Data* **1989**, *34*, 355-360.

(42) Dohrn, R.; Bünz, A.; Devlieghere, F.; Thelen, D. Experimental measurements of phase equilibria for ternary and quaternary systems of glucose, water, CO2 and ethanol with a novel apparatus. *Fluid Phase Equilibria* **1993**, *83*, 149-158.

(43) Rumpf, B.; Nicolaisen, H.; Öcal, C.; Maurer, G. Solubility of carbon dioxide in aqueous solutions of sodium chloride: experimental results and correlation. *Journal of solution chemistry* **1994**, *23*, 431-448.

(44) Bamberger, A.; Sieder, G.; Maurer, G. High-pressure (vapor+ liquid) equilibrium in binary mixtures of (carbon dioxide+ water or acetic acid) at temperatures from 313 to 353 K. *The Journal of Supercritical Fluids* **2000**, *17*, 97-110.

(45) Kiepe, J.; Horstmann, S.; Fischer, K.; Gmehling, J. Experimental determination and prediction of gas solubility data for CO2+ H2O mixtures containing NaCl or KCl at temperatures between 313 and 393 K and pressures up to 10 MPa. *Industrial & Engineering Chemistry Research* **2002**, *41*, 4393-4398.

(46) Bando, S.; Takemura, F.; Nishio, M.; Hihara, E.; Akai, M. Solubility of CO2 in aqueous solutions of NaCl at (30 to 60) C and (10 to 20) MPa. *Journal of Chemical & Engineering Data* **2003**, *48*, 576-579.

(47) Diamond, L. W.; Akinfiev, N. N. Solubility of CO2 in water from− 1.5 to 100 C and from 0.1 to 100 MPa: evaluation of literature data and thermodynamic modelling. *Fluid phase equilibria* **2003**, *208*, 265-290.

(48) Duan, Z.; Sun, R. An improved model calculating CO2 solubility in pure water and aqueous NaCl solutions from 273 to 533 K and from 0 to 2000 bar. *Chemical geology* **2003**, *193*, 257-271.

(49) Chapoy, A.; Mohammadi, A.; Chareton, A.; Tohidi, B.; Richon, D. Measurement and modeling of gas solubility and literature review of the properties for the carbon dioxide− water system. *Industrial & engineering chemistry research* **2004**, *43*, 1794-1802.

(50) Li, Z.; Dong, M.; Li, S.; Dai, L. Densities and solubilities for binary systems of carbon dioxide+ water and carbon dioxide+ brine at 59 C and pressures to 29 MPa. *Journal of Chemical & Engineering Data* **2004**, *49*, 1026-1031.

(51) Duan, Z.; Sun, R.; Zhu, C.; Chou, I.-M. An improved model for the calculation of CO2 solubility in aqueous solutions containing Na+, K+, Ca2+, Mg2+, Cl−, and SO42−. *Marine Chemistry* **2006**, *98*, 131-139.

(52) Liu, Y.; Hou, M.; Yang, G.; Han, B. Solubility of CO2 in aqueous solutions of NaCl, KCl, CaCl2 and their mixed salts at different temperatures and pressures. *The Journal of supercritical fluids* **2011**, *56*, 125-129.

(53) Guo, H.; Chen, Y.; Hu, Q.; Lu, W.; Ou, W.; Geng, L. Quantitative Raman spectroscopic investigation of geo-fluids high-pressure phase equilibria: Part I. Accurate calibration and determination of CO 2 solubility in water from 273.15 to 573.15 K and from 10 to 120MPa. *Fluid Phase Equilibria* **2014**, *382*, 70-79.

(54) King Jr, A. D.; Coan, C. Solubility of water in compressed carbon dioxide, nitrous oxide, and ethane. Evidence for hydration of carbon dioxide and nitrous oxide in the gas phase. *Journal of the American Chemical Society* **1971**, *93*, 1857-1862.

(55) Gillespie, P. C. Vapor-liquid and liquid-liquid equilibria: water-methane, water-carbon dioxide, water-hydrogen sulfide, water-npentane, water-methane-npentane. *Gas Processor's Association, Research Report* **1982**, *48*, 11.

(56) Spycher, N.; Pruess, K.; Ennis-King, J. CO2-H2O mixtures in the geological sequestration of CO2. I. Assessment and calculation of mutual solubilities from 12 to 100 C and up to 600 bar. *Geochimica et cosmochimica acta* **2003**, *67*, 3015-3031.

(57) Valtz, A.; Chapoy, A.; Coquelet, C.; Paricaud, P.; Richon, D. Vapour–liquid equilibria in the carbon dioxide–water system, measurement and modelling from 278.2 to 318.2 K. *Fluid phase equilibria* **2004**, *226*, 333-344.

(58) Spycher, N.; Pruess, K. CO2-H2O Mixtures in the Geological Sequestration of CO2. II. Partitioning in Chloride Brines at 12–100 C and up to 600 bar. *Geochimica et Cosmochimica Acta* **2005**, *69*, 3309-3320.

(59) Hou, S.-X.; Maitland, G. C.; Trusler, J. M. Measurement and modeling of the phase behavior of the (carbon dioxide+ water) mixture at temperatures from 298.15 K to 448.15 K. *The Journal of Supercritical Fluids* **2013**, *73*, 87-96.

(60) Goodman, J. B.; Krase, N. W. Solubility of nitrogen in water at high pressures and temperatures. *Industrial & Engineering Chemistry* **1931**, *23*, 401-404.

(61) Frolich, P. K.; Tauch, E.; Hogan, J.; Peer, A. Solubilities of gases in liquids at high pressure. *Industrial & Engineering Chemistry* **1931**, *23*, 548-550.

(62) Wiebe, R.; Gaddy, V.; Heinss Jr, C. Solubility of nitrogen in water in 250c from 25 to 1000 atmospheres. *Industrial & Engineering Chemistry* **1932**, *24*, 927-927.

(63) Saddington, A. W.; Krase, N. W. Vapor—Liquid Equilibria in the System Nitrogen—Water. *Journal of the American Chemical Society* **1934**, *56*, 353-361.

(64) Pray, H. A.; Schweickert, C.; Minnich, B. H. Solubility of hydrogen, oxygen, nitrogen, and helium in water at elevated temperatures. *Industrial & Engineering Chemistry* **1952**, *44*, 1146-1151.

(65) Smith, N. O.; Kelemen, S.; Nagy, B. Solubility of natural gases in aqueous salt solutions—II: Nitrogen in aqueous NaCl, CaCl2, Na2SO4 and MgSO4 at room temperatures and at pressures below 1000 psia. *Geochimica et Cosmochimica Acta* **1962**, *26*, 921-926.

(66) O'Sullivan, T. D.; Nagy, B. Solubility of natural gases in aqueous salt solutions—III Nitrogen in aqueous NaCl at high pressures. *Geochimica et Cosmochimica Acta* **1966**, *30*, 617-619.

(67) O'Sullivan, T. D.; Smith, N. O. Solubility and partial molar volume of nitrogen and methane in water and in aqueous sodium chloride from 50 to 125. deg. and 100 to 600 atm. *The Journal of Physical Chemistry* **1970**, *74*, 1460-1466.

(68) Japas, M. L.; Franck, E. High Pressure Phase Equilibria and PVT-Data. of the Water-Nitrogen System to 673 K and 250 MPa. *Berichte der Bunsengesellschaft für physikalische Chemie* **1985**, *89*, 793-800.

(69) Chapoy, A.; Mohammadi, A. H.; Tohidi, B.; Richon, D. Gas solubility measurement and modeling for the nitrogen+ water system from 274.18 K to 363.02 K. *Journal of Chemical & Engineering Data* **2004**, *49*, 1110-1115.

(70) Wiebe, R.; Gaddy, V.; Heins Jr, C. The solubility of nitrogen in water at 50, 75 and 100 from 25 to 1000 atmospheres. *Journal of the American Chemical Society* **1933**, *55*, 947-953.

(71) Mohammadi, A. H.; Chapoy, A.; Tohidi, B.; Richon, D. Water content measurement and modeling in the nitrogen+ water system. *Journal of Chemical & Engineering Data* **2005**, *50*, 541-545.

(72) Zenner, G.; Dana, L. In *Tilte*1963.

(73) Muirbrook, N.; Prausnitz, J. Multicomponent vapor-liquid equilibria at high pressures: Part I. Experimental study of the nitrogen—oxygen—carbon dioxide system at 0° C. *AIChE Journal* **1965**, *11*, 1092-1096.

(74) SARASHINA, E.; ARAI, Y.; SAITO, S. Vapor-liquid equilibria for the nitrogen-methane-carbon dioxide system. *Journal of Chemical Engineering of Japan* **1971**, *4*, 377-378.

(75) Somait, F. A.; Kidnay, A. J. Liquid-vapor equilibriums at 270.00 K for systems containing nitrogen, methane, and carbon dioxide. *Journal of Chemical and Engineering Data* **1978**, *23*, 301-305.

(76) Al-sahhaf, T.; Kidnay, A.; Sloan, E. Liquid–vapor equilibriums in the nitrogen+ carbon dioxide+ methane. *Ing. Eng. Chem. Fundam* **1983**, *22*, 372.

(77) Dorau, W.; Al-Wakeel, I.; Knapp, H. VLE data for CO2-CF2Cl2, N2-CO2, N2-CF2Cl2 and N2-CO2-CF2Cl. *Cryogenics* **1983**, *23*, 29-35.

(78) Weber, W.; Zeck, S.; Knapp, H. Gas solubilities in liquid solvents at high pressures: apparatus and results for binary and ternary systems of N2, CO2 and CH3OH. *Fluid Phase Equilibria* **1984**, *18*, 253-278.

(79) Fall, J. L.; Luks, K. D. Effect of additive gases on the liquid-liquid-vapor immiscibility of the carbon dioxide+ n-nonadecane mixtures. *Journal of Chemical and Engineering Data* **1986**, *31*, 332-336.

(80) Brown, T.; Kidnay, A.; Sloan, E. Vapor—liquid equilibria in the carbon dioxide-ethane system. *Fluid Phase Equilibria* **1988**, *40*, 169-184.

(81) Shibata, S. K.; Sandler, S. I. High-pressure vapor-liquid equilibria involving mixtures of nitrogen, carbon dioxide, and n-butane. *Journal of Chemical and Engineering Data* **1989**, *34*, 291-298.

(82) Shibata, S. K.; Sandler, S. I. High pressure vapor-liquid equilibria of mixtures of nitrogen, carbon dioxide, and cyclohexane. *Journal of Chemical and Engineering Data* **1989**, *34*, 419-424.

(83) Trappehl, G.; Knapp, H. Vapour-liquid equilibria in the ternary mixture N2-CH4-CO2 and the quaternary mixture N2-CH4-C2H6-C3H8. *Cryogenics* **1989**, *29*, 42-50.

(84) Al-Sahhaf, T. A. Vapor—liquid equilibria for the ternary system N2+ CO2+ CH4 at 230 and 250 K. *Fluid phase equilibria* **1990**, *55*, 159-172.

(85) Wang, X.; Wang, Y.; Shi, J.; Lu, B. C. Isothermal vapor-liquid equilibria at elevated pressures for the systems containing nitrogen, carbon dioxide, and chlorodifluoromethane. *Journal of Chemical and Engineering Data* **1991**, *36*, 436-439.

(86) Xu, N.; Dong, J.; Wang, Y.; Shi, J. High pressure vapor liquid equilibria at 293 K for systems containing nitrogen, methane and carbon dioxide. *Fluid phase equilibria* **1992**, *81*, 175-186.

(87) Seitz, J. C.; Blencoe, J. G.; Bodnar, R. J. Volumetric properties for {x1CO2+ x2CH4+ (1− x1− x2) N2} at the pressures (19.94, 39.94, 59.93, and 99.93) MPa and temperatures (323.15, 373.15, 473.15, and 573.15) K. *The Journal of Chemical Thermodynamics* **1996**, *28*, 539-550.

(88) Yucelen, B.; Kidnay, A. J. Vapor− liquid equilibria in the nitrogen+ carbon dioxide+ propane system from 240 to 330 K at pressures to 15 MPa. *Journal of Chemical & Engineering Data* **1999**, *44*, 926-931.

(89) Liu, Y.; Hou, M.; Ning, H.; Yang, D.; Yang, G.; Han, B. Phase equilibria of CO2+ N2+ H2O and N2+ CO2+ H2O+ NaCl+ KCl+ CaCl2 systems at different temperatures and pressures. *Journal of Chemical & Engineering Data* **2012**, *57*, 1928-1932.

(90) Foltran, S.; Vosper, M. E.; Suleiman, N. B.; Wriglesworth, A.; Ke, J.; Drage, T. C.; Poliakoff, M.; George, M. W. Understanding the solubility of water in carbon capture and storage mixtures: An FTIR spectroscopic study of H 2 O+ CO 2+ N 2 ternary mixtures. *International Journal of Greenhouse Gas Control* **2015**, *35*, 131-137.

(91) Tenorio, M.-J.; Parrott, A. J.; Calladine, J. A.; Sanchez-Vicente, Y.; Cresswell, A. J.; Graham, R. S.; Drage, T. C.; Poliakoff, M.; Ke, J.; George, M. W. Measurement of the vapour–liquid equilibrium of binary and ternary mixtures of CO2, N2 and H2, systems which are of relevance to CCS technology. *International Journal of Greenhouse Gas Control* **2015**, *41*, 68-81.

(92) Lasala, S.; Chiesa, P.; Privat, R.; Jaubert, J.-N. Measurement and prediction of multi-property data of CO2-N2-O2-CH4 mixtures with the “Peng-Robinson+ residual Helmholtz energy-based” model. *Fluid Phase Equilibria* **2017**, *437*, 166-180.

(93) Ke, J.; Suleiman, N.; Sanchez-Vicente, Y.; Murphy, T. S.; Rodriguez, J.; Ramos, A.; Poliakoff, M.; George, M. W. The phase equilibrium and density studies of the ternary

mixtures of CO2+ Ar+ N2 and CO2+ Ar+ H2, systems relevance to CCS technology. *International Journal of Greenhouse Gas Control* **2017**, *56*, 55-66.

(94) Xu, C.-G.; Li, X.-S. Research progress of hydrate-based CO 2 separation and capture from gas mixtures. *Rsc Advances* **2014**, *4*, 18301-18316.

(95) Eslamimanesh, A.; Mohammadi, A. H.; Richon, D.; Naidoo, P.; Ramjugernath, D. Application of gas hydrate formation in separation processes: A review of experimental studies. *The Journal of Chemical Thermodynamics* **2012**, *46*, 62-71.

(96) Hassanpouryouzband, A.; Yang, J.; Joonaki, E.; Tohidi, B.; Chuvilin, E.; Bukhanov, B.; Istomin, V. In *Tilte*2017.

(97) Kunz, O.; Wagner, W. The GERG-2008 wide-range equation of state for natural gases and other mixtures: an expansion of GERG-2004. *Journal of chemical & engineering data* **2012**, *57*, 3032-3091.

(98) Kontogeorgis, G. M.; Michelsen, M. L.; Folas, G. K.; Derawi, S.; von Solms, N.; Stenby, E. H. Ten years with the CPA (Cubic-Plus-Association) equation of state. Part 1. Pure compounds and self-associating systems. *Industrial & engineering chemistry research* **2006**, *45*, 4855-4868.

(99) Kontogeorgis, G. M.; Michelsen, M. L.; Folas, G. K.; Derawi, S.; von Solms, N.; Stenby, E. H. Ten years with the CPA (Cubic-Plus-Association) equation of state. Part 2. Cross-associating and multicomponent systems. *Industrial & Engineering Chemistry Research* **2006**, *45*, 4869-4878.

(100) Danesh, A.: *PVT and phase behaviour of petroleum reservoir fluids*; Elsevier, 1998; Vol. 47.

(101) Masoudi, R.; Arjmandi, M.; Tohidi, B. Extension of Valderrama–Patel–Teja equation of state to modelling single and mixed electrolyte solutions. *Chemical Engineering Science* **2003**, *58*, 1743-1749.

(102) von Solms, N.; Michelsen, M. L.; Kontogeorgis, G. M. Computational and physical performance of a modified PC-SAFT equation of state for highly asymmetric and associating mixtures. *Industrial & engineering chemistry research* **2003**, *42*, 1098-1105.

(103) Tsivintzelis, I.; Ali, S.; Kontogeorgis, G. M. Modeling phase equilibria for acid gas mixtures using the CPA equation of state. Part IV. Applications to mixtures of CO2 with alkanes. *Fluid Phase Equilibria* **2015**, *397*, 1-17.

(104) Soave, G. Equilibrium constants from a modified Redlich-Kwong equation of state. *Chemical Engineering Science* **1972**, *27*, 1197-1203.

(105) Kontogeorgis, G. M.; Yakoumis, I. V.; Meijer, H.; Hendriks, E.; Moorwood, T. Multicomponent phase equilibrium calculations for water–methanol–alkane mixtures. *Fluid Phase Equilibria* **1999**, *158*, 201-209.

(106) Valderrama, J. O. A generalized Patel-Teja equation of state for polar and nonpolar fluids and their mixtures. *Journal of chemical engineering of Japan* **1990**, *23*, 87-91.

(107) Avlonitis, D.; Danesh, A.; Todd, A. Prediction of VL and VLL equilibria of mixtures containing petroleum reservoir fluids and methanol with a cubic EoS. *Fluid Phase Equilibria* **1994**, *94*, 181-216.

(108) Chen, S. S.; Kreglewski, A. Applications of the Augmented van der Waals Theory of Fluids.: I. Pure Fluids. *Berichte der Bunsengesellschaft für physikalische Chemie* **1977**, *81*, 1048-1052.

(109) Hassanpouryouzband, A.; Joonaki, E.; Taghikhani, V.; Bozorgmehry Boozarjomehry, R.; Chapoy, A.; Tohidi, B. New Two-Dimensional Particle-Scale Model To Simulate Asphaltene Deposition in Wellbores and Pipelines. *Energy & Fuels* **2017**.

(110) Gross, J.; Sadowski, G. Perturbed-chain SAFT: An equation of state based on a perturbation theory for chain molecules. *Industrial & engineering chemistry research* **2001**, *40*, 1244-1260.

(111) Grenner, A.; Schmelzer, J.; von Solms, N.; Kontogeorgis, G. M. Comparison of two association models (Elliott− Suresh− Donohue and simplified PC-SAFT) for complex phase equilibria of hydrocarbon− water and amine-containing mixtures. *Industrial & engineering chemistry research* **2006**, *45*, 8170-8179.

(112) Aasberg-Petersen, K.; Stenby, E.; Fredenslund, A. Prediction of high-pressure gas solubilities in aqueous mixtures of electrolytes. *Industrial & engineering chemistry research* **1991**, *30*, 2180-2185.

(113) Haghighi, H.; Chapoy, A.; Tohidi, B. Freezing point depression of electrolyte solutions: experimental measurements and modeling using the cubic-plus-association equation of state. *Industrial & Engineering Chemistry Research* **2008**, *47*, 3983-3989.

(114) Mao, S.; Duan, Z. A thermodynamic model for calculating nitrogen solubility, gas phase composition and density of the N2–H2O–NaCl system. *Fluid phase equilibria* **2006**, *248*, 103-114.

(115) Haghighi, H.; Chapoy, A.; Burgess, R.; Tohidi, B. Experimental and thermodynamic modelling of systems containing water and ethylene glycol: Application to flow assurance and gas processing. *Fluid Phase Equilibria* **2009**, *276*, 24-30.

(116) Chapoy, A.; Burgass, R.; Tohidi, B.; Austell, J. M.; Eickhoff, C. Effect of common impurities on the phase behavior of carbon-dioxide-rich systems: minimizing the risk of hydrate formation and two-phase flow. *SPE Journal* **2011**, *16*, 921-930.
(117) Görgényi, M.; Dewulf, J.; Van Langenhove, H.; Héberger, K. Aqueous salting-out effect of inorganic cations and anions on non-electrolytes. *Chemosphere* **2006**, *65*, 802-810.

Chapter 3 - CO_2 Capture by Injection of Flue Gas or CO_2-N_2 Mixtures into Hydrate Reservoirs: Dependence of CO_2 Capture Efficiency on Gas Hydrate Reservoir Conditions

3.1 1. Introduction

Gas hydrate is a naturally occurring crystalline solid composed of a host lattice of water molecules that encages guest gas molecules without chemical bonding[1]. The principal guest molecule in naturally occurring hydrates is CH_4, very significant volume of which is trapped in natural sediments[2]. Methane hydrate (MH) is known to exist under permafrost, and in continental and margin sediments[3] potentially providing a sustainable energy resource[4] and also powerful reservoirs to mitigate increasing effect of CO_2[5] on the climate, with respect to reduced geological hazards[6] and sufficient energy efficiency[7].

CO_2 as the most important anthropogenic greenhouse gas is responsible for more than half of the increasing greenhouse effect[8]. However, given the existing infrastructure for production, transfer, and utilization, fossil fuels (main source of CO_2 emission) will continue to play a major role in heat and power generations for the predictable future[9]. Accordingly, techniques developed for carbon dioxide capture and storage (CCS) play a crucial role in control of global warming, standing as the major environmental challenge. Despite significant technological advancements in CO_2 storage (CS) techniques, challenges still exist in the development of complex and fully functional methods that can be applied on an industrial scale[10]. To address these challenges, CS in natural MH reservoirs has emerged, which is considered as a promising approach for permanent CS[5]. Furthermore, CO_2 hydrate (CH) is thermodynamically more stable than both MH structure I and II, enabling exothermic[11] replacement of CH_4 with CO_2. CO_2 replacement adds heat to the MH reservoir, increasing the methane production rate[12] and leading to more economic methane production. As a result, injection of CO_2 into MH reservoirs can not only recover methane by CO_2 replacement but also reduce the impact of hydrate dissociation on geomechanical stability of the hydrate deposits due to formation of CO_2 hydrate or CO_2-mixed hydrates. This secondary hydrate formation will also consume the released water and cement the released sands after MH dissociation, results in limiting the migration of water, and sand significantly, when compared with other methane recovery methods[13,14]. However, more thorough investigations are required to quantify this effect. Recent studies have included various approaches towards understanding the

CH_4−CO_2 replacement mechanism, including liquid CO_2 injection[15], kinetic study using in situ laser Raman spectroscopy[16], micro differential scanning calorimeter[17], and magnetic resonance imaging[18], and enhanced CH_4−CO_2 replacement in the presence of thermal stimulation[19]. Further information can be found elsewhere[20–22].

Despite all of the proposed benefits, CS in hydrate reservoirs has high-cost barriers that prevents its wide deployment[23–25]. In this case, CO_2 capture prior to storage is the major[26,27] cost. It was estimated that the cost of CO_2 separation and disposal from coal-fired power plants can increase the cost of electricity by about 75%[28]; much of this cost (up to 80%[28]) is caused by separation of CO_2, the removal of which leads to an increase in power efficiency from 26% to 38%[29]. In addition, another major energy penalty comes from compression of the flue gas before injection, which should be considered before any field trials. There are extensive efforts associated with improvement of the CO_2 capture efficiency, such as optimizing the capture plant design and capturing parameters, or developing new absorbents, adsorbents, membrane materials[30] whose principal aims are towards a breakthrough in the development of low-cost CO_2 capture technology. However, the predominant obstacles associated with the exploitation of this method, apart from the clear economic challenges, are connected with scaling up in order to encourage public investment[31].

Injection of CO_2-N_2 mixtures instead of pure CO_2 into gas hydrate reservoirs could significantly reduce CO_2 separation costs. It was reported that using (N_2+CO_2) gas mixtures improved CO_2-CH_4 exchange rate[6,32,33] and resulted in a higher methane recovery ratio[32] and higher mobility in sediments[34] compared to those of supercritical or pure CO_2. Moreover, an industrial scale test of CO_2 replacement in the North Slope of Alaska has shown that injecting a gas mixture of 23% CO_2 and 77% N_2 into a hydrate layer with simultaneous recovery of methane has proven successful, preventing CO_2 hydrate build-up around the injection well[35]. Overall performance was also excellent and incident-free, which is a very positive sign for the development of the technology. The CS efficiency for this case was more than 50%, whereas most of the injected N_2 was collected, and at the final depressurization stage below hydrate stability, produced gas increased from an initial 20,000 scf/day to 45,000 scf/day. This method offers significant potential for efficiency and economic improvements. Direct injection of flue gas from coal-fired power plant into hydrate reservoirs[36] was proposed as a potential method for reduction of the CCS cost by eliminating the major cost of CO_2 capture. This method is mainly based on methane production by shifting the methane hydrate stability zone rather than CO_2 replacement, leading to production of methane-rich gas mixtures with up to

70% methane and storage of up to 80% CO_2 present in flue gas. Given the results, this method has a great potential to attract the industrial attention. Regarding concerns with respect to the leakage of the injected gas, it's shown that CO_2 hydrate formation could provide an additional safety factor for sealing the reservoir by forming a hydrate cap which remarkably blocks further upward gas flow[37].

Although the above investigations demonstrate that injection of CO_2-N_2 gas mixtures could provide an economically-viable method for CCS in gas hydrate reservoirs, there remains a fundamental question: How does formation of the CO_2 and CO_2-mixed hydrates (i.e., CO_2 capture) depend on the reservoir conditions after CO_2-N_2 mixtures or flue gas injection into a gas hydrate reservoir? Accordingly, experiments were conducted to investigate the efficiency of CO_2 capture during methane recovery by direct injection of flue gas at different conditions, including flue gas injection pressure, reservoir temperature, and reservoir hydrate and water saturation. This was to find out if there are specific thermodynamic conditions that are most favorable for the CCS process in hydrate-bearing sediments.

3.2 Experimental Section

3.2.1 *Materials and experimental apparatus*

Research grade methane with a certified purity of 99.995 vol% was purchased from BOC Limited. A synthetic flue gas composed of 85.4 mol% nitrogen and 14.6 mol% CO_2[24,36] was utilized for simulating flue gas coming from coal-fired power plants, which was provided by BOC Limited. Deionized water was obtained using ELGA DV 25 Integral Water Purification System. It is worth to note that power-plant flue gas may contain O_2, Ar, SO_2 and water beside N_2 and CO_2[38], but small amount of these gases has very minor effect on the HSZ and can be neglected[39].

Experiments were carried out using a 316 stainless steel cylindrical autoclave, a schematic of which is shown in Figure 3.1. The high-pressure cell has a volume of 1700 cm^3 and a maximum working pressure of 40 MPa is surrounded by a cooling jacket. The jacket has two openings (inlet and outlet), which allows cooling fluid to circulate around the cell. The cooling fluid is circulated by a cryostat (Grant LTC) to obtain the desired temperature, ranging from 243.2 K to 303.2 K. The cell temperature was measured using a Platinum-Resistant Thermometer (PRT) coated in stainless steel with an uncertainty of 0.1 K. The Pressure was measured using a Druck pressure transducer (accuracy +/-0.05) MPa connected to top of the cell. The cell was kept vertical throughout the tests. Gas was

injected from the top-cap via a high-pressure valve. A high-pressure magnetic stirrer (Top Industrie SA, France, model 6180300B) is fixed on top of the cell to faster reach of equilibrium condition by use of a stainless-steel impeller, helping increase the surface contact of the components. The temperature and pressure of the system were recorded on a PC using LabView software interface (National Instruments) through a data acquisition device at regular time intervals. Gas samples were collected using high-pressure vessels. A Gas Chromatograph (GC) (Varian 3600, Agilent Technologies) was used to analyse gas samples.

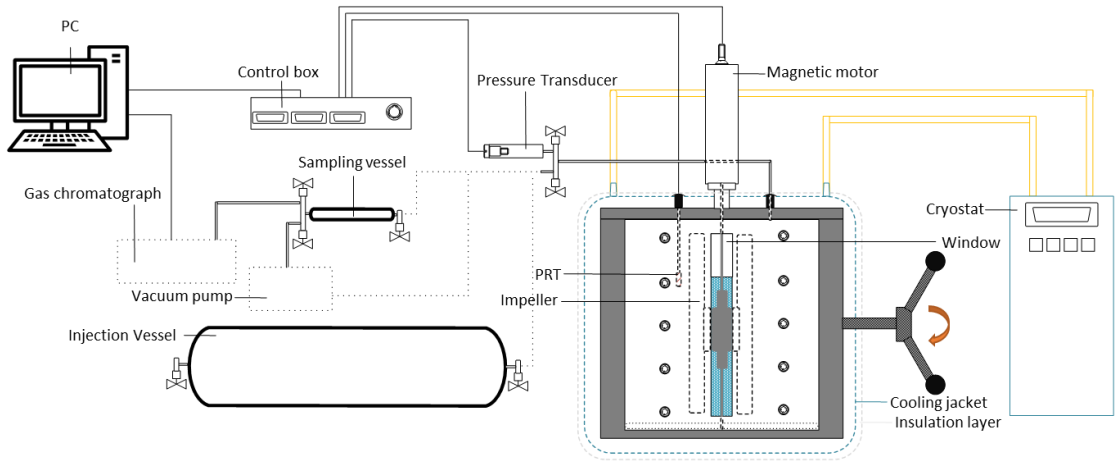

Figure 3.1 Schematic of the high-pressure autoclave

3.2.2 Method and procedure

Injection of flue gas or CO_2-N_2 mixtures into MH reservoirs shifts hydrate stability zone (HSZ) to higher pressure at the reservoir temperature, therefore, leads to MH decomposition and CO_2-mixed hydrate formation. By comparison to the fact that MH will start decomposition as long as the thermodynamic conditions are shifted outside the HSZ, formation of CO_2 hydrate or CO_2-mixed hydrate is a complex process. This may be associated to several factors, including the composition of fluids surrounding the methane hydrate crystals, temperature/pressure conditions, the ratio of MH to the injected flue gas, and mass/heat transfer process. In porous media the methane hydrate decomposition and CO_2-mixed hydrate formation takes a long time to reach equilibrium due to mass and heat transfer process constrained by fine pores[32]. To reduce the experimental time, all experiments were conducted in bulk conditions using an autoclave with a magnetic mixer (Figure 3.1). A synthetic flue gas was directly injected into MH and then the system was depressurised step by step. Once thermodynamic equilibrium was reached at each pressure stage at a set temperature, a gas sample was taken and its composition was analysed using a GC. The experiment was repeated at three different temperatures to

investigate the effect of reservoir temperature. Furthermore, to understand the dependence of the CO_2 capture efficiency on the MH reservoir volume and hydrate saturation, i.e., ratio of flue gas to MH, experiments were conducted in the presence of different amounts of MH initially formed before flue gas injection. It should be noted that less water was added to the system for the experiment with a low ratio of flue gas to MH to achieve the desired gas to hydrate ratio and to be able to have continuous mixing without blockage due to redundant hydrate formation.

Figure 3.2 presents the HSZs of the gas-water systems tested in this work together with the experimental temperature and pressure conditions. In order to mimic the temperature of typical MH reservoirs, experiments were conducted at temperature ranging from 273.2 to 283.2 K. All experiments were started at a pressure below the flue gas HSZ to avoid formation of CO_2-N_2 mixed hydrates. However, from a thermodynamic point of view, the possibility of CO_2-N_2-CH_4 mixture hydrate formation still exists at the experimental conditions. At the experimental conditions the other possible hydrate compositions are CO_2-CH_4 and N_2-CH_4 hydrates. Here, CO_2 will fill the large cavities, while N_2 will enter to small cavities for thermodynamic stabilization[11,40]. The main reason for MH dissociation and mixed hydrate formation is the chemical potential shift due to the change in the gas composition, but CO_2/CH_4 replacement could also occur owing to higher stability of CO_2 hydrate compared to MH. It should be noted that the mechanism of flue gas replacement with CH_4 is not fully understood and there are controversial ideas about that.[34,41] As can be seen, in all the experiments, the staged depressurisation process was stopped just above the methane hydrate decomposition pressure at the experimental temperature, since injected flue gas pressure must be higher than that of existing MH reservoirs. In the same line, the optimum conditions for CS can be defined as points at which the ratio of CO_2/(N_2+ CO_2) (C-ratio) in hydrate phase is maximum, or consequently the C-ratio in gas phase is minimum. It therefore is a key point to analyse the gas composition at each stage to determine the optimum conditions for CO_2 capture.

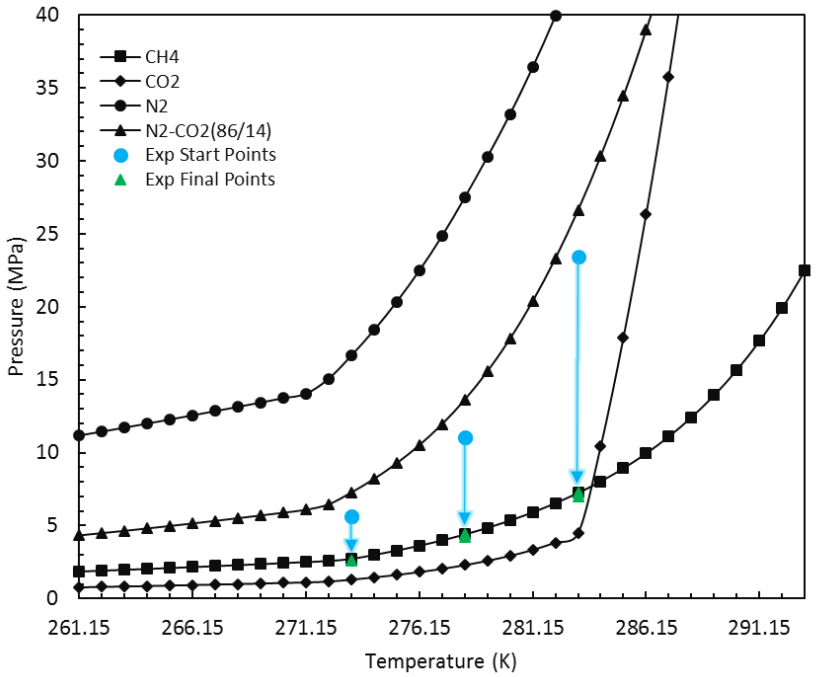

Figure 3. 2 The predicted hydrate stability zones of CH4, CO2, N2, flue gas, and the experimental conditions

The following general procedure was used for all the experiments. Deionised water was loaded in the autoclave. After vacuuming, methane was injected to the desired pressure at room temperature ~293 K. Then the system was set to the target temperature whilst stirring at 500 rpm to form MH. The stirrer was allowed to run until equilibrium was achieved, which was indicated by a stabilised system pressure. Following that, synthetic flue gas was injected to the autoclave, allowing the system to reach a pressure between the MH phase boundary and flue gas hydrate phase boundary (Figure 3.2). Gas samples were taken and analysed at specified time intervals, usually every 24 hours. The process was continued until an equilibrium was reached, at which no further changes in gas composition were observed. Following this, the system pressure was reduced to the next pressure stage by draining certain amount of the gas from the system after stopping the stirrer. The same procedure was repeated for each step up to the final pressure stage. The system composition which is made up of all gases in the water, hydrate and gas phases, were calculated using mass balance and measurement of the removed gas at end of each depressurization stage. These results can be found in Appendix B. Table 3.1 shows the experimental conditions including temperature, initial water amount, system pressure after methane injection at room temperature, start pressure and end pressure of depressurization, and molar ratio of initial flue gas to CH_4 in the autoclave.

Table 3.1 Experimental conditions

Exp.	T (K)	Water (g)	CH_4 injection P (MPa)	Start P (MPa)	End P (MPa)	Initial flue gas to CH_4 ratio(mol/mol)
1	273.2	1150	17.58	5.66	2.62	0.59
2	273.2	500	7.03	5.66	2.62	1.04
3	278.2	1150	19.31	11.03	4.41	0.82
4	278.2	500	8.62	11.05	4.21	1.62
5	283.2	1150	22.06	23.44	7.27	1.91
6	283.2	500	11.38	23.79	6.99	3.17

3.3 Results and Discussion

As with most gas injection methods, an investigation of the effects of pressure on CS through flue gas injection is necessary to determine at which pressure there is a maximum CS, for a particular MH reservoir at certain temperature. By optimizing the pressure of the injected gas and operating at such conditions close to the optimum pressure, the economics of the gas injection projects can be further improved. This knowledge is essential for field-scale applications as it is preferably based on the method efficiency. In this work pressure varied rather than temperature because it is relatively easier to control the reservoir pressure compared to the temperature. GC analysis results versus pressure were plotted as shown in Figure 3.3 a-f to determine the ideal pressure for each test. This pressure is seen in Figure 3.3 a-f where clear downward peaks were observed for C-ratio graphs. The initial reduction of this ratio can be justified by the fact that more CO_2 than N_2 goes to the hydrate phase (CO_2 hydrate or CO_2-mixed hydrates) due to relative thermodynamic stability of CO_2 at lower pressures and N_2 promotes CO_2-CH_4 molecule exchange by interfering CH_4 in small cages[32], which is in agreement with other published work[6]. The possible reason for the secondary increase after optimum pressure is that at lower pressures, N_2 molecules stop acting as promoting agents for CO_2 sequestration, which results in reduction in the driving force of N_2 on CH_4 hydrates. This in turn, will possibly lead to destabilization of those excess CO_2 hydrates, which were stabilized by N_2. Furthermore, sharper increase in the C-ratio at the final depressurization stage just above CH_4 hydrate dissociation pressure indicates some of CO_2-mixed hydrates were dissociated significantly above the CO_2 HSZ, assuming that there is no possibility of N_2 mixed hydrate formation at this condition. It should be noted that C-ratio changes were

sharper against pressure at lower temperatures and with higher MH saturation compared to those at higher temperatures and with lower MH saturation, respectively, indicating the higher chemical potential shift at former conditions compared to latter ones after flue gas injection. Accordingly, the trend of changes in the C-ratio for the gas phase shows that the occupancy ratio of large to small cages during CO_2 mixed hydrate formation changes with pressure. What's more, the experiments were conducted with two different amounts of initially formed MH to clarify the effect of hydrate saturation in the reservoir. Figure 3.3 indicates that at all temperatures, C-ratio decreased with increasing initial MH and water content, which can be attributed to CO_2-CH_4 replacement, higher solubility of CO_2 compared to N_2, and reformation new CO_2 rich hydrates. More CS through more MH can be considered as further support for CO_2-CH_4 replacement without full dissociation of hydrate structure, which is in agreement with another work[34]. This phenomena, has also been experimentally investigated by various laboratories using NMR. They reported that spontaneous exchange between the CH_4 and CO_2 guest molecule is governed by a direct solid-state conversion, which is very slow, and limited by mass transport via hydrate[42]. However, considering the lower concentration of CO_2 in the injected gas which could possibly reduce the possibility of CO_2-CH_4 exchange, further investigation is required for full understanding of the mechanism. In the same line, presence of more water in the system will assist the formation of new CO_2-rich hydrates, and the released heat from formation of new hydrate will increase the rate of CH_4 hydrate dissociation, and subsequently help the exchange process as well. As illustrated in Figure 3.3a-f, CH_4 graphs showed upward trends. Corresponding to the increase in CH_4 concentration in the gas phase, graphs for N_2 concentration showed continuous downward trends. Meanwhile, CO_2 concentration slightly increased after the initial reduction. This is continued until the end of the tests, which can be explained using the same reason for the increase in the C-ratio. It is clear from the aforementioned graphs that CH_4 percent in the gas phase increased with both reduction in the temperature and an increase in the amount of initially formed MH. Accordingly, more favourable conditions for CS are also more favourable for methane recovery. It should be noted that using this method will increase the separation cost of produced gas compared to pure CH_4, but it is clear from the results that, in all the optimum conditions the purity of CH_4 in the produced gas was relatively high, reducing the cost of separation. These results suggest that chemical shift method is able to efficiently recover CH_4 and facilitate the CH_4 transport from the hydrate phase to the gas phase.

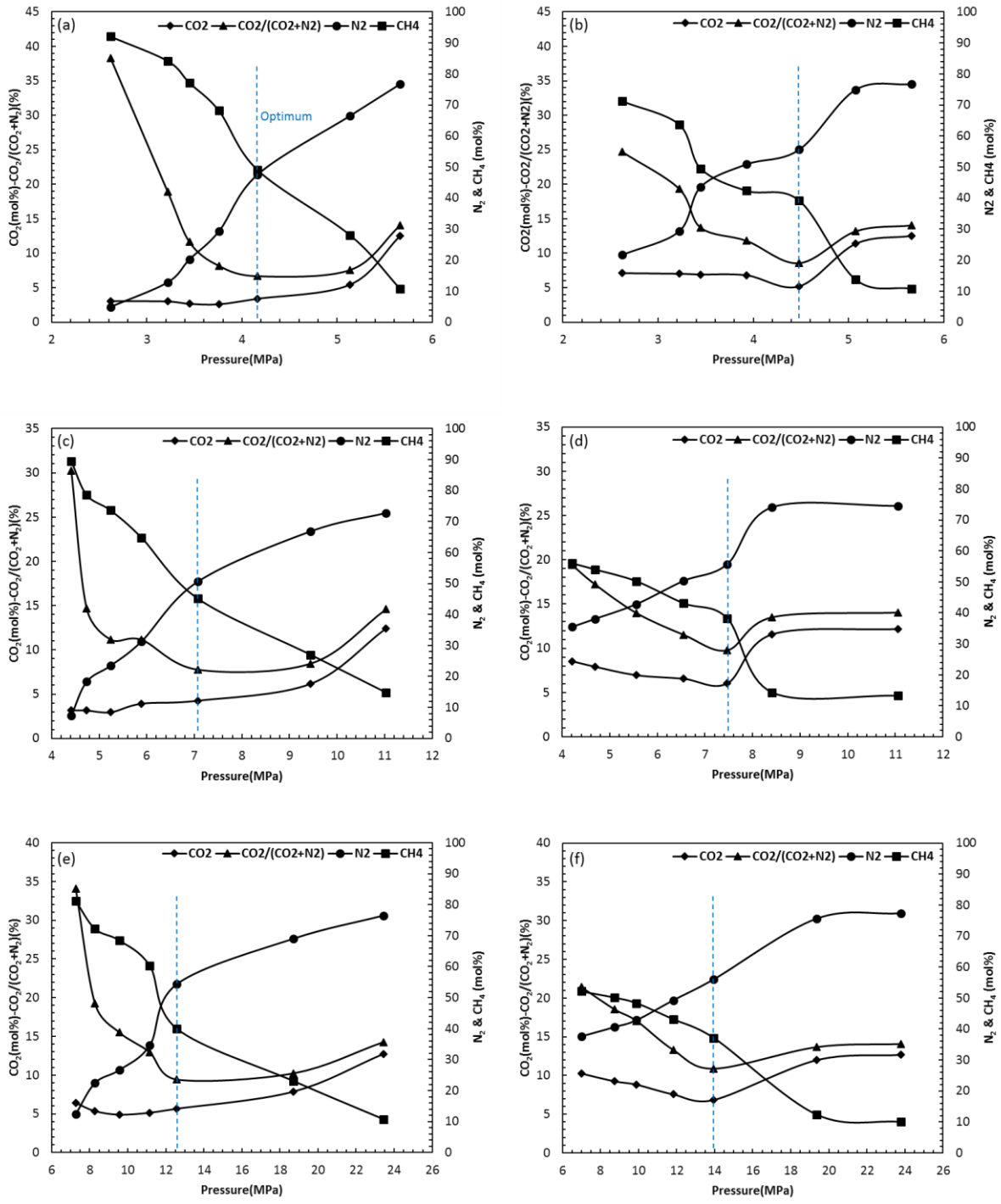

Figure 3.3 Variation in the gas composition change during the stepwise depressurization. (a)-(f) for Experiments 1-6.

Figure 3.4 and Table 3.2 show measured properties of the system at optimum conditions for all experiments. As shown in Figure 3.4-a, the C-ratio in the gas phase for the optimum pressure greatly increases with increase in the temperature, whereas there is no significant difference in this ratio for system composition (see Figure 3.4-b), which is reasonable as system compositions at start of experiments were equal and removed gas doesn't have a significant effect. This suggests that the lower temperatures favour more

CO_2 than N_2 in the hydrate phase. Furthermore, at the optimum pressure, the C-ratio in the gas phase is lower for the systems with more MH, while this ratio for system composition is higher for the systems with more MH than those with less MH. This can be attributed to the fact that the more MH and water have more capacity of storing CO_2. For each component in the system at each depressurization step, the total concentration will increase if the concentration of the component in the gas phase is less than that of the system composition, otherwise it will decrease. With this in mind, it is worth noting that, as shown in Figure 3.4 b, the overall C-ratio in the system was almost the same for experiments with the same amount of initial methane. However the ratio is lower for the experiments with lower initial MH owing to less increase of CH_4 in the gas phase during the initial steps compared to that of higher initial MH that results from less driving force through chemical potential shift. By comparing the slopes of CH_4 concentration in Figure 3.4-a, the temperature effect on CH_4 recovery for higher initial MH saturation is relatively higher than that with less MH at optimum conditions. However, the slope for the C-ratio was almost the same for both amounts of initial MH. This effect is possibly derived from higher concentrations of overall N_2 at lower MH concentrations and also higher temperatures (see Figure 3. 4-b), reducing the temperature effect by interfering MH at small pores without replacing with them. For overall system CH_4 at the optimum conditions, the concentration at higher temperatures is less than that at lower temperature. This could be plausibly justified by the fact that upon high pressure at start of the experiments at high temperature, relatively more flue gas was injected which, in turn, kept the total CH_4 concentration at lower state. In contrast, for the same reason, fractions of CO_2 and N_2 increase with temperature.

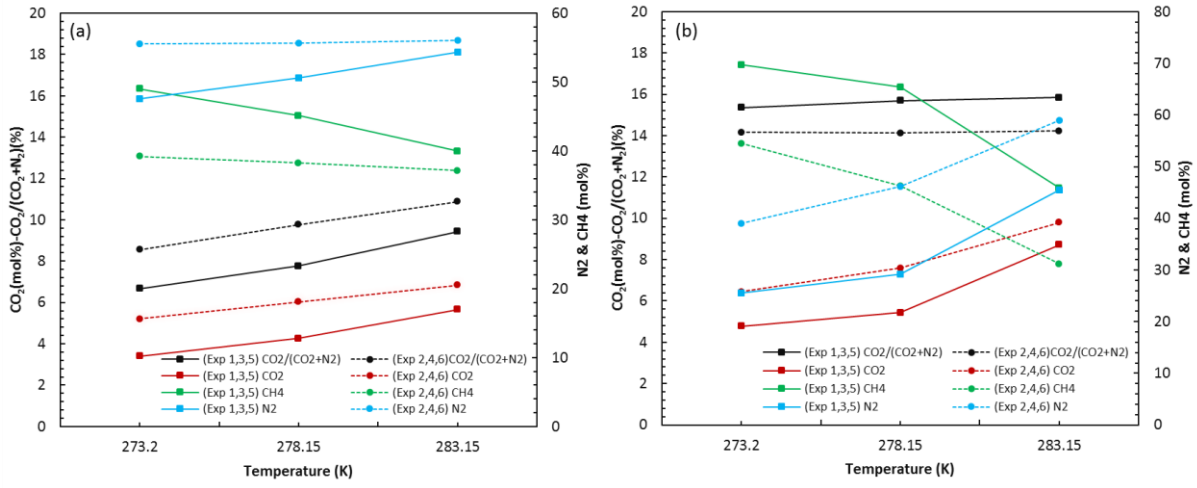

Figure 3.4 (a) The measured gas composition and (b) the system composition at optimum conditions for all experiments.

Table 3.2 The determined optimum conditions for CO2 capture as hydrates

Exp.	Pressure (MPa)	Gas phase composition				Overall composition			
		N_2 (mol%)	CH_4 (mol%)	CO_2 (mol%)	$CO_2/(CO_2+N_2)$	N_2 (mol%)	CH_4 (mol%)	CO_2 (mol%)	$CO_2/(CO_2+N_2)$
1	4.16	47.60	49.00	3.40	6.67	25.49	69.74	4.77	15.36
2	4.48	55.60	39.20	5.20	8.55	39.07	54.49	6.44	14.15
3	7.07	50.62	45.12	4.26	7.76	29.19	65.38	5.43	15.69
4	7.46	55.70	38.27	6.03	9.78	46.14	46.27	7.59	14.12
5	12.58	54.38	39.96	5.66	9.43	45.46	45.82	8.72	15.84
6	13.95	56.04	37.12	6.84	10.88	59.01	31.20	9.79	14.23

To depressurise the system some gas mixture had to be drained out from the system. This in turn will lead to a change in the system composition. Accordingly, because the system composition was changing during the depressurisation process, there was a need to define a parameter to eliminate the effect of these changes. Thus, "repartition" ratio, R is defined as the C-ratio in the gas phase divided by that in the overall system. This is to examine whether the apparent optimum in the current method is the true optimum. The R-values for each step in all experiments were calculated and are plotted in Figure 3.5, in which the minimum R-value at each test is the indication of the optimum point. The resulting optimum conditions from R-values for all experiments, as can be seen, were the same as those determined based on the gas composition of the existing system. Therefore, it can be concluded that optimum conditions can be determined by analysis of the gas composition after some gas was removed.

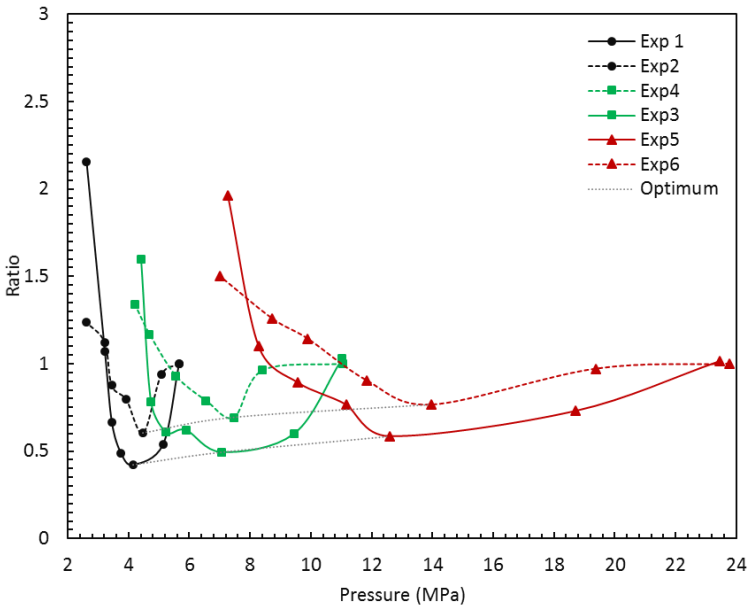

Figure 3.5 R-Values variation with the system pressure at the experimental temperatures

Figure 3.6 illustrates the optimum pressure for each experiment together with the predicted HSZs for CH_4-flue gas mixtures with different mole ratios of CH_4. As can be seen, all optimum conditions are in a pressure range between the HSZs of 30 mol% and 50 mole% methane, approaching the HSZs with 30 mol% methane as the initial MH decreases and approaching to the HSZs with 50 mol% methane as the initial MH increases. Furthermore, in terms of pressure, the two optimum CO_2 capture pressures are closer at lower temperature compared with those at higher temperatures. However, there are larger differences in C-ratio with change of pressure at lower temperature compared with higher temperatures (see Figure3). By taking the above two reasons into account, it can be concluded that the pressure effect on CO_2 capture efficiency is more significant at lower temperatures than at higher temperatures.

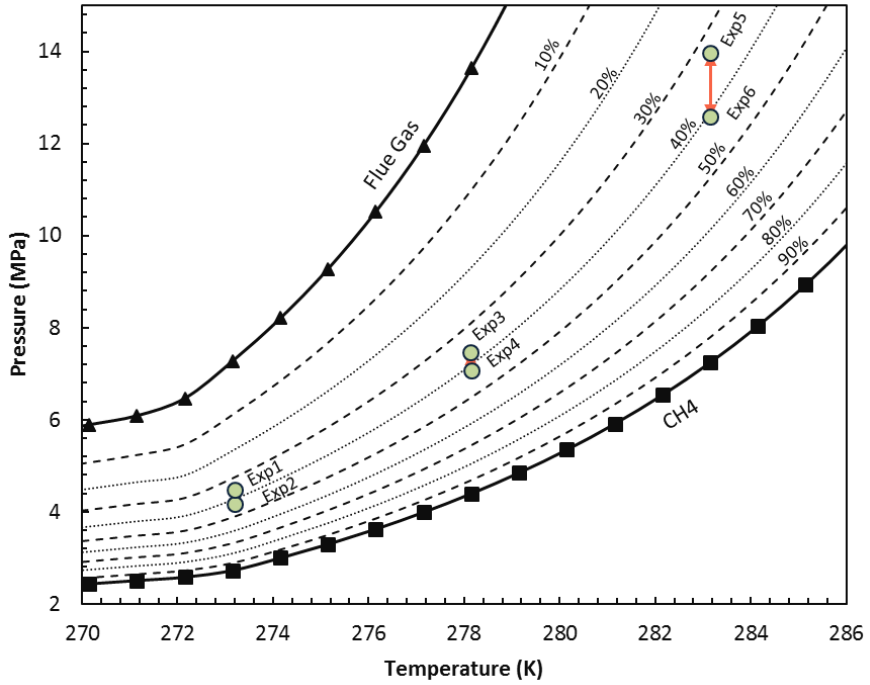

Figure 3.6 Location of the determined optimum conditions for CO2 capture for different gas hydrate reservoir conditions

3.4 References

(1) Sloan, E. D. *Nature* **2003**, *426* (November), 353.
(2) Kvenvolden, K. A.; McMenamin, M. A. **1980**.
(3) Kvenvolden, K. A.; Lorenson, T. D. American Geophysical Union, 2013; pp 3–18.
(4) Holder, G. D.; Kamath, V. A. *J. Chem. Thermodyn.* **1984**, *16* (4), 399–400.
(5) Onyango, P.; Jiang, S.; Uejima, H.; Shamblott, M. J.; Gearhart, J. D.; Cui, H.; Feinberg, A. P. *Proc. Natl. Acad. Sci. U. S. A.* **2002**, *1699* (10), 10599–10604.
(6) Park, Y.; Kim, D.-Y.; Lee, J.-W.; Huh, D.-G.; Park, K.-P.; Lee, J.; Lee, H. *Proc. Natl. Acad. Sci. U. S. A.* **2006**, *103* (34), 12690–12694.
(7) Ersland, G.; Husebø, J.; Graue, A.; Kvamme, B. *Energy Procedia* **2009**, *1* (1),

3477–3484.
(8) IPCC. *Weather* **2001**, *57*, 267–269.
(9) Dti, U. K. *Dep. Trade Ind. C.* **2007**.
(10) MacDowell, N.; Florin, N.; Buchard, A.; Hallett, J.; Galindo, A.; Jackson, G.; Adjiman, C. S.; Williams, C. K.; Shah, N.; Fennell, P. *Energy Environ. Sci.* **2010**, *3* (11), 1645–1669.
(11) Dornan, P.; Alavi, S.; Woo, T. K. *J. Chem. Phys.* **2007**, *127* (12), 124510–124700.
(12) Deusner, C.; Bigalke, N.; Kossel, E.; Haeckel, M. *Energies* **2012**, *5* (12), 2112–2140.
(13) Seo, Y.-T.; Moudrakovski, I. L.; Ripmeester, J. A.; Lee, J.; Lee, H. *Environ. Sci. Technol.* **2005**, *39* (7), 2315–2319.
(14) Yuan, Q.; Sun, C.-Y.; Liu, B.; Wang, X.; Ma, Z.-W.; Ma, Q.-L.; Yang, L.-Y.; Chen, G.-J.; Li, Q.-P.; Li, S. *Energy Convers. Manag.* **2013**, *67*, 257–264.
(15) Ota, M.; Morohashi, K.; Abe, Y.; Watanabe, M.; Smith, Jr., R. L.; Inomata, H. *Energy Convers. Manag.* **2005**, *46* (11), 1680–1691.
(16) Ota, M.; Abe, Y.; Watanabe, M.; Smith, R. L.; Inomata, H. *Fluid Phase Equilib.* **2005**, *228*, 553–559.
(17) Lee, S.; Lee, Y.; Lee, J.; Lee, H.; Seo, Y. *Environ. Sci. Technol.* **2013**, *47* (22), 13184–13190.
(18) Ersland, G.; Husebø, J.; Graue, A.; Baldwin, B. A.; Howard, J.; Stevens, J. *Chem. Eng. J.* **2010**, *158* (1), 25–31.
(19) Zhang, L.; Yang, L.; Wang, J.; Zhao, J.; Dong, H.; Yang, M.; Liu, Y.; Song, Y. *Chem. Eng. J.* **2017**, *308*, 40–49.
(20) Lee, H.; Seo, Y.; Seo, Y.-T.; Moudrakovski, I. L.; Ripmeester, J. A. *Angew. Chemie Int. Ed.* **2003**, *42* (41), 5048–5051.
(21) Goel, N. *J. Pet. Sci. Eng.* **2006**, *51* (3), 169–184.
(22) Ma, Z. W.; Zhang, P.; Bao, H. S.; Deng, S. *Renew. Sustain. Energy Rev.* **2016**, *53*, 1273–1302.
(23) Gough, C.; Mander, S.; Haszeldine, S. *Int. J. Greenh. Gas Control* **2010**, *4* (1), 1–12.
(24) Change, W. G. I. of the I. P. on C.; Metz, B.; Davidson, O.; Coninck, H. de; Loos, M.; Meyer, L. Cambridge University Press.
(25) Damen, K.; Troost, M. van; Faaij, A.; Turkenburg, W. *Prog. Energy Combust. Sci.* **2006**, *32* (2), 215–246.
(26) Feron, P. H. M.; Hendriks, C. A. *Oil Gas Sci. Technol.* **2005**, *60* (3), 451–459.
(27) Enterprise, S. *Scottish Enterp. Glas.* **2011**.
(28) Hendriks, C. A.; Blok, K.; Turkenburg, W. C. In *Climate and Energy: The Feasibility of Controlling CO2 Emissions*; Springer Netherlands: Dordrecht, 1989; pp 125–142.
(29) Peeters, A. N. M.; Faaij, A. P. C.; Turkenburg, W. C. *Int. J. Greenh. Gas Control* **2007**, *1* (4), 396–417.
(30) Pires, J. C. M.; Martins, F. G.; Alvim-Ferraz, M. C. M.; Simões, M. *Chem. Eng. Res. Des.* **2011**, *89* (9), 1446–1460.
(31) Boot-Handford, M. E.; Abanades, J. C.; Anthony, E. J.; Blunt, M. J.; Brandani, S.; Mac Dowell, N.; Fernández, J. R.; Ferrari, M.-C.; Gross, R.; Hallett, J. P. *Energy Environ. Sci.* **2014**, *7* (1), 130–189.
(32) Shin, K.; Park, Y.; Cha, M.; Park, K.-P.; Huh, D.-G.; Lee, J.; Kim, S.-J.; Lee, H. *Energy & Fuels* **2008**, *22* (5), 3160–3163.
(33) Koh, D.; Kang, H.; Kim, D.; Park, J.; Cha, M.; Lee, H. *ChemSusChem* **2012**, *5* (8), 1443–1448.
(34) Cha, M.; Shin, K.; Lee, H.; Moudrakovski, I. L.; Ripmeester, J. A.; Seo, Y.

Environ. Sci. Technol. **2015**, *49* (3), 1964–1971.
(35) Schoderbek, D.; Martin, K. L.; Howard, J.; Silpngarmlert, S.; Hester, K. In *OTC Arctic Technology Conference*; Offshore Technology Conference, 2012.
(36) Yang, J.; Okwananke, A.; Tohidi, B.; Chuvilin, E.; Maerle, K.; Istomin, V.; Bukhanov, B.; Cheremisin, A. *Energy Convers. Manag.* **2017**, *136*, 431–438.
(37) Tohidi, B.; Yang, J.; Salehabadi, M.; Anderson, R.; Chapoy, A. *Environ. Sci. Technol.* **2010**, *44* (4), 1509–1514.
(38) Ziabakhsh-Ganji, Z.; Kooi, H. *Appl. Energy* **2014**, *135*, 43–52.
(39) Chapoy, A.; Nazeri, M.; Kapateh, M.; Burgass, R.; Coquelet, C.; Tohidi, B. *Int. J. Greenh. Gas Control* **2013**, *19*, 92–100.
(40) Kvamme, B.; Iden, E.; Tveit, J.; Veland, V.; Zarifi, M.; Qorbani, K. *J. Chem. Eng. Data* **2017**, *62* (5), 1645–1658.
(41) Bai, D.; Zhang, X.; Chen, G.; Wang, W. *Energy Environ. Sci.* **2012**, *5* (5), 7033.
(42) Lee, H., Seo, Y., Seo, Y. T., Moudrakovski, I. L., & Ripmeester, J. A. Recovering methane from solid methane hydrate with carbon dioxide. Angewandte Chemie International Edition. **2003**, 42(41), 5048-5051.

Chapter 4 - Integrated CO_2 Sequestration and Methane Recovery by Injection of Flue Gas into Frozen Methane Hydrate Reservoirs

4.1 INTRODUCTION

The oceans, permafrost regions, and continental and marine sediments contain a huge volume of methane trapped in the form of gas hydrates[1] which could be a potential energy source [2] or CO_2 storage sink[3], depending upon human being actions, with respect to energy policy and anthropogenic global warming. These ice-like hydrates which are non-stoichiometric inclusion compounds with hydrogen bonded water cages enclathrated light guest molecules without chemical bonds[4,5], require suitable thermodynamic conditions including, pressure, temperature, and surrounded liquid and gas compositions to remain stable. Various approaches were taken to shift the system conditions out of the equilibrium in investigation of methane extraction from hydrate-bearing sediments. In comparison with those potential methods such as thermal stimulation[6], depressurization[7], chemical inhibitor injection[8], CO_2[9,10] or CO_2-mixed gases[11] (e.g. flue gas) injection, is more environmentally friendly because of their potential to capture CO_2 simultaneously with methane recovery. Moreover, injection of CO_2-mixed gases (mainly CO_2+N_2) produced directly from power stations rather than pure CO_2 is more economic owing to significant reduction in the total cost by avoidance of CO_2 separation cost[11–13].

Coal-fired power plants represent a substantial proportion of global anthropogenic CO_2 emissions which are the key contributors to global climate change[14]. The emission of CO_2 in pulverized coal plants causes by combustion of air and coal in a boiler to generate energy, producing flue gas with a low concentrated CO_2 (~14%). Emission of flue gas from a typical 600 MWE power plant could be more than 500 m^3 every second[15]. Accordingly, up-scaling post-combustion CO_2 capture from power-plant flue gas through sustainable methods is gaining importance to limit CO_2 emissions.

Previously, we presented initial results for injection of power-plant flue gas into gas hydrate reservoirs[16] above freezing temperatures and defined a method[11] to determine the optimum pressure of injection, where more detailed review of the past literature can be found. In recent year, several[13,17–19] investigations about various aspects of methane recovery by direct injection of flue gas have been reported, including limitations of CO_2/CH_4[17], effects of methane hydrate morphology and ratio of CO_2/N_2 in the injection gas[18], the effect of the sandstone permeability, and efficiency of the method in the

presence of thermal stimulation[13]. Here, referring to the previous chapter as a basis for our interpretations where necessary, we report new experimental results for the kinetics of optimized flue gas injection into methane hydrate reservoirs at sub-zero temperatures, covering all range of subglacial to under permafrost conditions, and further discuss and revisit previous results. The method efficiency under sub-zero temperature conditions was also investigated as major proportion of gas hydrate reservoirs locate underneath permafrost formations[20–22]. In addition, our previous experiments above water freezing point showed remarkably more favourable results for both CO_2 storage and methane recovery at lower temperatures, emphasizing the necessity of investigating the method efficiency under 0 ºC. One of the objectives of this study was to investigate the efficiency of the method (i.e. methane recovery and CO_2 storage percentages) in realistic time scale and hydrate reservoir conditions. The second key objective was to evaluate the impact of reservoir conditions on the kinetic efficiency to examine potential methane reservoirs for choosing an appropriate one for CO_2 storage. Lastly, the impact of global warming and natural temperature cycles on the stored CO_2 was also investigated to understand the potential hazards to the environment.

4.2 EXPERIMENTAL SECTION

4.2.1 Materials

A well-characterized silica sand from Fife (Scotland) was used as the mesoporous media, and a detailed analysis can be found in the Appendix C. Deionized water (total organic carbon <5 ppb) from an ELGA DV 25 Integral Water Purification was used for wetting sands, and experimental setup cleaning. The following gases from BOC Limited were used in the experiments: CO_2 (99.995 vol %), N_2 (99.995 vol %), and CH4 (99.995 vol %). Well-characterized sands from Fife, Scotland were used for simulating mesoporous hydrate reservoirs.

4.2.2 Apparatus

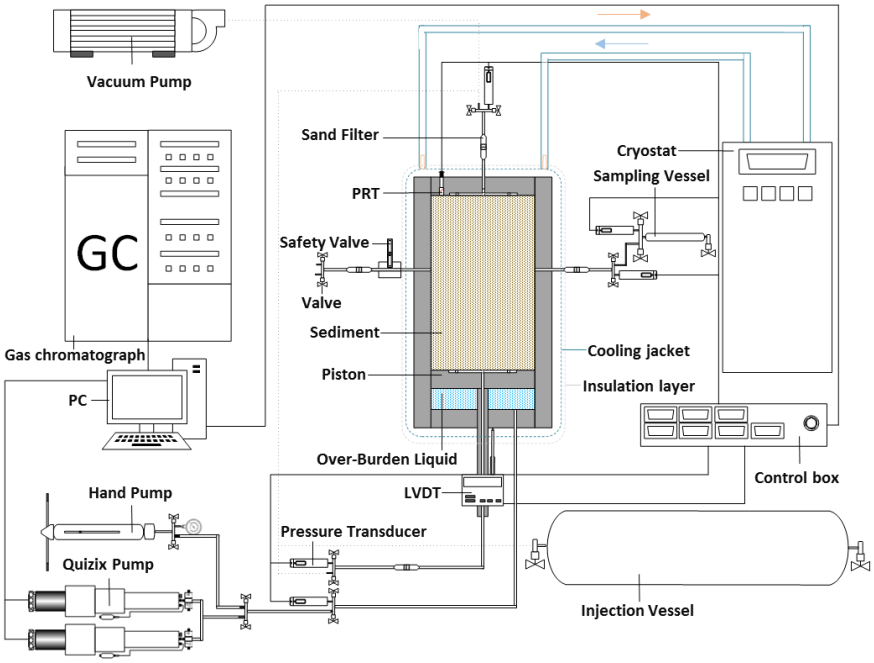

Figure 4.1 Schematic of the high-pressure cell setup

A high-pressure cylindrical cell setup was employed in all the experiments as shown in Figure 4.1. The cell body is made of 316 stainless steel. The geometric area exposed to the hydrate-bearing sediments has been placed between a fixed top cap and a bottom cap. A movable piston is mounted above the bottom cap to simulate the overburden pressure, moving up and down by withdrawal or injection of hydraulic fluid behind the piston. Thus, the reservoir is not in direct contact with hydraulic fluid. Hydraulic fluid injection/removal was performed using a dual-cylinder Quizix pump (SP-5200, Chandler Engineering) for maintaining the pressure or a hand pump for achieving initial compaction pressure. A linear variable differential transformer (LVDT) is mounted on the bottom cap to measure the piston movement; therefore, the reservoir volume could be calculated at any stage. For controlling the temperature during experiments, the cell is fitted in an aluminium jacket, which is cooled/heated as a whole by circulation of the cooling fluid (water/monoethylene glycol solution from a cryostat (Julabo MA-4). The cooling jacket is wrapped with an insulation layer to reduce the heat transfer from the surrounding environment and the temperature gradient. Two QUARTZDYNE pressure transducers (model QS30K-B, Quartzdyne Inc., U.S.A.)(+/- 0.005 MPa) and a Platinum Resistance Thermometer (PRT) (+/- 0.1 K) (placed in the top-cap) were used to measure the cell and overburden pressures, and the cell temperature, respectively. The temperature, all pressures (including pore pressure, overburden pressure, and pump pressure), and the LVDT displacement were monitored by a feedback system of the setup (LabVIEW software from National Instruments). All the gas injections, withdrawals, and

samplings, were operated using valves allocated at the top, bottom, and two sides. Finally, a Gas Chromatograph (GC) (Varian 3600, Agilent Technologies) was used to analyze the composition of gas samples for monitoring the evolution in gas composition within the system.

4.2.3 Procedure

In a typical test, 1076.6 g of the sand was partially saturated with 155.6 g deionized water. The wetted sediment was then loaded into the cell, and the system was evacuated to soak the remained air out. Following evacuation, the piston level was adjusted to compact the system with 3.45 MPa overburden pressure for at least a day. Prior to injection of the test gas, the system temperature was set to 298.15 K (to ensure there is no hydrate formation possibility in the working pressure range). A certain amount of CH_4 gas is then added through the valves from top and bottom until the desired initial pressure is reached. Subsequently, the system temperature was set to 273.35 K (just above freezing point of water) to form hydrate without appearance of ice in the system. The system pressure reduces as temperature reduces. Since water was exposed to the high pressure CH_4 well inside the HSZ at this point, hydrate formation was started, reducing the system pressure till the equilibrium point was reached at the experimental temperature. The onset of hydrate formation appeared at the point where there was a clear change in slope of the pressure profile during cooling. Hydrate formation period could take more than a week because there was no mixing in the system. Although some conventional temperature cycling methods (e.g. Stern's method[23]) could be used to accelerate the hydrate formation, the cryostat temperature kept unchanged to preserve the sediment structure built in an entirely controlled method. Hydrate formation/growth continued until stable pressure profile could be observed, confirming the completion of hydrate formation.

After completion of hydrate formation, the first test conducted at this hydrate formation temperature while for the other experiments, the bath temperature was re- set to the target temperature. At this point, hydrate, gas, water, and ice saturation were calculated and provided in Table 4.1. For purging the remaining methane gas and reducing the proportion of remaining free methane in the gas phase without dissociation of methane hydrate, flue gas was injected to the cell at the pressure approximately 10 times the equilibrium pressure of methane hydrate at the target temperature after hydrate formation. Then gas was slowly released out from the system until the system was depressurized to 0.7 MPa above flue gas hydrate phase boundary immediately to avoid or minimize formation of flue gas hydrates. Once the methane concentration has become less than 15% during

purging process, the injection port was closed, and the system pressure was reduced to a specified optimum point by moving the piston backward. These optimum pressures were determined by the method described in the previous chapter. At this step, pressure was maintained using a dual-cylinder Quizix pump and samples from the gas phase were collected at pre-determined time points to be analyzed using a GC. After reaching the steady state (no change in gas composition for 3 days), the system was depressurized in a stepwise manner to recover the remained methane. Experiment 2R was conducted to check the repeatability of the experiments, which was followed the same procedure as Experiment 2. However, after reaching equilibrium state at the target pressure, instead of depressurization, system was heated to room temperature (294.15 K) to investigate the dissociation of the formed hydrates.

Table 4.1 Hydrate, gas, water, and Ice+quasi liquid saturation after methane hydrate formation and before flue gas injection.

Experiment No.	1	2	3	4	5	6	7	2R
Temperature (K)	261.2	264.8	268.6	273.3	278.1	282.1	284.2	264.8
Hydrate saturation (vol%)	67.5	66.8	66.2	60.2	54.4	48.8	47.3	66.9
Gas saturation (vol%)	24.8	25.1	25.6	28.3	26.0	27.1	25.5	25.0
Water saturation (vol%)	0.0	0.0	0.0	11.5	19.6	24.1	27.2	0.0
Ice+Quasi liquid saturation (vol%)	7.7	8.1	8.2	0.0	0.0	0.0	0.0	8.1

As we previously defined the effect of pressure on the CO_2 storage and methane recovery, and indicated that there is an optimum pressure[11] at each temperature using simulated bulk conditions, it was necessary to determine the efficiency of method at realistic conditions. Furthermore, it is also important to characterize the kinetics of the process in such conditions as mass and heat transfer is strongly constrained by mesoporous media. Additionally, effect of ice on the kinetics of the process was investigated to cover the conditions of the methane hydrate reservoirs located in high-latitude regions of the Earth. Accordingly, the experiments were designed to fundamentally understand the kinetics and efficiency of methane recovery and CO_2 storage by injection of flue gas into hydrate-bearing sediments at the previously defined optimum pressures. The procedure was in all cases as described above. The experimental pressure/temperature conditions together with hydrate stability zones of N_2, CH_4, CO_2, flue gas, and different combinations of flue gas/CH_4 are provided in Figure 4.2. The green dots show the optimum conditions at which the system was kept at nearly constant pressure. According to Figure 4.2, the experiments sufficiently cover the temperature range of permafrost, sub permafrost, subglacial, and subsea sediments[24].

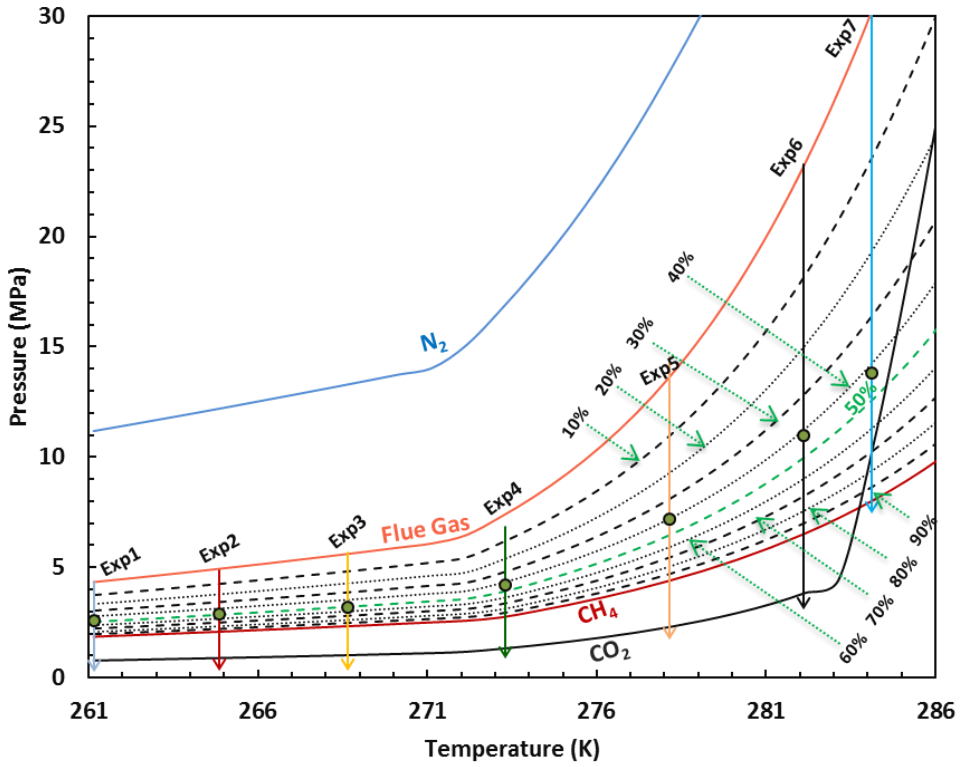

Figure 4.2 The predicted hydrate stability zones of CO_2, N_2, CH_4 and their mixtures and the experimental conditions. Dotted lines with indicated percentages correspond to different mixtures of CH_4 and Flue gas. For instance, the line labelled with 10% represents gas mixtures of CH_4 and Flue gas with molar ratio of 10/90, respectively.

4.3 RESULTS AND DISCUSSION

4.3.1 Kinetics of CO_2 Capture and CH_4 recovery at Optimum Pressure

Figure 4.3a-f show the evaluation in gas phase composition with time and pressure obtained by GC after flue gas was injected. As shown in Figure 4.3a and b methane concentration and $CO_2/(CO_2+N_2)$ ratio changes with pressure in all experiments observed to follow similar patterns, but were different in rate of changes, especially for those under water freezing conditions. Initially, these values fluctuate slightly as a consequence of the initial pressure reduction to set the system at target pressure. Methane concentration in the gas phase keeps growing and $CO_2/(CO_2+N_2)$ ratio keeps reducing at the target pressure until the system reaches equilibrium, this part was circled in Figure3 a-b. Gas concentration changes with time since the pressure set was plotted at Figure3 c-f. The main mechanism here is the chemical potential shift of the system to higher pressure after flue gas injection, which forces the methane molecules to go out of the clathrate cages and allow the CO_2 molecules to get inside the hydrate cages. This could either occur through CO_2 replacement or fully/partially dissociation of the existing methane hydrates and formation of new CO_2 or CO_2-mixed hydrates with the released hydrogen-bonded

water molecules. Recently, Schicks et. al.[25] investigated the exchange phenomena after injection of flue gas into methane hydrate reservoirs, where they didn't observe any indication for CO_2-CH_4 exchange or pure CO_2 hydrate formation. Considering the experimental conditions, formation of CO_2, CO_2-N_2, CO_2-CH_4, CO_2-N_2-CH_4, and N_2-CH_4 is possible in a thermodynamic point of view.

Here, we define half-time ($t_{1/2}$) as the time required for half the increase in methane concentration occurs between the setting pressure and the final equilibrium point. The defined half-time $t_{1/2}$ qualitatively reflects the economic viability of the proposed process for a certain reservoir, as for a reservoir with too high ($t_{1/2}$) industrial scale application of the method is not possible. ($t_{1/2}$) for all of the experiments calculated to be not more than 3 hours whereas the overall process could take up to 250 hours, indicating higher driving force due to higher chemical potential difference between gas and hydrate phase at initial times. A similar trend for the CO_2 and N_2 composition in the gas phase was observed (Figure3 d). This is because increase of methane concentration in the gas phase, dilutes CO_2 and N_2 concentration and consequently the driving force for removing the CH_4 molecules from the hydrate phase reduces. It's also possible that replacement occurs quickly on the surface of the methane hydrate, then the replacement rate decelerates considerably because of formation of a CO_2-CH_4 or CO_2-N_2 hydrate (CNH) layer on the surface, acting like a physical barrier. This layer prevents the CO_2 molecules from fluxing into inner side of methane hydrate, slowing down the replacement. Thus, after forming a layer of CO_2-CH_4 or CNH, replacement slows and limited diffusion transport becomes the main mechanism for the replacement. Similar explanation were presented in the literature[26–28]. In particular, Falenty et al. proposed shrinking core model for replacement of CO_2 with CH_4. In this model, replacement occurs initially on the surface of hydrate, and diffuses to inner layers by rearranging the cavities[29, 30], which is in agreement with our results.

It is known that during formation of CO_2-N_2 mixed hydrate CO_2 goes to the larges cavities, whereas N_2 will fill the small cavities[31]. To examine the selectivity of the CO_2 over N_2, $CO_2/(CO_2+N_2)$ ratio with time after pressure set was provided at Figure 4.3f which decreases with time, indicating stronger selectivity of the CO_2 over N_2 in all the experiments owing to relatively higher[32,33] stability of CO_2 than N_2 at the hydrate Phase. This shows relatively higher occupancy of large cavities than small cavities. These results are in agreement with previous studies[16,34].

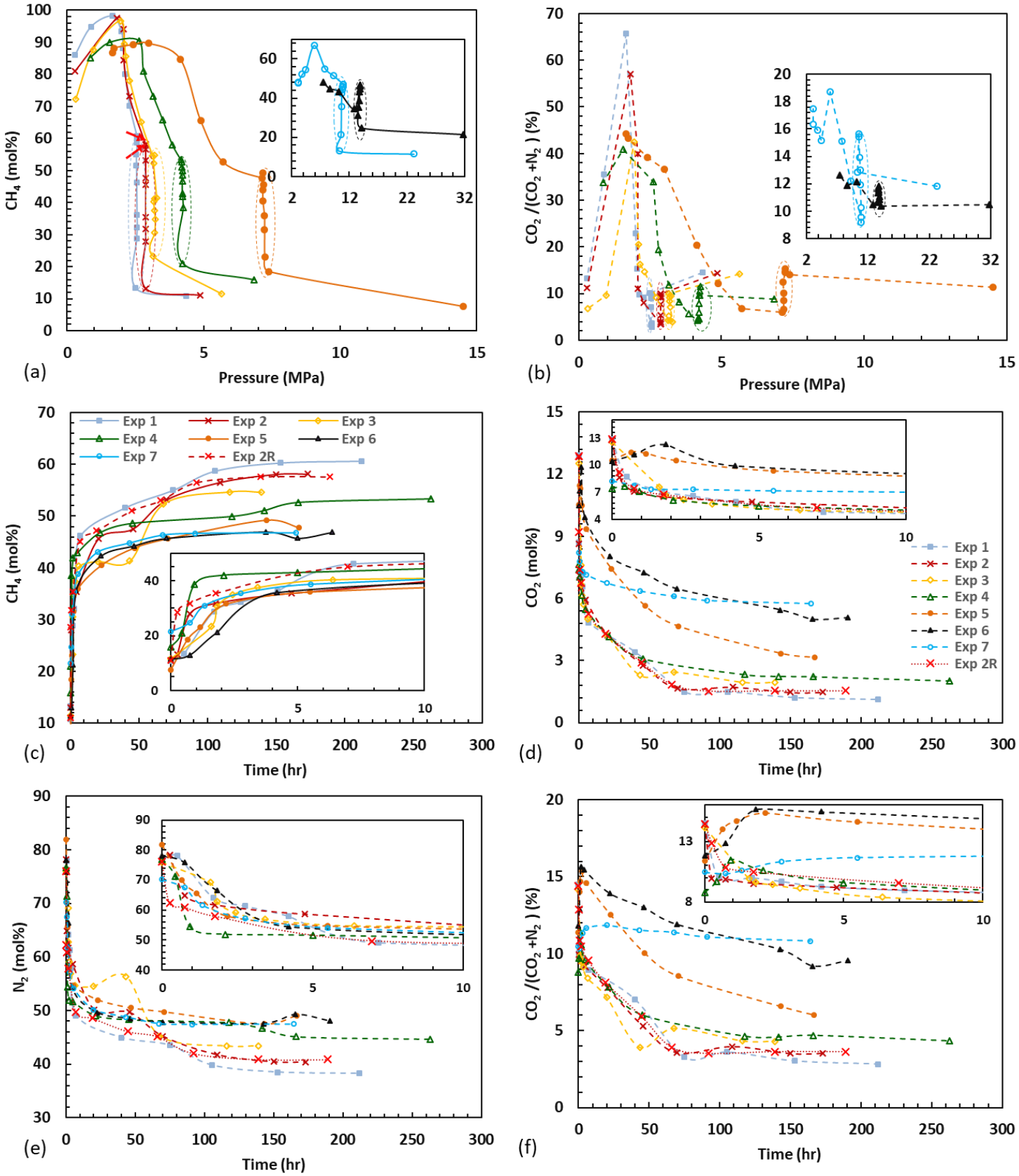

Figure 4.3 (a) CH4 concentration and (b) CO2/(CO2+N2) evolution with pressure after flue gas was injected. CH4(c), CO2(d), N2(e), and CO2/(CO2+N2) evolution with time after pressure was set to the optimum value.

4.3.2 Methane recovery during depressurisation

As mentioned in the previous section the system was depressurized step by step every 24 hours after reaching equilibrium state at a target pressure. As shown in Figure 4.3a, as the system pressure reduces CH_4 comes out of the hydrate phase and the percentage of CH_4 in the gas phase increases until passing CO_2 HSZ, after which CH_4 started to decrease because of dissociation of the CO_2 rich clathrates. Except for Experiment 7, where CH_4 in the gas phase increases after initial drop. This can be attributed to the fact that in this experiment the pressure of the CO_2 hydrate dissociation is higher than that of CH_4 hydrate (Figure 4.2), thus, CO_2-rich hydrates dissociate first, followed by dissociation of CH4-rich hydrate. Regarding $CO_2/(CO_2+N_2)$ ratio during the step-wise depressurization, Figure 4.3b shows upward trends until passing CO_2 HSZ. This could be justified by the fact, during depressurization N_2-rich gas was removed, and consequently overall $CO_2/(CO_2+N_2)$ ratio was increased as a consequence of dissociation of those hydrates with more CO_2 than N_2, and after passing CO_2 HSZ this ratio reached to its maximum amount because of the dissociation of CO_2-rich hydrate. The maximum pick of this graph could be used as an indicator of efficiency of the CO_2 capture at the optimum pressure, in a way that more CO_2 stored at the optimum pressure means more CO_2 trapped in hydrate phase so that this peak will be higher because of dissociation of more CO_2-rich hydrate.

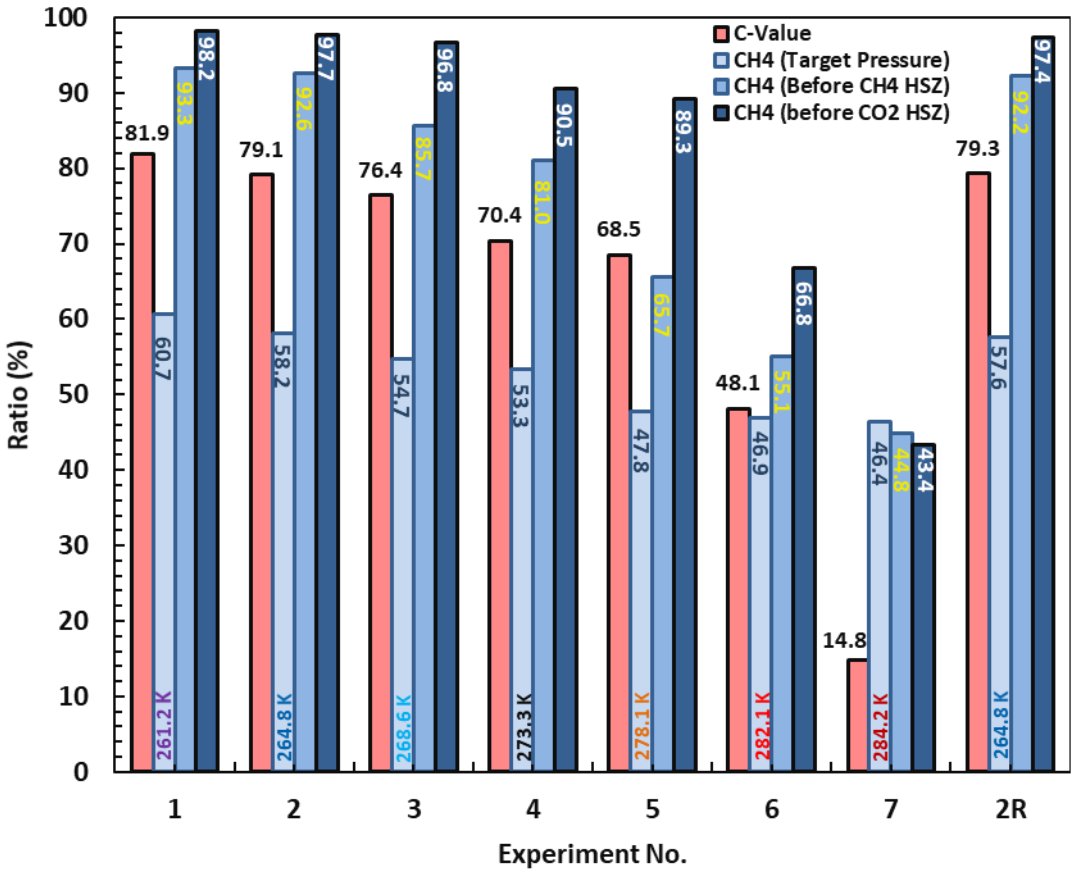

Figure 4.4 Calculated C-value, and CH_4 concentration at the optimum pressures after the system reached to the equilibrium and CH_4 concentration just before the system passed outside the CH_4 HSZ and CO_2 HSZ.

4.3.3 CO_2 capture and effect of hydrate reservoir temperature

Both methane recovery and CO_2 storage strongly depend on hydrate reservoir temperatures. The extent of changes in gas compositions at lower temperatures are typically larger than those at higher temperatures, as would be expected duo to the stronger selectivity of CO_2 to N_2 and CH_4 in hydrate phase at lower temperature that dominates the molecular exchange between the gas and hydrate phase. In addition, as can be seen in Figure 4.2, the experimental pressures for lower temperatures were also lower than those for higher temperatures due to the fact that hydrate dissociation points have lower pressures at lower temperatures. As a result, the compression cost for the reservoir with lower temperatures could be considerably lower. Although, lowering the temperature increases the time required for the process after ($t_{1/2}$), graphs for both methane recovery and CO_2 storage at negative temperatures show better efficiency in terms of time than positive ones at any times. With this in mind, the experiment at 261.2 K has the maximum efficiency for both methane recovery and CO_2 storage, indicating that the more CO_2 storage more Methane production. To be able to quantitatively analyses the results, C-value, is defined and referred as the molar ratio of stored CO_2 in the hydrate

phase after reaching equilibrium at target pressure to the injected total CO_2. C-value is calculated for each experiment and was plotted at Figure 4.4 together with CH4 concentration at gas phase at target pressure after reaching equilibrium, before passing CH_4 HSZ, and before passing CO_2 HSZ. As can be seen 81.9% of the injected CO_2 present in the flue gas was stored in the hydrate phase at 261.2 K, and the molar percentage of CH_4 in the gas phase reached to 60.65, 93.34, 98.18 at the optimum pressure, the boundary of CH_4 HSZ and CO_2 HSZ, respectively. For the experiments at higher temperatures, however, the figures in Figure 4.4 decreased and reached to the minimum at Experiment 7.

4.3.4 Response of CO_2-mixed hydrates to temperature rise

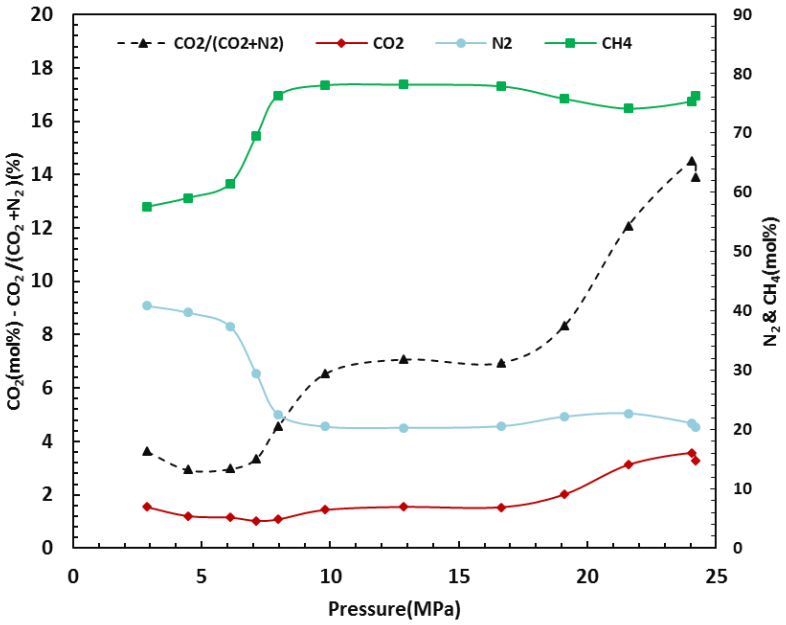

Figure 4.5 Gas composition evolution with pressure after cryostat temperature was set to 294.15 K at Experiment 2R.

Thermal stability of the stored CO_2 is also a major issue for the long-term stability of the CO_2 underground because the temperature cycle in the storage environment may keep altering the formed gas hydrates. This was the main reason to investigate the dissociation of formed hydrates at Experiment 2R using thermal stimulation beside investigation of the repeatability of the procedure. As can be clearly seen in Figure 4.3, before depressurization Experiments 2 and 2R showed well repeatable results. As mentioned before for Experiment 2R, the temperature of the system was increased to investigate the dissociation behavior of the previously formed hydrates at the optimum pressure. The gas composition evolution during dissociation was analyzed by GC and obtained composition results were plotted versus pressure in Figure 4.5. As a result of temperature rise the gas

phase starts to expand and the formed hydrates start to dissociate, which in turn leads to changes in the composition of the gas phase. As shown, initially concentration of the N_2 increases whereas concentration of CH_4, and CO_2 and $CO_2/(CO_2+N_2)$ reduces. The reduction of $CO_2/(CO_2+N_2)$ shows that initially those hydrates with relatively more N_2 start to decompose. This is a positive sign as it shows N_2 not only acts as promoting agent for CO_2/CH_4 replacement but also provides another safety factor for retention of the CO_2-rich hydrates during temperature rise. We have previously showed[35] the role of N_2 for providing safety factor for thermal stability of stored CO_2 by hydrate formation using flue gas in absence of initial methane hydrate in place. However, this is the first mention safety role of N_2 for methane recovery by flue gas injection. After this phase, there is a sharp change in the composition of the gas phase before reaching almost stable composition. In this period, the gas hydrates are quickly dissociating and the released gas are entering to the gas phase, thus, the absence of changes in the gas phase implies that composition of the gas phase in this period interestingly is similar to the composition of those hydrates which are dissociating. After this phase, there is another sharp increase followed by slight decrease in CO_2 concentration and $CO_2/(CO_2+N_2)$ ratio before system reaches equilibrium. This rise shows that hydrates with higher CO_2 content dissociate after dissociation of hydrates with lower CO_2 content. The possible explanation for slight decrease in the concentration of the CO_2 and $CO_2/(CO_2+N_2)$ ratio is the higher solubility of CO_2[36] compared to N_2 and CH_4.

4.4 REFERENCES

(1) Kvenvolden, K. A.; Lorenson, T. D. The Global Occurrence of Natural Gas Hydrate. In *Geophysical Monograph Series*; 2000; Vol. 124, pp 3–18. https://doi.org/10.1029/GM124p0003.

(2) Chong, Z. R.; Yang, S. H. B.; Babu, P.; Linga, P.; Li, X.-S. Review of Natural Gas Hydrates as an Energy Resource: Prospects and Challenges. *Appl. Energy* **2015**. https://doi.org/10.1016/j.apenergy.2014.12.061.

(3) House, K. Z.; Schrag, D. P.; Harvey, C. F.; Lackner, K. S. Permanent Carbon Dioxide Storage in Deep-Sea Sediments. *Proc. Natl. Acad. Sci.* **2006**, *103* (33), 12291–12295. https://doi.org/10.1073/pnas.0605318103.

(4) Sloan, E. D. Fundamental Principles and Applications of Natural Gas Hydrates. *Nature* **2003**, *426* (6964), 353–359. https://doi.org/10.1038/nature02135.

(5) Mehrabian, H.; Bellucci, M. A.; Walsh, M. R.; Trout, B. L. Effect of Salt on Antiagglomerant Surface Adsorption in Natural Gas Hydrates. *J. Phys. Chem. C* **2018**, *122* (24), 12839–12849. https://doi.org/10.1021/acs.jpcc.8b03154.

(6) Yin, Z.; Moridis, G.; Chong, Z. R.; Tan, H. K.; Linga, P. Numerical Analysis of Experiments on Thermally Induced Dissociation of Methane Hydrates in Porous Media. *Ind. Eng. Chem. Res.* **2017**, *57* (17), acs.iecr.7b03256. https://doi.org/10.1021/acs.iecr.7b03256.

(7) Terzariol, M.; Goldsztein, G.; Santamarina, J. C. Maximum Recoverable Gas from Hydrate Bearing Sediments by Depressurization. *Energy* **2017**, *141*, 1622–1628. https://doi.org/10.1016/j.energy.2017.11.076.

(8) Li, G.; Wu, D.; Li, X.; Zhang, Y.; Lv, Q.; Wang, Y. Experimental Investigation into the Production Behavior of Methane Hydrate under Methanol Injection in Quartz Sand. *Energy and Fuels* **2017**, *31* (5), 5411–5418. https://doi.org/10.1021/acs.energyfuels.7b00464.

(9) Merey, S.; Al-Raoush, R. I.; Jung, J.; Alshibli, K. A. Comprehensive Literature Review on CH4-CO2 Replacement in Microscale Porous Media. *J. Pet. Sci. Eng.* **2018**, *171*, 48–62. https://doi.org/10.1016/j.petrol.2018.07.032.

(10) Chen, Y.; Gao, Y.; Zhao, Y.; Chen, L.; Dong, C.; Sun, B. Experimental Investigation of Different Factors Influencing the Replacement Efficiency of CO2 for Methane Hydrate. *Appl. Energy* **2018**, *228*, 309–316. https://doi.org/10.1016/j.apenergy.2018.05.126.

(11) Hassanpouryouzband, A.; Yang, J.; Tohidi, B.; Chuvilin, E.; Istomin, V.; Bukhanov, B.; Cheremisin, A. CO2 Capture by Injection of Flue Gas or CO2-N2 Mixtures into Hydrate Reservoirs: Dependence of CO2 Capture Efficiency on Gas Hydrate Reservoir Conditions. *Environ. Sci. Technol.* **2018**, *52* (7), 4324–4330. https://doi.org/10.1021/acs.est.7b05784.

(12) Hassanpouryouzband, A.; Yang, J.; Tohidi, B.; Chuvilin, E.; Istomin, V.; Bukhanov, B.; Cheremisin, A. Insights into CO2 Capture by Flue Gas Hydrate Formation: Gas Composition Evolution in Systems Containing Gas Hydrates and Gas Mixtures at Stable Pressures. *ACS Sustain. Chem. Eng.* **2018**, *6* (5), 5732–5736. https://doi.org/10.1021/acssuschemeng.8b00409.

(13) Tupsakhare, S. S.; Castaldi, M. J. Efficiency Enhancements in Methane Recovery from Natural Gas Hydrates Using Injection of CO2/N2 Gas Mixture Simulating in-Situ Combustion. *Appl. Energy* **2019**, *236*, 825–836. https://doi.org/10.1016/j.apenergy.2018.12.023.

(14) IPCC. *2014: Climate Change 2014: Synthesis Report. Contribution of Working Groups I, II and III to the Fifth Assessment Report of the Intergovernmental Panel on Climate Change*; IPCC, 2014. https://doi.org/10.1017/CBO9781107415324.

(15) Merkel, T. C.; Lin, H.; Wei, X.; Baker, R. Power Plant Post-Combustion Carbon Dioxide Capture: An Opportunity for Membranes. *J. Memb. Sci.* **2010**, *359* (1–2), 126–139. https://doi.org/10.1016/j.memsci.2009.10.041.

(16) Yang, J.; Okwananke, A.; Tohidi, B.; Chuvilin, E.; Maerle, K.; Istomin, V.; Bukhanov, B.; Cheremisin, A. Flue Gas Injection into Gas Hydrate Reservoirs for Methane Recovery and Carbon Dioxide Sequestration. *Energy Convers. Manag.* **2017**, *136*, 431–438. https://doi.org/10.1016/j.enconman.2017.01.043.

(17) Peter, E.; Messah, M.; Chau, J. Gas Recovery Through the Injection of Carbon Dioxide or Concentrated Flue Gas in a Natural Gas Hydrate Reservoir. In *Offshore Technology Conference Asia*; Offshore Technology Conference, 2018. https://doi.org/10.4043/28374-MS.

(18) Li, B.; Xu, T.; Zhang, G.; Guo, W.; Liu, H.; Wang, Q.; Qu, L.; Sun, Y. An Experimental Study on Gas Production from Fracture-Filled Hydrate by CO2and CO2/N2replacement. *Energy Convers. Manag.* **2018**, *165*, 738–747. https://doi.org/10.1016/j.enconman.2018.03.095.

(19) Mu, L.; Von Solms, N. Experimental Study on Methane Production from Hydrate-Bearing Sandstone by Flue Gas Swapping. *Energy and Fuels* **2018**, *32* (8), 8167–8174. https://doi.org/10.1021/acs.energyfuels.8b01437.

(20) Wang, X.; Pan, L.; Lau, H. C.; Zhang, M.; Li, L.; Zhou, Q. Reservoir Volume of Gas Hydrate Stability Zones in Permafrost Regions of China. *Appl. Energy* **2018**, *225*, 486–500. https://doi.org/10.1016/j.apenergy.2018.04.125.

(21) Lin, Z.; Pan, H.; Fang, H.; Gao, W.; Liu, D. High-Altitude Well Log Evaluation of a Permafrost Gas Hydrate Reservoir in the Muli Area of Qinghai, China. *Sci. Rep.* **2018**, *8* (1), 12596. https://doi.org/10.1038/s41598-018-30795-x.

(22) Collett, T. S.; Lee, M. W.; Agena, W. F.; Miller, J. J.; Lewis, K. A.; Zyrianova, M. V.; Boswell, R.; Inks, T. L. Permafrost-Associated Natural Gas Hydrate Occurrences on the Alaska North Slope. *Mar. Pet. Geol.* **2011**, *28* (2), 279–294. https://doi.org/10.1016/j.marpetgeo.2009.12.001.

(23) Stern, L. A.; Kirby, S. H.; Durham, W. B. Peculiarities of Methane Clathrate Hydrate Formation and Solid-State Deformation, Including Possible Superheating of Water Ice. *Science (80-.).* **1996**, *273* (5283), 1843–1848. https://doi.org/10.1126/science.273.5283.1843.

(24) Portnov, A.; Vadakkepuliyambatta, S.; Mienert, J.; Hubbard, A. Ice-Sheet-Driven Methane Storage and Release in the Arctic. *Nat. Commun.* **2016**, *7*. https://doi.org/10.1038/ncomms10314.

(25) Schicks, J. M., Strauch, B., Heeschen, K. U., Spangenberg, E., & Luzi-Helbing, M. From Microscale (400 µl) to Macroscale (425 L): Experimental Investigations of the CO2/N2-CH4 Exchange in Gas Hydrates Simulating the Iġnik Sikumi Field Trial. Journal of Geophysical Research: Solid Earth. 2018, 123(5), 3608-3620.

(26) Geng, C. Y.; Wen, H.; Zhou, H. Molecular Simulation of the Potential of Methane Reoccupation during the Replacement of Methane Hydrate by CO2. *J. Phys. Chem. A* **2009**, *113* (18), 5463–5469. https://doi.org/10.1021/jp811474m.

(27) Bai, D.; Zhang, X.; Chen, G.; Wang, W. Replacement Mechanism of Methane Hydrate with Carbon Dioxide from Microsecond Molecular Dynamics Simulations. *Energy Environ. Sci.* **2012**, *5* (5), 7033–7041. https://doi.org/10.1039/c2ee21189k.

(28) Lee, B. R.; Koh, C. A.; Sum, A. K. Quantitative Measurement and Mechanisms for CH4production from Hydrates with the Injection of Liquid CO2. *Phys. Chem. Chem. Phys.* **2014**, *16* (28), 14922–14927. https://doi.org/10.1039/c4cp01780c.

(29) Falenty, A., Salamatin, A. N., & Kuhs, W. F. Kinetics of CO2-hydrate formation from ice powders: Data summary and modeling extended to low temperatures. The Journal of Physical Chemistry C. **2013**, 117(16), 8443-8457.

(30) Falenty, A., Qin, J., Salamatin, A. N., Yang, L., & Kuhs, W. F. Fluid composition and kinetics of the in situ replacement in CH4–CO2 hydrate system. The Journal of Physical Chemistry C. **2016**, 120(48), 27159-27172.

(31) Dornan, P.; Alavi, S.; Woo, T. K. Free Energies of Carbon Dioxide Sequestration and Methane Recovery in Clathrate Hydrates. *J. Chem. Phys.* **2007**, *127* (12), 124510–124700. https://doi.org/10.1063/1.2769634.

(32) Petuya, C.; Damay, F.; Chazallon, B.; Bruneel, J. L.; Desmedt, A. Guest Partitioning and Metastability of the Nitrogen Gas Hydrate. *J. Phys. Chem. C* **2018**, *122* (1), 566–573. https://doi.org/10.1021/acs.jpcc.7b10151.

(33) Chazallon, B.; Pirim, C. Selectivity and CO2 Capture Efficiency in CO2-N2 Clathrate Hydrates Investigated by in-Situ Raman Spectroscopy. *Chem. Eng. J.* **2018**, *342*, 171–183. https://doi.org/10.1016/j.cej.2018.01.116.

(34) Koh, D. Y.; Kang, H.; Kim, D. O.; Park, J.; Cha, M.; Lee, H. Recovery of Methane from Gas Hydrates Intercalated within Natural Sediments Using CO2 and a CO2/N2 Gas Mixture. *ChemSusChem* **2012**, *5* (8), 1443–1448. https://doi.org/10.1002/cssc.201100644.

(35) Hassanpouryouzband, A.; Yang, J.; Tohidi, B.; Chuvilin, E. M.; Istomin, V.; Bukhanov, B. A. Geological CO2 Capture and Storage with Flue Gas Hydrate Formation in Frozen and Unfrozen Sediments: Method Development, Real Time-Scale Kinetic Characteristics, Efficiency, and Clathrate Structural Transition. *ACS Sustain. Chem. Eng.* **2019**. https://doi.org/10.1021/acssuschemeng.8b06374.

(36) Hassanpouryouzband, A.; Vasheghani Farahani, M.; Yang, J.; Tohidi, B.; Chuvilin, E.; Istomin, V.; Bukhanov, B. A. Solubility of Flue Gas or Carbon Dioxide-Nitrogen Gas Mixtures in Water and Aqueous Solutions of Salts: Experimental Measurement and Thermodynamic Modelling. *Ind. Eng. Chem. Res.* **2019**. https://doi.org/10.1021/acs.iecr.8b04352.

Chapter 5 - Geological CO_2 Capture and Storage with Flue Gas Hydrate Formation in Frozen and Unfrozen Sediments: Method Development, Real Time-Scale Kinetic Characteristics, Efficiency, and Clathrate Structural Transition

5.1 Introduction

Increasing atmospheric CO_2 concentrations, owing to the continuous use of fossil fuels as the main energy source for humans, pose a hazard to human life[1], possibly have a major role in global warming[2], may change environmental life cycles[3,4], and have long-term importance for the foreseeable future[5]. The increase in temperature in high-latitude regions of the Earth in particular appears to be occurring twice as fast as the global average[6], notably where vast volumes of CH_4 in the form of clathrates exist under permafrost[7] and where a significant amount of organic carbon is accumulated in perennially frozen soil over millennia[8]—a situation that will exacerbate climate change by extensive methane venting to the atmosphere[9] (which mainly comes from decomposition of gas clathrates) and by conversion of the stored carbon to CH_4 and CO_2 through decomposition by soil microbes[10]. Accordingly, urgent[11] action is required to scale-up CO_2 capture and storage to limit CO_2 emissions and return to a "safe"[6] level (1987) of 350 ppm CO_2 in the atmosphere. Although the efficiency of different techniques for CCS have been improved considerably in recent years[12], large-scale, economical solutions are still lacking[5].

In the past decade, a number of studies[13] have been undertaken to develop realistic CCS methods, one of which is using gas hydrate-related technologies. Gas hydrates, or clathrate hydrates, are an ice-like group of crystalline inclusion compounds characterized by a host lattice of hydrogen-bonded water molecules that enclose suitably sized guest gas molecules without chemical bonding, usually at low temperatures and elevated pressures[14–16]. Capturing and storing CO_2 in the form of gas hydrates has been previously suggested as a possible approach to reduce CO_2 emissions, which can be categorized into two main approaches: First, methane hydrate reservoirs that exist under permafrost and in continental and margin sediments[7] can be used to store CO_2[17] by replacement of injected CO_2 molecules with CH_4 molecules[18], controlling the emissions of CO_2 while simultaneously allowing for a more economical and more efficient[19] deployment of methane hydrate sources with respect to the exothermic[20] nature of CO_2 replacement in

the hydrate lattice (This is due to the greater relative thermodynamic stability of CO_2 hydrate than both methane hydrate structure-I (sI) and structure-II (sII)). Furthermore, the optimization and development of this method have been extensively studied in the past two decades[21–23], and several successful field-scale applications, such as those located at the Alaska North Slope[24], have been reported. More recently, we have suggested direct injection of power plant flue gas (mainly N_2 and CO_2) into CH_4 hydrate reservoirs as a promising approach to reduce the cost by eliminating CO_2 capture from the atmosphere[25,26]. Second, efforts have been made to form gas hydrate from power plant flue gas[27], with the expectation that more CO_2 than N_2 will enter the hydrate phase[28–30], providing the possibility to separate and capture CO_2 after hydrate formation[31].

Here, we introduce a new approach to scale-up and reduce the cost of the CCS operation. The idea is that power plant flue gas, mainly consisting of N_2 and CO_2, can be directly injected into either simulated or natural (temporary and permanent storage, respectively) water/ice-saturated sediments at high pressures to store CO_2 in a solidified form, providing a realistic and efficient CCS method. Despite the promising prospects of hydrate-based CCS, a natural time-scale evaluation of flue gas hydrate formation kinetics inside mesoporous media does not yet exist. This work details the results of an experimental investigation into the kinetics of flue gas hydrate formation in well-characterized water/ice-saturated sediments from 261.1 K to 283.1 K, covering the temperature range of subglacial, permafrost, sub permafrost, and subsea sediments[32]. Using the newly measured formation kinetics data, we discuss the characteristics of flue gas hydrate formation kinetics with a particular focus on the effect of relevant parameters on CO_2 capture rate, capture efficiency and clathrate stoichiometry.

This study documents a method that could slow or even stop the rise of the CO_2 content in the atmosphere. While direct formation of CO_2-rich hydrates from power plant flue gas will reduce CO_2 emissions, the hydrate cap formed in sediments could also provide a safety[33] mechanism by blocking the pathway of those greenhouse gases released in response of permafrost to global warming. Additionally, we address the challenges regarding the effect of global warming on the stored CO_2-rich hydrates by investigating the kinetics of hydrate dissociation during temperature increase, ultimately showing that the CO_2 level in the atmosphere could be sustainably reduced or at least kept at the same level using the proposed method.

5.2 Methods

5.2.1 Materials

A well-characterized silica sand from Fife (Scotland) was used as the mesoporous media, and a detailed analysis can be found in the Appendix C. Deionized water was produced using an ELGA DV 25 Integral Water Purification System. For simulating flue gas, a gas mixture composed of 85.4 mol% nitrogen and 14.6 mol% CO_2 (both with certified purities of 99.9995 vol%) purchased from BOC Limited was used.

5.2.2 Experimental apparatus

Experiments were carried out using a stainless steel cylindrical cell setup. The setup is composed of a high-pressure cell (with a maximum inner volume of 802 cm^3 and a maximum working pressure of 40 MPa), movable piston, data measurement and monitoring system, and pressure/temperature maintaining system, as shown in Figure 5.1. The top cap of the cell is fixed, while the bottom cap has a movable piston, moving by injection or withdrawal of hydraulic fluid using a hand pump for initial overburden pressure and a Quizix pump for maintaining constant pressure. The piston movement enables an increase or reduction in the pore pressure within the cell without injecting or removing fluid from the cell, thus maintaining a closed system. A linear variable differential transformer (LVDT) is mounted to the tail rod of the piston to measure the piston displacement, enabling measurement of the exact volume of the cell in real time. The cell is located in a cooling jacket, and its temperature is maintained by circulating water/monoethylene glycol (60/40, vol/vol) from the temp bath (Julabo MA-4) through the shell side of the module. The temperature is measured using a platinum resistance thermometer (PRT), located inside the top cap, with a precision of +/- 0.1 K. The cell pressure and overburden pressure are measured by means of Quartzdyne pressure transducers (model QS30K-B, Quartzdyne Inc., U.S.A., pressure range 0-207 MPa) with an accuracy of +/- 0.0005 MPa. Pore pressure, temperature, pump pressure, overburden pressure, and piston displacement are recorded on a computer via a data acquisition system (LabVIEW software from National Instruments). Test fluids and samples for analysis are injected and collected through valves on the bottom cap, top cap, and side valves. The molar composition of the gas samples was analyzed using a gas chromatograph (GC) (Varian 3600, Agilent Technologies) (with calibration errors of ±0.5% for CO_2 and ±1.2% for N_2).

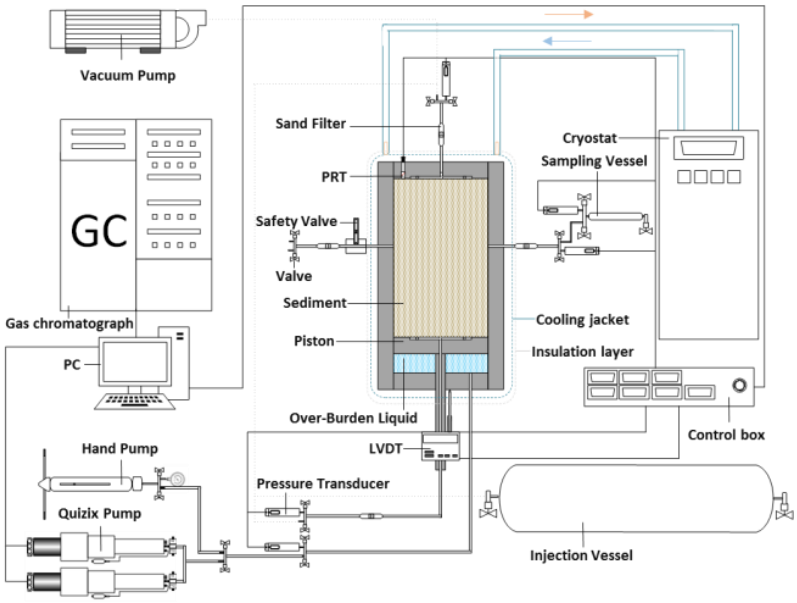

Figure 5.1 Schematic of the high pressure autoclave setup

5.2.3 Procedure

The following general procedure was used for all experiments. The cell was filled with partially water-saturated sand (1076.6 g sand/155.6 g water or 12.63 mass% water) and vacuumed after adjusting the piston level to control the volume of simulated sediment (approximately 148.94 mm height and 75.00 mm diameter or porosity of 37.9%). The fluid behind the piston was then maintained at a constant pressure (3.45 MPa) using the Quizix pump and the temperature bath was set at the target temperatures (see Table 5.1) for several days to ensure stabilization of the system. Then, the piston fluid inlet valve was closed, and flue gas was injected at the desired pressures. Gas samples for GC were collected at determined intervals according to the pressure decrease rate of the system. The sampling process was continued until hydrate formation finished, as evidenced by both the final stable CO_2 concentration in the gas phase and the pressure reading of the pressure transducer[28], except for Exp1, in which the test was stopped after 72 days because of the very slow formation rate. Finally, the bath temperature was set at 294.15 K, and the composition of the gas phase was analyzed during gas hydrate dissociation. The initial conditions for each experiment are shown in Table 5.1.

Table 5.1 Experimental temperature, initial pressure conditions, and quantity of injected gas

Exp. No	1	2	3	4	5	6	7	8	9
Temperature (K)	261.2	264.8	268.6	273.4	278.2	283.2	273.4	278.2	283.2
Start Pressure (MPa)	20.82	20.79	20.81	20.79	20.75	20.80	27.95	27.91	33.21
Injected Gas (mol)	1.0198	0.9974	0.9761	1.0009	0.9476	0.9111	1.2574	1.1974	1.3137

5.2.4 Methodology

Pure CO_2 forms simple (single guest) cubic sI clathrate hydrates with a formula of $2M_S \bullet 6M_{LI} \bullet 46H_2O$ (where M_S is a small 5^{12} (pentagonal dodecahedron) cavity and M_{LI} is a large $5^{12}6^2$ (tetrakaidecahedron) cavity) with compositions between $5\frac{3}{4}$ and $7\frac{2}{3}$ waters/guest, which are stable at considerably lower pressures when compared with simple N_2 hydrates. CO_2 occupies all the large M_{LI} cages (size ratio of 0.83) and some of the M_S cages (size ratio of 1). Additionally, N_2 can stabilize cubic s-II hydrates with a unit cell formula of $16\ M_S \bullet 8M_{LII} \bullet 136H_2O$ (where M_{LII} is a large $5^{12}6^4$ (hexakaidecahedron) cavity), occupying a fractionally higher number of MS cavities (single guest)[34]. In addition, owing to the small molecular size, two N_2 molecules can fit into a large MLII cavity[35,36]. While several powder X-ray diffraction, NMR spectroscopy, and Raman spectroscopy studies[37–39] (mainly on 10% and 20% CO_2 in N_2+CO_2 mixtures) at limited pressure and temperature ranges suggest that these mixtures only form s-I hydrate (except for 1% CO_2-99% N_2 mixture where the s-II hydrate is more stable), structures of CO_2+N_2 mixed hydrates have yet to be investigated to reveal the underlying physics. At the same time, the presence of mesoporous media can change the characteristics of hydrate equilibria[40]. Accordingly, this is another key parameter to be analyzed in order to understand the properties of CO_2+N_2 hydrate formation inside sediments.

Figure 5.2 provides the predicted results of sI and sII HSZs of gas-water systems for different combinations of CO_2 and N_2 together with the pressure/temperature conditions of the experiments. An in-house software (HydraFlash) [43–45] was used for prediction of the HSZs. Thermodynamic behavior of the fluid system at different pressures, temperatures and compositions were modelled using CPA equation of state for the non-solid phase, with the Peng-Robinson equation of state as the non-association part, and a modified van der Waals and Platteeuw method for the solid phase. To understand the effect of temperature under real conditions[32], Exp 1-6 were started at the same pressure, which was selected to represent ocean floor pressure according to the average depth of the oceans[41,42]. Exp 7-9 were performed to investigate the pressure effect. It should be noted that as all planned results were obtained using these 9 experiments, we performed only one experiment at very low temperature due to the length of time required to perform experiments at lower temperatures and higher pressures. The pressures for Exp 1-4 and 7 were well inside the N_2 HSZ, whereas the pressures for Exp 5 and 9 were between the flue gas and N_2 HSZs, the pressure for Exp 8 was just on the N_2 HSZ, and the pressure for Exp 6 was outside of the flue gas hydrate formation region. Accordingly, in Exp 1-5

and Exp 7-9, there is the possibility of CO_2 or CO_2-N_2 mixed hydrate formation, and in Exp 1-4 and 7, there is also possibility of N_2 hydrate formation. The sole purpose of Exp 6 was to observe CO_2 dissolution kinetics in the system. For some combinations of flue gas (sometimes up to ~8% CO_2 at lower temperatures), the pressures of sII HSZs are lower than those of sI, indicating the greater stability of sII hydrates from a thermodynamic perspective. Accordingly, Exp-5 and 9 were selected to be out of this region, whereas other experiments (except Exp 6) cross this region or finish (Exp 1 and 7) in this region. Several experimental obserevations20, all of which were performed outside of this region, suggest that CO_2 will go into large cages and N_2 will occupy small cages (for sI hydrates) in CO_2-N_2 mixed hydrates.

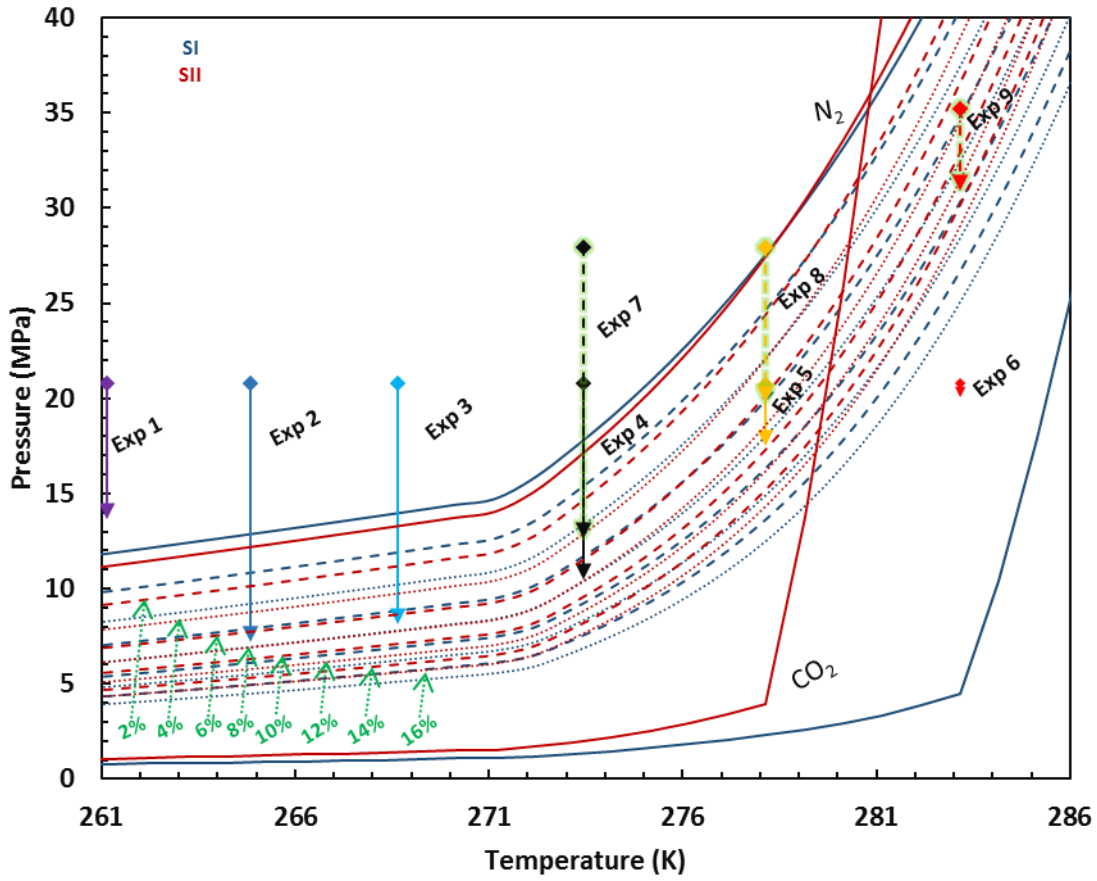

Figure 5.2 The predicted hydrate stability zones of CO_2, N_2, and their mixtures and the experimental conditions. The HSZs are predicted for both sI and sII. The paired phase boundaries of sI and sII of a CO_2-N_2 mixture are drawn in the same pattern of lines, blue (sI) and red (sII). An in-house software (HydraFlash) [43–45] was used for prediction of the HSZs. Thermodynamic behaviour of the fluid system at different pressures, temperatures and compositions were modelled using CPA equation of state for the non-solid phase, with the Peng-Robinson equation of state as the non-association part, and a modified van der Waals and Platteeuw method for the solid phase.

5.3 Results and Discussion

5.3.1 Formation kinetics

The pressure profile of the system after gas injection is illustrated over all of the experimental periods in Figure 5.3. A rapid pressure drop was observed just after gas injection, mainly as a result of gas solubility and gas contraction. This mechanism is clearer in the Exp 6 results, where the system pressure was outside the flue gas HSZ. However, in the other experiments, hydrate nucleation/growth was an additional reason for this initial reduction. As the gas was consumed by hydrate formation, the gas pressure showed a strongly negative decreasing slope. Here, the rate of gas pressure change decreased with time, corresponding to a reduction in the gas consumption rate. This is because the consumption of the gas molecules moves the system pressure closer to stable conditions, reducing the main driving force of hydrate formation. Furthermore, early hydrate crystal formations accumulate on the surface, reduce the surface contact of components and limit the mass/heat transport in the system. In addition, the free water content in the system reduces with hydrate formation, which could limit the hydrate formation rate by slowing down the adsorption of the CO_2/N_2 molecules at the crystal interface[46]. With regard to the pressure decrease during hydrate formation in Exp 3-5, it is slightly faster at lower temperatures, as the distance from stable conditions is relatively higher in terms of pressure difference (higher sub-cooling). However, the opposite trend was observed in Exp 1-2. This could be explained by the presence of less unfrozen (quasiliquid) water at lower temperatures. The quasiliquid water content acted as a limiting factor for hydrate formation and gas diffusion in the system, and consequently, a reduction in the hydrate formation rate at lower temperatures can occur. In addition, the gas diffusion rate is reduced at lower temperatures, which, in turn, increases the time required for gas molecules to contact the quasiliquid water. Furthermore, hydrates can directly form from ice crystals, which is slower at lower temperatures. Comparing the graph for Exp 3 with those for Exp 1 and 2 in Figure 5.3 suggests that there was enough quasiliquid water and sufficient surface contact between components in Exp 3, weakening the limiting effects on hydrate formation at this temperature. As seen, except for Exp 1, the pressure graphs for all experiments reached a plateau after the initial decrease, which was faster at higher temperatures. This can be attributed to the fact that the differences between hydrate formation rates are not large enough to cover the difference between stable pressure values. In Exp 1, as the hydrate formation rate decreased considerably

after a few months, the tests were stopped when the pressure versus time slope reached less than 0.0015 MPa/hr.

A comparison between the pressure decreases in Exp 4 and 5 with those of Exp 7 and 8 reveals that experiments at higher pressure take more time to stabilize. The first apparent reason for this observation is the pressure drop and consequently more hydrate formation at higher pressures. This can also increase the force required for diffusion through formed hydrate shells. As the same amount of water was present in all experiments, the second reason for this observation could be the previously discussed limiting role of free water, lowering the water to gas molar ratio at higher pressures. This is potentially the main reason for the very slow hydrate formation during the final stages of the higher pressure experiments. The faster hydrate formation in Exp 9 compared to Exp 7 and 8, considering its higher pressure and higher temperature, provides additional support for the above two explanations.

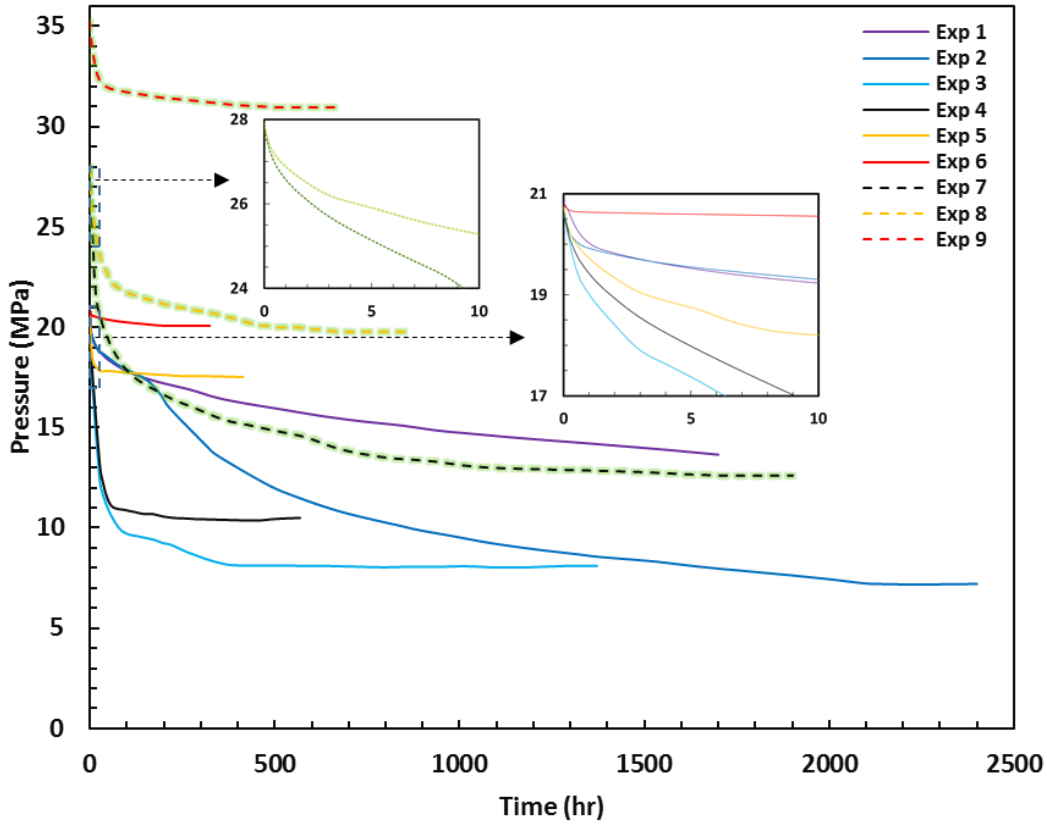

Figure 5.3 Changes in system pressure after flue gas was injected during clathrate formation inside water saturated sediments with the early phase magnified.

5.3.2 CO_2 capture

Figure 5.4 presents the CO_2 concentration changes in the gas phase throughout all experiments. An insertion of the initial stage is also shown in Figure 5.4. It should be noted that all samples were analyzed at least three times to reduce the GC measurement

uncertainty, which was calculated to be at most 0.1%. As shown in Figure 5.4, there is always an initial decrease in CO_2 concentration in all cases due to the higher solubility of CO_2 relative to N_2 in the aqueous phase at temperatures higher than 273.15 K (Exp 4-9) and higher stability of CO_2 relative to N_2 in the ice phase at temperatures under 273.15 K (Exp 1-3). Furthermore, it is clear that the relative rate of diffused CO_2 to N_2 into the ice phase is similar in Exp 1-3, indicating an insignificant role of temperature on the diffusion of gas into the ice crystals, at least in the early stages. However, for experiments above the freezing point of water (Exp 4-9), the relative rate of CO_2 to N_2 solubility in water increases at lower temperatures, due to hydrate formation requiring an induction time because there is always a time lag for hydrate formation after flue gas injection. As shown in the magnified part of Figure 5.4, clear downward peaks were observed for Exp 4, 5, 7, 8, and 9 just after flue gas injection was complete. Previously, we reported[28] this behavior for the same gas mixture under bulk conditions and attributed it to the effect of hydrate formation on water solubility and the presence of relatively more CO_2 to N_2 in the aqueous phase than in the hydrate phase. Regarding Exp 6, following approximately 200 hrs of initial logarithmic reduction, it reaches equilibrium at approximately 10.5% CO_2 in the gas phase.

The curves shown in Figure 5.4 provide other interesting information. The curves show that the CO_2 concentration in the gas phase reduced considerably faster in Exp 4 and 5 than in Exp 1-3. At the same injection pressures for higher temperatures, the CO_2 concentration reached a stable value faster. However, the final CO_2 concentration in the gas phase is smaller at lower temperatures, indicating a higher occupancy ratio of CO_2/N_2 in the hydrate phase. Slower changes in the CO_2 concentration were observed at higher pressures, which could be attributed to the same reason for the slower pressure change in these systems. In addition, the presence of more gas in the system leads to a reduced effect of hydrate formation on the changes in the composition of the gas phase. Although Exp 9 was conducted under higher pressure than Exp 6, there was a higher rate of CO_2 capture in Exp 9, indicating the efficiency of hydrate-based CO_2 capture compared with dissolution methods alone. Comparing Exp 4 with Exp 7 and Exp 5 with Exp 8, it should also be noted that the injection of gas at higher pressures caused a greater reduction in pressure, which in turn led to more hydrate formation and consequently a larger change in the CO_2 concentration. Accordingly, experiments at higher injection pressures in this method also have higher final equilibrium pressures. This is because binary N_2/CO_2 gases have higher HSZs at higher N_2 concentrations.

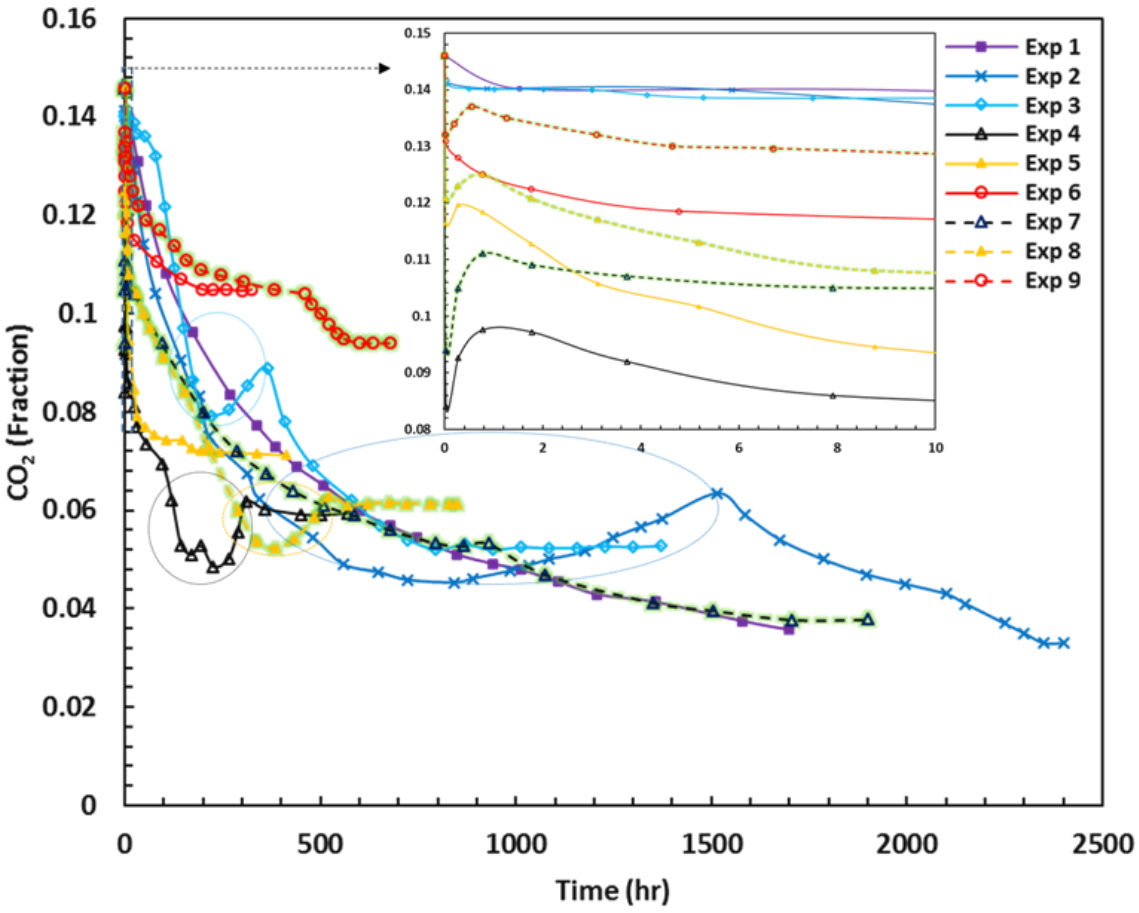

Figure 5.4 Changes in CO2 concentration in the gas phase during clathrate formation inside water saturated sediments after flue gas was injected. To reduce the GC measurement uncertainty for each point, all samples were analyzed at least three times.

5.3.3 Structural change

Next, we investigated the CO_2 concentration change during hydrate formation to further quantify the kinetics of flue gas hydrate formation. The possible explanation for these concavities is that these experiments were started inside the sII HSZ and finished outside of the sII HSZ, covering a wide range of HSZs in terms of concentration changes, which reduces the stability of hydrates formed at higher pressures. With this in mind, initially formed hydrates with relatively more CO_2 possibly dissociated, and new hydrates with less CO_2 formed. Curiously, the presence of more CO_2 at higher pressures indicates that there is an optimum pressure under which there is maximum CO_2 capture, which is consistent with our previous results[26]. Furthermore, a wider concavity in Exp 2 could show limited heat or mass transfer for dissociating hydrogen bonds at lower temperatures. More interestingly, as shown in Figure 5.4, HSZ zones of sII hydrates with CO_2 concentrations less than approximately 8% are more stable than those of sI, and the trend is opposite after passing approximately 8% CO_2 in the gas phase. In addition, these concavities are observed only in Exp 2-4 and 8 that passed this region (Exp 1, 5, and 7

were above or inside this zone). On the basis of the two above explanations, for Exp 2-4 and 8 sII hydrate formation is the only plausible hypothesis that could be offered to explain the reason behind the concavities observed in Figure 5.4. This does not conflict with other studies[37–39] on this subject that denied the presence of sII hydrate for more than 1% CO_2 concentration in the gas phase because the presented pressure-temperature conditions in our study for sII hydrate were not investigated in other studies. To confirm the structural changes, these experiments could be coupled with different spectroscopy techniques such as NMR to be able to measure the composition of the hydrate phase during formation.

Regarding the change in slope of Exp 5, 7 and 9, clear decrease after concavities in Exp 2, and 4, and slight decrease after concavities in Exp 4, and 8, we will discuss in the next section.

5.3.4 Pressure effect on CO_2 capture

The rate of CO_2 capture is highly sensitive to variations in pressure at each temperature. Figure 5.5 summarizes the changes in CO_2 concentration in the gas phase versus pressure under the conditions presented in the experimental section. Different parts of this Figure 5.5. were discussed in the previous sections. However, there are some interesting observations to be further addressed. The changes in the fraction of CO_2 in the gas phase is a measure of the relative stability of CO_2 to N_2 in the hydrate phase with respect to the pressure under which they form. The CO_2 concentration stays at approximately 14% in Exp 3 before reaching N_2 HSZ, whereas it begins reduction earlier in Exp 1 and 2. This could be explained by the presence of less quasiliquid water at the gas-water interface in Exp 1 and 2 and significantly higher stability of CO_2 than N_2 in the process of hydrate crystals accumulation at the gas/water interface, and the diffused gas contains a higher concentration of CO_2, in turn, leading to the formation of CO_2-rich hydrates. Because of the intensity of the lower temperature in Exp 1, the hydrate formation rate is very slow (Figure 5.5), whereas the slope of CO_2 concentration versus pressure is high (Figure 5.5). Furthermore, the CO_2 concentration significantly changes at the final pressure in Exp 2-5 and 7-9, which is most clear in Exp 3. Recently, we suggested[28] three different mechanisms for this behavior. In support of our above claims about the presence of sII CO_2-N_2 hydrates at higher pressures, the concavities of the curves in Figure 5.5 are consistent with the stability regions of sII hydrates in Figure 5.2. in addition, this behavior could be explained by shrinking core model, where the authors suggested that an initial fast surface reaction happens following by a slower stage limited by permeation. Here

permeation coefficient of gas molecules plays a crucial. Considering the high density and low permeability of CO_2 molecules, the secondary decrease in the concentration of the CO_2 molecules in the gas phase (Figure 5.5) could be explained by the mentioned model[47]. Slower kinetics of hydrate formation after initial fast hydrate formation (Figure 5.4) could also be explained by the shrinking core model.

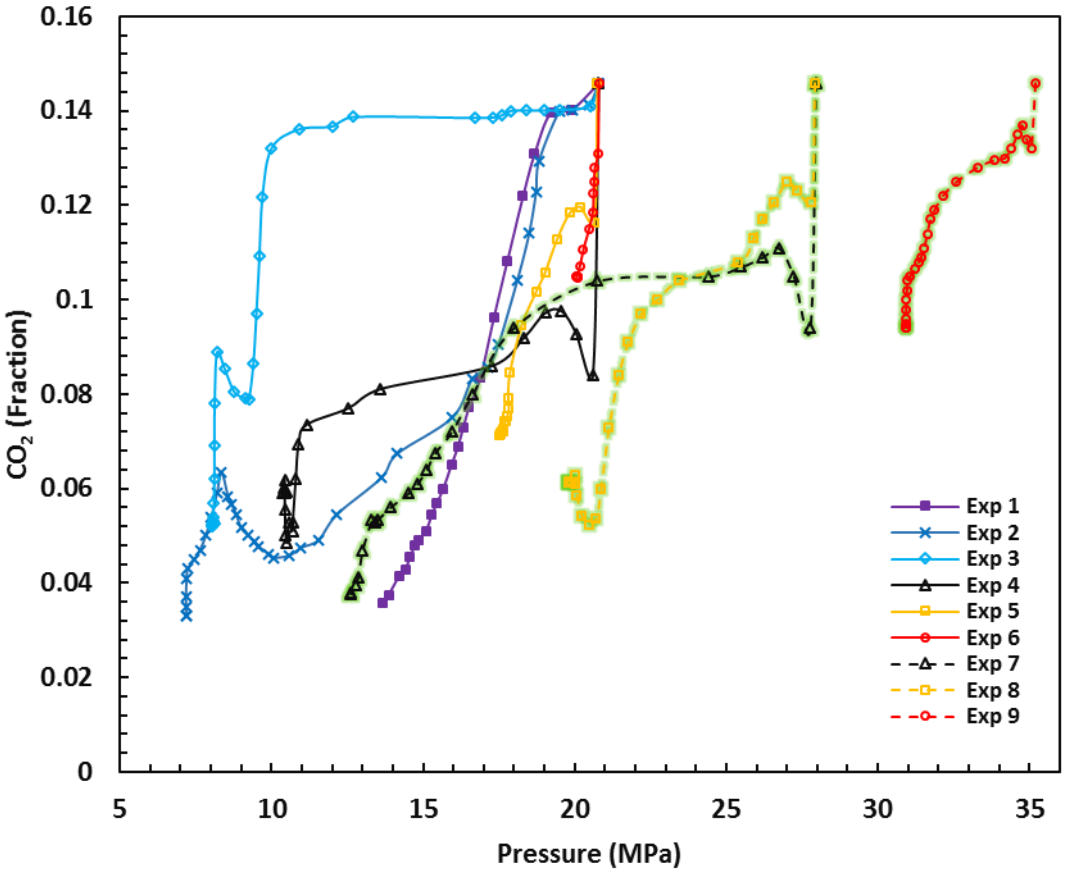

Figure 5.5 CO2 concentration in the gas phase versus system pressure during clathrate formation inside water saturated sediments. The changes in the fraction of CO2 in the gas phase is a measure of the relative stability of CO2 to N2 in the hydrate phase with respect to the pressure under which they form

5.3.5 Quantitative analysis

Because the initial and final pressures and CO_2 concentrations in each test were different, there was a need to define a parameter to be able to comparatively quantify the amount of captured CO_2. Accordingly, the capture ratio, C-value, is defined as the percentage of captured CO_2 moles inside the hydrate and water phase divided by the moles of initially injected CO_2. The C-values for each experiment were calculated and plotted in Figure 5.6 (quantities of the CO_2 concentration in the gas phase and hydrate/water phase are provided in the Appendix C). As noted before, in Exp 1, the test was stopped before reaching the final pressure, so the C-value for this test does not reflect equilibrium conditions. It is clear from the graph that either an increase in the pressure or a reduction

in the temperature caused an increase in the efficiency of the CO_2 capture, confirming the results shown in Figure 5.4. Hence, lower temperatures and higher pressures are more favorable for CO_2 capture if the hydrate formation time is not important, which is applicable in this case. An apparent trend of C-values indicates that it is possible to store more than 92% percent of the injected CO_2 by controlling pressure and by choosing an appropriate area for storage. The separation of CO_2 from flue gas before injection does not seem to have any significant impact in this method on increasing the capture ratio, while the separation of CO_2 from flue gas has a major[13] cost in typical CCS operations. Another interesting observation from Figure 5.6 is that injection of flue gas into frozen sediments could even capture and store more CO_2 from the injected flue gas, which suggests that hydrate formation plays a dominant role over CO_2 solution in water.

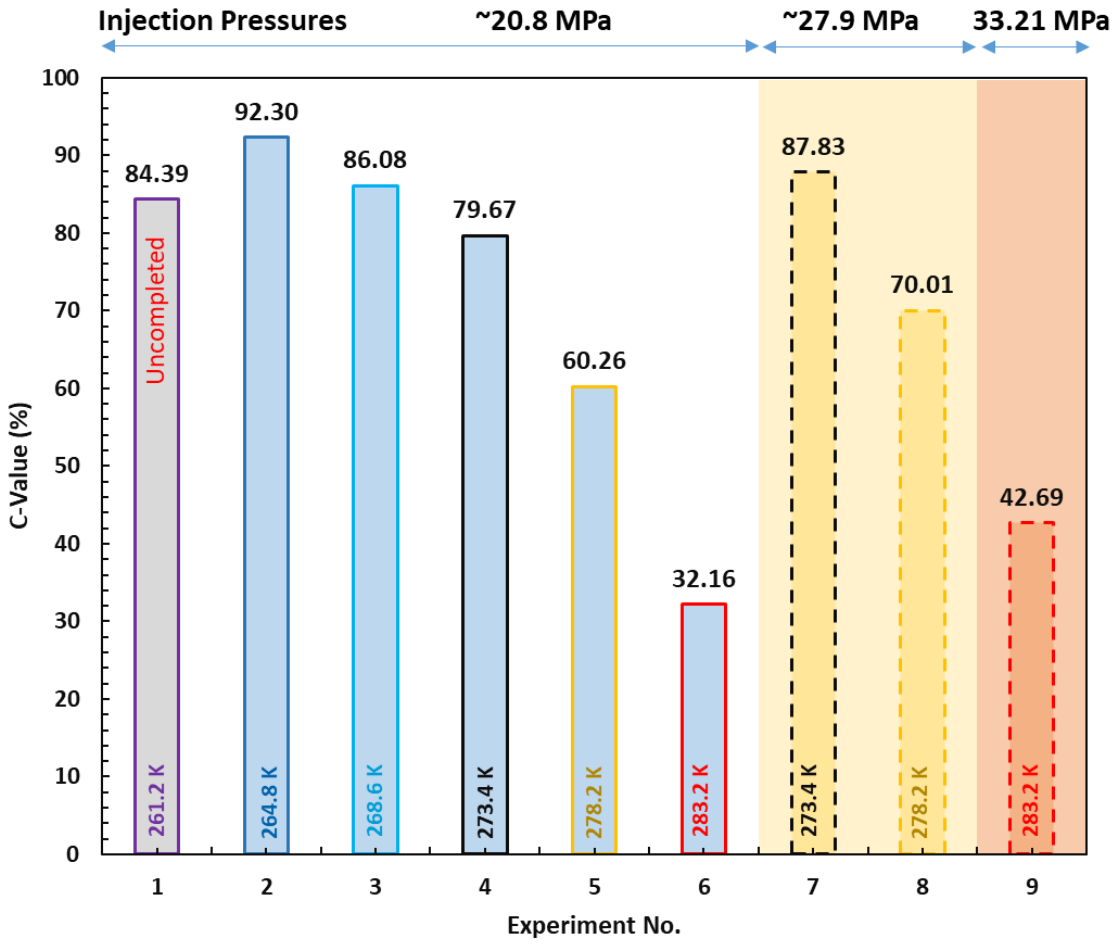

Figure 5.6 C-value variations under different experimental conditions. An apparent trend of C-values indicates that it is possible to store more than 92% percent of the injected CO2 by controlling pressure and by choosing an appropriate area for storage.

5.3.6 Dissociation of CO_2-N_2 mixed hydrates

To further understand the effect of environmental temperature changes during natural cycles or the effect of any sudden climate changes such as the hypothesis of Late Quaternary climate change[48] on the stored hydrates, the composition of the gas phase during dissociation of the formed hydrates was examined at the end of the tests after setting the cryostat to room temperature (294.15 K). As the temperature increased, the gas started to expand and hydrate dissociation began, causing CO_2 concentrations to change in the gas phase, as shown in Figure 5.7. Under frozen conditions (Exp 1-3), a constant CO_2 concentration was maintained and even slightly decreased at initial pressures after initiation of hydrate dissociation, which was followed by a fast release period. The decrease in the CO_2 concentration and relative stability of the CO_2 concentration range in terms of pressure change are both greater at lower temperatures. Especially for Exp 1, the CO_2 concentration in the region of relative pressure stability region is more than 60% of the total pressure rise by heating. The relative stability of CO_2 at early stages under frozen conditions suggests that more energy (in the form of heat) is required to overcome energy barriers and destabilize the CO_2 than N_2 inside clathrate cages. The rate of CO_2 concentration change for this experiment, however, is considerably higher during the second phase. This supports the conclusion that after the formation of N_2-rich gas hydrate at the water-gas interface, CO_2-rich gas hydrate formed inside the initially formed hydrate shells, which is in agreement with the above results of hydrate formation. Furthermore, the trends of CO_2 concentration change during hydrate dissociation generally follow the opposite pressure path from that in which they formed. During dissociation, the CO_2 concentration changes have a less steep slope at lower pressures and generally increase at higher pressures. This is one of the strongest advantages of this method because during small temperature changes, considerably more N_2 than CO_2 will be released, reducing the hazard from CO_2 release and increasing the safety associated with temperature changes. This results are in agreement with the work reported by Schicks et. al.[49, 50] about coexistence of different types of gas hydrates at the same conditions, as our results confirmed that CO_2-rich and N_2-rich hydrates exist together. As an additional support for clathrate structural change in Exp 2-4 and 8, there are sharp changes in the slope of the curves (circled part) only for these experiments, which are missing for the other ones. Finally, sharp drops in the CO_2 concentration at the end of the dissociation experiment are clearly from the dissolution of CO_2 in the water phase.

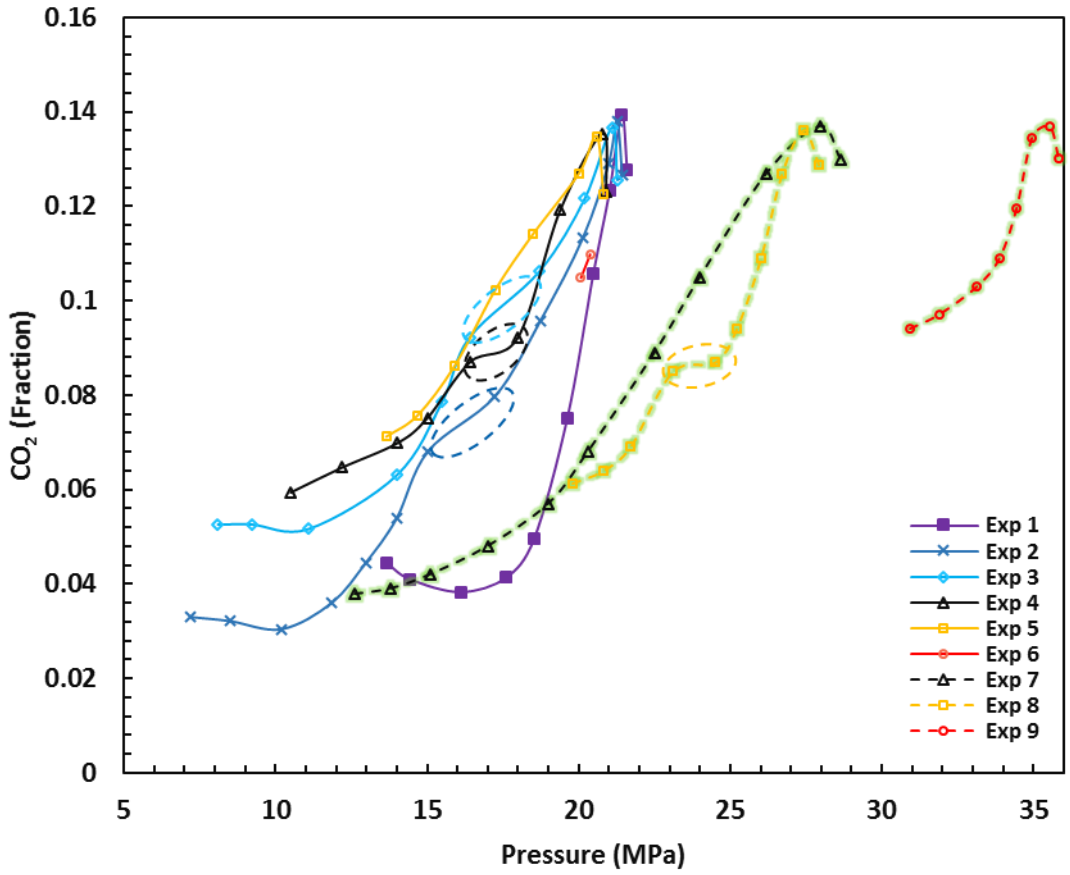

Figure 5.7 CO2 concentration in the gas phase versus system pressure during hydrate dissociation after bath temperature was set to 294.15 K.

5.4 References

(1) Myers, S. S.; Zanobetti, A.; Kloog, I.; Huybers, P.; Leakey, A. D. B.; Bloom, A. J.; Carlisle, E.; Dietterich, L. H.; Fitzgerald, G.; Hasegawa, T. Increasing CO2 threatens human nutrition. *Nature* **2014**, *510* (7503), 139–142.

(2) Seinfeld, J. H.; Pandis, S. N. *Atmospheric chemistry and physics: from air pollution to climate change*; John Wiley & Sons, 2016.

(3) Hansen, J.; Johnson, D.; Lacis, A.; Lebedeff, S.; Lee, P.; Rind, D.; Russell, G. Climate impact of increasing atmospheric carbon dioxide. *Science (80-.).* **1981**, *213* (4511), 957–966.

(4) Notz, D.; Stroeve, J. Observed Arctic sea-ice loss directly follows anthropogenic CO2 emission. *Science (80-.).* **2016**, *354* (6313), 747–750.

(5) MacDowell, N.; Florin, N.; Buchard, A.; Hallett, J.; Galindo, A.; Jackson, G.; Adjiman, C. S.; Williams, C. K.; Shah, N.; Fennell, P. An overview of CO 2 capture technologies. *Energy Environ. Sci.* **2010**, *3* (11), 1645–1669.

(6) Stocker, T. *Climate change 2013: the physical science basis: Working Group I contribution to the Fifth assessment report of the Intergovernmental Panel on Climate Change*; Cambridge University Press, 2014.

(7) Kvenvolden, K. A.; Lorenson, T. D. The Global Occurrence of Natural Gas Hydrate; American Geophysical Union, 2013; pp 3–18.

(8) Zimov, S. A.; Schuur, E. A. G.; Chapin, F. S. Permafrost and the global carbon budget. *Science (80-.).* **2006**, *312* (5780), 1612–1613.

(9) Shakhova, N.; Semiletov, I.; Salyuk, A.; Yusupov, V.; Kosmach, D.; Gustafsson, Ö. Extensive methane venting to the atmosphere from sediments of the East Siberian Arctic Shelf. *Science (80-.).* **2010**, *327* (5970), 1246–1250.

(10) Schuur, E. A. G.; Bockheim, J.; Canadell, J. G.; Euskirchen, E.; Field, C. B.; Goryachkin, S. V; Hagemann, S.; Kuhry, P.; Lafleur, P. M.; Lee, H. Vulnerability of permafrost carbon to climate change: Implications for the global carbon cycle. *AIBS Bull.* **2008**, *58* (8), 701–714.
(11) Haszeldine, R. S. Carbon capture and storage: how green can black be? *Science (80-.).* **2009**, *325* (5948), 1647–1652.
(12) Boot-Handford, M. E.; Abanades, J. C.; Anthony, E. J.; Blunt, M. J.; Brandani, S.; Mac Dowell, N.; Fernández, J. R.; Ferrari, M.-C.; Gross, R.; Hallett, J. P. Carbon capture and storage update. *Energy Environ. Sci.* **2014**, *7* (1), 130–189.
(13) Bui, M.; Adjiman, C. S.; Bardow, A.; Anthony, E. J.; Boston, A.; Brown, S.; Fennell, P. S.; Fuss, S.; Galindo, A.; Hackett, L. A. Carbon capture and storage (CCS): the way forward. *Energy Environ. Sci.* **2018**.
(14) Sloan, E. D. Fundamental principles and applications of natural gas hydrates. *Nature* **2003**, *426* (November), 353.
(15) Mehrabian, H.; Bellucci, M. A.; Walsh, M. R.; Trout, B. L. Effect of Salt on Anti-Agglomerant Surface Adsorption in Natural Gas Hydrates. *J. Phys. Chem. C* **2018**.
(16) Kim, E.; Ko, G.; Seo, Y. Greenhouse Gas (CHF3) Separation by gas hydrate formation. *ACS Sustain. Chem. Eng.* **2017**, *5* (6), 5485–5492.
(17) Onyango, P.; Jiang, S.; Uejima, H.; Shamblott, M. J.; Gearhart, J. D.; Cui, H.; Feinberg, A. P. Permanent carbon dioxide storage in deep-sea sediments. *Proc. Natl. Acad. Sci. U. S. A.* **2002**, *1699* (10), 10599–10604.
(18) Bai, D.; Zhang, X.; Chen, G.; Wang, W. Replacement mechanism of methane hydrate with carbon dioxide from microsecond molecular dynamics simulations. *Energy Environ. Sci.* **2012**, *5* (5), 7033.
(19) Deusner, C.; Bigalke, N.; Kossel, E.; Haeckel, M. Methane Production from Gas Hydrate Deposits through Injection of Supercritical CO2. *Energies* **2012**, *5* (12), 2112–2140.
(20) Dornan, P.; Alavi, S.; Woo, T. K. Free energies of carbon dioxide sequestration and methane recovery in clathrate hydrates. *J. Chem. Phys.* **2007**, *127* (12), 124510–124700.
(21) Lee, H.; Seo, Y.; Seo, Y.-T.; Moudrakovski, I. L.; Ripmeester, J. A. Recovering Methane from Solid Methane Hydrate with Carbon Dioxide. *Angew. Chemie Int. Ed.* **2003**, *42* (41), 5048–5051.
(22) Goel, N. In situ methane hydrate dissociation with carbon dioxide sequestration: Current knowledge and issues. *J. Pet. Sci. Eng.* **2006**, *51* (3), 169–184.
(23) Ma, Z. W.; Zhang, P.; Bao, H. S.; Deng, S. Review of fundamental properties of CO2 hydrates and CO2 capture and separation using hydration method. *Renew. Sustain. Energy Rev.* **2016**, *53*, 1273–1302.
(24) Schoderbek, D.; Martin, K. L.; Howard, J.; Silpngarmlert, S.; Hester, K. North slope hydrate fieldtrial: CO2/CH4 exchange. In *OTC Arctic Technology Conference*; Offshore Technology Conference, 2012.
(25) Yang, J.; Okwananke, A.; Tohidi, B.; Chuvilin, E.; Maerle, K.; Istomin, V.; Bukhanov, B.; Cheremisin, A. Flue gas injection into gas hydrate reservoirs for methane recovery and carbon dioxide sequestration. *Energy Convers. Manag.* **2017**, *136*, 431–438.
(26) Hassanpouryouzband, A.; Yang, J.; Tohidi, B.; Chuvilin, E. M.; Istomin, V.; Bukhanov, B. A.; Cheremisin, A. CO2 Capture by Injection of Flue Gas or CO2-N2 Mixtures into Hydrate Reservoirs: Dependence of CO2 Capture Efficiency on Gas Hydrate Reservoir Conditions. *Environ. Sci. Technol.* **2018**.
(27) Kang, S.-P.; Lee, H. Recovery of CO2 from flue gas using gas hydrate: thermodynamic verification through phase equilibrium measurements. *Environ.*

Sci. Technol. **2000**, *34* (20), 4397–4400.
(28) Hassanpouryouzband, A.; Yang, J.; Tohidi, B.; Chuvilin, E.; Istomin, V.; Bukhanov, B.; Cheremisin, A. Insights into CO2 Capture by Flue Gas Hydrate Formation: Gas Composition Evolution in Systems Containing Gas Hydrates and Gas Mixtures at Stable Pressures. *ACS Sustain. Chem. Eng.* **2018**.
(29) Koh, D.; Kang, H.; Kim, D.; Park, J.; Cha, M.; Lee, H. Recovery of methane from gas hydrates intercalated within natural sediments using CO2 and a CO2/N2 gas mixture. *ChemSusChem* **2012**, *5* (8), 1443–1448.
(30) Linga, P.; Kumar, R.; Englezos, P. Gas hydrate formation from hydrogen/carbon dioxide and nitrogen/carbon dioxide gas mixtures. *Chem. Eng. Sci.* **2007**, *62* (16), 4268–4276.
(31) Babu, P.; Linga, P.; Kumar, R.; Englezos, P. A review of the hydrate based gas separation (HBGS) process for carbon dioxide pre-combustion capture. *Energy* **2015**, *85*, 261–279.
(32) Portnov, A.; Vadakkepuliyambatta, S.; Mienert, J.; Hubbard, A. Ice-sheet-driven methane storage and release in the Arctic. *Nat. Commun.* **2016**, *7*.
(33) Tohidi, B.; Yang, J.; Salehabadi, M.; Anderson, R.; Chapoy, A. CO2 hydrates could provide secondary safety factor in subsurface sequestration of CO2. *Environ. Sci. Technol.* **2010**, *44* (4), 1509–1514.
(34) Sloan Jr, E. D.; Koh, C. *Clathrate hydrates of natural gases*; CRC press, 2007.
(35) Chazallon, B.; Itoh, H.; Koza, M.; Kuhs, W. F.; Schober, H. Anharmonicity and guest–host coupling in clathrate hydrates. *Phys. Chem. Chem. Phys.* **2002**, *4* (19), 4809–4816.
(36) Chazallon, B.; Pirim, C. Selectivity and CO2 capture efficiency in CO2-N2 clathrate hydrates investigated by in-situ Raman spectroscopy. *Chem. Eng. J.* **2018**, *342*, 171–183.
(37) Seo, Y.-T.; Lee, H. Structure and guest distribution of the mixed carbon dioxide and nitrogen hydrates as revealed by X-ray diffraction and 13C NMR spectroscopy. *J. Phys. Chem. B* **2004**, *108* (2), 530–534.
(38) Seo, Y.-T.; Moudrakovski, I. L.; Ripmeester, J. A.; Lee, J.; Lee, H. Efficient recovery of CO2 from flue gas by clathrate hydrate formation in porous silica gels. *Environ. Sci. Technol.* **2005**, *39* (7), 2315–2319.
(39) Lee, Y.; Lee, S.; Lee, J.; Seo, Y. Structure identification and dissociation enthalpy measurements of the CO 2+ N 2 hydrates for their application to CO 2 capture and storage. *Chem. Eng. J.* **2014**, *246*, 20–26.
(40) Waite, W. F.; Santamarina, J. C.; Cortes, D. D.; Dugan, B.; Espinoza, D. N.; Germaine, J.; Jang, J.; Jung, J. W.; Kneafsey, T. J.; Shin, H.; et al. PHYSICAL PROPERTIES OF HYDRATE-BEARING SEDIMENTS. **2009**, No. 2008, 1–38.
(41) Kasting, J. F.; Howard, M. T.; Wallmann, K.; Veizer, J.; Shields, G.; Jaffrés, J. Paleoclimates, ocean depth, and the oxygen isotopic composition of seawater. *Earth Planet. Sci. Lett.* **2006**, *252* (1–2), 82–93.
(42) Resing, J. A.; Sedwick, P. N.; German, C. R.; Jenkins, W. J.; Moffett, J. W.; Sohst, B. M.; Tagliabue, A. Basin-scale transport of hydrothermal dissolved metals across the South Pacific Ocean. *Nature* **2015**, *523* (7559), 200.
(43) Haghighi, H.; Chapoy, A.; Burgess, R.; Tohidi, B. Experimental and thermodynamic modelling of systems containing water and ethylene glycol: Application to flow assurance and gas processing. *Fluid Phase Equilib.* **2009**, *276* (1), 24–30.
(44) Mahabadian, M. A.; Chapoy, A.; Burgass, R.; Tohidi, B. Development of a multiphase flash in presence of hydrates: experimental measurements and validation with the CPA equation of state. *Fluid Phase Equilib.* **2016**, *414* (JANUARY), 117–132.

(45) Hassanpouryouzband, A.; Vasheghani Farahani, M.; Yang, J.; Tohidi, B.; Chuvilin, E.; Istomin, V.; Bukhanov, B. A. Solubility of Flue Gas or Carbon Dioxide-Nitrogen Gas Mixtures in Water and Aqueous Solutions of Salts: Experimental Measurement and Thermodynamic Modelling. *Ind. Eng. Chem. Res.* **2019**.

(46) Tung, Y.-T.; Chen, L.-J.; Chen, Y.-P.; Lin, S.-T. Growth of structure I carbon dioxide hydrate from molecular dynamics simulations. *J. Phys. Chem. C* **2011**, *115* (15), 7504–7515.

(47) Falenty, A., Qin, J., Salamatin, A. N., Yang, L., & Kuhs, W. F. Fluid composition and kinetics of the in situ replacement in CH4–CO2 hydrate system. The Journal of Physical Chemistry C. **2016**, 120(48), 27159-27172.

(48) Kennett, J. P.; Cannariato, K. G.; Hendy, I. L.; Behl, R. J. *Methane hydrates in quaternary climate change: the clathrate gun hypothesi*; Wiley Online Library, 2003.

(49) Schicks, J. M., & Ripmeester, J. A. *The coexistence of two different methane hydrate phases under moderate pressure and temperature conditions: Kinetic versus thermodynamic products.* **2004**, Angewandte Chemie International Edition, 43(25), 3310-3313.

(50) Schicks, J. M., & Luzi-Helbing, M. *Kinetic and thermodynamic aspects of clathrate hydrate nucleation and growth. Journal of Chemical & Engineering Data. **2014***, 60(2), 269-277.

Chapter 6 - Insights into the CO_2 Capture by Flue Gas Hydrate Formation: Gas Composition Evolution in Systems Containing Gas Hydrates and Gas Mixtures at Stable Pressures

6.1 Introduction

Gas hydrates are solid, non-stoichiometric inclusion compounds consisting of an open lattice of water molecules that encage small size guest gas molecules such as nitrogen (N_2) and carbon dioxide (CO_2), etc. without chemical bonding[1]. Between all potential guest molecules, CO_2 emanating from power plants[2] is responsible for the majority of the increasing greenhouse effect[3]. Accordingly, developing efficient methods for CO_2 capture is crucial in order to deal with this major environmental challenge[4]. To date, various methods that have different efficiencies at selected conditions have been developed[5]. In this regard, gas hydrate formation has been proposed as an alternative approach to separate CO_2 from power plant flue gas which mainly consists of N_2 and CO_2[6]. Furthermore, direct injection of CO_2-N_2 mixtures[7,8] and coal-fired flue gas[9] into methane hydrate reservoirs was proposed as a promising method for capture and geological storage of CO_2. These gas hydrate-based CO2 capture methods are environmentally cleaner and more cost effective compared to the conventional amine-based absorbance techniques[10,11]. Fulfilment of these methods requires the flue gas hydrate formation kinetics to be completely understood, reduction in the CO_2/N_2 ratio of the gas phase with time is the main indicator of efficiency and may even be the key factor in acceptance of these methods for use on an industrial scale. Only a limited number of investigations on this subject have been reported and the kinetics of flue gas or N_2-CO_2 hydrate formation hasn't been completely clarified. Different material and methods have been suggested to enhance the rate of gas hydrate formation[12] and the kinetics of CO_2 separation mechanism and process through hydrate formation have been investigated for systems containing CH_4, CO_2, N_2, and oxygen (O_2) [11,13], but little is discussed about when and how the system reaches equilibrium. Usually thermodynamic equilibrium of the gas mixture is considered to be when pressure is constant[14]. In this chapter, experimental results are reported to show that complex hydrate formation, decomposition, and molecular exchange were still occurring in the water-CO_2-N_2 gas mixture systems when the system pressure was constant.

6.2 Materials and Methods

The kinetics of flue gas hydrate formation was studied at 3 constant temperatures using a 316 stainless steel cylindrical autoclave (maximum working pressure of 20.7 MPa, and volume of 180.1 mL), a schematic diagram of which is shown in Figure 1. The autoclave was connected to a gas chromatograph (GC) (Varian 3600, Agilent Technologies) through an online magnetic capillary sampler system (RolsiTM) with zero dead volume. The moveable sampler was connected to the top cap and GC through a capillary tube (0.1 mm internal diameter), and heated line (T = 323.25 K), respectively. The temperature was maintained by a cryostat (Grant LTC) which pumps cooling fluid into the integral cooling jacket surrounding the cell. The system pressure and temperature were continuously monitored using a Quartzdyne pressure transducer (accuracy +/-0.0005 MPa) and a Platinum Resistant Thermometer (PRT) coated in stainless steel (uncertainty of 0.1 K), respectively, through a data acquisition device and a LabView software interface at regular time intervals. To help increase the surface contact of components, a high-pressure stirrer (Top Industrie SA, France, model 6180300B) was fixed at bottom of the cell. Visual high pressure windows were located at each side of the autoclave to visually observe hydrate formation and discriminate it from dissolution.

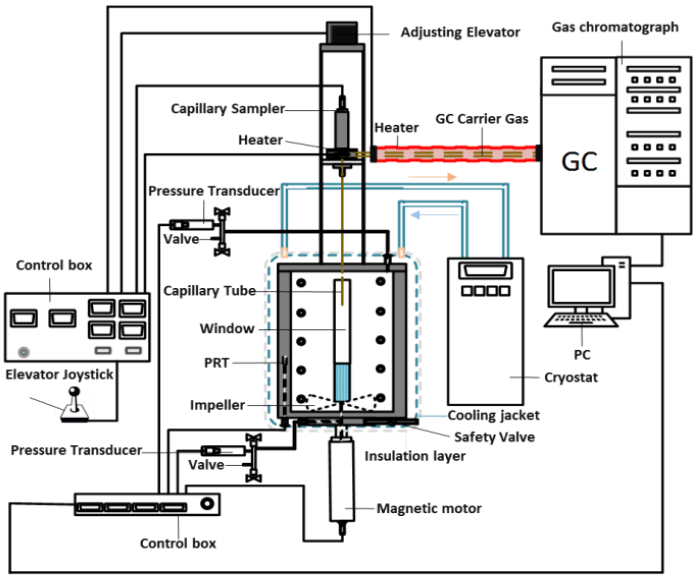

Figure 6.1 Schematic of the high-pressure autoclave setup

40% of the autoclave was filled with deionized water generated by an integral water purification system (ELGA DV 25), following which the system was vacuumed. For simplicity, a gas mixture of 85.4% N_2 and 14.6% CO_2 (purity of 99.995 vol% from BOC Limited) was used to simulate coal-fired flue gas[9,15]. After setting the system temperature to 294.15 K and starting stirrer, the simulated flue gas was injected continuously to reach 20.68 MPa. To control the hydrate

formation the stirrer was switched off until the system reached the target temperature. After reaching the target temperature, mixing was started and flue gas hydrates were formed at a constant temperature. Throughout the process the gas composition was analysed using GC.

Figure 6.2 presents the predicted[16] hydrate stability zones (HSZs) of the tested gas-water systems together with the experimental temperature and pressure conditions. As can be seen experiments were conducted at 3 different temperatures, and consequently 3 different pressures (Gas law). As shown, the experiment at 273.35 K started at a pressure inside the N_2 HSZ, but the other two experiments were outside the N_2 HSZ zone. Accordingly, thermodynamically for all experiments, there was the possibility of N_2-CO_2 mixed hydrates and CO_2 hydrate formation. However, N_2 hydrate formation may occur only in the first experiment. Regarding CO_2-N_2 mixed hydrates, according to thermodynamic stabilization, N_2 will fill the small cavities and CO_2 will enter the large cavities[17].

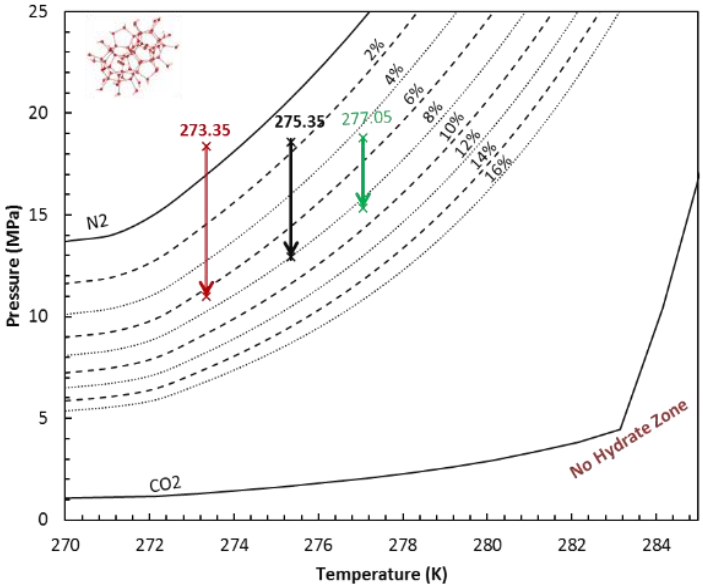

Figure 6.2 The predicted hydrate stability zones of N_2, CO_2, various N_2-CO_2 combinations, and the experimental conisations

6.3 Results and Discussion

Figure 6.3a shows the CO_2 in mole% in the gas phase throughout the experimental process at the set temperatures. As can be seen from Figure 6.3a, initially the molar fraction of CO_2 in the gas phase reduced from 14.6% to 12.4% at 294.15 K which is mainly due to the higher solubility of CO_2 in water compared to that of N_2, moving more CO_2 into the polar phase (Figure 6.4a). After cooling the system to the target temperature, the CO_2 percentage in the gas phase slightly reduced owing to further increases in CO_2 solubility with temperature reduction compared to that of N_2. For the same reason, the CO_2 fraction

in the gas phase was slightly smaller in the experiments at lower temperatures. It should be noted that, in the investigated system there is a possibility for formation of different kind of ions, which are illustrated in Figure 6.4d[18].

After hydrate formation started, there was an initial increase in the fraction of CO_2 in the gas phase for all experiments, which is magnified in Figure 6.3b. These increments infer that the CO_2/N_2 ratio in water phase was relatively higher than that in the hydrate phase at the pressures in Figure 6.3b. The difference became clearer at lower temperatures. This could be plausibly justified by the fact that according to Figure 6.2 showing that the first experiment was initiated at a pressure inside the N_2 HSZ and the second experiment was closer to N_2 HSZ than the third experiment, occupancy ratio of large to small cages in the formed hydrates was smallest for the first experiment and is smaller for the second experiment compared to the third one, which in turn leads to entering relatively more N_2 into hydrate phase at lower temperature given that the initial system pressure was similar. With regard to the aforementioned initial increment in the percentage of the CO_2 in the gas phase, the first hydrate crystals formed could affect the solubility of CO_2 in the water[19], as the solubility of a gas in a solvent could be significantly different in the presence of other solutes in the solution. After this phase, while the system pressure continuously decreased due to hydrate formation, the CO_2 percentage in the gas phase stayed almost stable with small fluctuations, i.e., no more CO_2 appeared to go into the hydrate lattice compared to N_2. This means that in this phase the ratio of CO_2/N_2 in the forming hydrate phase was equal to the ratio in the hydrate former gas phase and water phases, demonstrating a dynamical molecule exchanging process between these phases. At pressure near to the final equilibrium pressures the molar fraction of the CO_2 in the gas phase reduced sharply. The possible reason for these changes with only small pressure changes could be attributed the fact that the initially formed hydrates with relatively low CO_2 content dissociated and new CO_2-N_2 hydrates formed entrapping more CO_2. In addition, the final slight increase in the CO_2 percentage seen in all experiments could indicate that there is an optimum pressure at each specific temperature at which more CO_2 can be captured in hydrate (by keeping the pressure constant through gas injection) than at the final pressure where dissociation of the CO_2-N_2 mixed hydrate led to an increase in the CO_2 percentage. It is worth noting that further investigation is been in progress investigating the reasons for these final reductions and increments of the CO_2 content in the gas phase.

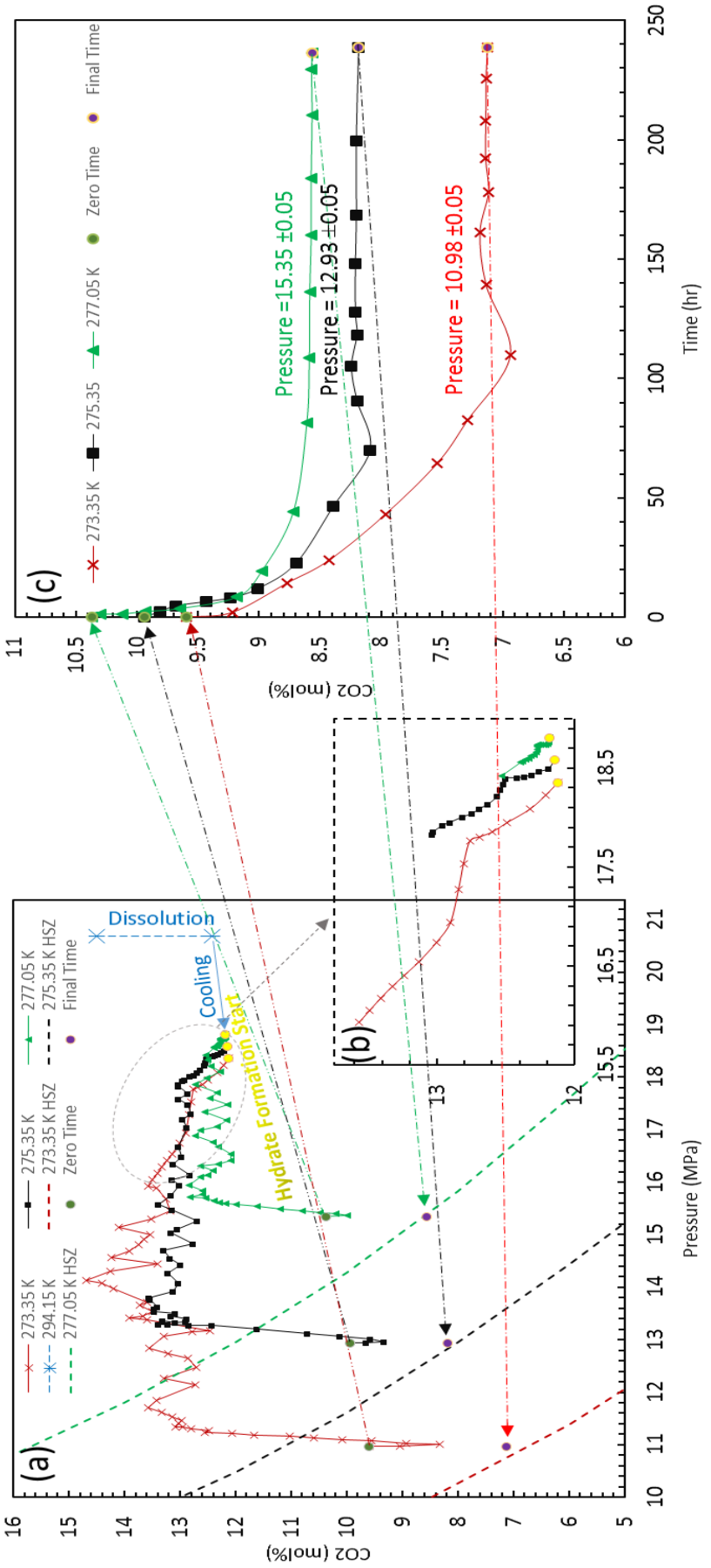

Figure 6. 3 (a) Variation in the CO_2 mole fraction in the gas phase versus pressure during experiments; (b) magnification of the selected part of the Figure 6.3a; (c) Variation in the CO_2 mole fraction in the gas phase versus time after reaching equilibrium pressure (More detailed results can be found in Append

A physical model of different stages of experiments is illustrated in Figure 6.4 to describe the kinetic process of CO_2 capture in flue gas hydrate formation. After reaching the final pressure (Figure 6.4b), as can be seen from Figure 6.3c, the system had not reached equilibrium and the CO_2 fraction in the gas phase was changing with time, while the pressure was almost constant (Figure 6.4c). It should be noted that there were still very small fluctuations in the pressure (less than 0.14 MPa), but these very small fluctuations were commonly seen in other hydrate tests and can be considered as negligible[14]. The reduction of the CO_2 percentage in the gas phase suggests that at a constant pressure, the amount of CO_2 entering into hydrate should be as same as the amount of N_2 escaping from the previously formed N_2-rich hydrates. Three different mechanisms could be suggested for this behaviour, as shown in a schematic illustration in Figure 6.4e-g. Initially, some of the first formed hydrates with relatively more N_2 in the hydrate phase were dissociated and new hydrates with relatively less N_2 were formed (Figure 6.4e). As a side note, there could be empty cages (Figure 6.4b-c) in the hydrate phase corresponding to the occupancy number, so the aforementioned secondary hydrate formation could occur by filling these cages with CO_2 molecules. Secondly, some of the hydrate cages containing N_2 were partially broken, CO_2-N_2 exchange occurred and residual rings formed new cages (Figure 6.4f). A similar behavior for CO_2/CH_4 replacement was reported in the literature[20]. Third, CO_2-N_2 replacement in the hydrate phase occurred without dissociation of initial hydrates (Figure 6.4g). There is also a similar observation for the behavior of CO_2-CH_4 replacement after injecting CO_2-N_2 gas into methane hydrate system[8].

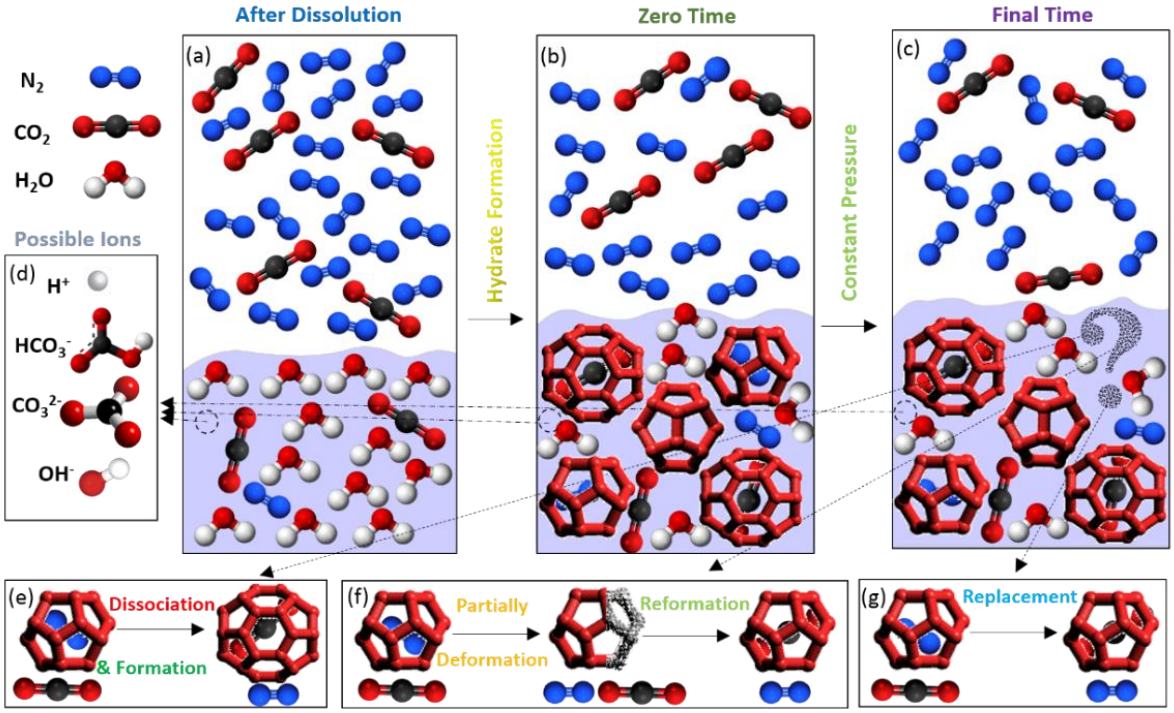

Figure 6. 4 Schematic illustration of the described flue gas hydrate formation experiments: (a) Dissolution of CO_2 and N_2 in water after injecting high pressure gas; (b) Formation of CO_2-N_2 hydrates after reaching to the target temperature; (c) Changing hydrate/gas phase composition after reaching final pressure; (d) Formation of different kinds of ions during experiment; (e)-(g) proposed mechanisms to explain the change in the hydrate/gas composition.

The first mechanism is thermodynamically more preferable, as CO_2 tends to enter large cavities, whereas N_2 goes for small cavities[17]. However, the possibility of secondary and tertiary mechanisms still exist as CO_2 could go to small cavities in some circumstances[21]. What's more, two small concavities can be seen in Figure 6.3c graphs for Experiments 1 and 2, which could be explained with the same reason as for the final increase in Figure 6.3a. Regarding Experiment 3, lack of increment in Figure 6.3c could be explained because the system was further outside the N_2 HSZ, reducing the difference in the composition of the formed hydrates at initial and final pressures. It's also confirmed that, under elevated subcooling there is possibility of hydrate formation with metastable occupancies, if the concentration of small guest molecules (such as N_2) in the hydrate phase and overall solution is comparable[22]. This could be another explanation for abovementioned behavior. In addition, our results are in agreement with the research conducted by Schicks et. al.[23, 24]. They reported coexistence of sI and sII hydrate at the conditions where only sI CH4 hydrate was stable and confirmed that metastable hydrates could form during hydrate growth. It should be noted that further investigation is required to deeply understand this phenomenon. The HSZs at the experimental temperatures are plotted as a function of pressure against CO_2 percentage in Figure 6.3a. The CO_2 concentration at the end of each experiment approached to the corresponding HSZ curve.

The final CO_2 concentration is 7.1% in Experiment 1 at 273.4 K 8.2% in Experiment 2 at 275.4 K, and 8. 6% in Experiment 3 at 277.1 K, suggesting lower temperatures favor more CO_2 than N_2 compared to higher temperature. Furthermore, it is clear from Figure 6.3c that more than 40% of the CO_2 capture through hydrate formation occurs at final pressures and it takes longer for tests at lower temperatures to reach equilibrium compared to those at higher ones. This indicates that although CO_2 capture at higher temperatures is less efficient in terms of captured CO_2 percentage, it could have the advantages of faster capture at certain conditions (Figure 6.S2 in Appendix C). Accordingly, temperature of the capture environment, temperature of the supplied water, energy loss for maintaining and keeping the temperature, and energy loss for the reactor's electrical part should be considered and the most economic temperature and the most economic residency time for reaction should be chosen.

6.4 References

(1) Koh, C. A. Towards a fundamental understanding of natural gas hydrates. *Chem. Soc. Rev.* **2002**, *31* (3), 157–167. DOI: 10.1039/B008672J

(2) Stocker, T. *Climate change 2013: the physical science basis: Working Group I contribution to the Fifth assessment report of the Intergovernmental Panel on Climate Change*; Cambridge University Press: Cambridge, U.K., 2014.

(3) Parrenin, F.; Masson-Delmotte, V.; Köhler, P.; Raynaud, D.; Paillard, D.; Schwander, J.; Barbante, C.; Landais, A.; Wegner, A.; Jouzel, J. Synchronous change of atmospheric CO2 and Antarctic temperature during the last deglacial warming. *Science (80-.).* **2013**, *339* (6123), 1060–1063. DOI: 10.1126/science.1226368

(4) Sumida, K.; Rogow, D. L.; Mason, J. A.; McDonald, T. M.; Bloch, E. D.; Herm, Z. R.; Bae, T.-H.; Long, J. R. Carbon Dioxide Capture in Metal–Organic Frameworks. *Chem. Rev.* **2011**, *112* (2), 724–781. DOI: 10.1021/cr2003272

(5) Boot-Handford, M. E.; Abanades, J. C.; Anthony, E. J.; Blunt, M. J.; Brandani, S.; Mac Dowell, N.; Fernández, J. R.; Ferrari, M.-C.; Gross, R.; Hallett, J. P. Carbon capture and storage update. *Energy Environ. Sci.* **2014**, *7* (1), 130–189. DOI: 10.1039/C3EE42350F

(6) Kang, S.-P.; Lee, H. Recovery of CO2 from Flue Gas Using Gas Hydrate: Thermodynamic Verification through Phase Equilibrium Measurements. *Environ. Sci. Technol.* **2000**, *34* (20), 4397–4400. DOI: 10.1021/es001148l

(7) Park, Y.; Kim, D.-Y.; Lee, J.-W.; Huh, D.-G.; Park, K.-P.; Lee, J.; Lee, H. Sequestering carbon dioxide into complex structures of naturally occurring gas hydrates. *Proc. Natl. Acad. Sci. U. S. A.* **2006**, *103* (34), 12690–12694. DOI: 10.1073/pnas.0602251103

(8) Cha, M.; Shin, K.; Lee, H.; Moudrakovski, I. L.; Ripmeester, J. A.; Seo, Y. Kinetics of Methane Hydrate Replacement with Carbon Dioxide and Nitrogen Gas Mixture Using in Situ NMR Spectroscopy. *Environ. Sci. Technol.* **2015**, *49* (3), 1964–1971. DOI: 10.1021/es504888n

(9) Yang, J.; Okwananke, A.; Tohidi, B.; Chuvilin, E.; Maerle, K.; Istomin, V.; Bukhanov, B.; Cheremisin, A. Flue gas injection into gas hydrate reservoirs for methane recovery and carbon dioxide sequestration. *Energy Convers. Manag.* **2017**, *136*, 431–438. DOI: 10.1016/j.enconman.2017.01.043

(10) Hassanpouryouzband, A.; Yang, J.; Tohidi, B.; Chuvilin, E. M.; Istomin, V.; Bukhanov, B. A.; Cheremisin, A. CO2 Capture by Injection of Flue Gas or CO2-N2 Mixtures into Hydrate Reservoirs: Dependence of CO2 Capture Efficiency on Gas Hydrate Reservoir Conditions. *Environ. Sci. Technol.* **2018**. DOI: 10.1021/acs.est.7b05784

(11) Babu, P.; Linga, P.; Kumar, R.; Englezos, P. A review of the hydrate based gas separation (HBGS) process for carbon dioxide pre-combustion capture. *Energy* **2015**, *85*, 261–279. DOI: 10.1016/j.energy.2015.03.103

(12) Linga, P.; Clarke, M. A. A Review of Reactor Designs and Materials Employed for Increasing the Rate of Gas Hydrate Formation. *Energy & Fuels* **2016**, *31* (1), 1–13. DOI: 10.1021/acs.energyfuels.6b02304

(13) Linga, P.; Kumar, R.; Englezos, P. Gas hydrate formation from hydrogen/carbon dioxide and nitrogen/carbon dioxide gas mixtures. *Chem. Eng. Sci.* **2007**, *62* (16), 4268–4276. DOI: 10.1016/j.ces.2007.04.033

(14) Tohidi, B.; Burgass, R. W.; Danesh, A.; Østergaard, K. K.; Todd, A. C. Improving the Accuracy of Gas Hydrate Dissociation Point Measurements. *Ann. N. Y. Acad. Sci.* **2000**, *912* (1), 924–931.DOI: 10.1111/j.1749-6632.2000.tb06846.x

(15) Change, W. G. I. of the I. P. on C.; Metz, B.; Davidson, O.; Coninck, H. de; Loos, M.; Meyer, L. Working Group III of the Intergovernmental Panel on Climate Change. IPCC Special Report on Carbon Dioxide Capture and Storage. Cambridge University Press: Cambridge, U.K., 2005.

(16) Haghighi, H.; Chapoy, A.; Burgess, R.; Tohidi, B. Experimental and

thermodynamic modelling of systems containing water and ethylene glycol: Application to flow assurance and gas processing. *Fluid Phase Equilib.* **2009**, *276* (1), 24–30. DOI: 10.1016/j.fluid.2008.10.006

(17) Dornan, P.; Alavi, S.; Woo, T. K. Free energies of carbon dioxide sequestration and methane recovery in clathrate hydrates. *J. Chem. Phys.* **2007**, *127* (12), 124510–124700. DOI: 10.1063/1.2769634

(18) Pitzer, K. S. Thermodynamics of electrolytes. I. Theoretical basis and general equations. *J. Phys. Chem.* **1973**, *77* (2), 268–277. DOI: 10.1021/j100621a026

(19) Servio, P.; Englezos, P. Effect of temperature and pressure on the solubility of carbon dioxide in water in the presence of gas hydrate. *Fluid Phase Equilib.* **2001**, *190* (1), 127–134. DOI: 10.1016/S0378-3812(01)00598-2

(20) Bai, D.; Zhang, X.; Chen, G.; Wang, W. Replacement mechanism of methane hydrate with carbon dioxide from microsecond molecular dynamics simulations. *Energy Environ. Sci.* **2012**, *5* (5), 7033–7041. DOI: 10.1039/C2EE21189K

(21) Sloan Jr, E. D.; Koh, C. *Clathrate hydrates of natural gases*; CRC press, 2007.

(22) Song, B.; Nguyen, A. H.; Molinero, VCan Guest Occupancy in Binary Clathrate Hydrates Be Tuned through Control of the Growth Temperature?. *J. Phys. Chem. C* **2014**, *118* (40), 23022–23031. DOI: 10.1021/jp504852k

(23) Schicks, J. M., & Ripmeester, J. A. The coexistence of two different methane hydrate phases under moderate pressure and temperature conditions: Kinetic versus thermodynamic products. **2004**, Angewandte Chemie International Edition, 43(25), 3310-3313.

(24) Schicks, J. M., & Luzi-Helbing, M. Kinetic and thermodynamic aspects of clathrate hydrate nucleation and growth. Journal of Chemical & Engineering Data. **2014**, 60(2), 269-277.

Chapter 7 - Methane Recovery from Gas Hydrate-bearing Sediments: An Experimental Study on the Gas Permeation Characteristics under Varying Pressure

7.1 Introduction

Gas hydrates are ice-like crystalline compounds composed of cages of water molecules and enclathrated guest molecules [1,2]. They form under conditions of high pressure and low temperature. When the guest molecules are a mixture of the components of natural gas such as methane, ethane, propane, carbon dioxide, and nitrogen, they are referred to as natural gas hydrates [3]. Natural gas hydrates occur in nature under the subsurface of permafrost regions and in the continental margins of world oceans [4–6]. Due to its overwhelming abundance in nature, gas hydrate is regarded as a potential future source of low carbon energy as the global energy system is being decarbonized gradually. This has elicited tremendous research effort towards the development of commercially viable and environmentally safe production techniques [7]. Three major techniques have been proposed, namely, depressurization, thermal stimulation, and chemical inhibitor injection [8,9]. Depressurisation induces hydrate dissociation by reducing the system pressure below the hydrate stability pressure at the prevailing reservoir temperature. Thermal stimulation introduces external heat to shift the system temperature away from equilibrium thus decompose hydrate. The external heat source can be hot water, steam, hot brine or an electromagnetic heat source [10–15]. Injection of chemicals such as glycols and methanol alters the hydrate equilibrium chemically to dissociate hydrate. Combination of any two of the mentioned techniques has also been shown to improve gas recovery efficiency. The most characterised is thermal stimulation combined with depressurisation [16–19]. CO_2 or CO_2-mixed injection technique can also be utilized for methane recovery based on CO_2-CH_4 exchange [20–23] and chemical potential shift [7,24–27] and for geological carbon capture and storage [28,29]. Moreover, direct injection of flue gas in permafrost region for CO_2 storage and secondary sealing of CH_4 release into atmosphere through formation of a gas hydrate layer has been proposed [30]. Natural gas hydrate exploitation by CO_2/H_2 injection is also considered as another promising technique, in which the role of H_2 is to decrease the partial pressure of methane and break methane hydrate stability [31,32].

Apart from flow assurance considerations, particularly avoidance of hydrate reformation in the downhole separation systems [33,34], the efficiency of gas production from sediments

strongly depends on the permeability of hydrate deposits [9]. The permeability of hydrate-bearing porous media differs markedly from that of non-hydrate-bearing porous media. In general, permeability of hydrate-bearing sediments is reduced due to the presence of gas hydrate in pores. The permeability change is complicated as it is affected by a number of geological formation factors such as hydrate saturation, porosity, and sediment mineralogy [35,36]. In particular, the extent of permeability reduction depends on the hydrate formation sites in the porous media. Empirical modelling of permeability showed that, if hydrates form on the surfaces of grains, the reduction in permeability is gradual and minimal, therefore, the effect on fluid flow is also minimal. If hydrates form in the middle of the pores, permeability reduction is pronounced, and even reduces to zero if the pore bodies are completely blocked [37]. Also, permeability in the presence of hydrate changes as hydrate dissociates. This change impacts directly on pressure communication, fluid flow and ultimately, gas production from hydrate-bearing sediments. Recently, a critical path analysis (CPA) was conducted by Daigle to predict permeability to either water or gas over the entire range of the measured hydrate saturation [38]. It was showed that CPA can appropriately assisted for determination of permeability in hydrate-bearing sediments. However, permeability and relative permeability in gas hydrate-bearing sediments are still peculiar properties which is imperative to be studied.

Permeability measurements using natural core samples in in-situ conditions from hydrate-bearing sediments is often costly and difficult to achieve [9,39]. Pressure coring helps to maintain the samples at near in-situ conditions but does not completely eliminate sample disturbance during coring [40]. Also, creep and diffusion processes may cause hydrate re-distribution and change physical properties of the cores when pressure cores are stored for a long time [9]. Laboratory synthesis of artificial hydrate cores is therefore, a viable alternative for permeability measurements and studies. It has the flexibility of synthesising hydrates with characteristics of interest such as hydrate saturations and preparation processes despite differences in pore-scale growth habits, time scales of hydrate formation, and spatial distribution [41]. Further discussion in this regard can be found elsewhere [42,43]. It should be noted that controlled synthesis of methane hydrate-bearing sediments in laboratory, particularly in a way it forms in nature, has always been a challenge due to low solubility of methane in water [43]. As a result, hydrate formation from methane gas dissolved in water is a slow process. Hence, more expedient techniques are usually followed in laboratory such as dissolved gas method, partial water saturation method, ice-seeding method, and hydrate premixing method [9]. Each method could result in different pore-scale habits and different permeation characteristics accordingly [44].

Nevertheless, the partial water saturation method followed in this work has shown to be fast and reliable enough to make homogeneous synthetic gas hydrate-bearing sediments at desired saturations [7,26,29,30,45].

Given the significance of permeability change and the importance of its predictability in the successful exploitation of natural gas hydrate reservoirs, researchers attempted to understand gas permeation mechanisms in hydrate-bearing sediments using different porous media including glass beads, sand, and clay. Kumar et al. experimentally determined gas permeability of packed glass beads with varying saturation of CO_2 hydrate [46]. Their results were compared with the theoretical estimates of Kozeny grain models [37] for grain coating and pore filling permeability models. They observed that for hydrate saturations less than 35%, the measured permeability values agree better with the grain coating model. On the other hand, for hydrate saturations greater than 35%, the measured permeability values agree better with pore filling models. Kneafsey et al. measured gas permeability with a core holder for dry, moist, frozen, and hydrate-bearing sediments composed of sand and sand/silt mixtures [39]. They reported that permeability reduced in an order of dry sediments, moist sediments, frozen sediments, and that increase in hydrate saturation resulted in decrease in the permeability of hydrate-bearing sediments. In their water flood experiments, it was observed that water flood was not possible for the sand and sand/silt sediments with the highest hydrate saturation due to extremely low permeability. Delli and Grozic conducted a series of water relative permeability measurements using a triaxial cell [47]. They formed CO_2 hydrate of saturations up to 45% in Ottawa sand. Their results indicated a gradual reduction in the permeability as hydrate saturation increased, suggesting that hydrate grows in the pore bodies. They developed a hybrid model using a weighted combination of the Kozeny grain-coating and pore-filling models [48]. They compared their hybrid model alongside existing theoretical permeability models with the experimental results. Their hybrid model gave closer values to the experimental permeability. Li et al. measured the absolute and water effective permeability of methane hydrate-bearing quartz sand cores with hydrate saturations ranging from 0-31% pore volume at a constant pore pressure of 15 MPa [49]. They used three different grain size ranges of quartz sand of 200-300, 300-450, and 450-600 μm, respectively. Their calculated absolute permeability was significantly higher in the quartz sand with the high grain size. Also, the water effective permeability reduced as the methane hydrate saturation increased. In the hydrate-bearing cores, the measured permeability characteristics for hydrate saturations lower than 10% and higher than 10%

differs. Permeability reduction due to increase in hydrate saturation was very significant for the hydrate-bearing sand packs with less than 10% hydrate and became much smaller for those with hydrate saturation above 10%.

Permeability measurement techniques for hydrate bearing sediments have evolved from steady-state gas or water flow to the use of nuclear magnetic resonance (NMR) and X-Ray computed tomography (CT). Kneafsey et al. performed gas permeability measurements on partially saturated sand packs under confining stress using CT scanning [39]. It was observed gas permeation processes are spatially dependent. They reported decreasing effective permeability as the pore spaces in the samples became increasingly occupied by gas hydrate. Recently, percolation characteristics of gas hydrate-bearing sediments were comprehensively studied via combining pore network models (PNM) with micro-CT imaging [50–53]. They extracted the pore network models from the processed 3D micro-CT images taken from laboratory-formed methane hydrate sediments, performed numerical simulations and investigated the effect of hydrate saturation, wettability, interfacial tension, and particle size on the permeability. These studies confirmed that obtaining a realistic structure of hydrate-bearing sediments from micro-CT imaging into pore network model substantially improves the accuracy of the simulations. Chen et al. also used micro-CT for monitoring hydrate growth in a sandpack under the excess gas condition [54]. They also performed Lattice Boltzmann Method (LBM) for pore-scale determination of gas relative permeability as a function of hydrate saturation. Kleinberg et al. used NMR to study hydrate formation, hydrate growth, and its effect on the relative permeability of water [37]. They reported that at substantial hydrate saturation, NMR relaxation time measurements showed that hydrate preferentially replaced water in the largest pores rather than coating grain surfaces. The relative permeability to water reduced significantly. The extent of the reduction agreed with hydrate formation in pore bodies rather than on grain surfaces.

A few studies on permeability of hydrate-bearing sediments were reported for clayey sediments. Liu et al. investigated the dependence of gas permeability on methane hydrate-bearing kaolin in the presence of different saturations of hydrate under effective axial stress of 1 MPa and 3 MPa [55]. Ice-seeding method was used to form hydrate. They observed that with increasing hydrate saturation, gas permeability decreases when the hydrate saturation was less than 4.23% and increases when hydrate saturation was between 4.23% and 40.46%. The initial decrease in permeability was attributed to hydrate blockage of flow channels. They further stated that clay particles form aggregate structures during hydrate formation. The inter-aggregate spaces provide more conduits

for gas flow, hence the increased permeability at high hydrate saturations. There was a critical hydrate saturation at which the effect of blockage and clay particle aggregation offset each other. At this point, the permeability to gas of the hydrate-bearing sediment equals to that of non-hydrate-bearing clayey sediments. Permeability measurement experiments were conducted with montmorillonite [55] and the observed results were similar to that observed with kaolin by Liu et al. [55].

Although great efforts were made to measure permeability of a variety of gas hydrate-bearing sediments, there is a paucity of information of the mechanisms behind the observed permeation behaviour aforementioned. Moreover, it is noted that the experiments reported in literature were all conducted at constant differential pressures. However, under in-situ conditions in the presence of confining pressure, fluid flow may not be achieved until the viscous force overcomes capillary sealing. The capillary sealing can be measured in terms of breakthrough pressure [56] which is the excess pressure of the non-wetting fluid phase at which the wetting phase is displaced enough to create a continuous flow path for the non-wetting phase.

In this work, we experimentally explored the characteristics of gas permeation through three distinctive types of sedimentary cores under varying differential pressure, including silica sand packs, sand-clay cores, and a consolidated sandstone core sample. It was aimed at having a deep insight into the permeation-control mechanisms and when these mechanisms become a dominant factor for the gas flow through different sediments in the absence and presence of gas hydrates. The first two types of core samples would simulate unconsolidated hydrate-free and hydrate-bearing sediments. Addition of clay would also give us more insights regarding the influence of mineralogy and grain size distribution on the gas permeation characteristics. The effect of degree of consolidation and pore size distribution on the gas flow and permeability could also be investigated from the experiments carried on the consolidated sandstone core sample.

7.2 Experimental Section

7.2.1 Materials

Research-grade methane with certified purity of 99.995 vol. % was supplied by BOC Limited. Deionized water was produced by an integral water purification system (ELGA DV 25). Experiments were conducted on three different types of core samples: (i) 100 wt. % silica sand (from Fife, Scotland), (ii) 95 wt.% silica sand + 5 wt.% montmorillonite clay (from Sardinia, Italy), and (iii) a consolidated sandstone core sample (from Elgin, Scotland). The silica sand has a density of 2.64 g/cm^3, particle sizes ranging from 1.2 µm to 600 µm, and a mean diameter of 256.5 µm. The montmorillonite clay has a density of 2.7 g/cm^3, particle sizes ranging from 0.1 to 150 µm, and a mean diameter of 2.1 µm. The consolidated sandstone core sample has a grain density of 2.55 g/cm^3, pore sizes ranging from 0.1 to 300 µm, and a mean pore size of 66.8 µm.

7.2.2 Experimental apparatus

Figure 7.1 shows a schematic representation of the apparatus used for measuring gas permeability. The core holder is made up of a cylindrical high-pressure stainless-steel vessel (maximum working pressure: 34.5 MPa) with 4 and 10.8 cm inner and outer diameters, respectively and a total length of 34 cm. For each end, there is a threaded stainless-steel endcap, having a 1/8 in. diameter hole to serve as a connection for fluid inlet/outlet. The threads allow for the injected gas to be distributed to its entire inflow face and collected from all parts of its outflow face. A Viton rubber sleeve with inner diameter of 4 cm and length of 19.5 cm is also fitted inside the vessel in order to appropriately hold the core samples and make a gas-tight seal on the cylindrical walls of the sample when applying a confining pressure. When placed in the core holder, the sample is connected to the both endcaps. Moreover, there are two ports provided on the body of the core holder, one midway through the length of the vessel to apply desired radial confining pressure and the other, near one end of the vessel to exert axial confining pressure, if needed.

A copper coil is wound around the core holder and connected to a cryostat (Grant LTC) for the cooling fluid circulation. The core holder is then completely immersed in a water bath which is insulated to minimize the heat exchange with the environment. A Quizix pump (SP-5200 Pump System) is also connected to the pressure port at the middle of the cell through valve V7 to inject confining fluid (water) into the confining fluid chamber in order to maintain a constant confining pressure.

For a typical permeability measurement experiment, methane is injected from the source cell into the core sample through the inlet valve V1 and leaves the sample through the outlet valve V3. It should be noted that methane is pre-cooled to the temperature of the system by passing through a 2-meter length of 1/8 in. pipe coil immersed in the water bath before entering the core sample. A back-pressure regulator connected to the exit line maintains the pore pressure of the sample at the set point during permeability measurement. The gas exiting the back-pressure regulator flows into a gas meter to measure the flow rate at reference conditions of temperature and pressure under which the gas flow rate is measured, and then is vented to atmosphere. Two Quartzdyne pressure transducers (QS30K−B, Quartzdyne Inc., USA) with an accuracy of ±0.005 MPa are used to precisely measure the inlet and outlet pressures, respectively. A calibrated platinum-resistance thermometer (Pt100, supplied by TC Ltd.) with an accuracy of better than ± 0.1 K is also attached to the body of the vessel to measure the system temperature. Data from the pressure transducers, the thermometer, and the Quizix pump are acquired by a data acquisition system (DAS) and recorded on a PC with a LabVIEW software interface.

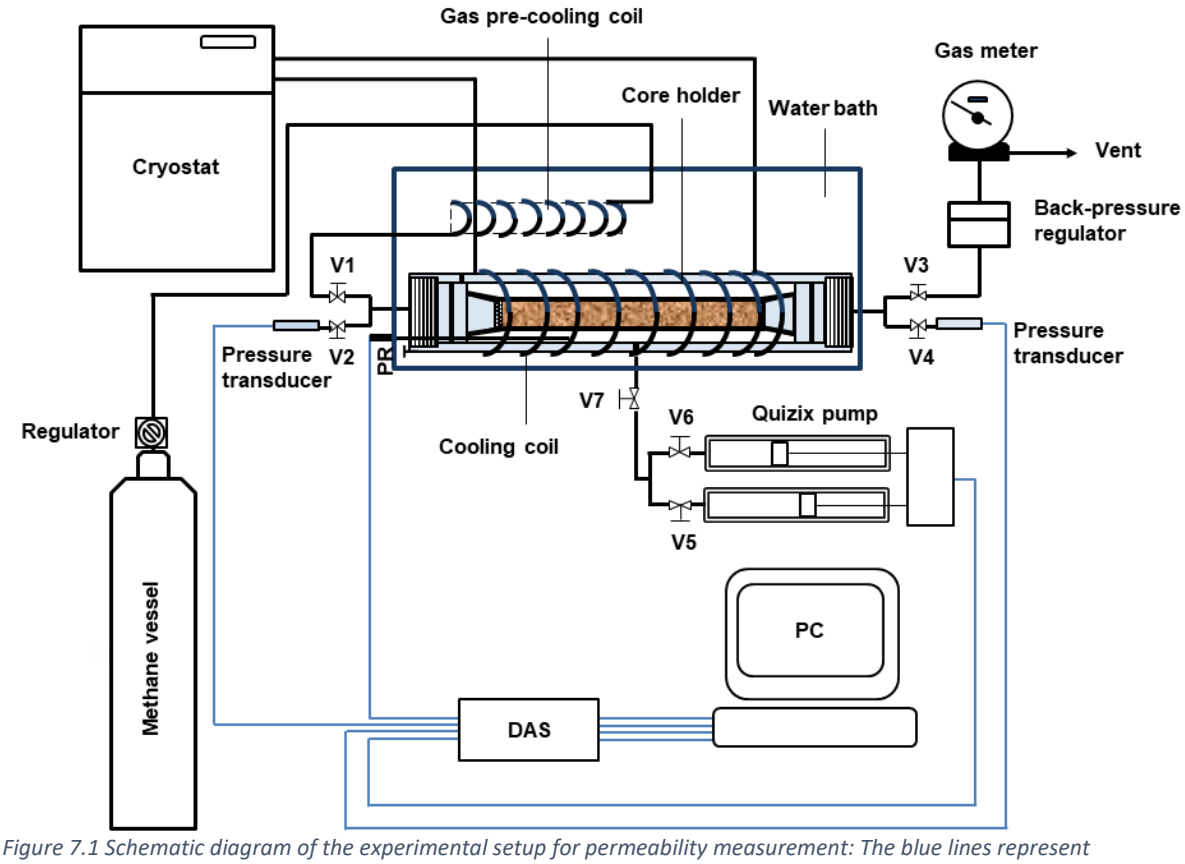

Figure 7.1 Schematic diagram of the experimental setup for permeability measurement: The blue lines represent cables for electrical communications while the black lines represent conduits for the fluid flow.

7.3 Experimental procedure

7.3.1 Hydrate-free core samples

The sediment minerals were firstly dried in an oven at 343 K over 24 hours; then, a given quantity of which (100 wt. % silica sand or 95 wt. % silica sand + 5 wt. % montmorillonite) was thoroughly mixed and wetted with 14.3 wt. % of deionized water to obtain a homogeneous mixture. It should be noted that this is the procedure we follow to make our synthetic test specimens and the micro-textures of the sediment grains were visually examined in our previous works using ESEM to make sure that particles are well mixed [45]. The sample was then loaded into the sleeve in layers, and the desired packing was achieved using a cylindrical pestle rod. The core sample was placed into the vessel and the endcaps were positioned to hold the core sample in place and the vessel was immersed in the water bath and vacuumed.

Both the back-pressure regulator and the pressure regulator on the methane source cell were set to 3.45 MPa while the inlet and outlet valves (V1 and V3, respectively) were fully closed to disconnect the core sample from the gas source. Thereafter, the confining pressure was incrementally applied via the Quizix pump while allowing the gas injection to the core sample (by opening the inlet valve V1) until the pore pressure of the system reached 3.45 MPa and the confining pressure was 6.9 MPa. Throughout the experiments, the confining pressure was maintained at 3.45 MPa higher than the pore pressure of the system to ensure an appropriate sealing around the core sample and prevent bypassing of the gas. The inlet and outlet valves were then fully opened to allow for the gas flow. When steady-state conditions (constant flow rate and inlet/outlet pressures) were achieved, the gas flow rate measured at reference pressure (P_r) and temperature (T_r) together with inlet and outlet pressures were recorded for the calculation of the gas permeability according to Darcy's equation (See Eq.(6)). The permeability measurement was then repeated at different differential pressures by increasing the inlet pressure in steps. It should be noted that throughout the experiments, the inlet pressure was set sufficiently small to (i) permit use of the Darcy's equation for calculation of the gas permeability and (ii) keep water immobile to have only a single phase (gas) flow in the system. After each experiment, three samples were taken from the top, middle, and bottom of silica sand and silica sand-montmorillonite clay core samples and their water content was measured in order to ensure that water was homogeneously distributed and kept immobile during the test.

7.3.2 Hydrate-bearing core samples

The sediment core samples were prepared, packed and loaded to the high-pressure core holder following the similar procedure described in Section 2.3.1. Permeability of hydrate-bearing sediments to gas was measured for a series of methane hydrate saturation. For a typical methane hydrate saturation, while the outlet valve V3 was shut and the confining pressure kept at 3.45 MPa higher than the pore pressure using the Quizix pump, methane was injected into the core sample according to the desired pressure for hydrate formation. The system temperature was then set to 293 K and allowed to equilibrate over 24 hours. When the equilibrium was achieved, the system temperature was set to 273.7 K to initiate the methane hydrate formation. As the pore pressure decreased gradually due to the gas consumption for the hydrate formation, the confining pressure was also adjusted accordingly to maintain the 3.45 MPa pressure difference. This continued until the pressure change became insignificant signifying the completion of the hydrate formation. Upon the completion of the hydrate formation, the back-pressure regulator was set to 3.45 MPa to maintain the constant pore pressure. For pore pressure in excess of 3.45 MPa after the hydrate formation, the excess gas was vented, and for pore pressure less than 3.45 MPa, gas was injected from the methane source cell. This ensured that the pore pressure was well above the methane hydrate equilibrium phase boundary at 273.7 K at which no hydrate dissociation occurred. Afterwards, the inlet pressure was set to 3.45 MPa with the aid of the regulator on the methane source cell. The inlet and outlet valves were then closed to allow the system to attain pressure equilibrium. After the equilibrium was attained, both valves were fully opened for the gas flow through the core sample. When the steady state conditions were achieved, the gas flow rate was measured at P_r and T_r. The inlet and outlet pressures were also recorded for the calculation of the gas permeability according to Darcy's equation. Then, the inlet pressure was increased to measure the core sample permeability to gas at different differential pressures. The differential pressure exerted on the samples were also small enough to allow for use of Darcy's equation while keeping water phase in the system immobile and more importantly preventing hydrate formation/dissociation during the experiments.

7.4 Calculation of the saturations and permeability

The saturations of gas hydrate, water, and gas was calculated based on the real gas equation of state:

$$PV = ZnRT \tag{1}$$

where P, T, and V denote the pore pressure, system temperature, and gas volume, respectively. Z and n are the compressibility factor and the number of moles of methane gas, respectively. R is the gas constant.

The porosity of specimens was determined by gravimetric method:

$$\phi = 1 - \frac{M_s}{V_b \rho_s} \tag{2}$$

where ϕ is the porosity, M_s is the mass of the dry specimen, ρ_s is the average grain density of the sediment (i.e. a sum of the product of the weight fraction and the density of each mineral component), and V_b is the bulk volume of the specimen. After completion of the methane hydrate formation, the saturation of the methane hydrate, water, and gas were calculated using below equations:

$$S_h = \frac{V_h}{V_p} = \frac{\left(\frac{m_{CH_4}}{MW_{CH_4}} - \frac{PV}{ZRT}\right)\left(MW_{CH_4} + MW_w \gamma\right)}{V_p \rho_h} \tag{3}$$

$$S_w = \frac{V_w}{V_p} = \frac{V_{w0} - \left(\frac{m_{CH_4}}{MW_{CH_4}} - \frac{PV}{ZRT}\right)\frac{\gamma MW_w}{\rho_w}}{V_p} \tag{4}$$

$$S_g = 1 - S_h - S_w \tag{5}$$

in which S_h, S_w, and S_g represent hydrate saturation, water saturation, and gas saturation, respectively. V_h and V_p are the methane hydrate volume and pore volume, respectively. MW_{CH4} and MW_w are the molecular weight of methane and water, respectively (MW_{CH4} = 16.04 g/mol and MW_w = 18.01 g/mol) and m_{CH4} is the mass of the injected methane. γ is the hydration number and ρ_h is the bulk density of the methane hydrate ($\gamma \cong 6.0$ and $\rho_h \cong 0.92$ g/cm^3) [3]. V_w and V_{w0} represent the water volume after and prior to the hydrate formation, respectively and ρ_w is the density of water, 1.0 g/cm^3.

The gas permeability was calculated using Darcy's equation [57]:

$$k_g = \frac{2\mu P_r q_r Z_m}{Z_r G_f (P_i^2 - P_o^2)} \tag{6}$$

where k_g is the permeability of the core sample to gas and P_i, P_o, and P_r, stand for inlet pressure, outlet pressure, and the reference pressure at which the flow rate q_r was measured, respectively. Z_r and Z_m are the methane compressibility factor at reference and mean pore pressures, respectively. μ is the gas viscosity and G_f is the geometric factor which for axial flow could be expressed by:

$$G_f = \frac{\pi D^2}{4L} \tag{7}$$

in which L and D are the core length and diameter, respectively.

The permeability of a porous medium to gas depends on the mean free path of the flowing gas due to gas slippage pointed out by Klinkenberg. As presented by Klinkenberg, gas permeability measured at several different mean pore pressures could be extrapolated to infinite mean pore pressure using Eq.(8) to find the Klinkenberg permeability, k_∞, which is equal to the permeability of the medium obtained by a non-reactive fluid [57]:

$$k_g = k_\infty \left(1 + \frac{b}{P_m}\right) \tag{8}$$

where b is the gas slippage factor and P_m is the mean pore pressure expressed by:

$$P_m = \frac{P_i + P_o}{2} \tag{9}$$

According to Eq.(8), it is expected for gas permeability to be linearly proportional with the reciprocal of the mean pore pressure [58]. It should be noted that the difference between the permeability measured by gas becomes higher than that measured by a non-reactive fluid when the medium permeability decreases. Further discussion regarding the gas slippage and Klinkenberg effect can be found elsewhere [57].

7.5 Results and Discussion

As mentioned before, two types of core samples composed of 100 wt. % silica sand and 95 wt. % silica sand + 5 wt. % montmorillonite clay were used to simulate unconsolidated hydrate-free and hydrate-bearing sediments. Addition of 5 wt. % montmorillonite was to enable us to investigate the effect of sediment mineralogy on gas flow. The third series of experiments was conducted on a consolidated sandstone core sample to study the effect of the degree of consolidation and pore size distribution on gas flow and permeability. Table 7.1 summarizes the properties and the initial parameters of the core samples before the permeability measurements.

Table 7.1 Properties and parameters of the sediment core samples

Sedimentary Mineral	Core Sample	Initial Porosity (%)	Saturation (vol. %)		
			S_h	S_g	S_w
100 wt. % Silica sand	1	40.0	0	32.1	67.9
	2	40.3	17.6	42.9	39.5
	3	40.3	22.7	42.5	34.8
	4	40.6	40.3	41.8	17.9
	5	40.3	59.7	39.6	0.7
95 wt. % Silica sand + 5 wt. % Montmorillonite	6	36.2	0	33.6	66.4
	7	36.2	22.9	30.1	47.0
	8	34.5	28.1	23.8	48.1
	9	36.2	35.0	27.5	37.5
Consolidated sandstone	10	18.2	0	45.0	55.0
	11	18.2	15.0	45.0	40.0
	12	18.2	44.0	45.0	11.0

7.5.1 Permeability of silica sand core samples

The sand packs were 155 mm in length and 38.1 mm in diameter. Gas permeability was measured at five different methane hydrate saturations (S_h): 0, 17.6, 22.7, 40.3, and 59.7. The measured permeability values are shown in Figure 7.2.

(A)

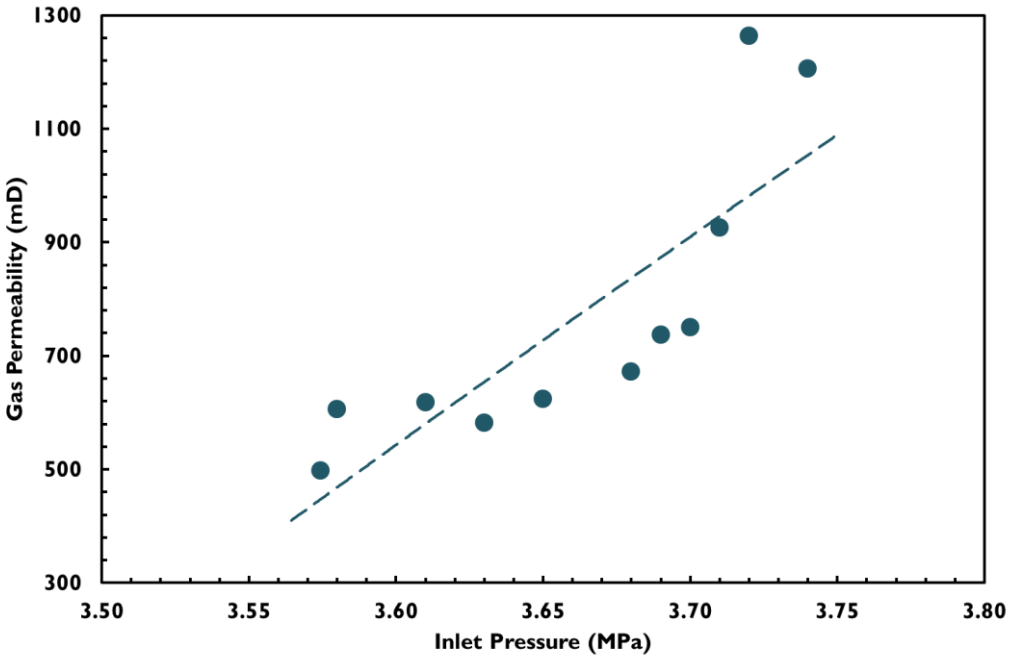

(B)

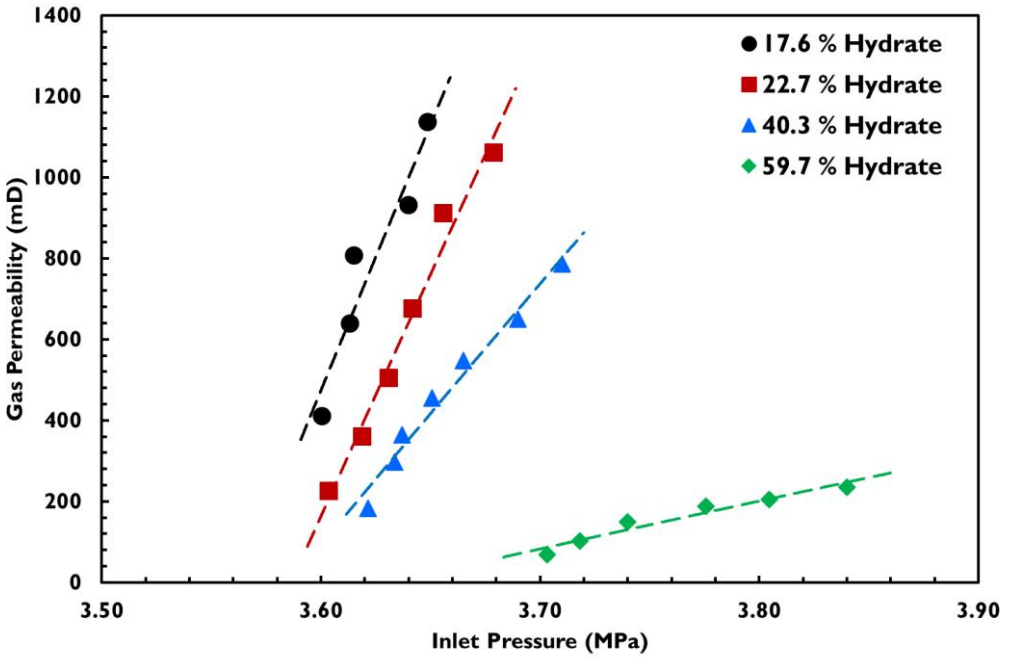

Figure 7.2 Gas permeability of sand packs against the inlet pressure: (A) hydrate-free sand pack, (B) hydrate-bearing sand pack at different saturations of methane hydrate. As shown, the gas permeability behaviour is mainly dominated by the breakthrough capillary pressure

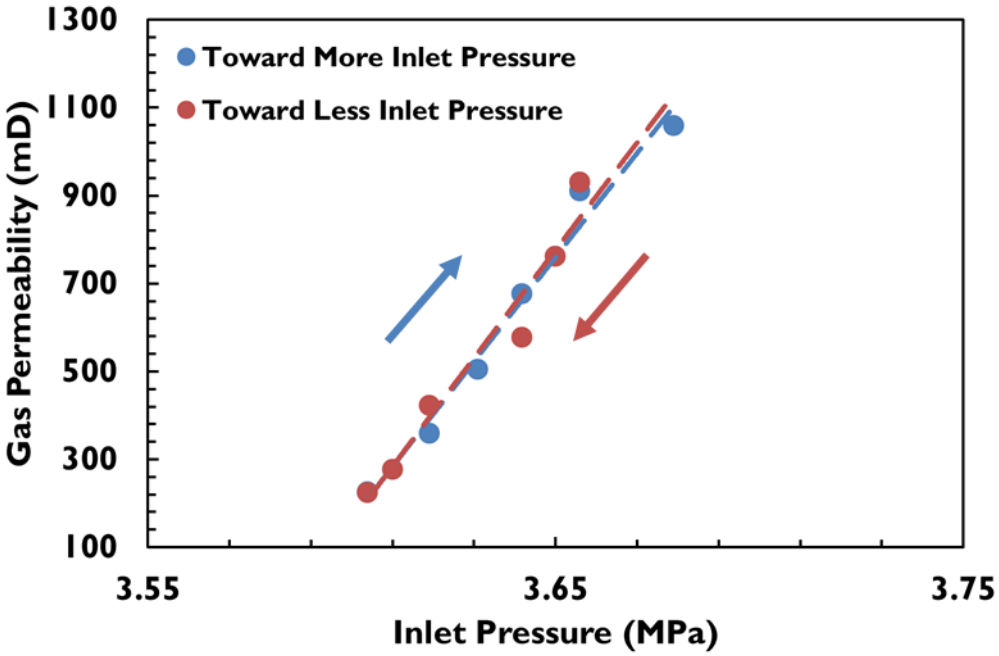

Figure 7.3 Gas permeability of sand packs at 22.7 vol. % methane hydrates saturation taken firstly toward more inlet pressure and then in a reverse manner. Gas permeability trends have an acceptable match with each other confirming no hydrate formation/dissociation and water production during the experiments

In Figure 7.2-(A), the gas permeability for both hydrate-free and hydrate-bearing samples increases with the inlet pressure and accordingly mean pore pressure given that the outlet pressure of the system was maintained at 3.4 MPa, apparently opposite of what would be expected according to Klinkenberg effect (See Eq.(8)). On one hand, the silica sand has coarse grains (average size of 256.5 μm), leading to large intergranular pore spaces in its packs hence the reduced restriction to flow. On the other hand, Klinkenberg effect is expected to be less influential on the gas permeability in high-permeable media. Therefore, the measured gas permeability is weakly affected by Klinkenberg effect. Instead, owing to the dominance of viscous forces over the capillary forces on pathways previously filled with water, particularly those critical narrow ones, more contribution to the gas flow occurs as the inlet pressure hence the differential pressure increase.

As observed in Figure 7.2-(B), since methane hydrate forms in the pores, preferably in the large ones, the restrictions to the fluid flow gradually increases, causing reduction in the permeability of the medium, which its severity strongly depends on the pore-scale growth habits of hydrates. This observation is also corroborated by the differential pressure at gas breakthrough which was 0.151, 0.154 and 0.172 MPa for 17.6, 22.7 and 40.3 % hydrate saturations, respectively; then, at 59.7 %, the differential pressure at gas breakthrough was 0.253 MPa confirming the strong impact of the pore-scale habits of methane hydrate on the permeability of the host sediment. In fact, pore-scale habits

altered from the pore-filling to the cementation at hydrate saturations higher than 50 %, having two main consequences:

1. When more hydrates form in the pore spaces, the size of the remaining pores available for the fluid flow becomes smaller, resulting in a higher capillary sealing hence higher breakthrough pressure to initiate the gas flow. Therefore, one can conclude that the breakthrough capillary pressure plays a dominant role in the permeability of the coarse sand packs.
2. At higher hydrates saturations hence lower water saturations, the sand grains become cemented and consolidated by the hydrates, creating more pore-throats and making channels critically contributing to the gas flow narrower. Therefore, it would result in Klinkenberg effect to be more influential. This is confirmed by changes in the slopes of gas permeability values versus the inlet pressure at different hydrate saturations.

It should be noted that the permeability measurement for 22.7 % methane hydrate saturation was conducted first with increasing the inlet pressure and then in a reverse manner with decreasing the inlet pressure. It can be seen from Figure 7.3 that the permeability profile in both cases follows identical patterns. This repeatability evidently supports our assumption that the pore water in the core sample remained immobile throughout the experiments and its re-distribution does not have measurable effect on the gas permeability, given that a typical gas velocity is less than 5 cm/s. Furthermore, it confirms that the inlet pressure was sufficiently set near HSZ of methane hydrate so that there was no hydrate formation/dissociation, thus the hydrate saturation did not change during permeability measurement.

7.5.2 Permeability of silica sand-montmorillonite clay core samples

In order to investigate the effect of the grain mineralogy and pore size on the gas permeation, 5 wt. % montmorillonite clay was added to the silica sand. The core sample dimensions were the same as those of the silica sand core samples. Gas permeability was measured at four different methane hydrate saturations of 0, 22.9, 28.1, and 35.0 and the results are indicated in Figure 7.4. As can be seen, the medium permeability to the gas is considerably impacted due to the presence of the clay.

As shown in Figure 7.4-(A), the fine grain particles of the clay (with mean grain size of 2.1 μm) could fill in the large pore spaces and form fine pore-dominated sediments. As a consequence, the gas permeation behaviour through the sand-clay core sample is

significantly different from those obtained for the silica sand core sample (See Figure 7.2-(A)). The silica sand has a large particle size hence large intergranular and interconnected pore spaces due to higher resistance to compaction. Thus, the restriction to the gas flow is relatively small and Klinkenberg effect is not influential. However, for the case of the sand-clay sample, fine clay particles play an important role in reducing the pore-throat sizes hence highlighting Klinkenberg effect. This can be simply justified according to the fact that the montmorillonite clay particles in the large pores of the silica sand form fine channels for the gas flow, which become more significant, given that montmorillonite clay could swell greatly after absorbing water because montmorillonite is a strong absorbent of water [59]. In such fine pores, the gas slippage is expected to occur, and the behaviour of the gas permeability becomes mainly dominated by Klinkenberg effect rather than breakthrough capillary pressure. Therefore, it can be seen here that the gas permeability of the sediments decreases as the inlet pressure increases.

Figure 7.4-(B) shows that the presence of methane hydrate significantly changed the gas permeation behaviour in the sand-clay core samples. First of all, the permeability of the hydrate-free sand-clay core sample is up to two orders of magnitude higher than those with methane hydrate. This is simply understood because gas hydrates prefer to form in large pore spaces [60,61], therefore, tend to substantially reduce the pore size, resulting in severe restrictions for the fluid flow [62].

Next, it is interesting to observe that the higher saturations of methane hydrate led to higher gas permeability for the hydrate-bearing sand-clay core samples, which is apparently in contrast with most of the other works reported in literature. Similar observation was also reported by Wu et al. [55]. For the three tests with a certain saturation of hydrate, after most of the limited large pores were blocked by hydrate crystals, furthermore hydrate crystals could act as coarse grains pushing apart the sediment grains hence enlarging the sediment pores [9], a phenomenon known as hydrate-forced heave. This phenomenon led to the increase in the sediment porosity and as a consequence, gas permeability as the hydrate saturation increased [63] by altering the pore structures of the sediments, similar to the clay in soils [64]. Once the hydrate saturation becomes above a critical value, agglomeration could be dominant over pore clogging. The hydrate crystals could aggregate fine clay particles and form inter-aggregation pores (macro pores) that are considerably larger than the inter-particle pores (micro pores) [65]. If the above assumptions are true, it could be anticipated that there should be a critical hydrate saturation for a specific porous medium according to its grain types and size distribution.

When the hydrate saturation is smaller than it, hydrate formation will significantly reduce the permeability by clogging pores; once the hydrate saturation becomes higher than that, hydrate-forced heave or aggregating will dominate the effect on permeability. This anticipation could also be validated through comparing the gas permeability behaviour of the hydrate-bearing sand-clay core samples with those of silica sand samples (See Figure 7.2-(B)). However, further investigation is required in this regard.

The third particularity is the non-monotonous change of the gas permeability against the inlet pressure. The gas permeability increased initially, then gradually decreased after reaching a maximum value as the inlet pressure increased. This observation may be attributed to two underlying processes. The first possible reason could be hydrate-forced heave, as discussed before; the growth of hydrate crystals may slightly push apart sediment grains, enlarging channels for the gas flow, in which the capillary sealing plays an important role in the permeability. At the beginning, increase in the inlet pressure broke through more enlarged capillary pores, therefore, leading to increase in the gas permeability. As can also be seen in Figure 7.4-(B), the breakthrough capillary pressure is lower for the sand-clay core sample with higher methane hydrate saturation. This is agreeable with the previous discussion that higher saturation of methane hydrate resulted in severe effect of hydrate-forced heave on the pores of the sand-clay core samples, whilst the presence of methane hydrate resulted in contrary effect on the breakthrough capillary pressure of the sand cores. Moreover, the capillary breakthrough process created more change in the permeability for the core sample with more methane hydrate, further supporting the hydrate-forced heave assumption. The maximum values are 0.27, 0.62, and 1.79 mD for 22.9, 28.1, and 35.0 % hydrate saturations, respectively. Beyond the maximum point, a majority of the large pores that had been created by hydrate-forced heave were already broken through; therefore, the gas flow is no longer capillary dominated but the viscous dominated. Thus, gas slippage occurred and Klinkenberg effect became significant, leading to gradual decrease in the measured permeability as the inlet pressure increased further.

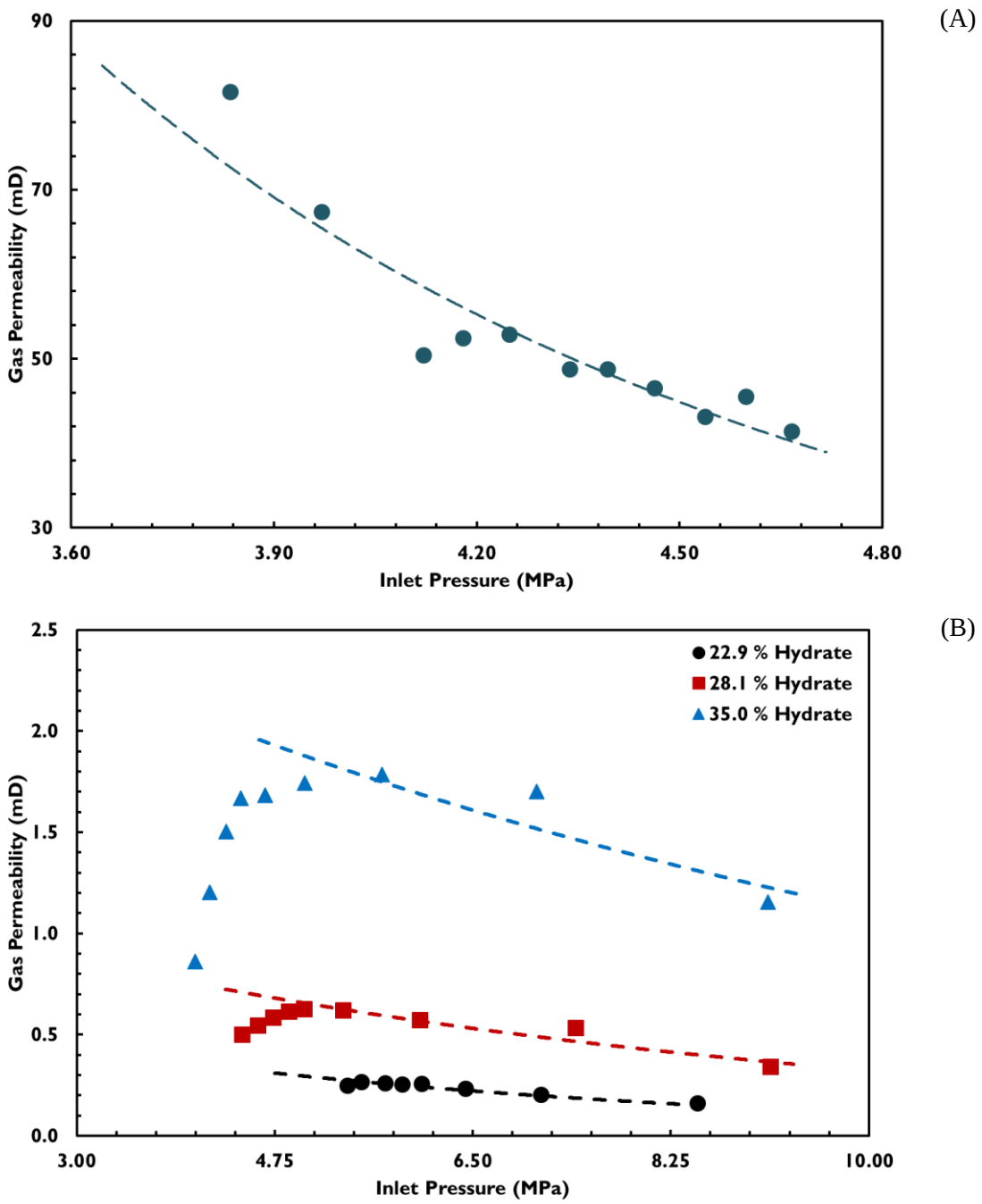

Figure 7.4 Gas permeability of sand-clay core sample against the inlet pressure: (A) hydrate-free sample, (B) hydrate-bearing sample at different saturations of methane hydrate

7.5.3 Permeability of consolidated sandstone core sample

Permeability of a consolidated sandstone core sample to gas was also measured to investigate how the presence of gas hydrates affect the gas permeation characteristics through well-consolidated porous media where the mineralogical grains are immobile compared with two previous cases studies. The sandstone core sample was made in dimensions similar to the unconsolidated cores to be able to fit in the same rubber sleeve, 155 mm in length and 38.1 mm in diameter.

Figure 7.5 shows the measured gas permeability of the sandstone core sample for both hydrate-free and hydrate-bearing cases. As observed in Figure 7.5-(A), the gas permeability increases with increasing the inlet pressure, similar to that observed for the unconsolidated silica sand core sample in Figure 7.2-(A). This means the pores of the sandstone core sample were large enough that the capillary breakthrough dominated the gas slippage phenomenon. However, the orders of magnitude of the measured permeability are different, which can be simply understood by having a look at the porosity values, given the permeability and porosity of a medium are generally proportional to each other.

As indicated in Figure 7.5-(B), the presence of methane hydrate resulted in the gas permeability to be severely reduced. Moreover, since the sandstone core sample was well-consolidated, no hydrate-forced heave occurred. Therefore, in contrast to the observations for the sand-clay samples, the higher the hydrate saturation, the lower the porous medium permeability to methane. It can also be seen that the presence of methane hydrate altered the response of the gas permeability to the pressure change, i.e. the permeability decreased with increasing the inlet pressure, then approaching a relative constant value as the inlet pressure continuously increased. This could be attributed to the fact that the methane hydrate crystals preferably occupied the large pores, either fully blocking the large pores or partially clogging them and forming fine throat channels. As observed in Figure 7.5-(B), much higher inlet pressure was required to be able to break through the capillary pressure in the hydrate-bearing cases than that in the absence of hydrate, evidently supporting the assumption that formation of methane hydrate transformed the large pores into fine channels for the gas flow where the collision of methane gas molecules with the pore walls could result in the gas slippage to occur and consequently Klinkenberg effect to be dominant.

The gas permeability measurement for the 15.0 % hydrates saturation was carried out first with increasing the inlet pressure and then in a reverse manner to check the repeatability of the experimental results. As brought in Figure 7.6, the measurements were repeatable, confirming that the re-distribution of the pore water had no significant influence on the permeability under the experimental conditions.

(A)

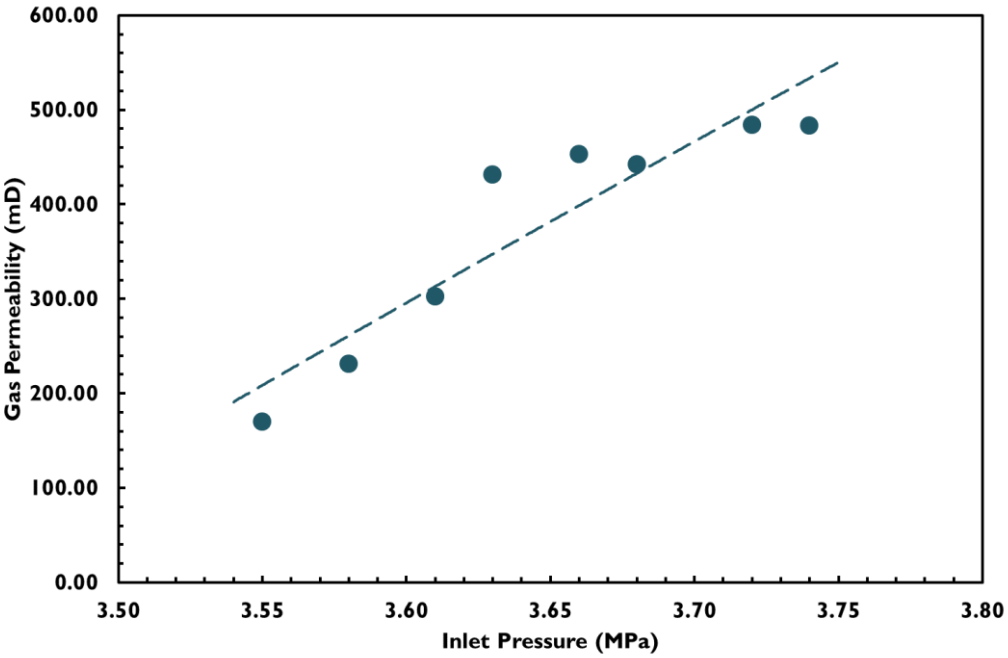

(B)

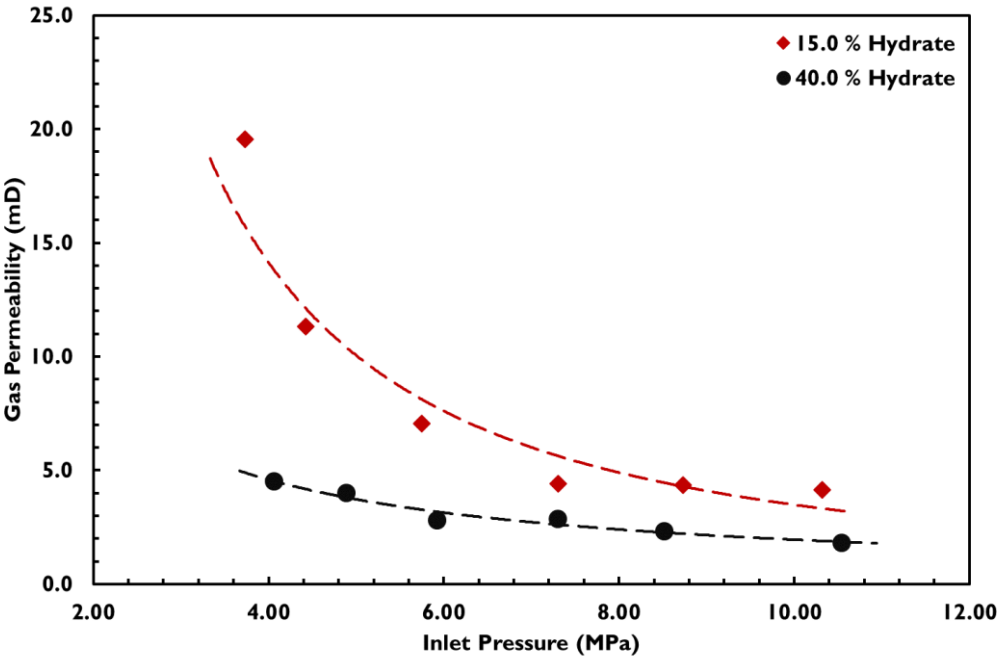

Figure 7.5 Gas permeability of consolidated core sample against the inlet pressure: (A) hydrate-free sample, (B) hydrate-bearing sample at different saturations of methane hydrate

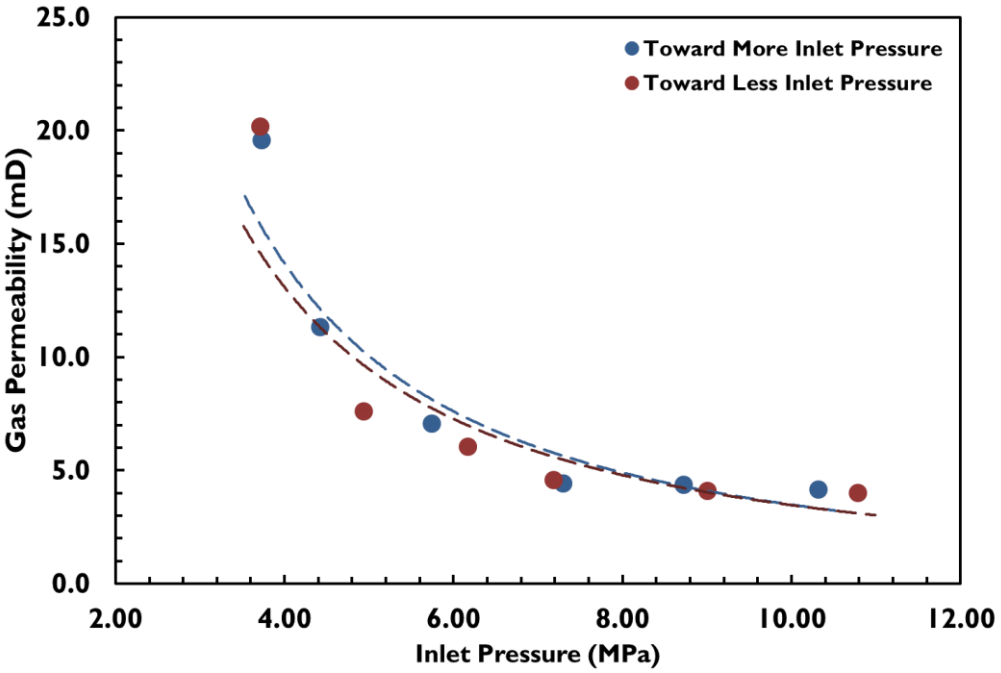

Figure 7.6 Gas permeability of consolidated core sample at 15.0 vol. % methane hydrates saturation taken firstly toward more inlet pressure and then in a reverse manner

7.6 References

(1) Sloan, E. D. Fundamental Principles and Applications of Natural Gas Hydrates. *Nature* **2003**, *426* (6964), 353–359. DOI: 10.1038/nature02135.

(2) Mehrabian, H.; Bellucci, M. A.; Walsh, M. R.; Trout, B. L. Effect of Salt on Antiagglomerant Surface Adsorption in Natural Gas Hydrates. *J. Phys. Chem. C* **2018**, *122* (24), 12839–12849. DOI: 10.1021/acs.jpcc.8b03154.

(3) Sloan, E. D.; Koh, C. A. *Clathrate Hydrates of Natural Gases - Chemical Industries/119*; CRC press, 2008.

(4) Kvenvolden, K. A. C. N.-G. 0.-2910. Methane Hydrate - a Major Reservoir of Carbon in the Shallow Geosphere. *Chem. Geol.* **1988**, *71* (1–3), 41–51.

(5) Collett, T. S. Potential of Gas Hydrates Outlined. *Oil Gas J.* **1992**, *90* (25), 84–87.

(6) Max, M. D.; Johnson, A. H. *Exploration and Production of Oceanic Natural Gas Hydrate*; Springer, 2016. DOI: 10.1007/978-3-319-43385-1.

(7) Hassanpouryouzband, A.; Yang, J.; Tohidi, B.; Chuvilin, E.; Istomin, V.; Bukhanov, B.; Cheremisin, A. CO2 Capture by Injection of Flue Gas or CO2-N2 Mixtures into Hydrate Reservoirs: Dependence of CO2 Capture Efficiency on Gas Hydrate Reservoir Conditions. *Environ. Sci. Technol.* **2018**, *52* (7), 4324–4330. DOI: 10.1021/acs.est.7b05784.

(8) Holder, G.; Kamath, V.; Godbole, S. THE POTENTIAL OF NATURAL GAS HYDRATES AS AN Energy Source. *Annu. Rev. Energy* **1984**, *9* (November), 427–445.

(9) Waite, W. F.; Santamarina, J. C.; Cortes, D. D.; Dugan, B.; Espinoza, D. N.; Germaine, J.; Jang, J.; Jung, J. W.; Kneafsey, T. J.; Shin, H. Physical Properties of Hydrate-bearing Sediments. *Rev. Geophys.* **2009**, *47* (4).

(10) Castaldi, M. J.; Zhou, Y.; Yegulalp, T. M. Down-Hole Combustion Method for Gas Production from Methane Hydrates. *J. Pet. Sci. Eng.* **2007**, *56* (1–3), 176–185. DOI: 10.1016/j.petrol.2006.03.031.

(11) Fitzgerald, G. C.; Castaldi, M. J. Thermal Stimulation Based Methane Production from Hydrate Bearing Quartz Sediment. *Ind. Eng. Chem. Res.* **2013**, *52* (19), 6571–6581. DOI: 10.1021/ie400025f.

(12) Linga, P.; Haligva, C.; Nam, S. C.; Ripmeester, J. A.; Englezos, P. Recovery of Methane from Hydrate Formed in a Variable Volume Bed of Silica Sand Particles. *Energy and Fuels* **2009**, *23* (11), 5508–5516. DOI: 10.1021/ef900543v.

(13) Linga, P.; Haligva, C.; Nam, S. C.; Ripmeester, J. A.; Englezos, P. Gas Hydrate Formation in a Variable Volume Bed of Silica Sand Particles. *Energy and Fuels* **2009**, *23* (11), 5496–5507. DOI: 10.1021/ef900542m.

(14) Elistratov, S. L.; Misyura, S. Y.; Manakov, A. Y.; Shubnikov, A. E.; Nakoryakov, V. E. Combustion of Methane Hydrates. *J. Eng. Thermophys.* **2013**, *22* (2), 87–92. DOI: 10.1134/s181023281302001x.

(15) Schicks, J. M.; Spangenberg, E.; Giese, R.; MLuzi-Helbin, M.; Priegnitz, M.; Beeskow-Strauch, B. A Counter-Current Heat-Exchange Reactor for the Thermal Stimulation of Hydrate-Bearing Sediments. *Energies* **2013**, *6* (6), 3002–3016. DOI: 10.3390/en6063002.

(16) Falser, S.; Uchida, S.; Palmer, A. C.; Soga, K.; Tan, T. S. Increased Gas Production from Hydrates by Combining Depressurization with Heating of the Wellbore. *Energy and Fuels* **2012**, *26* (10), 6259–6267. DOI: 10.1021/ef3010652.

(17) Li, B.; Li, X. Sen; Li, G.; Feng, J. C.; Wang, Y. Depressurization Induced Gas Production from Hydrate Deposits with Low Gas Saturation in a Pilot-Scale Hydrate Simulator. *Appl. Energy* **2014**, *129*, 274–286. DOI: 10.1016/j.apenergy.2014.05.018.

(18) Loh, M.; Too, J. L.; Falser, S.; Linga, P.; Khoo, B. C.; Palmer, A. Gas Production from Methane Hydrates in a Dual Wellbore System. *Energy and Fuels* **2015**, *29* (1), 35–42. DOI: 10.1021/ef501769r.
(19) Yamaguchi, T.; Miyazaki, K.; Zyvoloski, G.; Komai, T.; Tenma, N.; Sakamoto, Y. Laboratory-Scale Experiments of the Methane Hydrate Dissociation Process in a Porous Media and Numerical Study for the Estimation of Permeability in Methane Hydrate Reservoir. *J. Thermodyn.* **2010**, *2010*, 1–13. DOI: 10.1155/2010/452326.
(20) Nakano, S.; Sangawa, H.; Matsubara, T.; Ohgaki, K.; Takano, K. Methane Exploitation by Carbon Dioxide from Gas Hydrates. Phase Equilibria for CO2-CH4 Mixed Hydrate System. *J. Chem. Eng. Japan* **2005**, *29* (3), 478–483. DOI: 10.1252/jcej.29.478.
(21) Masuda, Y.; Maruta, H.; Naganawa, S.; Amikawa, K.; Nagao, J.; Hironori, H.; Konno, Y. Methane Recovery from Hydrate-Bearing Sediments by N2–CO2 Gas Mixture Injection: Experimental Investigation on CO2–CH4 Exchange Ratio. In *Proceedings of the 7th International Conference on Gas Hydrates, Edinburgh, Scotland, United Kingdom*; 2011.
(22) Martin, K. L.; Howard, J.; Silpngarmlert, S.; Schoderbek, D.; Hester, K. North Slope Hydrate Fieldtrial: CO2/CH4 Exchange. In *OTC Arctic Technology Conference*; Offshore Technology Conference, 2012. DOI: 10.4043/23725-ms.
(23) Kang, H.; Koh, D. Y.; Lee, H. Nondestructive Natural Gas Hydrate Recovery Driven by Air and Carbon Dioxide. *Sci. Rep.* **2014**, *4*, 1–8. DOI: 10.1038/srep06616.
(24) Kang, H.; Koh, D.; Kim, D.; Park, J.; Cha, M.; Lee, H. Recovery of Methane Intercalated in Natural Gas Hydrate Sediments Using a Carbon Dioxide and Flue Gas Mixture. In *Isope*; International Society of Offshore and Polar Engineers, 2012; Vol. 4, pp 67–71.
(25) Yang, J.; Hassanpouryouzband, A.; Chuvilin, E.; Tohidi, B.; Istomin, V.; Bukhanov, B.; Joonaki, E. A Novel Method for CO2 Storage and Methane Recovery in Gas Hydrate Reservoirs through Injection of Flue Gas From Coal-Fired Power Plants. In *79th EAGE Conference and Exhibition 2017*; 2017. DOI: 10.3997/2214-4609.201700788.
(26) Hassanpouryouzband, A.; Yang, J.; Tohidi, B.; Chuvilin, E.; Istomin, V.; Bukhanov, B.; Cheremisin, A. Insights into CO2 Capture by Flue Gas Hydrate Formation: Gas Composition Evolution in Systems Containing Gas Hydrates and Gas Mixtures at Stable Pressures. *ACS Sustain. Chem. Eng.* **2018**, *6* (5), 5732–5736. DOI: 10.1021/acssuschemeng.8b00409.
(27) Okwananke, A.; Yang, J.; Tohidi, B.; Chuvilin, E.; Istomin, V.; Bukhanov, B.; Cheremisin, A. Enhanced Depressurisation for Methane Recovery from Gas Hydrate Reservoirs by Injection of Compressed Air and Nitrogen. *J. Chem. Thermodyn.* **2018**, *117*, 138–146. DOI: 10.1016/j.jct.2017.09.028.
(28) Hassanpouryouzband, A.; Farahani, M. V.; Yang, J.; Tohidi, B.; Chuvilin, E.; Istomin, V.; Bukhanov, B. Solubility of Flue Gas or Carbon Dioxide-Nitrogen Gas Mixtures in Water and Aqueous Solutions of Salts: Experimental Measurement and Thermodynamic Modeling. *Ind. Eng. Chem. Res.* **2019**, *58* (8), 3377–3394. DOI: 10.1021/acs.iecr.8b04352.
(29) Istomin, V.; Tohidi, B.; Bukhanov, B.; Okwananke, A.; Maerle, K.; Yang, J.; Cheremisin, A.; Chuvilin, E. Flue Gas Injection into Gas Hydrate Reservoirs for Methane Recovery and Carbon Dioxide Sequestration. *Energy Convers. Manag.* **2017**, *136*, 431–438. DOI: 10.1016/j.enconman.2017.01.043.
(30) Hassanpouryouzband, A.; Yang, J.; Tohidi, B.; Chuvilin, E. M.; Istomin, V.; Bukhanov, B. A. Geological CO2 Capture and Storage with Flue Gas Hydrate

Formation in Frozen and Unfrozen Sediments: Method Development, Real Time-Scale Kinetic Characteristics, Efficiency, and Clathrate Structural Transition. *ACS Sustain. Chem. Eng.* **2019**. DOI: 10.1021/acssuschemeng.8b06374.

(31) Wang, X.-H.; Sun, Y.-F.; Wang, Y.-F.; Li, N.; Sun, C.-Y.; Chen, G.-J.; Liu, B.; Yang, L.-Y. Gas Production from Hydrates by CH4-CO2/H2 Replacement. *Appl. Energy* **2017**, *188*, 305–314.

(32) Sun, Y.-F.; Zhong, J.-R.; Li, R.; Zhu, T.; Cao, X.-Y.; Chen, G.-J.; Wang, X.-H.; Yang, L.-Y.; Sun, C.-Y. Natural Gas Hydrate Exploitation by CO 2/H 2 Continuous Injection-Production Mode. *Appl. Energy* **2018**, *226*, 10–21.

(33) Fu, W.; Wang, Z.; Sun, B.; Chen, L. A Mass Transfer Model for Hydrate Formation in Bubbly Flow Considering Bubble-Bubble Interactions and Bubble-Hydrate Particle Interactions. *Int. J. Heat Mass Transf.* **2018**, *127*, 611–621.

(34) Fu, W.; Wang, Z.; Sun, B.; Ji, C.; Zhang, J. Multiple Controlling Factors for Methane Hydrate Formation in Water-Continuous System. *Int. J. Heat Mass Transf.* **2019**, *131*, 757–771.

(35) Moridis, G. J.; Kowalsky, M. B.; Pruess, K. TOUGH + HYDRTE v1 . 2 a Code for the Simulation of System b Ehavior in h Ydrate-Bearing Geologic Media. *Berkeley, CA* **2014**, 264.

(36) Nimblett, J.; Ruppel, C. Permeability Evolution during the Formation of Gas Hydrates in Marine Sediments. *J. Geophys. Res. Solid Earth* **2003**, *108* (B9). DOI: 10.1029/2001jb001650.

(37) Kleinberg, R. L.; Brewer, P. G.; Yesinowski, J. P.; Peltzer, E. T.; Flaum, C.; Griffin, D. D.; Malby, G. E. Deep Sea NMR: Methane Hydrate Growth Habit in Porous Media and Its Relationship to Hydraulic Permeability, Deposit Accumulation, and Submarine Slope Stability. *J. Geophys. Res. Solid Earth* **2003**, *108* (B10). DOI: 10.1029/2003jb002389.

(38) Daigle, H. Relative Permeability to Water or Gas in the Presence of Hydrates in Porous Media from Critical Path Analysis. *J. Pet. Sci. Eng.* **2016**, *146*, 526–535.

(39) Kneafsey, T. J.; Seol, Y.; Gupta, A.; Tomutsa, L. Permeability of Laboratory-Formed Methane-Hydrate-Bearing Sand: Measurements and Observations Using X-Ray Computed Tomography. *SPE J.* **2011**, *16(01)*, 78–94.

(40) Dickens, G. R.; O'Neil, J. R.; Rea, D. K.; Owen, R. M. Dissociation of Oceanic Methane Hydrate as a Cause of the Carbon Isotope Excursion at the End of the Paleocene. *Paleoceanography* **1995**, *10* (6), 965–971. DOI: 10.1029/95PA02087.

(41) Yang, J.; Tohidi, B.; Chapoy, A. Impact of Sedimentary Mineralogy on the Geophysical and Geomechanical Properties of Hydrate-Bearing Sediments. In *Sixth International Conference on Gas Hydrates, Sponsor, Vancouver, BC, Canada*; 2008; pp 6–10.

(42) Long, D.; Lovell, M. A.; Rees, J. G.; Rochelle, C. A. Sediment-Hosted Gas Hydrates: New Insights on Natural and Synthetic Systems. *Geol. Soc. London, Spec. Publ.* **2009**, *319* (1), 1–9.

(43) Choi, J.; Dai, S.; Cha, J.; Seol, Y. Laboratory Formation of Noncementing Hydrates in Sandy Sediments. *Geochemistry, Geophys. Geosystems* **2014**, *15* (4), 1648–1656.

(44) Spangenberg, E.; Kulenkampff, J.; Naumann, R.; Erzinger, J. Pore Space Hydrate Formation in a Glass Bead Sample from Methane Dissolved in Water. *Geophys. Res. Lett.* **2005**, *32* (24), 1–4. DOI: 10.1029/2005GL024107.

(45) Yang, J.; Hassanpouryouzband, A.; Tohidi, B.; Chuvilin, E.; Bukhanov, B.; Istomin, V.; Cheremisin, A. Gas Hydrates in Permafrost: Distinctive Effect of Gas Hydrates and Ice on the Geomechanical Properties of Simulated Hydrate-Bearing Permafrost Sediments. *J. Geophys. Res. Solid Earth* **2019**.

(46) Kumar, A.; Maini, B.; P.R. Bishnoi; Clarke, M.; Zatsepina, O.; Srinivasan, S.

Experimental Determination of Permeability in the Presence of Hydrates and Its Effect on the Dissociation Characteristics of Gas Hydrates in Porous Media. *J. Pet. Sci. Eng.* **2010**, *70* (1–2), 114–122. DOI: 10.1016/j.petrol.2009.10.005.

(47) Delli, M. L.; Grozic, J. L. H. Experimental Determination of Permeability of Porous Media in the Presence of Gas Hydrates. *J. Pet. Sci. Eng.* **2014**, *120*, 1–9. DOI: 10.1016/j.petrol.2014.05.011.

(48) Richards, L. A. *Physics of Flow through Porous Media*; University Of Toronto Press: London, 2010; Vol. 22. DOI: 10.2136/sssaj1958.03615995002200020033x.

(49) Li, G.; Wu, D. M.; Li, X. Sen; Lv, Q. N.; Li, C.; Zhang, Y. Experimental Measurement and Mathematical Model of Permeability with Methane Hydrate in Quartz Sands. *Appl. Energy* **2017**, *202*, 282–292. DOI: 10.1016/j.apenergy.2017.05.147.

(50) Wang, J.-Q.; Zhao, J.-F.; Yang, M.-J.; Li, Y.-H.; Liu, W.-G.; Song, Y.-C. Permeability of Laboratory-Formed Porous Media Containing Methane Hydrate: Observations Using X-Ray Computed Tomography and Simulations with Pore Network Models. *Fuel* **2015**, *145*, 170–179.

(51) Wang, J.; Zhao, J.; Zhang, Y.; Wang, D.; Li, Y.; Song, Y. Analysis of the Influence of Wettability on Permeability in Hydrate-Bearing Porous Media Using Pore Network Models Combined with Computed Tomography. *J. Nat. Gas Sci. Eng.* **2015**, *26*, 1372–1379.

(52) Wang, J.; Zhao, J.; Zhang, Y.; Wang, D.; Li, Y.; Song, Y. Analysis of the Effect of Particle Size on Permeability in Hydrate-Bearing Porous Media Using Pore Network Models Combined with CT. *Fuel* **2016**, *163*, 34–40.

(53) Wang, J.; Zhang, L.; Zhao, J.; Ai, L.; Yang, L. Variations in Permeability along with Interfacial Tension in Hydrate-Bearing Porous Media. *J. Nat. Gas Sci. Eng.* **2018**, *51*, 141–146. DOI: 10.1016/j.jngse.2017.12.029.

(54) Chen, X.; Verma, R.; Espinoza, D. N.; Prodanović, M. Pore-Scale Determination of Gas Relative Permeability in Hydrate-Bearing Sediments Using X-Ray Computed Micro-Tomography and Lattice Boltzmann Method. *Water Resour. Res.* **2018**, *54* (1), 600–608.

(55) Lv, Q.; Zhao, J.; Song, Y.; Li, Y.; Wu, Z.; Ling, Z.; Liu, W. Experimental Study on the Gas Phase Permeability of Methane Hydrate-Bearing Clayey Sediments. *J. Nat. Gas Sci. Eng.* **2016**, *36*, 378–384. DOI: 10.1016/j.jngse.2016.10.055.

(56) Smith, J. D.; Chatzis, I.; Ioannidis, M. A. A New Technique to Measure the Breakthrough Capillary Pressure. *J. Can. Pet. Technol.* **2005**, *44* (11), 25–31. DOI: 10.2118/05-11-01.

(57) American Petroleum Institute. Recommended Practices for Core Analysis Section 1- Planning a Coring Program. *API Recomm. Pract. 40* **1998**, No. February.

(58) Klinkenberg, L. J. The Permeability of Porous Media to Liquids and Gases. In *SOCAR Proceedings*; American Petroleum Institute, 2012; Vol. 2012, pp 57–73. DOI: 10.5510/OGP20120200114.

(59) Aksu, I.; Bazilevskaya, E.; Karpyn, Z. T. Swelling of Clay Minerals in Unconsolidated Porous Media and Its Impact on Permeability. *GeoResJ* **2015**, *7*, 1–13. DOI: 10.1016/j.grj.2015.02.003.

(60) Biderkab, A. B.; Burgass, R. W.; Tohidi, B.; Clennell, M. Ben; Anderson, R. Visual Observation of Gas-Hydrate Formation and Dissociation in Synthetic Porous Media by Means of Glass Micromodels. *Geology* **2002**, *29* (9), 867. DOI: 10.1130/0091-7613(2001)029<0867:vooghf>2.0.co;2.

(61) Priest, J. A.; Rees, E. V. L.; Clayton, C. R. I. Influence of Gas Hydrate Morphology on the Seismic Velocities of Sands. *J. Geophys. Res. Solid Earth*

2009, *114* (11), B11205. DOI: 10.1029/2009JB006284.
(62) Ikeda, I.; Narita, H.; Komai, T.; Sakamoto, Y.; Miyazaki, K.; Takahara, N.; Nishikawa, Y.; Minagawa, H. Relation Between Permeability and Pore-Size Distribution of Methane-Hydrate-Bearing Sediments. In *Offshore Technology Conference*; Offshore Technology Conference, 2008. DOI: 10.4043/19305-ms.
(63) Cook, A. E.; Goldberg, D.; Kleinberg, R. L. Fracture-Controlled Gas Hydrate Systems in the Northern Gulf of Mexico. *Mar. Pet. Geol.* **2008**, *25* (9), 932–941. DOI: 10.1016/j.marpetgeo.2008.01.013.
(64) Barden, L.; Madedor, A. O.; Sides, G. R. The Flow of Air and Water in Partly Saturated Clay Soil. In *Developments in Soil Science*; Elsevier, 1972; Vol. 2, pp 299–311. DOI: 10.1016/S0166-2481(08)70548-8.
(65) Zdravkov, B. D.; Čermák, J. J.; Šefara, M.; Janků, J. Pore Classification in the Characterization of Porous Materials: A Perspective. *Cent. Eur. J. Chem.* **2007**, *5* (2), 385–395. DOI: 10.2478/s11532-007-0017-9.

Chapter 8- Gas Hydrates in Permafrost: Distinctive Effect of Gas Hydrates and Ice on the Geomechanical Properties of Simulated Hydrate-Bearing Permafrost Sediments

8.1 Introduction

Very large volumes of methane hydrate have been found in permafrost regions in the Arctic, for example in the West Siberian basin[1–3], the Mackenzie Delta of Canadian Arctic[4,5], and the Northern Alaska [6,7]. It is estimated that about 5×10^2 to 1.2×10^6 Tcf of methane hydrates are buried in the permafrost regions in the Arctic[8]. Burning methane gas produced from methane hydrate releases up to 5 times less carbon dioxide compared to burning coal[9]. Therefore, gas hydrate is considered to be a potential low-carbon energy resource for the near future [5,10–13].

Gas hydrate is a type of ice-like crystalline solid with physical properties similar to those of ice. Gas hydrate can decompose and release the gas molecules bonded in the hydrate lattice if either the temperature or pressure is outside the hydrate stability zone (HSZ)[14]. Based on this principle, several methods have been developed to produce methane or natural gas from gas hydrate deposits, such as depressurization, thermal stimulation, inhibitor injection [12]and carbon dioxide (CO_2) replacement[15]. In practice, the CO_2 replacement method recovers methane using CO_2-CH_4 (methane) molecule exchange by injection of CO_2-N_2 (nitrogen) mixtures or flue gas into gas hydrate deposits[16–19]. Drilling through permafrost layers could cause wellbore instability[20]. Gas hydrates in permafrost are extremely sensitive to thermal influences due to global warming, seasonal change, geothermal fluxes, and human activities. Rising temperatures could result in hydrate decomposition hence changes in the mechanical and thermal properties of frozen hydrate-bearing sediments, creating serious geologic hazards that are responsible for methane gas blowout[21,22], sliding of seafloor and permafrost-under-laid continental slopes[23,24].

In past decades, extensive experimental investigations have been carried out to investigate how gas hydrates influence the geomechanical strength of sediments hence the slope stability of both onshore and offshore permafrost. Winter at al.[25] determined the mechanical strength and geophysical properties of gas hydrate-bearing sediment samples that were taken from the JAPEX/JNOC/GSC Mallik 2L-38 gas hydrate research well using a purpose-built gas hydrate and sediment test laboratory instrument. For simplicity,

some workers examined the mechanical properties of sediments containing tetrahydrofuran (THF) hydrate instead of methane or natural gas hydrates[26–28]. Experimental results generated using triaxial testing systems as well as direct shear apparatuses showed the mechanical properties and deformation behavior of gas hydrate-bearing sediments[29–33]. Small-strain mechanical properties of hydrate-bearing sediments such as sand, silt, and clay were investigated using resonant column apparatus[34] and bender-element devices[35]. In general, the studies showed that the presence of hydrates leads to higher stiffness, shear strength and smaller pre-failure dilation. Three physical contact models proposed by Dvorkin et al.[36] have been widely applied to describe the effect of hydrates, including pore filling, load bearing, and cementation. Moreover, apart from the mineralogical composition of sediments, initial distribution of water in pores, for example, dissolved water, partially saturated water or water from melting ice grains is known to be one of the key factors altering gas hydrate behaviour in sediments[27,37,38].

In permafrost both ice and gas hydrates may exist together. The crystal structure of ice (i.e., Ih) and clathrate gas hydrate consists of water molecules that are hydrogen-bonded in solid lattices. Water is frozen to form ice by rearrangement of water molecules into hexagonal structures at subzero temperature, whilst at low temperature and elevated pressure conditions water molecules form a network of cage-like structures (clathrate lattices) by enclosing suitably sized ‘guest’ molecules such as methane, ethane, propane and CO_2. Hydrate particles can float in pore water, bear load between sediment grains or cement sediment grains, in comparison, ice crystals always tend to stick to sediment grains. The coexistence of ice and gas hydrate plays a substantial role in the geological structure hence stabilization of both onshore and offshore permafrost. Although the mechanical and rheological properties of frozen soils have been thoroughly investigated[39–41], little work on gas hydrate-bearing frozen sediments has been reported in literature, therefore, there is lack of fundamental knowledge of unique characteristics of the ice-hydrate-bearing sediments compared to solely frozen soils or hydrate-bearing unfrozen sediments.

In recent years, mechanical properties have been investigated using a triaxial system for synthetic sediments containing both ice and hydrates of carbon dioxide or methane hydrate, and in simulated hydrate decomposition scenarios[42,43] investigated the mechanical behaviours of so-called permafrost-associated methane hydrate-bearing sediments under different recovering techniques. All these triaxial tests used mixtures of

hydrate particles, ice powders, and clay (kaolinite) grains. As a result, their specimens were compacted packs of the three solid particles, lacking cohesion and cementation of ice and hydrate to the sediment grains, leading to the determined deviatoric stress and shear strength being significantly lower than other measurements[44]. In this work, a new experimental method was developed to synthesize gas hydrate-bearing frozen sediments. Following the established experimental procedures, the effect of gas hydrate and ice on the geomechanical properties of simulated permafrost sediments was compared, by triaxial compression tests on frozen and unfrozen sediments in the absence and presence of methane hydrate using a purpose-built triaxial testing system. The aim was to gain a better understanding of how water freezing and hydrate bearing differently influence the geomechanical properties of hydrate-bearing permafrost.

8.2 Method

Triaxial shearing was carried out to determine the shearing strength and deformation behavior of artificial sediments at different conditions: at 273.4 K (unfrozen hydrate-free), at 263.1 K (frozen hydrate-free), at 273.4 K with about 25 vol% methane hydrate (unfrozen hydrate-bearing), and at 263.1 K with about 25 vol% methane hydrate (frozen hydrate-bearing). At each condition three similar specimens were sheared under three different effective confining pressures, respectively, i.e., 0.5, 1.0, and 1.5 MPa in order to determine cohesion and internal friction angle. During loading the pore pressure was maintained at 5.0 MPa to simulate permeable geological formations under a lithostatic pressure of about several hundred meters underneath ground or seafloor where permafrost is present.

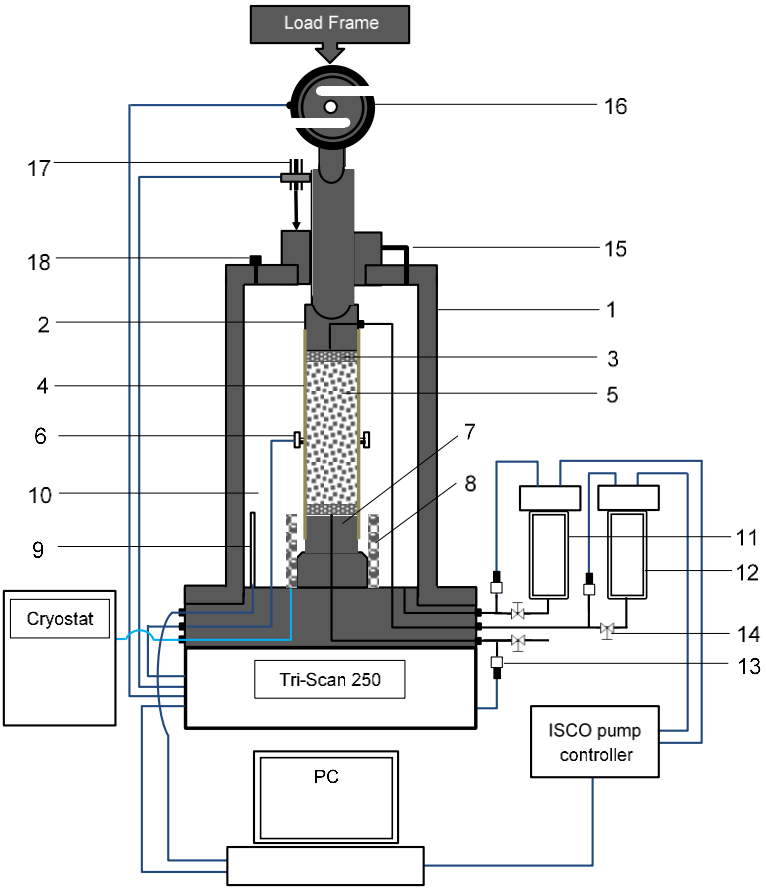

Figure 8.1 Schematic of the Tri-Scan 250 triaxial testing system1-cell body, 2-top cap, 3-porous disk, 4-rubber membrane, 5-specimen, 6-radial displacement transducer, 7- base pedestal, 8-cooling coil, 9-PRT probe, 10-confining fluid, 11-ISCO pump-A (cell pressure controller), 12-ISCO pump-B (back pressure or pore pressure controller), 13-pore pressure transducer, 14-volve, 15-blanced ram assembly, 16-load cell, 17-axial LVDT, 18-air bleed bolt

8.2.1 Triaxial testing system

A triaxial testing system (Tri-Scan 250 from VJ Tech Ltd) was used in this work. It can work at temperatures from -253 to 323 K and pressures up to 40 MPa to simulate the geological and thermodynamic conditions in sediments containing gas hydrates. The triaxial system consists of a high-pressure cell, a load frame (250 kN), a dual-ISCO pump pressure controller (D260), both axial and radial displacement transducers (not installed in this work), a multi-channel data acquisition module. Triaxial tests are controlled by a commercial testing software (Clisp Studio). A cooling coil is installed around the base pedestal and is connected to a cryostat (Julabo FP50) to achieve the required temperature. The system temperature is measured by a platinum resistance temperature (PRT) probe that is mounted beside the test specimen. The pore water pressure (PWP) is measured by a VJ Tech pressure transducer and the back pressure (BP) and confining pressure are measured individually by the dual ISCO pump pressure transducers. The load and axial

shearing rate are measured by a load cell of the Tri-Scan 250 and a linear variable differential transmitter (LVDT), respectively. A built-in balanced ram is used to compensate the cell pressure on the ram. Figure 8.1 is a schematic diagram of the triaxial testing system.

8.2.2 Specimens

Synthetic sediments composed of 75 wt% silica sand, 20 wt% silt and 5 wt% bentonite clay were used to simulate typical loamy sand in permafrost. The silica sand was from Fife, Scotland and the silt was made by grinding the silica sand. The grain density of the sand was 2.64 g/cm^3. The bentonite clay was originally from Jembel, Turkmenistan and its grain density was 2.7 g/cm^3. Table 8.1 shows the mineralogical composition of the sand and clay. Figure 8.2 shows the particle size distribution of the sand, silt, clay and the synthetic sediment. A Malvern laser diffraction particle size analyzer (MS1000) was used to analyze the particle size of the sand and silt, while the particle size of the bentonite clay was determined by analysis of ESEM (environmental scanning electron microscope, PHILIPS XL30) images of the dry bentonite clay. The mean size and specific area are 257 μm and 0.059 m^2/cm^3 for the sand, 8.9 μm and 2.3 m^2/cm^3 for the silt, 34.6 μm and 0.71 m^2/cm^3 for the clay, respectively. The micro textures of the sediment grains were visually examined using the same ESEM. Figure 8.3 shows the ESEM images of the sand, silt, clay and the sediment of 75% sand + 20% silt + 5% bentonite. The sand grains are round granular particles and some of them have micro fractures, the silt grains become angular fine particles, the clay grains consist of loose and micro "plate-shaped" particles. The sediment is a mixture of the sand, silt and clay, showing complex characteristics under the ESEM. The test specimens were made of the synthetic sediment partially saturated with a water content of around 15.5 wt% to dry sediments and manually compacted in a rubber membrane sleeve of about 50 mm in diameter and 100 mm in length. Manual compaction resulted in a porosity of around 32%.

Table 8.1 Mineralogical composition of the silica sand/silt and clay

Silica sand	Component	Quartz	Microcline	Calcite	Kaolinite
	Ratio (wt%)	97	3	trace	trace
Bentonite clay	Component	Montmorillonite	Andesine	Biotite	Calcite
	Ratio (wt%)	93.4	2.9	2.9	0.8

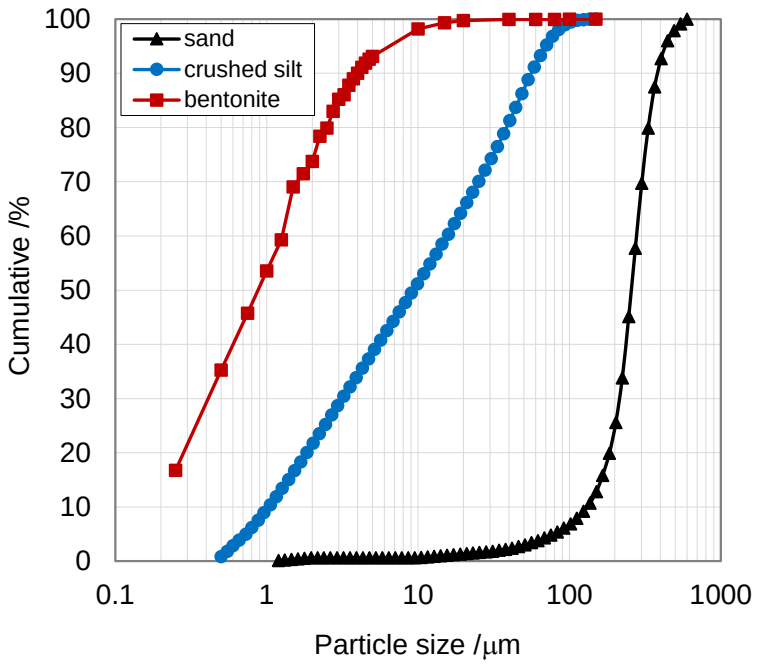

Figure 8.2 Particle size distribution of the silica sand, artificial silt, and bentonite clay

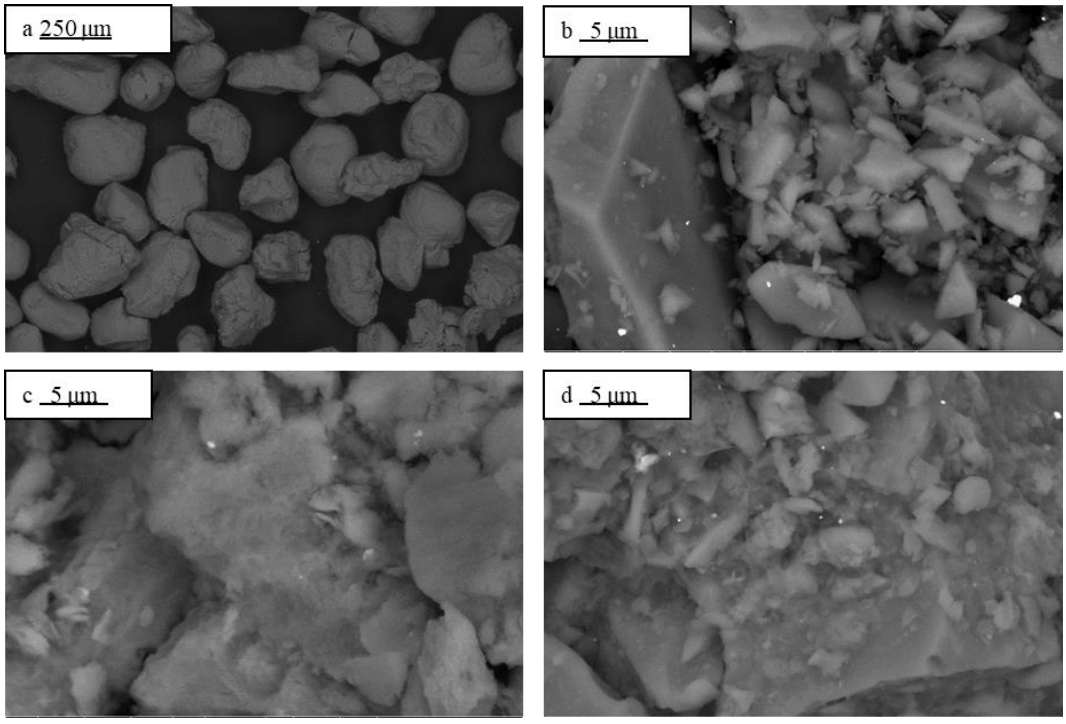

Figures 3 ESEM images of the sediment grains: (a) sand; (b) silt; (c) bentonite clay; (d) synthetic sediment.

8.2.3 Procedures

A wet specimen was installed and vacuum was applied to remove air present in the pores of the specimen. An effective confining pressure of 0.5 MPa was applied by injecting aqueous monoethylene glycol (MEG) solution using an ISCO pump (Pump-A in Figure 8.1). Then the specimen was consolidated under a load of 0.5 MPa for 1 to 2 hours until

the axial creep strain rate of the specimen became smaller than 5.6×10^{-8} 1/S (i.e., axial creep less than 0.01 mm in half an hour). Methane was injected into the pre-consolidated specimen until the pore pressure reached 15 MPa at room temperature, while the confining pressure was increased simultaneously to maintain a constant effective confining pressure of around 0.5 MPa. The methane-pressurized specimen was directly cooled down to a target temperature just above 273.1 K to form hydrate. During cooling and hydrate formation, the confining pressure was adjusted to maintain the confining pressure around 0.5 MPa above the pore pressure. After completion of hydrate formation which was indicated by a constant pore pressure, the effective confining pressure was adjusted to the desired value, for example, 0.5, or 1.0, or 1.5 MPa, and the cell temperature was set to the shearing temperature, 273.4 K for unfrozen specimens and 263.1 K for frozen specimens. After freezing, the pore pressure was gradually reduced to, and maintained at 5 MPa by connecting to a piston vessel in which the pressure was controlled by another ISCO pump (Pump-B in Figure 8.1). The system was left at the desired temperature, pore pressure, and confining pressure over night to allow the system to settle at the shearing conditions.

The porosity (ϕ) of the specimen was determined based on the known grain density of sediments and the dimensions of specimens:

$$\phi = 1 - \frac{M}{V_t \rho_s} \tag{1}$$

where M is the mass of the dry specimen, ρ_s is the average grain density of the sediment (i.e., a sum of the product of the weight ratio and the density of each mineral component), $V_t = \pi R^2 H$ is the bulk volume of the specimen, where R and H are the radius and height of the specimen, respectively. Methane hydrate saturation (S_h) was calculated using Equation 2:

$$S_h = \frac{V_h}{V_p} = \left(\left(\frac{M_{CH4}}{M_g} - \frac{PV}{ZRT}\right)(M_g + M_w\gamma)\right)/(V_p\rho_h) \tag{2}$$

where V_h and V_p are the methane hydrate volume and pore volume, respectively. M_g and M_w are the molecular weight of methane and water, respectively. M_{CH4} is the mass of the injected methane. P, T, and V represent the pore pressure, temperature, and gas volume. Z is the compressibility factor of methane gas and R is gas constant. γ is hydration number and ρ_h is the bulk density of gas hydrate. For methane hydrate, $M_g = 16$, $M_w = 18$, $\gamma \cong 6.0$, $\rho_h \cong 0.92$ g/cm^3. After hydrate formation the water saturation (S_w) and gas saturation (S_g) were calculated:

$$S_w = \frac{V_w}{V_p} = (V_{w0} - (\frac{M_{CH4}}{M_g} - \frac{PV}{ZRT})\frac{\gamma M_w}{\rho_w}) / V_p \quad (3)$$

And

$$S_g = \frac{V_g}{V_p} = 1 - S_h - S_w \quad (4)$$

where V_w and V_{w0} represent the water volume after and before hydrate formation, respectively; ρ_w is the density of water, i.e., 1 g/cm^3. In this work it was assumed water was completely frozen at 263.1 K, therefore, ice saturation was calculated using the water saturation divided by the ice density (approximately 0.92 g/cm^3).

8.3 Results and Discussion

It has been reported that frozen hydrate-bearing sediments appear to have a much lower permeability compared to unfrozen ones in the absence of gas hydrate[45,46]. Consequently, the shearing rate was set at 0.1%/min mainly to prevent any excess pressure in the pores during compression, giving enough time to allow pore pressure changes to equalise throughout the specimen[47]. Furthermore, a strain rate of 0.1%/min was commonly applied to shear sediment specimens containing gas hydrates by other workers[30,31,42,43]. Table 8.2 shows the initial parameters of the specimens before shearing. It should be noted that the unfrozen water content at 263.1 K was estimated less than 3% in the specimens based on Istomin et al.[48], therefore, this was neglected in the calculated ice saturation in Table 8.2.

Table 8.2 Initial physical parameters of specimens before shearing

Initial specimen parameters	Tests		
Unfrozen and hydrate-free	Test 1-0.5	Test 1-1.0	Test 1-1.5
Water ratio (wt%) (vol%)	15.2 (81.2)	15.3 (85.5)	15.3 (90.2)
Hydrate saturation (vol%)	0.0	0.0	0.0
Gas saturation (vol%)	18.8 (N_2)	14.5 (N_2)	9.8 (N_2)
Water saturation (vol%)	81.2	85.5	90.2
Frozen and hydrate-free	Test 2-0.5	Test 2-1.0	Test 2-1.5
Water ratio (wt%) (vol%)	15.5 (86.7)	15.5 (84.9)	15.5 (83.0)
Hydrate saturation (vol%)	0.0	0.0	0.0
Gas saturation (vol%)	13.3 (N_2)	15.1 (N_2)	17.0 (N_2)
Ice saturation (vol%)	86.7	84.9	83.0
Unfrozen and hydrate-bearing	Test 3-0.5	Test 3-1.0	Test 3-1.5
Water ratio (wt%) (vol%)	15.5 (86.3)	15.5 (86.4)	15.5 (86.7)
Hydrate saturation (vol%)	25.5	24.3	27.9
Gas saturation (vol%)	8.6	8.8	7.7
Water saturation (vol%)	65.9	66.9	64.4
Frozen and hydrate-bearing	Test 4-0.5	Test 4-1.0	Test 4-1.5
Water ratio (wt%) (vol%)	15.6 (85.4)	15.5 (85.2)	15.5 (86.8)
Hydrate saturation (vol%)	21.1	22.4	23.6
Gas saturation (vol%)	10.4	10.4	8.5
Ice saturation (vol%)	68.5	67.2	67.9

8.3.1 Shear characteristics

Unfrozen hydrate-free Figure 8.4 shows the logged evolution of the deviator stress with the axial strain. In Test 1 at 273.4 K in the absence of methane hydrate, the unfrozen hydrate-free specimen behaved like typical soils under 0.5 MPa of effective confining pressure. When loading started, the deviator stress almost vertically increased to 0.7, 0.5, 0.7 MPa under a confining pressure of 0.5, 1.0, and 1.5 MPa, respectively, and then the sand-silt-bentonite clay grains were compacted so that the deviator stress gradually increased. Similar stress-strain behavior was also observed by other workers[49,50]. The maximum deviator stress resulted in a collapse of the compacted sediment grains, leading to relatively open structure like micro fractures and the grains were forced to move downward into the void spaces. The grain compaction and downward movement were relatively slow processes, which is corresponding to the slow and long strain softening process after the peak strength was reached. Under the higher effective confining pressure of 1.0 and 1.5 MPa, the specimens were further compacted thus appearing as dense soils. By comparison with the specimen under 0.5 MPa of confining pressure, the deviator stress increased relatively steeply and fell off once the maximum deviator stress was reached, which could be attributed to the fact that the sediment grains along the shearing plane

rode over each other. It should be noted that two events happened to the specimen under 1.0 MPa of confining pressure (the blue round points in Test 1). The discontinuity just before the peak stress in the deviator stress-axial strain curve was due to a brief pause of the shearing process to solve a mechanical problem. Next, the sharp drop in the deviator stress resulted from breakage of the rubber membrane.

Frozen hydrate-free For the hydrate-free specimens frozen at 263.1 K (Test 2), the initial cohesiveness increased to 2.0 MPa for the three effective confining pressures. The deviator stress vertically rose to about 2.0 MPa at the beginning of shearing. This suggests that the ice cemented the sediment grains against the initially applied loading. Gradual strain hardening started following that, which is similar to that observed in the unfrozen hydrate-free sediments in Test 1. By contrast, with the unfrozen specimens at 273.6 K, sharp strain softening occurred once the failure point was reached. At the end of shearing (at an axial strain of 13.5%, 26.0%, and 28.2% under 0.5, 1.0, and 1.5 MPa, respectively), somewhat brittle characteristic of the specimens frozen at 263.1 K was observed. As shown in Table 8.2, ice filled about 85% of the pore volume after freezing. We interpret the brittle-like failure resulting from the breakage of crystalline ice structures in the specimens.

Unfrozen hydrate-bearing In Test 3 with the unfrozen specimens containing about 22 vol% of methane hydrate at 273.4 K, the gradual compression started at about 1 MPa, a little higher than those of the unfrozen hydrate-free specimens in Test 1 and half of the frozen hydrate-free specimens in Test 2. The deviator stress steeply rose to higher than 1 MPa during the initial compression, which was similar to that observed in the hydrate-free specimens frozen at 263.1 K. This could be evidence that methane hydrate did cement the sediment grains to some extent. Then the deviator stress linearly increased as the axial strain increased. After the deviator stress reached a peak, strain softening started. No brittle failure points appeared. These characteristics are in contrast to those observed for the unfrozen hydrate-free sediments at 273.4 K and the frozen hydrate-free sediments at 263.1 K. The result may suggest that the presence of about 22% methane hydrate not only strengthened the sediment but also made the unfrozen sediment more ductile compared to the brittle-like failure of the frozen sediments in the absence of methane hydrate. After the peak stress the deviator stress fluctuated in a small range, which could be an indication that hydrate crystals became detached from the sediment grains or resisted grains riding over each other[27]. It should be noted that the difference in the gas

saturation (Table 8.2) might also be a factor contributing to the strengthening effect observed in Test 2 (freezing) and Test 3 (hydrate bearing), although the ice saturation in Test 2 is much higher than that of methane hydrate in Test 3.

Frozen and hydrate-bearing In comparison with the Tests 1-3, the specimens with methane hydrate of 21.1 to 23.6% and frozen at 263.1 K showed that the gradual compression did not start until the deviator stress reached 2 MPa, which is similar to those measured in Test 2. This suggests that ice enhanced cohesiveness more than these saturations of methane hydrate did. Apart from the highest peak shear stress, brittle-like failure occurred in the frozen hydrate-bearing specimens. Given that brittle-like failure was also observed for the frozen hydrate-free specimens in Test 2, the presence of a low saturation of methane hydrate did not alter the brittle-like failure of the frozen specimens[41]. Furthermore, the stress-strain curves of the frozen hydrate-bearing sediments look smoother than the others. This could be related to the fact that the specimens had the lowest void after methane hydrate formation and freezing. This indicates that the high porosity filling of ice and hydrate led to smaller void spaces for the sediment grains to move downwards during compression.

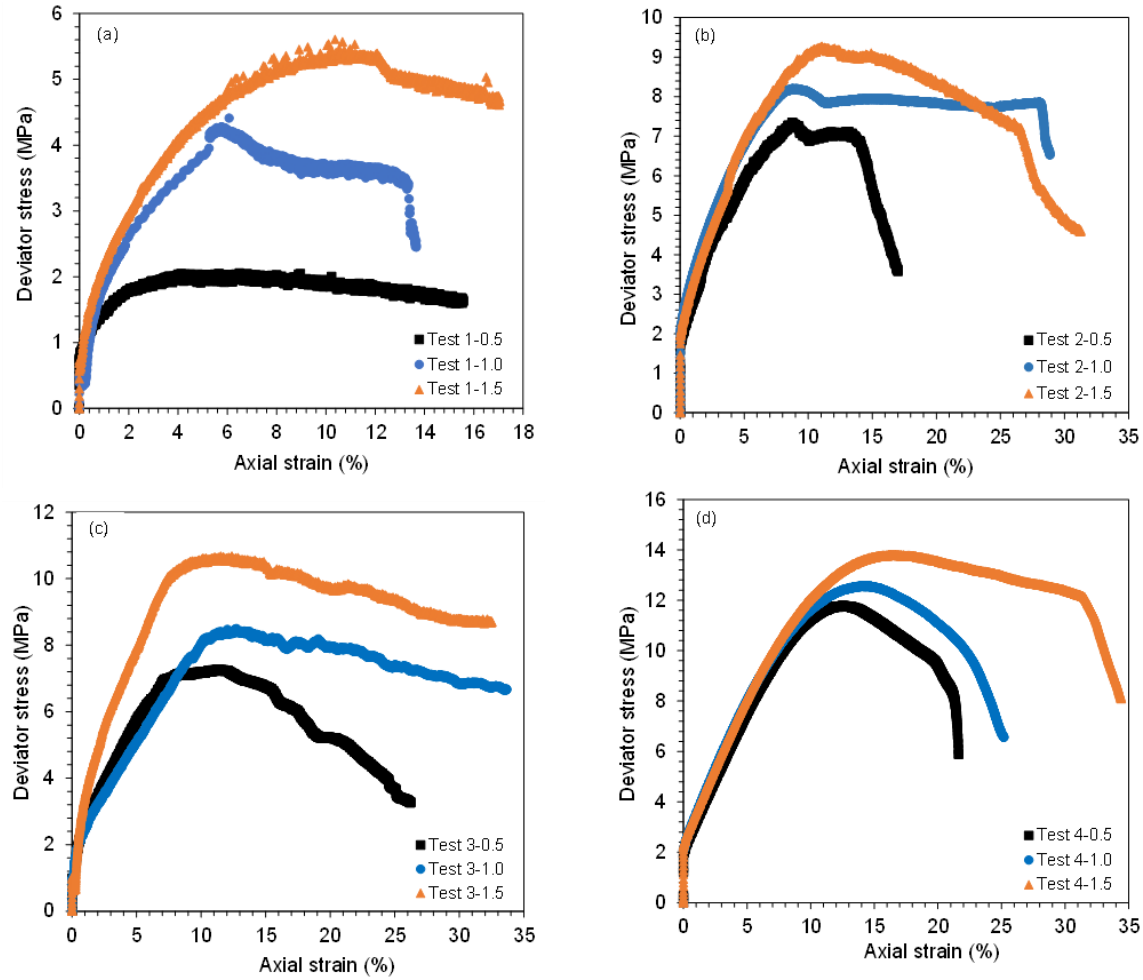

Figure 8.4 Shear characteristics of unfrozen and frozen sediments in the absence and presence of methane hydrate. (a) Test 1: hydrate-free at 273.4 K, (b) Test 2: hydrate-free and frozen at 263.1 K, (c) Test 3 with methane hydrate at 273.4 K, and (d) Test 4 with methane hydrate frozen at 263.1 K. In the legend the numbers "0.5, 1.0, 1.5" denote the effective confining pressures in MPa.

8.3.2 Deformation behavior

Volume strain was measured to reflect the deformation behavior of the sediments during shearing. The ISCO Pump-B was connected to a piston vessel that was full of methane (not shown in Figure 8.1). The outlet of the methane gas vessel was connected to the PWP port and the backpressure port of the triaxial cell. Changes in the specimen pore volume can be measured by the ISCO Pump-B set at the desired pore pressure. Given that the sediment grains are incompressible under the experimental pressure, the changes in the bulk volume of a specimen should be equal to the changes in the pore volume of the specimen. Expansion of a specimen in volume is called dilation, corresponding to a negative volume strain and compression in volume means a positive volume strain. Figure 8.5 illustrates the determined cumulative volume strain versus axial strain.

Unfrozen hydrate-free In Test 1, under 0.5 MPa of confining pressure, the initial volume strain of zero indicates the unfrozen hydrate-free specimen experienced a little lateral expansion, which was balanced by the axial compression at a rate of 0.1 mm/min. Then continuous dilatation occurred while axial compression proceeded. Given that the pore pressure was maintained at 5 MPa, it could be expected that fine fractures or voids were formed due to the sediment grains riding over each other, leading to lateral expansion. When the confining pressure was at 1.0 MPa, the measured volumetric strain was zero until the membrane was broken at 13.5% of axial strain. (The membrane breakage led to a vertical rise of the volumetric strain-axial strain curve). This suggests that the specimen had been experiencing a literal dilatation that was consistently equal to the axial compression. Under 1.5 MPa of confining pressure, the specimen showed larger compression and then the specimen volume remained constant after a quick compression at about 2% of axial strain, i.e., it laterally dilated at a rate at which it was axially compressed. Quick dilatation occurred at about 12% of axial strain where the peak deviator stress was reached (Figure 8.4). The higher the confining pressure, the smaller the dilatation, because the confining stress tends to hold the sediment grains together by increasing the inter-particle forces such as internal friction force and interlock force against the lateral expansion.

Frozen hydrate-free For the hydrate-free sediments, freezing at 263.1 Ksignificantly reduced the dilatation of the specimens during shearing. This is attributed to the fact that ice crystals cemented the sediment grains and filled more void spaces than the original water did. The specimens quickly collapsed once the failure stress was reached, which is indicated by the sharp falling of the volumetric strain-axial strain curves.

Unfrozen hydrate-bearing At 273.4 K, the specimens whose void spaces were filled with about 22 vol% methane hydrate slightly dilated in radial direction while compressed in its length. Continuous large dilatation did not start until the failure deviator stress was reached. After the failure points, large dilatation gradually occurred and no sudden dilatation was observed throughout shearing. By comparison with the unfrozen hydrate-free sediments in Test 1 and the frozen hydrate-free sediments in Test 2, it could be said that the presence of about 22 vol% methane hydrate enhanced the shear strength as much as the sediments frozen at 263.1 Kand made the unfrozen hydrate-bearing sediments less brittle than those hydrate-free sediments frozen at 263.1 K. However, the low saturation

of methane hydrate could not hinder lateral expansion as freezing at 263.1 Kdid. Increase in confining pressure led to significant reduction in dilatation.

Frozen hydrate-bearing In Test 4 the specimens were formed with an average saturation of about 22 vol% and frozen at 263.1 K. The presence of both methane hydrate and ice further limited lateral expansion and delayed the occurrence of quick dilatation compared to the frozen and hydrate-free specimens in Test 2 and the unfrozen hydrate-bearing specimens in Test 3.

Similar characteristics of volumetric strain were observed for frozen soils by Zhang et al.[51]. However, some particulars of the observed deformation behavior are different from other frozen soils[52]. This could be attributed to the fact that there is no literature reporting triaxial compression experiments that are really comparable with this work: specific synthetic loamy sand sediments sheared at constant pore pressure and in the presence of water, gas, ice, and methane hydrate in pores.

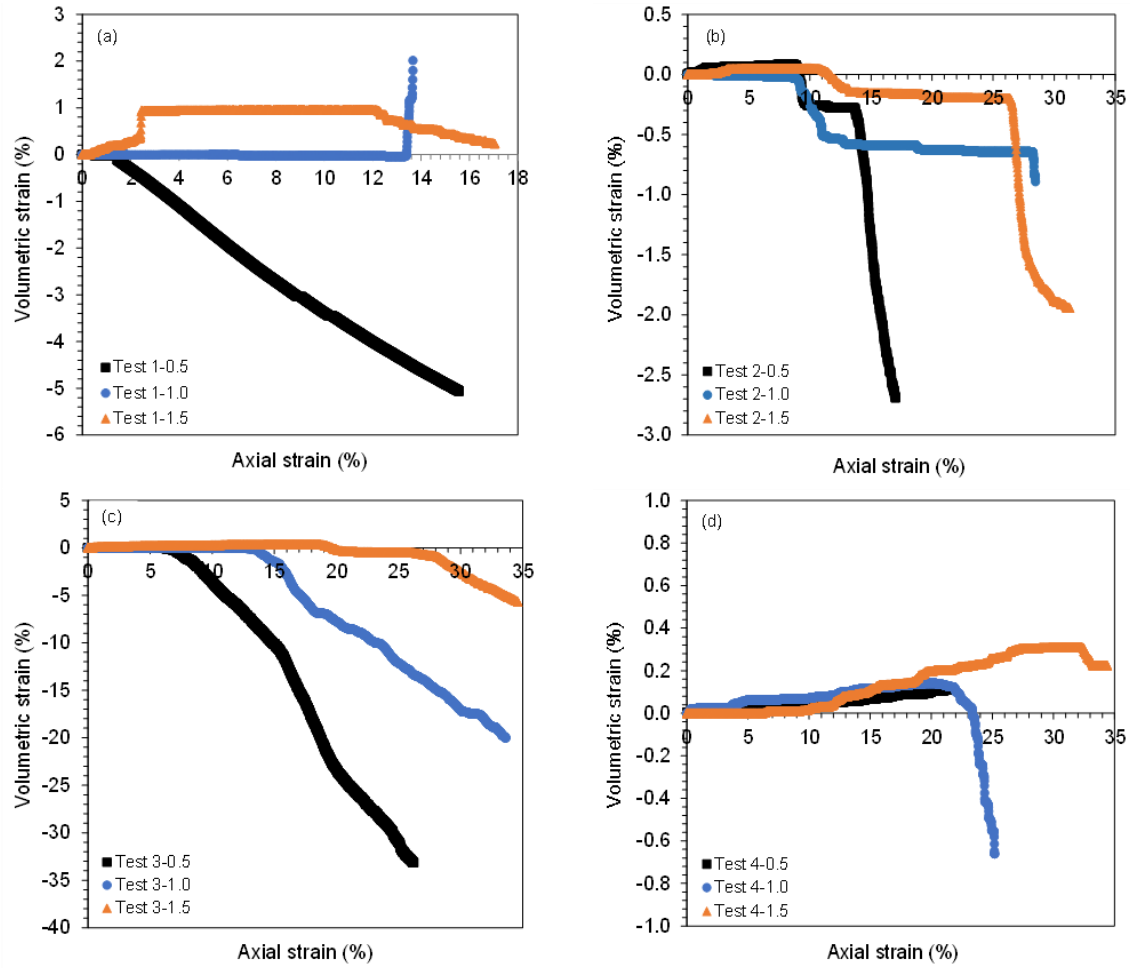

Figure 8.5 Deformation behavior of unfrozen and frozen sediments in the absence and presence of methane hydrate. (a) Test 1: hydrate-free at 273.4 K, (b) Test 2: hydrate-free and frozen at 263.1 K, (c) Test 3 with methane hydrate at 273.4 K, and (d) Test 4 with methane hydrate frozen at 263.1 K.

8.3.3 Determined mechanical properties

Mechanical properties were determined and shown in Table 8.3, including shear strength τ, stiffness (scant Young's modulus E_{50}), cohesion C and angle of internal friction ϕ, (P_{ec} denotes effective confining pressure). The scant Young's modulus was determined tangentially from the start to the middle of the linear section of the stress versus strain curves in Figure 8.4. The cohesion and friction angle were determined according to Mohr-Coulomb equation in terms of effective stress[53]. As a typical example, Figure 8.6 represents the Mohr-Coulomb circles for determination of the cohesion and friction angle of the frozen hydrate-free sediments in Test 2.

Table 8.3 The determined shear strength, stiffness, cohesion, and friction angle

Test	P_{ec} (MPa)	τ (MPa)	E_{50} (MPa)	*C* (MPa)	ϕ (°)
Test 1	0.5	2.6	80	0.1	38.0
	1.0	5.4	95		
	1.5	7.0	106		
Test 2	0.5	7.9	110	1.9	39.5
	1.0	9.2	119		
	1.5	10.8	107		
Test 3	0.5	7.7	117	1.2	29.2
	1.0	9.5	86		
	1.5	12.3	201		
Test 4	0.5	12.3	112	3.0	31.5
	1.0	13.6	122		
	1.5	15.3	117		

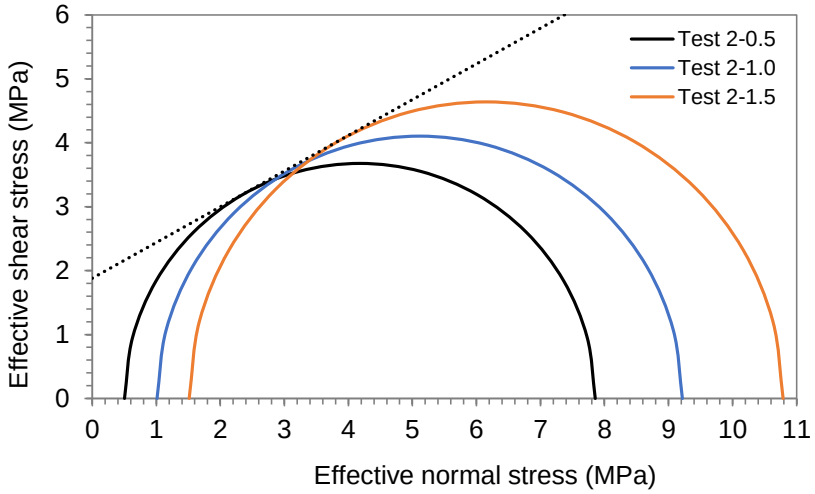

Figure 8.6 Mohr-Coulomb circle of Test 2 with specimens frozen at 263.1 K in the absence of hydrate

Figure 8.7 illustrates the effect of hydrate bearing and freezing on shear strength. Under the same confining pressure, the hydrate-free sediments frozen at 263.1 K (Test 2) were mechanically stronger than the unfrozen hydrate-free sediments at 273.4 K(Test 1); the unfrozen sediments with around 22 vol% methane hydrate (Test 3) were at least as strong as the frozen hydrate-free sediments with an average ice saturation of around 85 vol%. The presence of methane hydrate in about 22 vol% of the pore spaces led to a shear strength similar to that by ice filling 85 vol% of the pore spaces. Only based on the existing mechanisms such pore filling, load bearing and grain cementation, it cannot be fully understood why such a low saturation of methane hydrate resulted in a mechanical strength similar to freezing at 263.1 K, even if hydrate crystals tend to cement the sediment grains in partially water-saturated sediments[37]. In Test 4 the specimens which were formed with about 22 vol% methane hydrate and frozen at 263.1 K show the highest

shear strength compared to the other three groups of specimens. Moreover, the presence of about 22 vol% methane hydrate led to similar enhancement of the shear strength for both unfrozen and frozen specimens. Finally, it can also be seen that the shear strength increases as the confining pressure rises.

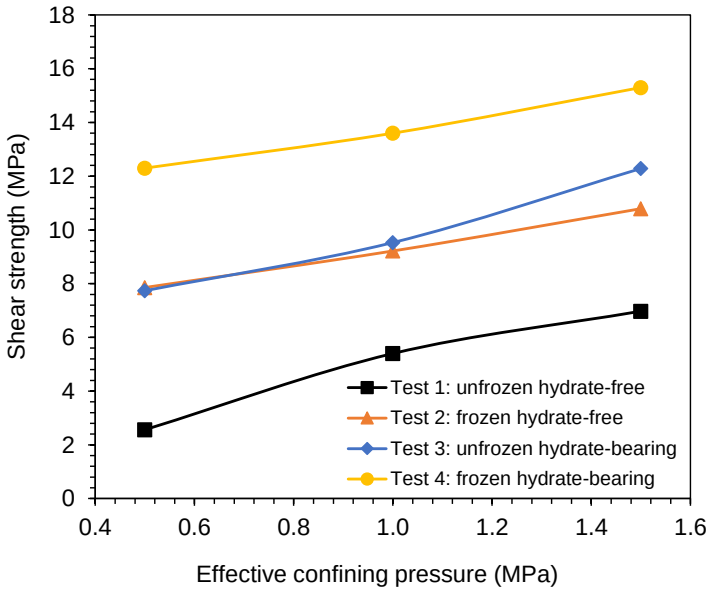

Figure 8.7 The determined shear strength shows the effect of hydrate bearing and freezing on shear strength.

In Table 8.3 the measured cohesion and angle of internal friction of the unfrozen and hydrate-free specimens in Test 1 is very small. This is because the specimens were of normally consolidated sand-silt-clay packs[53]. The presence of methane hydrate and freezing significantly increased the cohesion of the sediments by hydrate and ice cementing. However, it is interesting to see that hydrate formation in the specimens resulted in reduction in the internal friction, whilst freezing did not. This means that the presence of 22 vol% of methane hydrate appeared to be weakening the inter friction and interlocking between the grains, causing the large dilatation observed in the unfrozen hydrate-bearing sediments in Test 3 (Figure 8.5). To the best of our knowledge, no such experimental observations have been reported. One hypothesis could be due to particle assemblages. Methane hydrate crystals might locally bond together the fine clay and silt particles as well as sand particles, forming particle lumps that were wrapped with hydrate crusts. The hydrate-wrapped particle lumps behaved as loose sand particles so that the friction angle reduced to the typical range of loose sand[53]. The measured scant Young's modulus in Table 8.3 shows that the presence of hydrate and ice measurably increased the stiffness of the specimens. However, it seems that hydrate-bearing did not create much change in the stiffness of frozen sediments.

3.4 Effect of gas hydrate saturation

One series of triaxial experiments were conducted to investigate the effect of hydrate saturation on the geomechanical properties of simulated permafrost sediments. The same synthetic sediments were used to make the specimens. The specimens were formed with different saturations of methane hydrate and frozen at 270.1 K. Shearing was performed at the same conditions: temperature 270.1 K, pore pressure 5.0 MPa, effective confining pressure 1.0 MPa, and shearing rate 0.1 mm/min. Table 8.4 shows the saturation of methane hydrate, ice and gas before shearing.

Table 8.4 Saturation of methane hydrate, ice, and gas

Initial specimen	Test 5	Test 6	Test 7	Test 8	Test 9
Hydrae saturation (vol%)	0.0	16.7	27.4	33.2	51.7
Gas saturation (vol%)	12.1	9.2	9.0	15.7	17.6
Ice saturation (vol%)	87.9	74.1	63.6	51.1	30.7

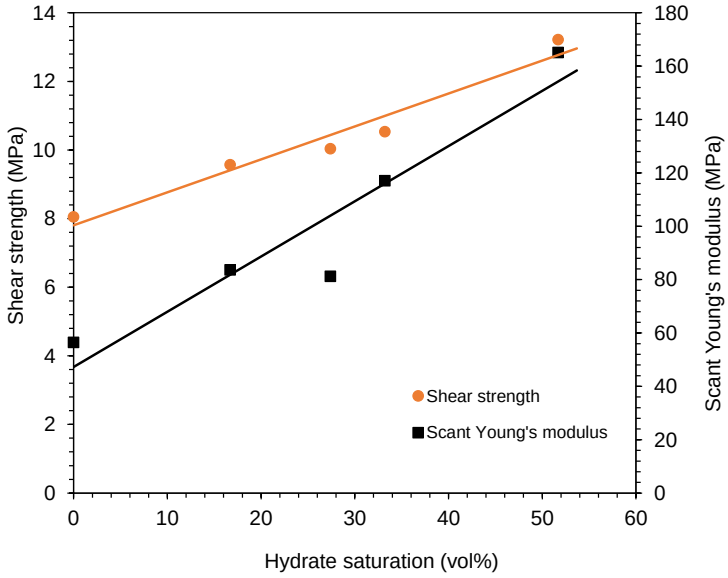

Figure 8.8 Effect of different saturations of methane hydrate on the shear strength and stiffness of frozen sediments

Figure 8.8 shows that the determined shear/peak strength and stiffness linearly increase as the hydrate saturation increases. Similar linear relationships between shear strength and stiffness versus hydrate saturation were also reported for unfrozen silica sand containing methane hydrate[29,30]. The determined shear strength is largely higher than those reported by Liu et al.[42], Song et al.[54], and Li et al.[43]. As mentioned in the Introduction, this is because different methods were used to make the simulated permafrost sediments. It should be noted that from Specimens 5 to 9, the shear strength gradually increased with the increase in methane hydrate saturation even if the ice

saturation in the specimens decreased. This result suggests that gas hydrate plays a dominant role in the geomechanical properties of the simulated permafrost sediments.

8.4 Physical model of hydrate reinforcement of sediments

The existing models of gas hydrate particle association, i.e., pore filling, load bearing and cementation, are insufficient to fully interpret why the presence of only around 22 vol% methane hydrate at 273.4 K(Test 3 in Figure 8.4) resulted in a shear strength as strong as around 85 vol% of water frozen at 263.1 K(Test 2 in Figure 8.4), and made the unfrozen hydrate-bearing specimens more ductile compared to those with the frozen hydrate-free ones. One of the possible explanations is that the intrinsic strength of methane hydrate is 20 to 30 times stronger than that of ice at a temperature near the freezing point[55]. Moreover, water films between hydrate crusts or crystals and grain surfaces[56,57], unfrozen water[58], and pressure melting[59,60] in the sediments further weakens the interparticle contacts by reducing the internal friction force and interlocking interaction. However, these factors fail to explain the unexpectedly high effect of a low hydrate saturation on the mechanical properties of sediments in comparison with freezing at 263.1 K.

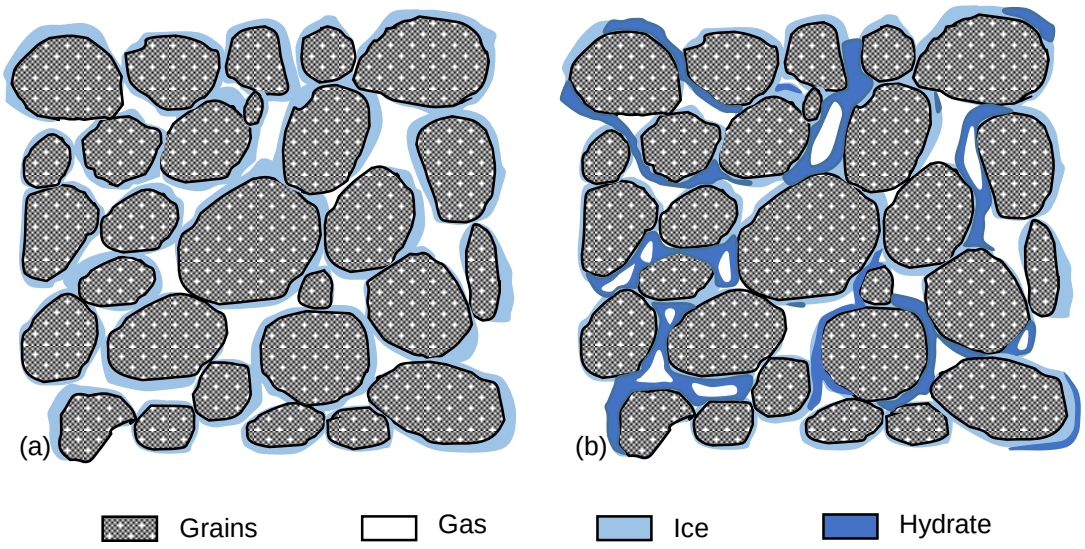

Figure 8.9 Schematic of the hypothetical hydrate networks or frame structures. (a) Ice wraps sediment grains with point-contact, (b) Hydrate networks extend across adjacent grains.

In partially water-saturated sediments, as shown Figure 8.9a, it is likely that water attached to the surface of the sediment grains in addition to some of the water absorbed by the clay[37]. Ice formed from the water partially filling sediment pores cements the grains mostly at the grain-grain contacts or very limited areas adjacent to grain contact points. On the other hand, this type of water distribution makes it possible to connect the remaining pore spaces and form channels. The injected methane gas fills these channels

and appears as gas bubbles that are surrounded by water. Methane hydrate always starts to form at the interface between water and methane gas, transforming the gas bubbles into either gas-filled or solid methane hydrate crystalline bars. These hydrate bars can grow locally or extend across adjacent grains through a mass transfer process and finally create mini or macro hydrate networks or hydrate frame structures throughout the specimens. In addition to the existing position models aforementioned, these hydrate-associated structures substantially enhance the shear strength of the specimens and make them significantly more ductile, just like reinforcing concrete using steel bars. Figure 8.9b illustrates the schematic modes of the gas hydrate networks or frame structures. As a result, it is presumed that, apart from the existing models of hydrate location in pores including pore filling, load bearing, and cementation, the patterns or morphology of hydrate crystals should be considered to understand the effect of hydrate bearing on the mechanical properties of sediments.

It is plausible to anticipate the effect of micro hydrate frame structures may substantially depend on initial water content and distribution in sediments before hydrate and ice formation. The typical water saturation of about 86.5 vol% to pore volume (15.5 wt% to dry sediments, Table 8.2) was used in this work, which leads to the strong effect of the micro hydrate frame structures. Observations of gas hydrate formation using synchrotron X-ray microscopy technique and magnetic resonance imaging technique suggested that gas hydrate crusts tend to form and wrap sediment grains in the presence of a very low water content, whilst it is likely that hydrates start to form at gas-water interfaces, grow into the water body and suspend in the water[56,57,61]. Consequently, changes in initial water saturation may alter the structure of the micro hydrate network in permafrost sediments. More experiments have been planned to further investigate how initial water saturation affects geomechanical properties of hydrate-bearing permafrost sediments.

8.5 References

(1) Makogon, Y. F.; Trebin, F. A.; Trofimuk, A. A.; Tsarev, V. P.; Cherskiy, N. V. Detection of a Pool of Natural Gas in a Solid (Hydrate Gas) State. In *Doklady Akademii nauk SSSR*; 1972; Vol. 196, pp 197–200. https://doi.org/10.1167/12.9.1206.

(2) Yakushev, V. S.; Chuvilin, E. M. Natural Gas and Gas Hydrate Accumulations within Permafrost in Russia. *Cold Reg. Sci. Technol.* **2000**, *31* (3), 189–197.

(3) Safronov, A. F.; Shits, E. Y.; Grigor'Ev, M. N.; Semenov, M. E. Formation of Gas Hydrate Deposits in the Siberian Arctic Shelf. *Russ. Geol. Geophys.* **2010**, *51* (1), 83–87.

(4) Judge, A. S.; Majorowicz, J. A. Geothermal Conditions for Gas Hydrate Stability in the Beaufort-Mackenzie Area: The Global Change Aspect. *Glob. Planet. Change* **1992**, *6* (2–4), 251–263.

(5) Collett, T. S. Potential of Gas Hydrates Outlined. *Oil Gas Journal;(United States)* **1992**, *90* (25).

(6) Bird, K. J.; Magoon, L. B. *Petroleum Geology of the Northern Part of the Arctic National Wildlife Refuge, Northeastern Alaska*; US Government Printing Office, 1987.

(7) Collett, T. S. Gas Hydrate Resources of Northern Alaska. *Bull. Can. Pet. Geol.* **1997**, *45* (3), 317–338.

(8) Max, M. D.; Lowrie, A. Oceanic Methane Hydrates: A "Frontier" Gas Resource. *J. Pet. Geol.* **1996**, *19* (1), 41–56.

(9) Rubin, E.; De Coninck, H. IPCC Special Report on Carbon Dioxide Capture and Storage. *UK Cambridge Univ. Press. TNO Cost Curves CO2 Storage, Part* **2005**, *2*, 14.

(10) Kvenvolden, K. A. Methane Hydrate - A Major Reservoir of Carbon in the Shallow Geosphere? *Chem. Geol.* **1988**, *71* (1–3), 41–51. https://doi.org/10.1016/0009-2541(88)90104-0.

(11) Milkov, A. V. Global Estimates of Hydrate-Bound Gas in Marine Sediments: How Much Is Really out There? *Earth-Science Rev.* **2004**, *66* (3–4), 183–197.

(12) Holder, G. D.; Kamath, V. A.; Godbole, S. P. The Potential of Natural Gas Hydrates as an Energy Resource. *Annu. Rev. Energy* **1984**, *9* (1), 427–445.

(13) Max, M. D.; Johnson, A. H. *Exploration and Production of Oceanic Natural Gas Hydrate: Critical Factors for Commercialization*; Springer, 2018.

(14) Dendy Sloan, E.; Koh, C. *Clathrate Hydrates of Natural Gases, Third Edition*; CRC press, 2007; Vol. 20074156. https://doi.org/10.1201/9781420008494.

(15) Ohgaki, K.; Takano, K.; Sangawa, H.; Matsubara, T.; Nakano, S. Methane Exploitation by Carbon Dioxide from Gas Hydrates—Phase Equilibria for CO2-CH4 Mixed Hydrate System—. *J. Chem. Eng. Japan* **1996**, *29* (3), 478–483.

(16) Masuda, Y.; Maruta, H.; Naganawa, S.; Amikawa, K.; Nagao, J.; Hironori, H.; Konno, Y. Methane Recovery from Hydrate-Bearing Sediments by N2–CO2 Gas Mixture Injection: Experimental Investigation on CO2–CH4 Exchange Ratio. In *Proceedings of the 7th International Conference on Gas Hydrates, Edinburgh, Scotland, United Kingdom*; 2011.

(17) Schoderbek, D.; Martin, K. L.; Howard, J.; Silpngarmlert, S.; Hester, K. North Slope Hydrate Fieldtrial: CO2/CH4 Exchange. In *OTC Arctic Technology Conference*; Offshore Technology Conference, 2012.

(18) Yang, J.; Okwananke, A.; Tohidi, B.; Chuvilin, E.; Maerle, K.; Istomin, V.; Bukhanov, B.; Cheremisin, A. Flue Gas Injection into Gas Hydrate Reservoirs for Methane Recovery and Carbon Dioxide Sequestration. *Energy Convers. Manag.* **2017**, *136*, 431–438. https://doi.org/10.1016/j.enconman.2017.01.043.

(19) Hassanpouryouzband, A.; Yang, J.; Tohidi, B.; Chuvilin, E.; Istomin, V.; Bukhanov, B.; Cheremisin, A. CO2 Capture by Injection of Flue Gas or CO2-N2 Mixtures into Hydrate Reservoirs: Dependence of CO2 Capture Efficiency on Gas Hydrate Reservoir Conditions. *Environ. Sci. Technol.* **2018**, *52* (7), 4324–4330. https://doi.org/10.1021/acs.est.7b05784.

(20) Collett, T. S. Detailed Analysis of Gas Hydrate Induced Drilling and Production Hazards. In *Proc. 4th Int. Conf. Gas Hydrate, 2002*; 2002.

(21) Westbrook, G. K.; Thatcher, K. E.; Rohling, E. J.; Piotrowski, A. M.; Pälike, H.; Osborne, A. H.; Nisbet, E. G.; Minshull, T. A.; Lanoisellé, M.; James, R. H. Escape of Methane Gas from the Seabed along the West Spitsbergen Continental Margin. *Geophys. Res. Lett.* **2009**, *36* (15).

(22) Shakhova, N.; Semiletov, I.; Leifer, I.; Salyuk, A.; Rekant, P.; Kosmach, D. Geochemical and Geophysical Evidence of Methane Release over the East Siberian Arctic Shelf. *J. Geophys. Res. Ocean.* **2010**, *115* (C8).

(23) Nisbet, E. G.; Piper, D. J. W. Giant Submarine Landslides. *Nature* **1998**, *392* (6674), 329.

(24) Paull, C. K.; Ussler, W.; Dillon, W. P. Is the Extent of Glaciation Limited by Marine Gas-hydrates? *Geophys. Res. Lett.* **1991**, *18* (3), 432–434.

(25) Winters, W. J. Properties of Samples Containing Natural Gas Hydrate from the JAPEX/JNOC/GSC Mallik 2L-38 Gas Hydrate Research Well, Determined Using Gas Hydrate And Sediment Test Laboratory Instrument (GHASTLI). *Bull. Geol. Surv. Canada* **1999**, No. 544, 241–250.

(26) Parameswaran, V. R.; Paradis, M.; Handa, Y. P. Strength of Frozen Sand Containing Tetrahydrofuran Hydrate. *Can. Geotech. J.* **1989**, *26* (3), 479–483.

(27) Yun, T. S.; Santamarina, J. C.; Ruppel, C. Mechanical Properties of Sand, Silt, and Clay Containing Tetrahydrofuran Hydrate. *J. Geophys. Res. Solid Earth* **2007**, *112* (B4). https://doi.org/10.1029/2006JB004484.

(28) Lee, J. Y.; Santamarina, J. C.; Ruppel, C. Mechanical and Electromagnetic Properties of Northern Gulf of Mexico Sediments with and without THF Hydrates. *Mar. Pet. Geol.* **2008**, *25* (9), 884–895.

(29) Masui, A.; Haneda, H.; Ogata, Y.; Aoki, K. Effects of Methane Hydrate Formation on Shear Strength of Synthetic Methane Hydrate Sediments. In *The Fifteenth International Offshore and Polar Engineering Conference*; International Society of Offshore and Polar Engineers, 2005.

(30) Miyazaki, K.; Masui, A.; Sakamoto, Y.; Aoki, K.; Tenma, N.; Yamaguchi, T. Triaxial Compressive Properties of Artificial Methane-hydrate-bearing Sediment. *J. Geophys. Res. solid earth* **2011**, *116* (B6).

(31) Hyodo, M.; Li, Y.; Yoneda, J.; Nakata, Y.; Yoshimoto, N.; Nishimura, A.; Song, Y. Mechanical Behavior of Gas-saturated Methane Hydrate-bearing Sediments. *J. Geophys. Res. Solid Earth* **2013**, *118* (10), 5185–5194.

(32) Santamarina, J. C.; Dai, S.; Terzariol, M.; Jang, J.; Waite, W. F.; Winters, W. J.; Nagao, J.; Yoneda, J.; Konno, Y.; Fujii, T. Hydro-Bio-Geomechanical Properties of Hydrate-Bearing Sediments from Nankai Trough. *Mar. Pet. Geol.* **2015**, *66*, 434–450.

(33) Liu, Z.; Dai, S.; Ning, F.; Peng, L.; Wei, H.; Wei, C. Strength Estimation for Hydrate-bearing Sediments from Direct Shear Tests of Hydrate-bearing Sand and Silt. *Geophys. Res. Lett.* **2018**, *45* (2), 715–723.

(34) Priest, J. A.; Best, A. I.; Clayton, C. R. I. A Laboratory Investigation into the Seismic Velocities of Methane Gas Hydrate-bearing Sand. *J. Geophys. Res. solid earth* **2005**, *110* (B4).

(35) Lee, J. Y.; Francisca, F. M.; Santamarina, J. C.; Ruppel, C. Parametric Study of the Physical Properties of Hydrate-bearing Sand, Silt, and Clay Sediments: 2. Small-strain Mechanical Properties. *J. Geophys. Res. Solid Earth* **2010**, *115* (B11).

(36) Dvorkin, J.; Helgerud, M. B.; Waite, W.; Kirby, S.; Nur, A. Natural Gas Hydrate in Oceanic and Permafrost Environments. Kluwer Acad. Publ., Dordrecht 2000.

(37) Waite*, W. F.; Winters, W. J.; Mason, D. H. Methane Hydrate Formation in Partially Water-Saturated Ottawa Sand. *Am. Mineral.* **2004**, *89* (8–9), 1202–1207.

(38) Waite, W. F.; Santamarina, J. C.; Cortes, D. D.; Dugan, B.; Espinoza, D. N.; Germaine, J.; Jang, J.; Jung, J. W.; Kneafsey, T. J.; Shin, H. Physical Properties of Hydrate-bearing Sediments. *Rev. Geophys.* **2009**, *47* (4).

(39) Andersland, O. B.; Akili, W. Stress Effect on Creep Rates of a Frozen Clay Soil. *Geotechnique* **1967**, *17* (1), 27–39.

(40) TSytovich, N. A. *Mechanics of Frozen Ground*; Scripta Book Co., 1975.

(41) Arenson, L. U.; Springman, S. M.; Sego, D. C. The Rheology of Frozen Soils. *Appl. Rheol.* **2007**, *17* (1), 12147.

(42) Liu, W.; Zhao, J.; Luo, Y.; Song, Y.; Li, Y.; Yang, M.; Zhang, Y.; Liu, Y.; Wang, D. Experimental Measurements of Mechanical Properties of Carbon Dioxide Hydrate-Bearing Sediments. *Mar. Pet. Geol.* **2013**, *46*, 201–209.

(43) Li, Y.; Liu, W.; Zhu, Y.; Chen, Y.; Song, Y.; Li, Q. Mechanical Behaviors of Permafrost-Associated Methane Hydrate-Bearing Sediments under Different Mining Methods. *Appl. Energy* **2016**, *162*, 1627–1632.

(44) Waite, W. F.; Santamarina, J. C.; Cortes, D. D.; Dugan, B.; Espinoza, D. N.; Germaine, J.; Jang, J.; Jung, J. W.; Kneafsey, T. J.; Shin, H.; et al. Physical Properties of Hydrate-Bearing Sediments. *Rev. Geophys.* **2009**, *47* (2008), RG4003. https://doi.org/10.1029/2008RG000279.Table.

(45) Seyfried, M. S.; Murdock, M. D. Use of Air Permeability to Estimate Infiltrability of Frozen Soil. *J. Hydrol.* **1997**, *202* (1–4), 95–107.

(46) Konno, Y.; Yoneda, J.; Egawa, K.; Ito, T.; Jin, Y.; Kida, M.; Suzuki, K.; Fujii, T.; Nagao, J. Permeability of Sediment Cores from Methane Hydrate Deposit in the Eastern Nankai Trough. *Mar. Pet. Geol.* **2015**, *66*, 487–495.

(47) Head, K. H. *Manual of Soil Laboratory Testing. Volume 3: Effective Stress Tests.*; John Wiley & Sons, 1998.

(48) Istomin, V.; Chuvilin, E.; Bukhanov, B.; Uchida, T. Pore Water Content in Equilibrium with Ice or Gas Hydrate in Sediments. *Cold Reg. Sci. Technol.* **2017**, *137*, 60–67.

(49) Azhar, A. T. S.; Norhaliza, W.; Ismail, B.; Abdullah, M. E.; Zakaria, M. N. Comparison of Shear Strength Properties for Undisturbed and Reconstituted Parit Nipah Peat, Johor. In *IOP Conference Series: Materials Science and Engineering*; IOP Publishing, 2016; Vol. 160, p 12058.

(50) Della, N.; Muhammed, R. D.; Canou, J.; Dupla, J. C. Influence of Initial Conditions on Liquefaction Resistance of Sandy Soil from Chlef Region in Northern Algeria. *Geotech. Geol. Eng.* **2016**, *34* (6), 1971–1983.

(51) Zhang, S.; Lai, Y.; Sun, Z.; Gao, Z. Volumetric Strain and Strength Behavior of Frozen Soils under Confinement. *Cold Reg. Sci. Technol.* **2007**, *47* (3), 263–270. https://doi.org/10.1016/J.COLDREGIONS.2006.10.001.

(52) Arenson, L. U.; Springman, S. M. Triaxial Constant Stress and Constant Strain Rate Tests on Ice-Rich Permafrost Samples. *Can. Geotech. J.* **2005**, *42* (2), 412–430.

(53) Szefer, P.; Namiesnik, J. *Analytical Measurements in Aquatic Environments*; 2009.

(54) Song, Y.; Zhu, Y.; Liu, W.; Li, Y.; Lu, Y.; Shen, Z. The Effects of Methane Hydrate Dissociation at Different Temperatures on the Stability of Porous Sediments. *J. Pet. Sci. Eng.* **2016**, *147*, 77–86.

(55) Durham, W. B.; Kirby, S. H.; Stern, L. A.; Zhang, W. The Strength and Rheology of Methane Clathrate Hydrate. *J. Geophys. Res. Solid Earth* **2003**, *108* (B4).

(56) Chaouachi, M.; Falenty, A.; Sell, K.; Enzmann, F.; Kersten, M.; Haberthür, D.; Kuhs, W. F. Microstructural Evolution of Gas Hydrates in Sedimentary Matrices Observed with Synchrotron X-ray Computed Tomographic Microscopy. *Geochemistry, Geophys. Geosystems* **2015**, *16* (6), 1711–1722.

(57) Yang, L.; Falenty, A.; Chaouachi, M.; Haberthür, D.; Kuhs, W. F. Synchrotron X-ray Computed Microtomography Study on Gas Hydrate Decomposition in a Sedimentary Matrix. *Geochemistry, Geophys. Geosystems* **2016**, *17* (9), 3717–3732.

(58) Chamberlain, E.; Groves, C.; Perham, R. The Mechanical Behaviour of Frozen Earth Materials under High Pressure Triaxial Test Conditions. *Geotechnique* **1972**, *22* (3), 469–483.

(59) Goodman, D. J.; King, G. C. P.; Millar, D. H. M.; Robin, G. de Q. Pressure-Melting Effects in Basal Ice of Temperate Glaciers: Laboratory Studies and Field Observations under Glacier d'Argentiere. *J. Glaciol.* **1979**, *23* (89), 259–271.

(60) Jones, S. J. The Confined Compressive Strength of Polycrystalline Ice. *J. Glaciol.* **1982**, *28* (98), 171–178.

(61) Zhao, J.; Yang, L.; Xue, K.; Lam, W.; Li, Y.; Song, Y. In Situ Observation of Gas Hydrates Growth Hosted in Porous Media. *Chem. Phys. Lett.* **2014**, *612*, 124–128. https://doi.org/10.1016/J.CPLETT.2014.07.066.

Chapter 9 - Conclusions and Recommendation for Further Research

Industrial scale implementation of CO2 capture and geological storage is demanding economically viable technologies. We have conducted a series of work to investigate the proposed gas hydrate-based technologies as alternative options to make CCS economically feasible. It is believed that enhancing the technologies at a conceptual process level is crucial to help evolve the realistic viability of the proposed methods and identifying the critical influencing parameters that must be considered for field applications in future.

In **Chapter 2**, a new highly accurate methodology was applied for determination of flue gas (i.e. CO2 and N2) solubility in water and brine. Three types of CO2-N2 mixtures were tested to simulate coal-fired flue gas, gas-fired flue gas, and syngas, respectively. The solubility was measured for pure water and aqueous NaCl solutions of three different salinities from 273.25 to 303.05 K and pressures up to 22 MPa.

The solubility of the simulated flue gases increases as the pressure increases or the temperature decreases, or as the mole fraction of the gas component in the vapor phase increases (see Figure 9.1). It was also observed that influenced by the salting-out effect, the solubility of CO2 and N2 decreases with increase in the concentration of NaCl in the aqueous phase.

A thermodynamic model was used to predict the solubility values by adjusting the binary interaction parameters. Three different equations of state including CPA-SRK72, VPT and PC-SAFT were employed to determine the fugacity values. It was shown that VPT equation is more accurate than the other equations of state at lower temperatures, particularly when the simulated gas-fired flue gas is injected into water or when the concentration of NaCl is low. The statistical-based equations of state i.e. CPA-SRK72 and PC-SAFT become more reliable and accurate for CO2-rich flue gas/syngas or high saline solutions.

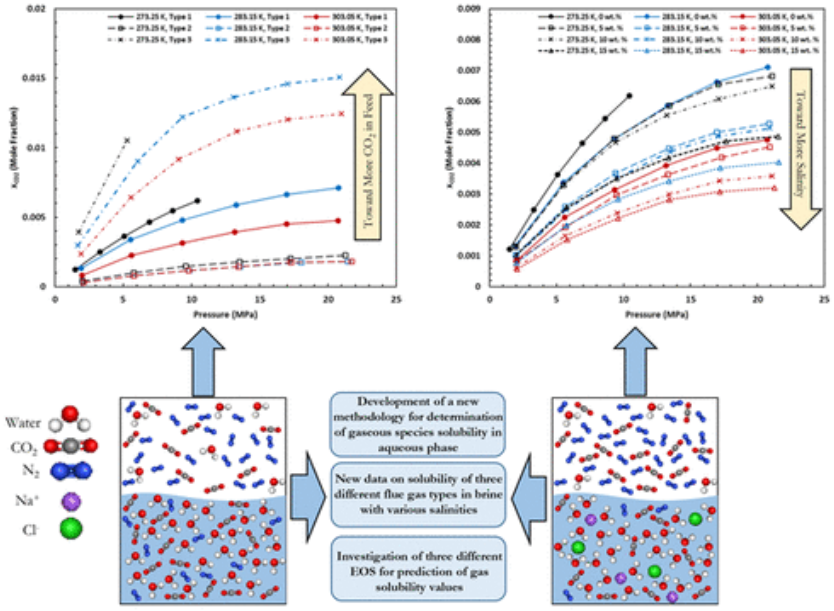

Figure 9.1 Table of content art for chapter 2

The results of this study could be effectively used to enrich the open literature in terms of the solubility of CO2 in the presence of the other main components of the flue gas like N2, which provides a comprehensive solubility database for the CCS schemes in saline aquifers to modify their methodology in order to use the flue gas rather than pure CO2. Lastly, the obtained experimental results together with adjusted modeling parameters are useful data in application of hydrate-based methods for CO2 separation, capture and storage.

In **Chapter 3** and **Chapter 4**, through our experiments and analysis, we have identified the optimum conditions and key parameters for improving the overall economic feasibility of the CS at MH reservoirs (**Chapter 3**), and investigated kinetics of the proposed method in realistic conditions (**Chapter 4**). By taking results of these chapters into account, we suggest a simple field trial plan for both CCS and recover methane by continuous injection of flue gas into a gas hydrate deposit, in which reservoir pressure can be controlled and adjusted to near the optimum pressure according to the reservoir temperature and MH saturation reduction. This can be implemented through different scenarios, for example, one injection well and one production well, or one injection well and multiple production wells, or one well for both injection and production through a puff & huff process. In this regard, for reaching our goal of economic and sustainable CS and energy recovery, concerted collaborative effort among researchers from different fields will be required to facilitate flue gas process and transfer through pipelines from the power plants, to determine the optimum well locations and injection/production rate,

to understand more about the geological impact of the current method, and also to recognize the possible side effect that may happen to the environment.

In **Chapter 5**, we proposed an innovative approach for geological CCS by direct injection of flue gas into water/ice-bearing sediments in the absence of initial methane gas hydrates in place, integrating CO2 capture and storage into one simple process, and consequently reducing the cost of CCS significantly by comparison with conventional gas hydrate-based CCS methods. The presence of N2 in the feed gas facilitates the movement of the gas and reduces the corrosion of facilities in comparison with supercritical CO2. The proposed method shows very high efficiency, with greater than 92% stable CO2 capture under certain conditions, meeting the technical requirements of typical industrial-scale geological CO2 storage operations reported in literature. These results indicate that injection of a binary CO2-N2 composition is a promising approach to further push CO2 into the clathrate phase. Kinetics of the proposed process was experimentally investigated under simulated natural conditions and on real-time scales. This is the first study to analyze the binary gas hydrate formation kinetics in both frozen and unfrozen mesoporous media under realistic conditions. The results also demonstrate the first experimental evidence backed by thermodynamic modeling results for the formation of sII clathrates by CO2-N2 mixed gas with high CO2 content. Moreover, considering the a sudden rise in the environmental temperature, we found that the presence of N2 in the system provides a considerably wider safety net for the stability of CO2 in the clathrate phase. Accordingly, this CCS method could reduce the risk of leakage for stored CO2 into nature, making it highly attractive for large-scale CCS. Finally, effect of the presence of different salts, and effect of impurities in the injected gas on both hydrate formation and dissociation, and effect of the application of this method on life cycle in the injection environment could be investigated following this work.

Taking all of the results presented in **Chapter 6** into account, it is clear that, for systems containing gas mixtures, reaching constant pressure can't be considered independently as a sign of thermodynamic equilibrium and further changes in the composition of different phases can occur at the final or stable pressure. This study substantiates the crucial role of the hydrate formation kinetics to achieve a high efficiency of CO2 separation and storage. The observed compositional changes in both gas phase and hydrate phase for flue gas-water systems could occur in other gas mixture systems, typically water-natural gas systems, which should be closely examined if the kinetics of hydrate formation is

important. Although the presented work revealed some kinetic properties of flue gas hydrate formation, it is clear that more fundamental experiments are required for a better understanding of the observed phenomenon. These experiments could be coupled with different spectroscopy techniques such as NMR to be able to measure the composition of the hydrate phase during hydrate formation/dissociation. Moreover, effect of gas to water ratio, pressure, temperature, and different compositions on both hydrate formation and dissociation also needs to be investigated following this work.

In **Chapter 7**, gas permeability was measured under varying differential pressure for three different types of sedimentary core samples to investigate their gas permeation characteristics both in the presence and in the absence of natural gas hydrates. The experimental results showed that the observed phenomena regarding the gas permeation at different gas hydrate-bearing sediments could be dominated by different mechanisms including capillary breakthrough, pore/grain size distribution, hydrate clogging, hydrate-forced heave or agglomeration, and Klinkenberg Effect. Results show that, for the highly porous and permeable silica sand core samples, the gas permeability increases with increasing the inlet pressure (and accordingly differential pressure) at both hydrate-free and hydrate-bearing cases, due to dominance of the capillary breakthrough mechanism over the gas slippage. For the sand-clay core samples containing 5 wt% montmorillonite, due to the presence of fine clay particles swelled by water in large pores, the pathways available for the gas flow was reduced and the gas permeability of the porous medium was dominated by Klinkenberg Effect. For the consolidated sandstone core sample, the gas permeation characteristics were considerably altered. For hydrate-free case, the breakthrough capillary pressure dominated the gas permeation so that the gas permeability increased with the inlet pressure, similar to that of unconsolidated silica sand packs. However, hydrate formation clogged the original large pores thus resulted in the gas slippage to be influential, resulting in Klinkenberg Effect to be dominant. Following this work, more systematic experiments to cover wide range of sediments, water permeability, development of permeability models to be able to describe the migration mechanism alternation could be conducted.

In **Chapter 8**, the shear characteristics and deformation behavior of four types of artificial sediments were investigated at different conditions, including unfrozen hydrate-free, frozen hydrate-free, unfrozen hydrate-bearing, and frozen hydrate-bearing sediments. Results show that ice and gas hydrates distinctively affect the shearing characteristics and deformation behavior of the specimens, though they are both water-based crystalline solids.

Both methane hydrate and ice significantly enhanced the shear strength of sediments. Under the same confining pressure the presence of 25 vol% methane hydrate in the unfrozen sediments led to a shear strength as strong as those of the frozen hydrate-free specimens in which 86 vol% of the pore spaces were occupied by ice at 263.1 K. Coexistence of both gas hydrate and ice resulted in the highest shear strength. The sediments that were initially saturated with about 85 vol% of water frozen at 263.1 K experienced brittle-like failure. In contrast, those sediments containing about 25 vol% methane hydrate showed large dilatation but no quick failure occurred.

Methane hydrate plays a dominant role in the geomechanical properties of the simulated permafrost sediments compared to ice. It was found that the existing hydrate position models seem insufficient to interpret the large strengthening in the shear strength and the ductile deformation for the low saturation of methane hydrate. As a result, it was hypothesized that formation of hydrate networks or frame structures may play a substantial role in the observed reinforcement of both unfrozen and frozen sediments. Finally, effect of water content, and mineral type on geomechanical properties of gas hydrate bearing sediments together with experimental measurement of geophysical properties of these sediments could be investigated following this work.

Appendix A for Chapter 2

Verification of the Methodology

The methodology followed previously by the apparatus used in this study proved it to be appropriate to measure the vapor-liquid equilibria in a wide range of operating conditions and different fluids with reasonable accuracy [1]. To test the reliability of the proposed method, we measured the solubility of pure CO2 in water, which is known to cause complexities to the experimental conditions such as equipment corrosion, and compared the results with the available literature data

The equilibrium mole fractions of CO2 in the aqueous phase measured in the temperatures ranging from 278.25 to 308.25 K and pressures up to 6 MPa are presented in Table S1 and plotted in Figure S1 compared to the experimental data reported in the open literature. A reasonable agreement between our measurements and the data presented in the open literature is observed which confirms the reliability of the experimental approach used in this study.

Table S1 Comparison of experimental data for CO_2-water binary system (This work vs. literature)

Pressure (MPa)	x_{CO2} (Mole Fraction)		Relative Deviation (%)	Reference
	This Work	Literature Data		
T = 274.05 K				
0.25	0.0035	0.0032	9.38	[2]
0.51	0.0069	0.0061	13.11	[2]
0.71	0.0095	-	-	-
1.32	0.0153	0.0160	4.38	[2]
1.84	0.0191	-	-	-
2.01	0.0203	-	-	-
T = 278.25 K				
0.13	0.0010	0.0011	9.09	[3]
0.50	0.0061	0.0059	3.39	[4]
0.76	0.0087	0.0085	2.35	[4]
1.02	0.0109	0.0111	1.80	[4]
1.13	0.0121	0.0120	0.83	[2]
1.45	0.0148	0.0150	1.33	[2]
1.98	0.0186	0.0181	2.76	[3]
T = 288.25 K				
0.09	0.0008	0.0010	20.00	[3]
0.29	0.0029	0.0026	11.37	[2]
0.54	0.0052	0.0049	6.10	[2]
1.01	0.0090	0.0087	3.45	[4]
1.59	0.0126	0.0128	1.41	[2]
1.95	0.0149	0.0143	4.20	[4]
2.75	0.0194	0.0188	3.19	[4]
3.72	0.0239	0.0234	2.14	[4]
T = 293.15 K				
0.15	0.0009	0.0007	28.57	[3]
0.32	0.0023	-	-	-
0.48	0.0036	-	-	-
1.12	0.0071	-	-	-
1.42	0.0093	-	-	-
2.95	0.0155	0.0142	9.15	[3]
4.10	0.0191	0.0193	1.04	[3]
5.10	0.0213	0.0200	6.50	[3]
T = 308.25 K				
0.24	0.0008	-		-
0.59	0.0029	0.0028	3.57	[4]
1.04	0.0058	-	-	-
1.39	0.0078	-	-	-
1.90	0.0105	0.0121	13.22	[4]
4.00	0.0164	0.0156	5.13	[4]
5.95	0.0200	0.0203	1.48	[4]

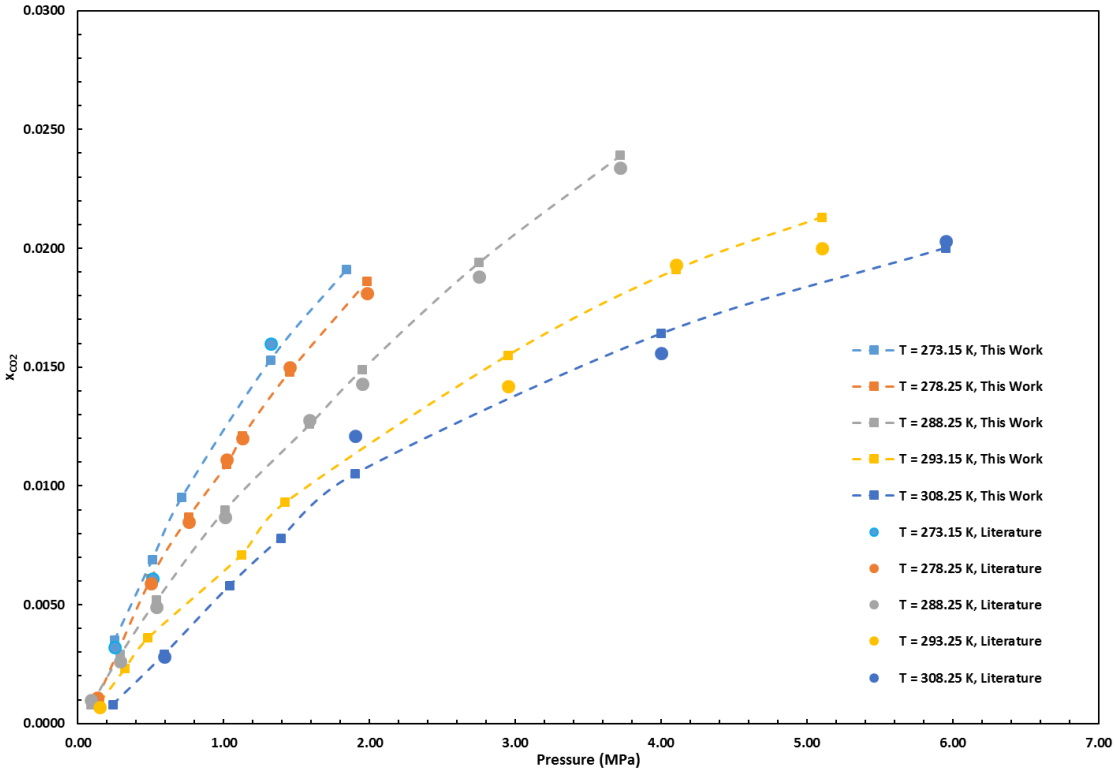

Figure S1 P-xCO2 diagram of CO2-water binary system (This work vs. literature)

Uncertainty measurement

Temperature uncertainty

Uncertainty of temperature measurement was calculated using Eq.(S1):

$$U_c(T) = \sqrt{u_{System}^2 + u_{Calibration}^2 + u_{Repeatability}^2} \quad \text{(S1)}$$

where the system and repeatability uncertainties are 0.1 K. Eq.(S2) was also used to convert the actual measured temperature by PRT to calibrated temperature in the vessel:

$$T_{Cal} = 0.9724T + 0.8664 \quad \text{(S2)}$$

By taking the derivative of the Eq.(S2), one can obtain the expression for calculating $u_{Calibration}$:

$$u_{Calibation} = \left|\frac{dT_{Cal}}{dT}\right| \delta T \quad \text{(S3)}$$

in which δT is 0.1 K. Using Eq.(S1), $U_c(T)$ is calculated equal to 0.172 K for all points.

Pressure uncertainty

Eq.(S4) was used to calculate the pressure uncertainty:

$$U_c(P) = \sqrt{u_{System}^2 + u_{Calibration}^2 + u_{Repeatability}^2} \quad \text{(S4)}$$

For the pressure range we dealt with in this study, a pressure transducer with $u_{Repeatability}$ equal to 0.005 MPa was used to measure the pressure of the system. Eq.(S5) was also applied to convert the actual measured pressure by the transducer to calibrated pressure of the vessel:

$$P_{Cal} = 10^{-5}P^2 + P - 0.0006 \quad \text{(S5)}$$

Therefore, the expression for $u_{Calibration}$ is obtained by taking derivative of the Eq.(S5):

$$u_{Calibration} = \left|\frac{dP_{Cal}}{dP}\right| \delta P \quad \text{(S6)}$$

where δP is 0.005 MPa.

The pressure of the system was not disturbed during sampling owing to use of the capillary sampler. In other words, the capillary sampler allowed for a few microliter samples to be taken, avoiding any noticeable pressure change due to sampling. Therefore, u_{System} for these measurements was considered equal to zero. Assuming maximum value for uncertainty of calibration over the pressure range, $U_c(P)$ was found to be 0.007 MPa for all the measured points.

Uncertainty of solubility measurement

Eq.(S7) expresses the uncertainty of the solubility measurements:

$$U_c(x_i) = \sqrt{u^2_{Measurement} + u^2_{Repeatability}} \qquad \text{(S7)}$$

where i is either CO_2 or N_2. The average standard deviation of the test was considered as $u_{Repeatability}$ and reported as 0.000021.

It should be noted that only the uncertainty of measurements for CO_2 solubility is presented here and the procedure for N_2 is similar. We simplified the main expression for the solubility calculation presented in Figure 1.2 in form of Eq.(S8) to calculate the uncertainty of the solubility measurements:

$$x_{CO_2} = \frac{A}{A + B + n_L} \qquad \text{(S8)}$$

where A and B are defied as:

$$A = n^{Injected}_{CO_2} - n^{Vapor}_{CO_2} \qquad \text{(S9)}$$

$$B = n^{Injected}_{N_2} - n^{Vapor}_{N_2} \qquad \text{(S10)}$$

We split A function into two expressions for ease of calculations:

$$A = A_1 - A_2 \qquad \text{(S11)}$$

where:

$$A_1 = A_{11} - A_{12} \qquad \text{(S12)}$$

$$A_2 = A_{21} - A_{22} \qquad \text{(S13)}$$

and:

$$A_{11} = \frac{y_{CO_2,Source} P_{1,Source} V_{Source}}{z_{1,Source} R T_{1,Source}} \qquad \text{(S14)}$$

$$A_{12} = \frac{y_{CO_2,Source} P_{2,Source} V_{Source}}{z_{2,Source} R T_{2,Source}} \qquad \text{(S15)}$$

$$A_{21} = \frac{y_{CO_2,Vessel} P_{Vessel} V_{V_{Vessel}}}{z_{Vessel} R T_{Vessel}} \qquad \text{(S16)}$$

$$A_{22} = \frac{y_{CO_2,Vessel} P_{Vessel} m_L}{z_{Vessel} R T_{Vessel} \rho_L} \qquad \text{(S17)}$$

The uncertainty of the measurement can be found using Eq.(S18):

$$u_{Measurement} = dx_{CO_2}$$

$$= x_{CO_2}\sqrt{\frac{(B+n_L)^2\Delta A^2}{A^2(A+B+n_L)^2} + \frac{\Delta B^2 + \Delta n_L^2}{(A+B+n_L)^2}} \quad \text{(S18)}$$

The uncertainty of function A is obtained as:

$$\Delta A = \sqrt{\Delta A_1^2 + \Delta A_2^2} \quad \text{(S19)}$$

where:

$$\Delta A_1 = \sqrt{\Delta A_{11}^2 + \Delta A_{12}^2} \quad \text{(S20)}$$

$$\Delta A_2 = \sqrt{\Delta A_{21}^2 + \Delta A_{22}^2} \quad \text{(S21)}$$

and:

$$\frac{\Delta A_{11}}{A_{11}} = \sqrt{\left(\frac{\Delta y_{CO_2,Source}}{y_{CO_2,Source}}\right)^2 + \left(\frac{\Delta P_{1,Source}}{P_{1,Source}}\right)^2 + \left(\frac{\Delta z_{1,Source}}{z_{1,Source}}\right)^2 + \left(\frac{\Delta T_{1,Source}}{T_{1,Source}}\right)^2} \quad \text{(S22)}$$

$$\frac{\Delta A_{12}}{A_{12}} = \sqrt{\left(\frac{\Delta y_{CO_2,Source}}{y_{CO_2,Source}}\right)^2 + \left(\frac{\Delta P_{2,Source}}{P_{2,Source}}\right)^2 + \left(\frac{\Delta z_{2,Source}}{z_{2,Source}}\right)^2 + \left(\frac{\Delta T_{2,Source}}{T_{2,Source}}\right)^2} \quad \text{(S23)}$$

$$\frac{\Delta A_{21}}{A_{21}} = \sqrt{\left(\frac{\Delta y_{CO_2,Vessel}}{y_{CO_2,Vessel}}\right)^2 + \left(\frac{\Delta P_{Vessel}}{P_{Vessel}}\right)^2 + \left(\frac{\Delta z_{Vessel}}{z_{Vessel}}\right)^2 + \left(\frac{\Delta T_{Vessel}}{T_{Vessel}}\right)^2} \quad \text{(S24)}$$

$$\frac{\Delta A_{22}}{A_{22}} \quad \text{(S25)}$$

$$= \sqrt{\left(\frac{\Delta y_{CO_2,Vessel}}{y_{CO_2,Vessel}}\right)^2 + \left(\frac{\Delta P_{Vessel}}{P_{Vessel}}\right)^2 + \left(\frac{\Delta z_{Vessel}}{z_{Vessel}}\right)^2 + \left(\frac{\Delta T_{Vessel}}{T_{Vessel}}\right)^2 + \left(\frac{\Delta m_L}{m_L}\right)^2 + \left(\frac{\Delta \rho_L}{\rho_L}\right)^2}$$

The formulation for function B is the same except CO_2 is replaced by N_2. Furthermore, the uncertainty of the moles of liquid phase can be found as:

$$\Delta n_L = \frac{\Delta m_L}{M_L} \quad \text{(S26)}$$

Table S2 presents the uncertainties of all the parameters involved in Eq.(22-26):

Table S2 VLE Uncertainties of physical properties measured/calculated for the solubility measurements

No.	Parameter	Uncertainty
1	y_{CO_2}	$\Delta y_{CO_2} = 0.0001$
2	P	$\Delta P = 0.005\ MPa$
3	z	$\Delta z = 0.05$ [5]
4	T	$\Delta T = 0.1\ K$
5	m_L	$\Delta m_L = 0.01\ g$
6	ρ_L	$\Delta \rho_L = 0.001 \rho_L$

Finally, the expanded uncertainty of the measurement with 95% level of confidence (k = 2) can be calculated using the Eq. (S27):

$$U(x_i) = 2U_c(x_i) \quad \text{(S27)}$$

Experimental equilibrium compositions of the liquid and vapor phases for CO_2+N_2+Water ternary systems

Table S3 VLE data for injected gas type 1

Temperature (K)	Pressure (MPa)	Experimental Data (Mole Fraction)						
		Aqueous Phase		Expanded Uncertainty (k = 2)		Vapor Phase		
		CO_2	N_2	CO_2	N_2	CO_2	N_2	Standard Deviation
273.25	1.51	0.0012	0.0002	0.00014	0.00003	0.0664	0.9336	0.00016
273.25	3.30	0.0025	0.0005	0.00028	0.00006	0.0714	0.9286	0.00012
273.25	5.08	0.0036	0.0008	0.00042	0.00010	0.0758	0.9242	0.00022
273.25	6.92	0.0046	0.0010	0.00052	0.00011	0.0806	0.9194	0.00022
273.25	8.63	0.0055	0.0012	0.00072	0.00014	0.0845	0.9155	0.00014
273.25	10.46	0.0062	0.0014	0.00078	0.00016	0.0883	0.9117	0.00013
283.15	1.93	0.0013	0.0003	0.00014	0.00004	0.0770	0.9230	0.00027
283.15	5.55	0.0034	0.0007	0.00044	0.00008	0.0851	0.9149	0.00014
283.15	9.35	0.0048	0.0011	0.00057	0.00012	0.0933	0.9067	0.00024
283.15	13.30	0.0059	0.0014	0.00068	0.00016	0.1005	0.8995	0.00011
283.15	16.96	0.0066	0.0017	0.00084	0.00022	0.1051	0.8949	0.00014
283.15	20.78	0.0071	0.0020	0.00091	0.00024	0.1093	0.8907	0.00010
303.05	1.98	0.0008	0.0002	0.00010	0.00003	0.0958	0.9042	0.00017
303.05	5.63	0.0022	0.0005	0.00027	0.00006	0.1018	0.8982	0.00028
303.05	9.35	0.0031	0.0008	0.00038	0.00010	0.1069	0.8931	0.00015
303.05	13.17	0.0039	0.0011	0.00047	0.00013	0.1119	0.8881	0.00028
303.05	16.97	0.0045	0.0013	0.00055	0.00015	0.1158	0.8842	0.00013
303.05	20.75	0.0048	0.0015	0.00055	0.00018	0.1184	0.8816	0.00030

Table S4 VLE data for injected gas type 2

Temperature (K)	Pressure (MPa)	Experimental Data (Mole Fraction)						
		Aqueous Phase		Expanded Uncertainty (k = 2)		Vapor Phase		
		CO_2	N_2	CO_2	N_2	CO_2	N_2	Standard Deviation
273.25	2.03	0.0004	0.0004	0.00006	0.00004	0.0164	0.9836	0.00022
273.25	5.77	0.0010	0.0009	0.00013	0.00011	0.0184	0.9816	0.00018
273.25	9.58	0.0015	0.0014	0.00018	0.00016	0.0206	0.9794	0.00027
273.25	13.55	0.0018	0.0019	0.00022	0.00021	0.0229	0.9771	0.00007
273.25	17.26	0.0020	0.0023	0.00024	0.00027	0.0241	0.9759	0.00028
273.25	21.27	0.0023	0.0027	0.00028	0.00031	0.0253	0.9747	0.00029
283.15	2.05	0.0003	0.0003	0.00004	0.00004	0.0200	0.9800	0.00003
283.15	5.74	0.0008	0.0008	0.00010	0.00010	0.0215	0.9785	0.00022
283.15	9.84	0.0012	0.0012	0.00015	0.00014	0.0237	0.9763	0.00017
283.15	13.58	0.0014	0.0016	0.00018	0.00020	0.0252	0.9748	0.00023
283.15	18.06	0.0017	0.0020	0.00021	0.00023	0.0262	0.9738	0.00002
283.15	21.50	0.0018	0.0023	0.00024	0.00028	0.0272	0.9728	0.00023
303.05	2.10	0.0003	0.0003	0.00004	0.00004	0.0200	0.9800	0.00003
303.05	5.78	0.0008	0.0008	0.00009	0.00009	0.0215	0.9785	0.00012
303.05	9.80	0.0012	0.0012	0.00015	0.00014	0.0237	0.9763	0.00007
303.05	13.45	0.0014	0.0016	0.00016	0.00019	0.0252	0.9748	0.00004
303.05	17.30	0.0017	0.0020	0.00020	0.00026	0.0262	0.9738	0.00022
303.05	21.74	0.0018	0.0023	0.00020	0.00026	0.0272	0.9728	0.00002

Table S5 VLE data for injected gas type 3

Temperature (K)	Pressure (MPa)	Experimental Data (Mole Fraction)						
		Aqueous Phase		Expanded Uncertainty (k = 2)		Vapor Phase		
		CO_2	N_2	CO_2	N_2	CO_2	N_2	Standard Deviation
273.25	1.73	0.0039	0.0002	0.00044	0.00003	0.2105	0.7895	0.00009
273.25	5.31	0.0105	0.0007	0.00134	0.00008	0.2495	0.7505	0.00001
283.15	1.68	0.0030	0.0002	0.00034	0.00003	0.2460	0.7540	0.00017
283.15	6.07	0.0090	0.0006	0.00117	0.00007	0.2738	0.7262	0.00008
283.15	9.34	0.0122	0.0009	0.00156	0.00011	0.2915	0.7085	0.00013
283.15	13.09	0.0136	0.0013	0.00166	0.00015	0.3139	0.6861	0.00000
283.15	17.06	0.0146	0.0016	0.00182	0.00018	0.3302	0.6698	0.00020
283.15	20.85	0.0151	0.0019	0.00174	0.00021	0.3428	0.6572	0.00021
303.05	1.92	0.0024	0.0001	0.00028	0.00001	0.2808	0.7192	0.00024
303.05	5.59	0.0064	0.0004	0.00079	0.00005	0.2965	0.7035	0.00004
303.05	9.06	0.0091	0.0006	0.00110	0.00007	0.3109	0.6891	0.00026
303.05	13.30	0.0112	0.0008	0.00140	0.00010	0.3268	0.6732	0.00017
303.05	17.03	0.0120	0.0010	0.00148	0.00012	0.3375	0.6625	0.00011
303.05	20.99	0.0125	0.0012	0.00147	0.00015	0.3462	0.6538	0.00022

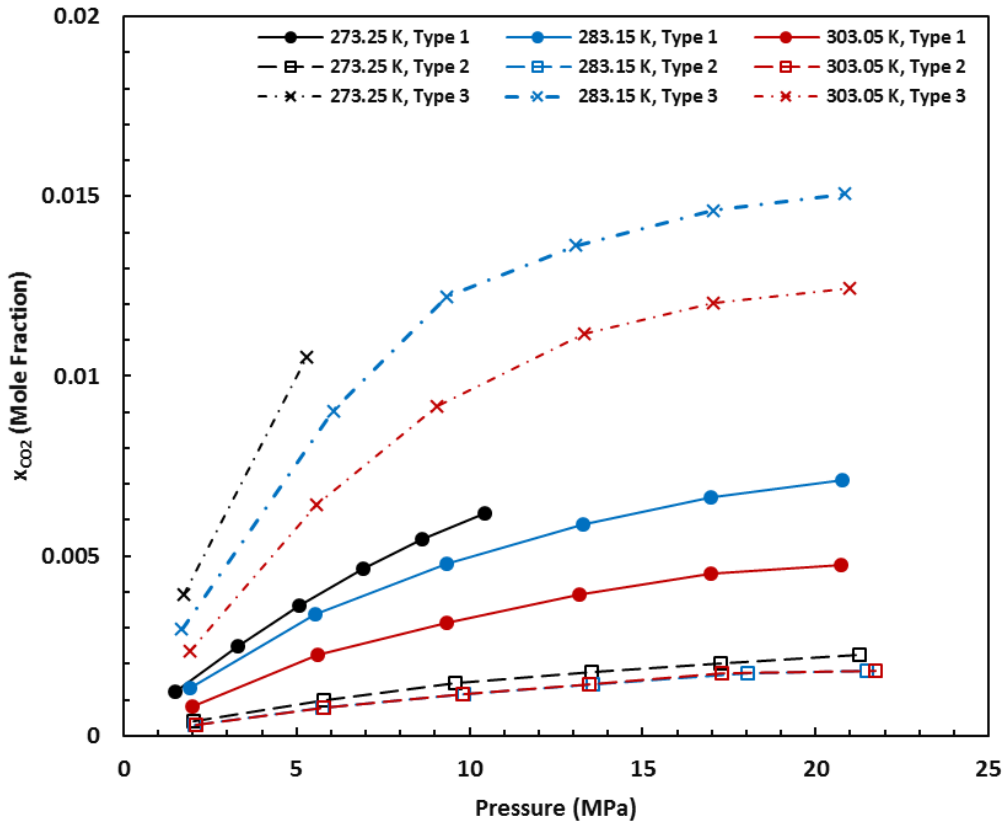

Figure S2 Experimentally determined equilibrium mole fraction of CO_2 in the liquid phase for N_2+CO_2+water systems

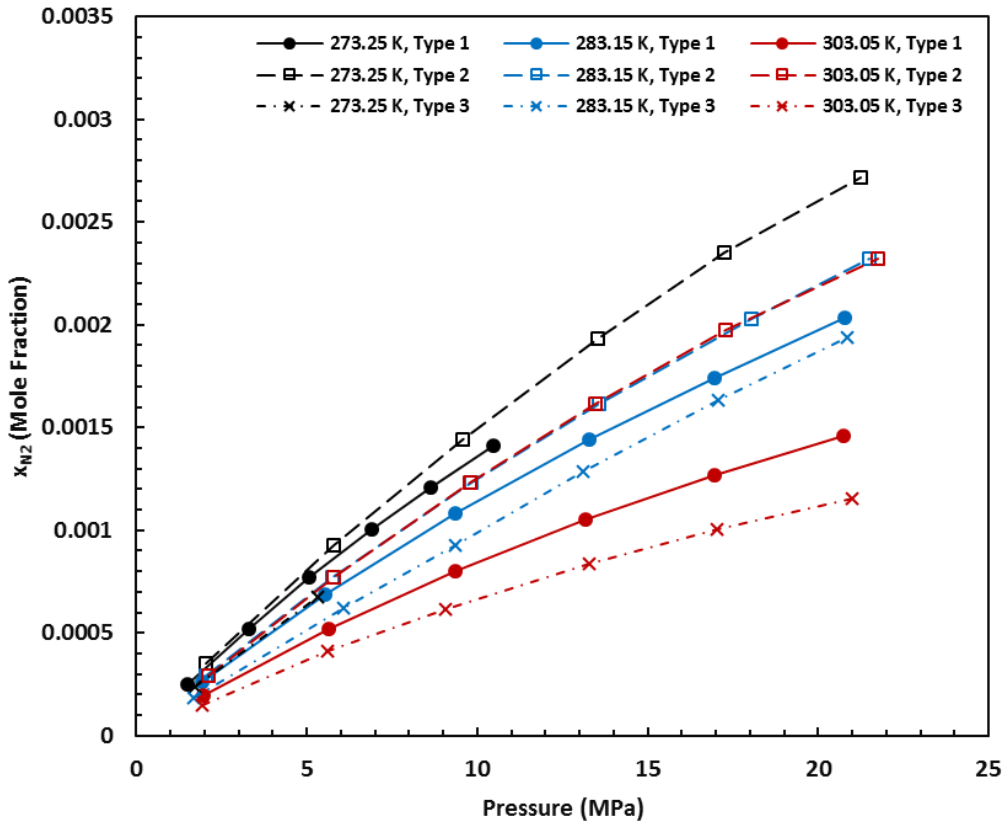

Figure S3 Experimentally determined equilibrium mole fraction of N_2 in the liquid phase for N_2+CO_2+water systems

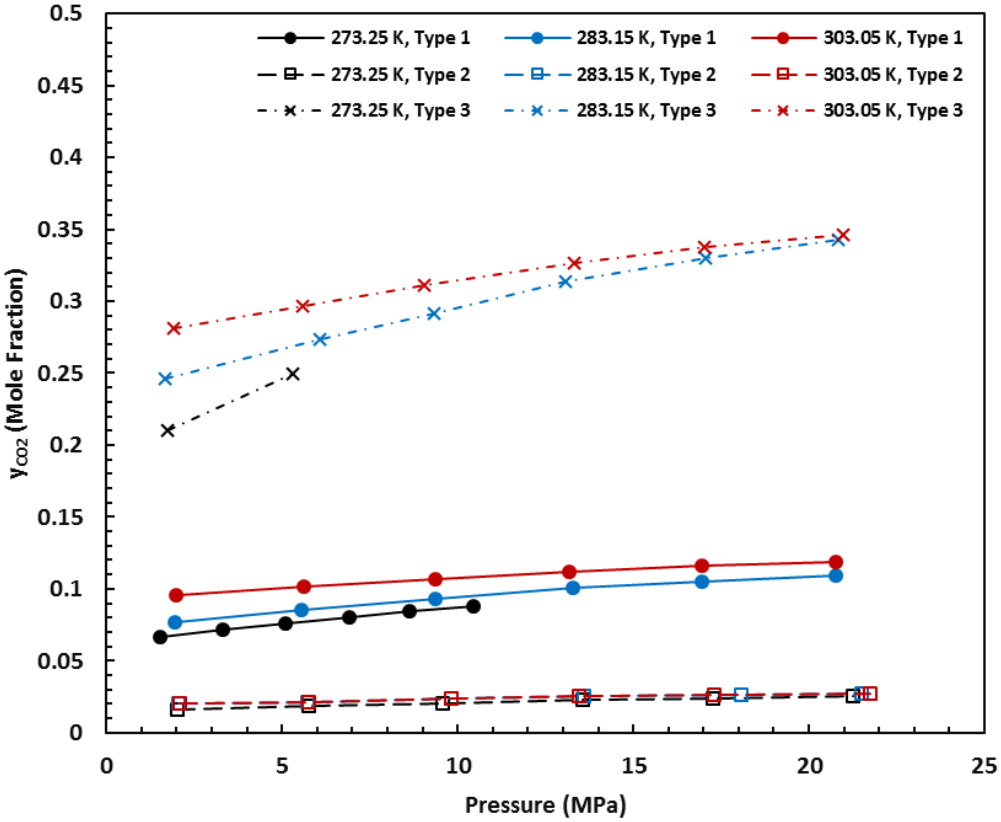

Figure S4 Experimentally determined equilibrium mole fraction of CO_2 in the vapor phase for N_2+CO_2+water systems

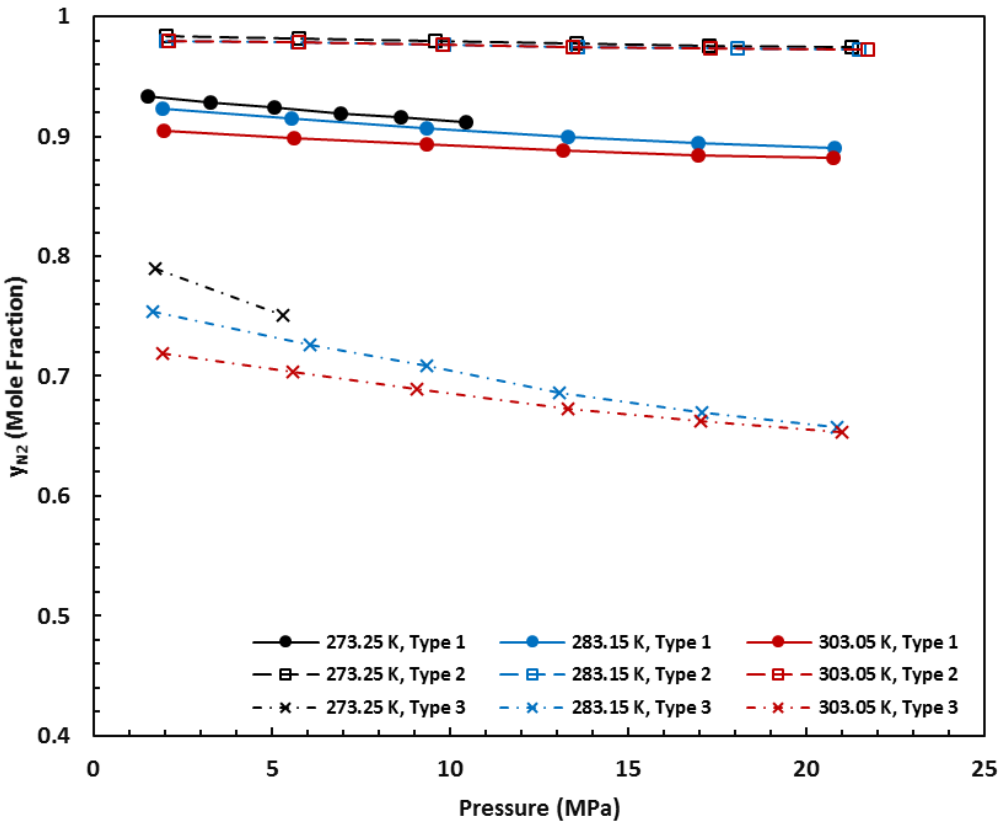

Figure S5 Experimentally determined equilibrium mole fraction of N_2 in the vapor phase for N_2+CO_2+water systems

Experimental equilibrium compositions of the liquid and vapor phases for CO_2+N_2+Brine ternary systems

Table S6 VLE data for NaCl concentration of 5 wt. %

Temperature (K)	Pressure (MPa)	Experimental Data (Mole Fraction)						
		Aqueous Phase		Expanded Uncertainty (k = 2)		Vapor Phase		
		CO_2	N_2	CO_2	N_2	CO_2	N_2	Standard Deviation
273.25	1.96	0.0013	0.0002	0.00017	0.00003	0.0734	0.9266	0.00025
273.25	5.52	0.0033	0.0006	0.00040	0.00007	0.0824	0.9176	0.00024
273.25	9.31	0.0048	0.0009	0.00057	0.00012	0.0917	0.9083	0.00000
273.25	13.43	0.0059	0.0013	0.00069	0.00015	0.1001	0.8999	0.00018
273.25	17.08	0.0066	0.0015	0.00076	0.00019	0.1063	0.8937	0.00025
273.25	21.10	0.0068	0.0018	0.00083	0.00021	0.1120	0.8880	0.00009
283.15	1.97	0.0010	0.0002	0.00012	0.00003	0.0860	0.9140	0.00010
283.15	5.66	0.0026	0.0005	0.00032	0.00005	0.0948	0.9052	0.00012
283.15	9.42	0.0037	0.0008	0.00045	0.00009	0.1027	0.8973	0.00011
283.15	13.38	0.0045	0.0011	0.00056	0.00014	0.1090	0.8910	0.00010
283.15	16.98	0.0050	0.0014	0.00058	0.00016	0.1134	0.8866	0.00027
283.15	20.89	0.0053	0.0016	0.00063	0.00019	0.1175	0.8825	0.00013
303.05	2.08	0.0009	0.0002	0.00011	0.00003	0.1006	0.8994	0.00019
303.05	5.65	0.0019	0.0004	0.00023	0.00004	0.1063	0.8937	0.00030
303.05	9.49	0.0030	0.0007	0.00038	0.00009	0.1124	0.8876	0.00015
303.05	13.33	0.0036	0.0009	0.00041	0.00011	0.1172	0.8828	0.00030
303.05	17.32	0.0042	0.0011	0.00051	0.00012	0.1206	0.8794	0.00006
303.05	20.93	0.0045	0.0013	0.00053	0.00016	0.1230	0.8770	0.00020

Table S7 VLE data for NaCl concentration of 10 wt. %

Temperature (K)	Pressure (MPa)	Experimental Data (Mole Fraction)						
		Aqueous Phase		Expanded Uncertainty (k = 2)		Vapor Phase		
		CO_2	N_2	CO_2	N_2	CO_2	N_2	Standard Deviation
273.25	2.00	0.0013	0.0002	0.00015	0.00003	0.0847	0.9153	0.00023
273.25	5.59	0.0033	0.0004	0.00041	0.00005	0.0924	0.9076	0.00015
273.25	9.42	0.0047	0.0006	0.00062	0.00007	0.1005	0.8995	0.00030
273.25	13.26	0.0056	0.0008	0.00069	0.00009	0.1076	0.8924	0.00000
273.25	17.12	0.0061	0.0010	0.00075	0.00013	0.1131	0.8869	0.00013
273.25	21.08	0.0065	0.0012	0.00074	0.00015	0.1167	0.8833	0.00015
283.15	2.02	0.0010	0.0001	0.00011	0.00001	0.0943	0.9057	0.00004
283.15	5.72	0.0025	0.0004	0.00029	0.00004	0.1016	0.8984	0.00004
283.15	9.49	0.0035	0.0006	0.00044	0.00007	0.1088	0.8912	0.00007
283.15	13.49	0.0044	0.0008	0.00053	0.00010	0.1155	0.8845	0.00028
283.15	17.09	0.0049	0.0009	0.00056	0.00010	0.1196	0.8804	0.00018
283.15	20.93	0.0051	0.0011	0.00059	0.00013	0.1229	0.8771	0.00022
303.05	1.98	0.0006	0.0001	0.00007	0.00001	0.1085	0.8915	0.00021
303.05	5.64	0.0017	0.0003	0.00021	0.00004	0.1136	0.8864	0.00019
303.05	9.51	0.0024	0.0005	0.00031	0.00006	0.1187	0.8813	0.00027
303.05	13.44	0.0030	0.0006	0.00036	0.00007	0.1222	0.8778	0.00004
303.05	17.20	0.0034	0.0008	0.00042	0.00009	0.1249	0.8751	0.00022
303.05	21.11	0.0036	0.0009	0.00043	0.00011	0.1271	0.8729	0.00021

Table S8 VLE data for NaCl concentration of 15 wt. %

Temperature (K)	Pressure (MPa)	Experimental Data (Mole Fraction)						
		Aqueous Phase		Expanded Uncertainty (k = 2)		Vapor Phase		
		CO_2	N_2	CO_2	N_2	CO_2	N_2	Standard Deviation
273.25	1.99	0.0010	0.0001	0.00011	0.00001	0.0943	0.9057	0.00006
273.25	5.76	0.0026	0.0003	0.00031	0.00004	0.1017	0.8983	0.00012
273.25	9.50	0.0035	0.0004	0.00040	0.00006	0.1085	0.8915	0.00025
273.25	13.36	0.0042	0.0006	0.00052	0.00007	0.1142	0.8858	0.00001
273.25	17.66	0.0047	0.0007	0.00056	0.00008	0.1196	0.8804	0.00020
273.25	21.56	0.0049	0.0008	0.00061	0.00010	0.1235	0.8765	0.00009
283.15	1.98	0.0008	0.0001	0.00010	0.00001	0.1019	0.8981	0.00030
283.15	5.74	0.0020	0.0003	0.00023	0.00004	0.1084	0.8916	0.00026
283.15	9.58	0.0028	0.0004	0.00034	0.00004	0.1135	0.8865	0.00015
283.15	13.41	0.0034	0.0006	0.00040	0.00007	0.1178	0.8822	0.00029
283.15	17.24	0.0039	0.0007	0.00050	0.00009	0.1221	0.8779	0.00017
283.15	21.60	0.0040	0.0008	0.00047	0.00010	0.1258	0.8742	0.00016
303.05	2.07	0.0006	0.0001	0.00007	0.00001	0.1151	0.8849	0.00001
303.05	5.81	0.0015	0.0002	0.00018	0.00003	0.1185	0.8815	0.00015
303.05	9.59	0.0022	0.0004	0.00025	0.00006	0.1210	0.8790	0.00018
303.05	13.43	0.0028	0.0005	0.00033	0.00007	0.1231	0.8769	0.00027
303.05	17.20	0.0031	0.0006	0.00037	0.00007	0.1253	0.8747	0.00020
303.05	21.28	0.0032	0.0008	0.00039	0.00009	0.1274	0.8726	0.00009

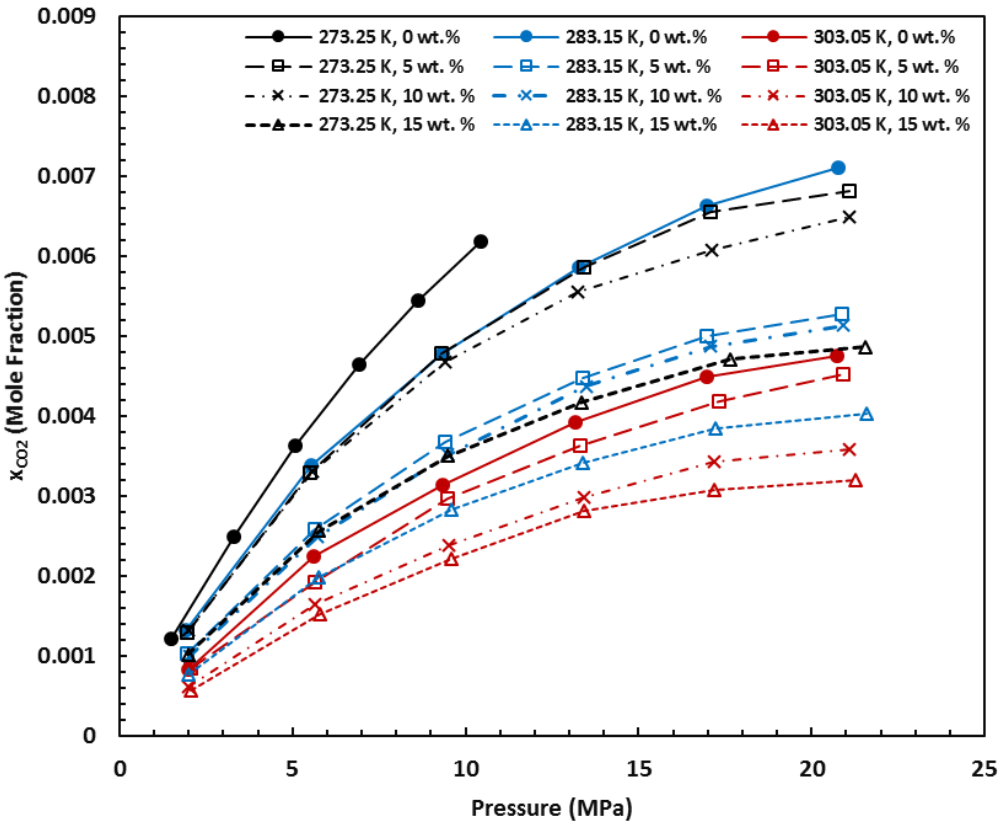

Figure S6 Experimentally determined equilibrium mole fraction of CO_2 in the liquid phase for N_2+CO_2+brine systems

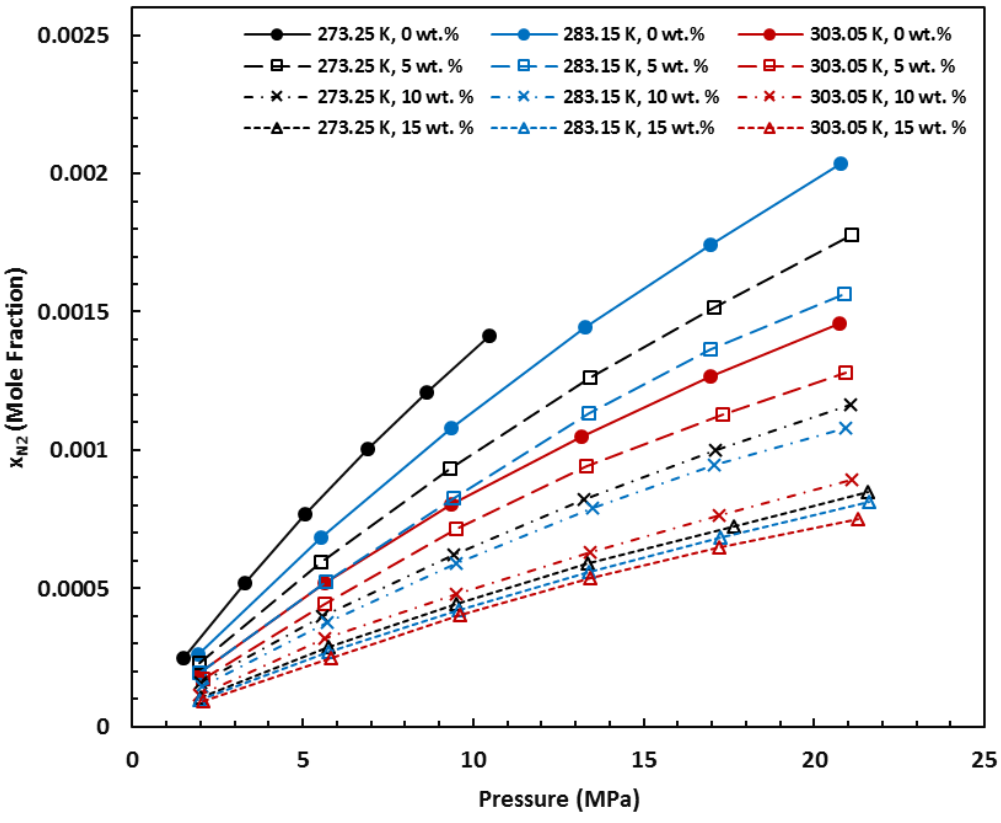

Figure S7 Experimentally determined equilibrium mole fraction of N_2 in the liquid phase for N_2+CO_2+brine systems

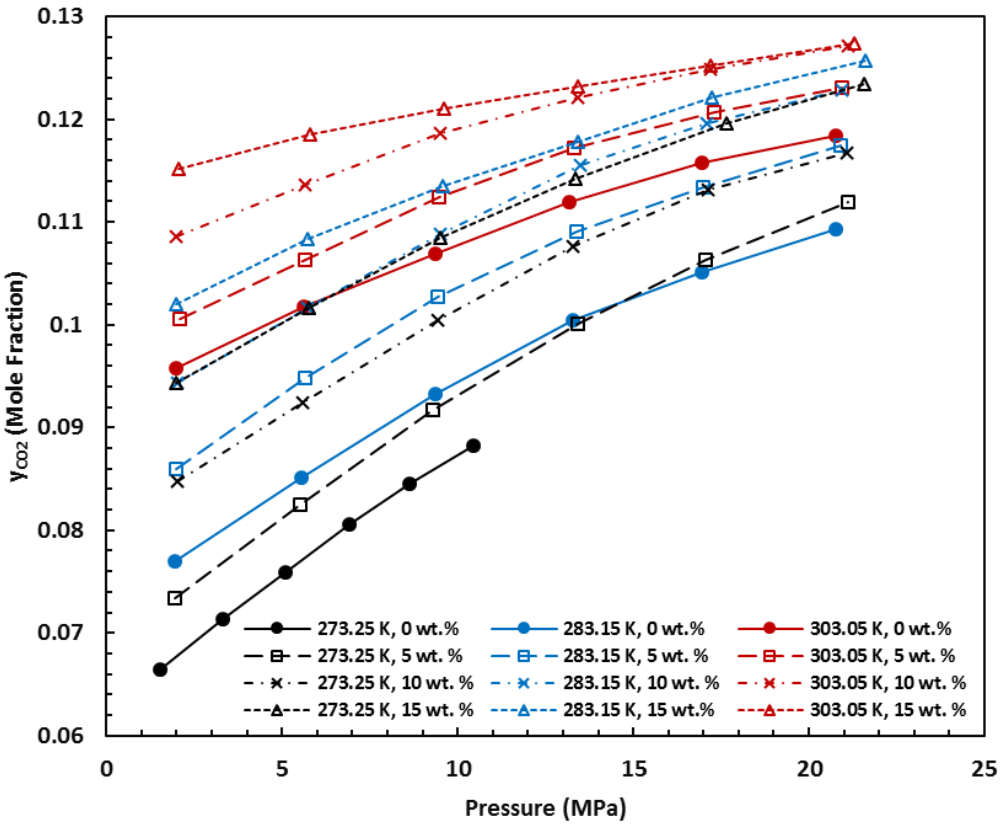

Figure S8 Experimentally determined equilibrium mole fraction of CO_2 in the vapor phase for N_2+CO_2+brine systems

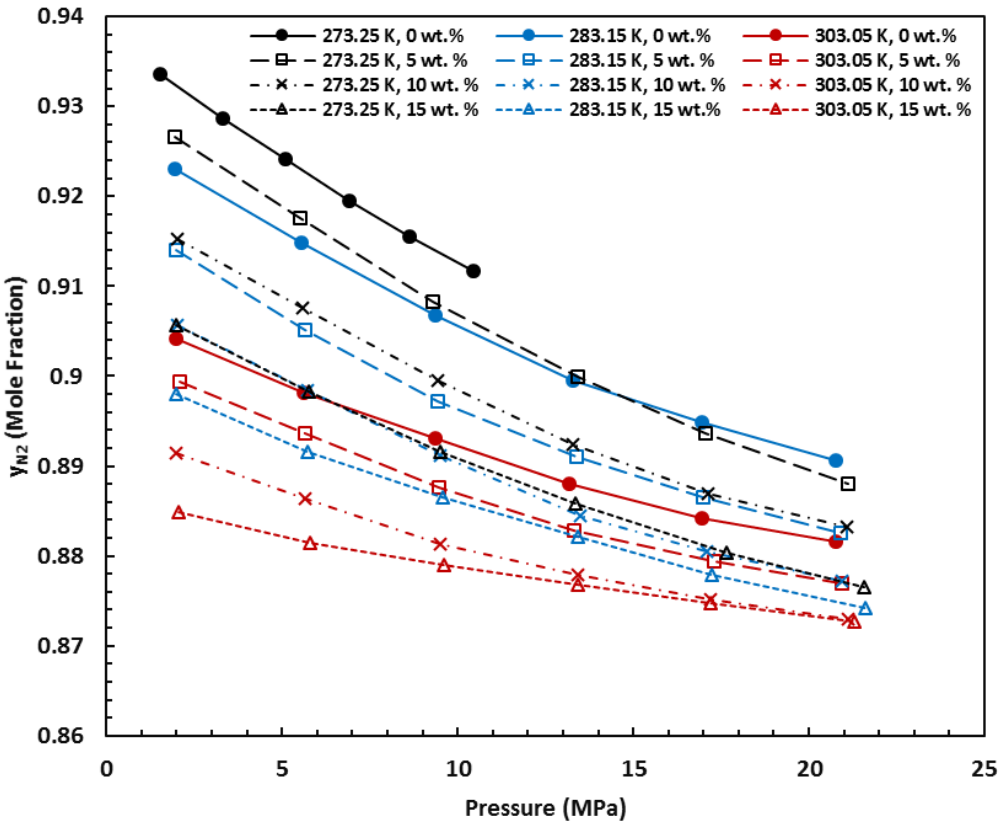

Figure S9 Experimentally determined equilibrium mole fraction of N_2 in the vapor phase for N_2+CO_2+brine systems

Predicted equilibrium compositions of the liquid and vapor phases for CO_2+N_2+Water ternary systems

Predictions of CPA-SRK72

Table S9 VLE data for injected gas type 1 predicted by CPA-SRK72

Temperature (K)	Pressure (MPa)	Predictions Made by CPA-SRK72 (Mole Fraction)				Relative Deviation (%)			
		Aqueous Phase		Vapor Phase		Aqueous Phase		Vapor Phase	
		CO_2	N_2	CO_2	N_2	CO_2	N_2	CO_2	N_2
273.25	1.51	0.0011	0.0003	0.0722	0.9193	7.67	2.24	8.73	1.53
273.25	3.30	0.0023	0.0005	0.0763	0.9163	7.71	4.47	6.88	1.33
273.25	5.08	0.0033	0.0008	0.0803	0.9125	8.98	6.50	5.87	1.26
273.25	6.92	0.0043	0.0011	0.0840	0.9088	8.28	8.14	4.32	1.15
273.25	8.63	0.0050	0.0013	0.0873	0.9056	7.75	8.65	3.31	1.08
273.25	10.46	0.0058	0.0015	0.0904	0.9024	6.85	8.60	2.46	1.02
283.15	1.93	0.0012	0.0003	0.0844	0.9099	8.60	2.78	9.68	1.42
283.15	5.55	0.0031	0.0007	0.0916	0.9037	9.51	1.27	7.59	1.22
283.15	9.35	0.0045	0.0011	0.0981	0.8980	6.82	3.54	5.15	0.96
283.15	13.30	0.0055	0.0015	0.1046	0.8933	7.01	5.02	4.16	0.70
283.15	16.96	0.0061	0.0019	0.1092	0.8896	7.94	6.44	3.95	0.59
283.15	20.78	0.0065	0.0022	0.1136	0.8862	8.58	6.96	3.93	0.50
303.05	1.98	0.0008	0.0002	0.0970	0.9007	1.83	6.02	1.26	0.39
303.05	5.63	0.0021	0.0005	0.1021	0.8969	6.29	4.33	0.32	0.14
303.05	9.35	0.0032	0.0008	0.1065	0.8929	0.97	0.81	0.38	0.03
303.05	13.17	0.0040	0.0011	0.1100	0.8894	2.98	2.42	1.69	0.15
303.05	16.97	0.0047	0.0013	0.1132	0.8863	5.23	5.31	2.26	0.24
303.05	20.75	0.0052	0.0016	0.1156	0.8839	8.71	7.83	2.33	0.26

Table S10 VLE data for injected gas type 2 predicted by CPA-SRK72

Temperature (K)	Pressure (MPa)	Predictions Made by CPA-SRK72 (Mole Fraction)				Relative Deviation (%)			
		Aqueous Phase		Vapor Phase		Aqueous Phase		Vapor Phase	
		CO_2	N_2	CO_2	N_2	CO_2	N_2	CO_2	N_2
273.25	2.03	0.0004	0.0004	0.0178	0.9798	4.43	2.60	8.82	0.38
273.25	5.77	0.0009	0.0010	0.0201	0.9783	4.69	4.04	8.92	0.33
273.25	9.58	0.0013	0.0015	0.0225	0.9764	7.91	5.14	8.93	0.30
273.25	13.55	0.0017	0.0020	0.0244	0.9748	7.19	5.07	6.55	0.23
273.25	17.26	0.0019	0.0025	0.0260	0.9736	7.39	4.91	8.07	0.24
273.25	21.27	0.0020	0.0029	0.0274	0.9725	9.54	6.63	8.28	0.22
283.15	2.05	0.0003	0.0003	0.0215	0.9778	7.45	2.05	7.55	0.22
283.15	5.74	0.0007	0.0008	0.0234	0.9763	9.17	1.24	8.88	0.22
283.15	9.84	0.0011	0.0012	0.0250	0.9748	7.59	0.37	5.23	0.15
283.15	13.58	0.0013	0.0016	0.0262	0.9736	6.76	0.04	4.09	0.12
283.15	18.06	0.0016	0.0020	0.0275	0.9724	9.00	0.41	5.03	0.15
283.15	21.50	0.0017	0.0023	0.0282	0.9717	6.55	0.51	3.66	0.12
303.05	2.10	0.0003	0.0003	0.0215	0.9778	7.45	2.05	7.55	0.22
303.05	5.78	0.0007	0.0008	0.0234	0.9763	9.17	1.24	8.88	0.22
303.05	9.80	0.0011	0.0012	0.0250	0.9748	7.59	0.37	5.23	0.15
303.05	13.45	0.0013	0.0016	0.0262	0.9736	6.76	0.04	4.09	0.12
303.05	17.30	0.0016	0.0020	0.0273	0.9726	9.81	0.25	4.27	0.13
303.05	21.74	0.0017	0.0023	0.0282	0.9717	6.55	0.51	3.66	0.12

Table S11 VLE data for injected gas type 3 predicted by CPA-SRK72

Temperature (K)	Pressure (MPa)	Predictions Made by CPA-SRK72 (Mole Fraction)				Relative Deviation (%)			
		Aqueous Phase		Vapor Phase		Aqueous Phase		Vapor Phase	
		CO_2	N_2	CO_2	N_2	CO_2	N_2	CO_2	N_2
273.25	1.73	0.0037	0.0002	0.2218	0.7618	5.87	2.46	5.33	3.50
273.25	5.31	0.0100	0.0007	0.2585	0.7354	5.26	4.22	3.57	2.01
283.15	1.68	0.0028	0.0002	0.2569	0.7423	5.19	0.93	4.42	1.55
283.15	6.07	0.0088	0.0006	0.2798	0.7199	2.61	2.81	2.21	0.87
283.15	9.34	0.0120	0.0010	0.2977	0.7020	1.57	3.23	2.11	0.91
283.15	13.09	0.0144	0.0013	0.3151	0.6847	5.64	0.17	0.37	0.20
283.15	17.06	0.0158	0.0016	0.3295	0.6702	8.15	1.20	0.21	0.07
283.15	20.85	0.0164	0.0019	0.3390	0.6607	9.14	1.79	1.11	0.54
303.05	1.92	0.0023	0.0001	0.2848	0.7127	2.61	4.12	1.44	0.90
303.05	5.59	0.0061	0.0004	0.3027	0.6963	4.37	2.08	2.11	1.03
303.05	9.06	0.0089	0.0006	0.3134	0.6858	3.10	3.90	0.80	0.47
303.05	13.30	0.0113	0.0009	0.3260	0.6733	1.17	6.39	0.26	0.02
303.05	17.03	0.0126	0.0011	0.3345	0.6648	4.62	8.07	0.90	0.36
303.05	20.99	0.0134	0.0013	0.3414	0.6579	7.20	9.31	1.40	0.64

Predictions of VPT

Table S12 VLE data for injected gas type 1 predicted by VPT

Temperature (K)	Pressure (MPa)	Predictions Made by VPT (Mole Fraction)				Relative Deviation (%)			
		Aqueous Phase		Vapor Phase		Aqueous Phase		Vapor Phase	
		CO_2	N_2	CO_2	N_2	CO_2	N_2	CO_2	N_2
273.25	1.51	0.0012	0.0002	0.0663	0.9332	1.65	0.11	0.17	0.03
273.25	3.30	0.0025	0.0005	0.0704	0.9294	1.65	0.29	1.46	0.09
273.25	5.08	0.0037	0.0008	0.0749	0.9250	1.62	0.44	1.25	0.09
273.25	6.92	0.0047	0.0010	0.0794	0.9205	2.04	0.80	1.45	0.11
273.25	8.63	0.0056	0.0012	0.0833	0.9166	2.22	1.02	1.41	0.12
273.25	10.46	0.0063	0.0014	0.0871	0.9128	2.36	1.23	1.33	0.12
283.15	1.93	0.0013	0.0003	0.0790	0.9203	2.46	0.58	2.67	0.30
283.15	5.55	0.0033	0.0007	0.0872	0.9125	2.80	0.27	2.43	0.26
283.15	9.35	0.0048	0.0011	0.0933	0.9065	0.44	0.11	0.04	0.03
283.15	13.30	0.0060	0.0014	0.0998	0.9000	1.98	0.39	0.63	0.05
283.15	16.96	0.0067	0.0017	0.1048	0.8951	1.75	0.17	0.30	0.02
283.15	20.78	0.0073	0.0020	0.1088	0.8910	2.83	0.51	0.45	0.04
303.05	1.98	0.0009	0.0002	0.0925	0.9052	6.55	1.65	3.43	0.11
303.05	5.63	0.0022	0.0005	0.0989	0.9001	0.09	1.73	2.81	0.21
303.05	9.35	0.0033	0.0008	0.1044	0.8950	6.00	4.04	2.35	0.21
303.05	13.17	0.0042	0.0011	0.1088	0.8907	6.37	6.41	2.80	0.29
303.05	16.97	0.0048	0.0014	0.1126	0.8869	5.79	8.55	2.77	0.31
303.05	20.75	0.0052	0.0016	0.1155	0.8841	9.24	10.64	2.43	0.28

Table S13 VLE data for injected gas type 2 predicted by VPT

Temperature (K)	Pressure (MPa)	Predictions Made by VPT (Mole Fraction)				Relative Deviation (%)			
		Aqueous Phase		Vapor Phase		Aqueous Phase		Vapor Phase	
		CO_2	N_2	CO_2	N_2	CO_2	N_2	CO_2	N_2
273.25	2.03	0.0004	0.0004	0.0163	0.9834	0.88	0.15	0.69	0.02
273.25	5.77	0.0010	0.0009	0.0182	0.9817	1.55	0.10	1.22	0.01
273.25	9.58	0.0015	0.0014	0.0203	0.9796	2.26	0.34	1.46	0.02
273.25	13.55	0.0019	0.0019	0.0221	0.9778	5.30	1.41	3.16	0.07
273.25	17.26	0.0021	0.0023	0.0236	0.9763	6.33	2.19	2.01	0.04
273.25	21.27	0.0024	0.0027	0.0248	0.9751	4.72	1.14	1.79	0.04
283.15	2.05	0.0003	0.0003	0.0188	0.9806	7.09	0.55	6.18	0.06
283.15	5.74	0.0008	0.0008	0.0209	0.9788	3.84	0.17	2.69	0.03
283.15	9.84	0.0013	0.0012	0.0228	0.9771	7.11	0.20	4.11	0.08
283.15	13.58	0.0015	0.0016	0.0242	0.9756	7.96	0.02	3.84	0.08
283.15	18.06	0.0018	0.0020	0.0257	0.9742	5.16	0.09	1.75	0.03
283.15	21.50	0.0020	0.0023	0.0266	0.9733	7.85	0.23	2.35	0.05
303.05	2.10	0.0003	0.0003	0.0188	0.9806	7.09	0.55	6.18	0.06
303.05	5.78	0.0008	0.0008	0.0209	0.9788	3.84	0.17	2.69	0.03
303.05	9.80	0.0013	0.0012	0.0228	0.9771	7.11	0.20	4.11	0.08
303.05	13.45	0.0015	0.0016	0.0242	0.9756	7.96	0.02	3.84	0.08
303.05	17.30	0.0018	0.0020	0.0255	0.9744	3.42	0.25	2.51	0.05
303.05	21.74	0.0020	0.0023	0.0266	0.9733	7.85	0.23	2.35	0.05

Table S14 VLE data for injected gas type 3 predicted by VPT

Temperature (K)	Pressure (MPa)	Predictions Made by VPT (Mole Fraction)				Relative Deviation (%)			
		Aqueous Phase		Vapor Phase		Aqueous Phase		Vapor Phase	
		CO_2	N_2	CO_2	N_2	CO_2	N_2	CO_2	N_2
273.25	1.73	0.0041	0.0002	0.2004	0.7992	4.59	0.87	4.83	1.24
273.25	5.31	0.0111	0.0007	0.2375	0.7623	5.32	2.35	4.81	1.58
283.15	1.68	0.0032	0.0002	0.2289	0.7703	9.66	1.31	6.97	2.17
283.15	6.07	0.0099	0.0006	0.2615	0.7382	9.59	5.32	4.51	1.66
283.15	9.34	0.0129	0.0009	0.2847	0.7151	5.59	5.61	2.36	0.94
283.15	13.09	0.0148	0.0012	0.3060	0.6938	8.50	7.44	2.52	1.12
283.15	17.06	0.0158	0.0015	0.3229	0.6769	8.49	9.15	2.22	1.06
283.15	20.85	0.0164	0.0018	0.3337	0.6661	8.51	9.33	2.66	1.36
303.05	1.92	0.0025	0.0002	0.2738	0.7238	5.67	2.91	2.50	0.64
303.05	5.59	0.0065	0.0004	0.2968	0.7022	0.92	0.38	0.10	0.19
303.05	9.06	0.0091	0.0006	0.3106	0.6886	0.31	1.96	0.10	0.07
303.05	13.30	0.0113	0.0009	0.3257	0.6737	1.37	3.93	0.35	0.07
303.05	17.03	0.0125	0.0011	0.3354	0.6640	3.93	4.98	0.63	0.22
303.05	20.99	0.0133	0.0012	0.3430	0.6563	6.97	5.92	0.92	0.39

Predictions of PC-SAFT

Table S15 VLE data for injected gas type 1 predicted by PC-SAFT

Temperature (K)	Pressure (MPa)	Predictions Made by PC-SAFT (Mole Fraction)				Relative Deviation (%)			
		Aqueous Phase		Vapor Phase		Aqueous Phase		Vapor Phase	
		CO_2	N_2	CO_2	N_2	CO_2	N_2	CO_2	N_2
273.25	1.51	0.0012	0.0002	0.0711	0.9285	4.45	12.17	6.97	0.54
273.25	3.30	0.0024	0.0005	0.0748	0.9250	4.42	12.93	4.76	0.39
273.25	5.08	0.0035	0.0007	0.0791	0.9207	4.52	11.95	4.31	0.37
273.25	6.92	0.0044	0.0009	0.0835	0.9164	4.33	11.51	3.61	0.33
273.25	8.63	0.0052	0.0011	0.0873	0.9126	4.49	12.50	3.35	0.32
273.25	10.46	0.0059	0.0012	0.0911	0.9088	4.83	13.51	3.25	0.33
283.15	1.93	0.0012	0.0002	0.0825	0.9168	7.62	12.44	7.11	0.67
283.15	5.55	0.0031	0.0006	0.0903	0.9094	8.18	9.67	6.06	0.59
283.15	9.35	0.0045	0.0010	0.0964	0.9034	5.80	7.38	3.37	0.37
283.15	13.30	0.0055	0.0013	0.1031	0.8967	5.59	7.84	2.63	0.31
283.15	16.96	0.0062	0.0016	0.1082	0.8917	7.03	8.50	2.95	0.36
283.15	20.78	0.0066	0.0018	0.1123	0.8875	7.17	10.19	2.72	0.35
303.05	1.98	0.0008	0.0002	0.0957	0.9020	0.07	12.43	0.09	0.24
303.05	5.63	0.0021	0.0005	0.1021	0.8969	6.91	11.90	0.33	0.14
303.05	9.35	0.0031	0.0007	0.1077	0.8917	2.62	10.90	0.74	0.16
303.05	13.17	0.0038	0.0009	0.1123	0.8872	3.82	10.93	0.33	0.10
303.05	16.97	0.0043	0.0011	0.1163	0.8833	4.82	11.82	0.39	0.10
303.05	20.75	0.0046	0.0013	0.1193	0.8803	2.57	11.90	0.75	0.15

Table S16 VLE data for injected gas type 2 predicted by PC-SAFT

Temperature (K)	Pressure (MPa)	Predictions Made by PC-SAFT (Mole Fraction)				Relative Deviation (%)			
		Aqueous Phase		Vapor Phase		Aqueous Phase		Vapor Phase	
		CO_2	N_2	CO_2	N_2	CO_2	N_2	CO_2	N_2
273.25	2.03	0.0004	0.0003	0.0175	0.9821	5.41	11.84	7.09	0.15
273.25	5.77	0.0009	0.0008	0.0196	0.9803	5.75	12.40	6.10	0.13
273.25	9.58	0.0014	0.0013	0.0218	0.9781	6.62	9.59	5.60	0.13
273.25	13.55	0.0017	0.0018	0.0237	0.9762	5.63	9.33	3.72	0.10
273.25	17.26	0.0019	0.0021	0.0252	0.9747	6.30	10.32	4.85	0.13
273.25	21.27	0.0020	0.0024	0.0265	0.9734	9.28	11.28	4.92	0.13
283.15	2.05	0.0003	0.0003	0.0198	0.9796	1.23	13.35	1.37	0.04
283.15	5.74	0.0008	0.0007	0.0219	0.9778	2.95	10.78	2.14	0.07
283.15	9.84	0.0012	0.0011	0.0239	0.9759	1.52	11.05	0.77	0.04
283.15	13.58	0.0014	0.0014	0.0255	0.9744	2.50	11.69	1.18	0.05
283.15	18.06	0.0016	0.0018	0.0271	0.9728	6.97	11.80	3.44	0.11
283.15	21.50	0.0017	0.0020	0.0280	0.9719	5.89	13.40	2.79	0.09
303.05	2.10	0.0003	0.0003	0.0198	0.9796	1.23	13.35	1.37	0.04
303.05	5.78	0.0008	0.0007	0.0219	0.9778	2.95	10.78	2.14	0.07
303.05	9.80	0.0012	0.0011	0.0239	0.9759	1.52	9.84	0.77	0.04
303.05	13.45	0.0014	0.0015	0.0255	0.9744	2.50	9.83	1.18	0.05
303.05	17.30	0.0016	0.0018	0.0268	0.9731	6.97	8.90	2.29	0.08
303.05	21.74	0.0018	0.0021	0.0280	0.9719	3.14	10.82	2.79	0.09

Table S17 VLE data for injected gas type 3 predicted by PC-SAFT

Temperature (K)	Pressure (MPa)	Predictions Made by PC-SAFT (Mole Fraction)				Relative Deviation (%)			
		Aqueous Phase		Vapor Phase		Aqueous Phase		Vapor Phase	
		CO_2	N_2	CO_2	N_2	CO_2	N_2	CO_2	N_2
273.25	1.73	0.0039	0.0002	0.2113	0.7883	0.52	11.06	0.38	0.15
273.25	5.31	0.0109	0.0006	0.2415	0.7584	3.50	7.33	3.23	1.05
283.15	1.68	0.0031	0.0002	0.2367	0.7625	4.89	11.54	3.79	1.13
283.15	6.07	0.0097	0.0006	0.2638	0.7359	7.30	9.74	3.66	1.34
283.15	9.34	0.0127	0.0008	0.2852	0.7146	4.34	8.35	2.17	0.86
283.15	13.09	0.0146	0.0011	0.3062	0.6936	7.34	11.46	2.46	1.10
283.15	17.06	0.0158	0.0014	0.3233	0.6765	8.13	12.40	2.10	1.00
283.15	20.85	0.0163	0.0017	0.3341	0.6657	8.34	13.25	2.53	1.28
303.05	1.92	0.0024	0.0001	0.2810	0.7166	0.33	13.46	0.06	0.36
303.05	5.59	0.0062	0.0004	0.3015	0.6975	4.00	13.25	1.70	0.86
303.05	9.06	0.0087	0.0006	0.3145	0.6848	5.09	9.75	1.16	0.63
303.05	13.30	0.0107	0.0008	0.3293	0.6701	4.25	7.32	0.76	0.46
303.05	17.03	0.0117	0.0009	0.3390	0.6604	2.83	7.79	0.45	0.32
303.05	20.99	0.0123	0.0011	0.3466	0.6528	0.95	8.45	0.10	0.15

Predicted equilibrium compositions of the liquid and vapor phases for CO_2+N_2+Brine ternary systems

Predictions of CPA-SRK72

Table S18 VLE data for NaCl concentration of 5 wt. % predicted by CPA-SRK72

Temperature (K)	Pressure (MPa)	Predictions Made by CPA-SRK72 (Mole Fraction)				Relative Deviation (%)			
		Aqueous Phase		Vapor Phase		Aqueous Phase		Vapor Phase	
		CO_2	N_2	CO_2	N_2	CO_2	N_2	CO_2	N_2
273.25	1.96	0.0012	0.0002	0.0784	0.9162	7.20	1.96	6.78	1.11
273.25	5.52	0.0031	0.0006	0.0873	0.9086	5.10	5.08	5.84	0.98
273.25	9.31	0.0046	0.0010	0.0956	0.9013	4.74	6.61	4.28	0.77
273.25	13.43	0.0056	0.0014	0.1035	0.8944	4.84	7.24	3.38	0.61
273.25	17.08	0.0062	0.0016	0.1093	0.8896	5.56	8.33	2.79	0.45
273.25	21.10	0.0066	0.0019	0.1153	0.8846	3.86	8.20	2.94	0.38
283.15	1.97	0.0010	0.0002	0.0906	0.9087	6.51	1.40	5.40	0.58
283.15	5.66	0.0025	0.0005	0.0978	0.9019	4.56	0.09	3.12	0.36
283.15	9.42	0.0036	0.0008	0.1038	0.8960	1.39	0.41	1.01	0.14
283.15	13.38	0.0045	0.0011	0.1092	0.8906	0.82	1.04	0.18	0.04
283.15	16.98	0.0051	0.0014	0.1131	0.8867	1.55	0.12	0.26	0.01
283.15	20.89	0.0055	0.0016	0.1166	0.8833	4.57	2.35	0.79	0.09
303.05	2.08	0.0008	0.0002	0.1063	0.8916	6.43	5.36	5.70	0.87
303.05	5.65	0.0019	0.0004	0.1106	0.8885	0.76	8.39	4.01	0.58
303.05	9.49	0.0029	0.0007	0.1149	0.8844	1.54	8.14	2.22	0.35
303.05	13.33	0.0037	0.0009	0.1182	0.8813	1.65	5.72	0.83	0.17
303.05	17.32	0.0043	0.0011	0.1211	0.8785	2.98	5.25	0.34	0.10
303.05	20.93	0.0047	0.0012	0.1230	0.8766	4.56	5.86	0.04	0.05

Table S19 VLE data for NaCl concentration of 10 wt. % predicted by CPA-SRK72

Temperature (K)	Pressure (MPa)	Predictions Made by CPA-SRK72 (Mole Fraction)				Relative Deviation (%)			
		Aqueous Phase		Vapor Phase		Aqueous Phase		Vapor Phase	
		CO_2	N_2	CO_2	N_2	CO_2	N_2	CO_2	N_2
273.25	2.00	0.0012	0.0002	0.0930	0.9037	6.86	3.79	9.80	1.26
273.25	5.59	0.0031	0.0004	0.1013	0.8966	7.51	6.51	9.62	1.22
273.25	9.42	0.0044	0.0007	0.1082	0.8907	6.91	8.58	7.73	0.99
273.25	13.26	0.0052	0.0009	0.1143	0.8852	5.93	9.51	6.20	0.80
273.25	17.12	0.0057	0.0011	0.1189	0.8810	6.11	9.89	5.17	0.67
273.25	21.08	0.0060	0.0013	0.1222	0.8778	7.31	8.91	4.66	0.63
283.15	2.02	0.0009	0.0001	0.1000	0.8994	9.80	1.90	6.03	0.70
283.15	5.72	0.0023	0.0004	0.1067	0.8931	6.12	0.23	4.94	0.59
283.15	9.49	0.0033	0.0006	0.1123	0.8875	6.47	0.81	3.18	0.41
283.15	13.49	0.0040	0.0008	0.1173	0.8825	9.15	0.96	1.53	0.22
283.15	17.09	0.0044	0.0010	0.1206	0.8792	9.31	2.28	0.87	0.14
283.15	20.93	0.0047	0.0011	0.1235	0.8764	7.55	4.41	0.52	0.09
303.05	1.98	0.0006	0.0001	0.1086	0.8892	5.31	0.62	0.06	0.25
303.05	5.64	0.0017	0.0003	0.1139	0.8852	0.78	3.66	0.25	0.13
303.05	9.51	0.0025	0.0005	0.1176	0.8815	4.52	2.42	0.96	0.02
303.05	13.44	0.0031	0.0007	0.1209	0.8786	5.43	5.92	1.02	0.08
303.05	17.20	0.0036	0.0008	0.1231	0.8764	5.15	6.92	1.43	0.15
303.05	21.11	0.0039	0.0010	0.1251	0.8745	7.74	7.98	1.58	0.18

Table S20 VLE data for NaCl concentration of 15 wt. % predicted by CPA-SRK72

Temperature (K)	Pressure (MPa)	Predictions Made by CPA-SRK72 (Mole Fraction)				Relative Deviation (%)			
		Aqueous Phase		Vapor Phase		Aqueous Phase		Vapor Phase	
		CO_2	N_2	CO_2	N_2	CO_2	N_2	CO_2	N_2
273.25	1.99	0.0009	0.0001	0.0994	0.9003	8.70	0.84	5.33	0.59
273.25	5.76	0.0024	0.0003	0.1067	0.8932	6.25	2.20	4.92	0.57
273.25	9.50	0.0033	0.0005	0.1127	0.8872	4.93	2.23	3.88	0.48
273.25	13.36	0.0040	0.0006	0.1180	0.8819	5.19	1.76	3.38	0.45
273.25	17.66	0.0044	0.0007	0.1224	0.8775	7.36	3.35	2.37	0.33
273.25	21.56	0.0046	0.0009	0.1255	0.8744	5.64	2.75	1.63	0.24
283.15	1.98	0.0007	0.0001	0.1033	0.8961	2.35	0.61	1.30	0.22
283.15	5.74	0.0019	0.0003	0.1105	0.8892	3.94	0.27	1.99	0.27
283.15	9.58	0.0027	0.0004	0.1158	0.8840	3.39	0.05	2.02	0.28
283.15	13.41	0.0033	0.0006	0.1201	0.8797	3.44	0.08	1.94	0.28
283.15	17.24	0.0037	0.0007	0.1234	0.8765	4.34	0.38	1.02	0.16
283.15	21.60	0.0040	0.0008	0.1262	0.8736	1.57	0.20	0.37	0.07
303.05	2.07	0.0006	0.0001	0.1142	0.8838	3.13	2.37	0.84	0.12
303.05	5.81	0.0015	0.0002	0.1175	0.8817	4.08	1.71	0.86	0.02
303.05	9.59	0.0021	0.0004	0.1207	0.8787	3.58	5.21	0.22	0.04
303.05	13.43	0.0027	0.0005	0.1235	0.8760	5.62	4.88	0.28	0.10
303.05	17.20	0.0030	0.0006	0.1256	0.8740	1.35	3.40	0.23	0.08
303.05	21.28	0.0034	0.0007	0.1274	0.8722	4.81	1.28	0.00	0.05

Predictions of VPT

Table S21 VLE data for NaCl concentration of 5 wt. % predicted by VPT

Temperature (K)	Pressure (MPa)	Predictions Made by VPT (Mole Fraction)				Relative Deviation (%)			
		Aqueous Phase		Vapor Phase		Aqueous Phase		Vapor Phase	
		CO_2	N_2	CO_2	N_2	CO_2	N_2	CO_2	N_2
273.25	1.96	0.0013	0.0002	0.0710	0.93	4.69	0.65	3.29	0.22
273.25	5.52	0.0034	0.0006	0.0803	0.92	3.45	1.13	2.59	0.22
273.25	9.31	0.0050	0.0009	0.0890	0.91	4.90	2.36	2.87	0.28
273.25	13.43	0.0061	0.0012	0.0972	0.90	4.63	3.68	2.88	0.31
273.25	17.08	0.0068	0.0015	0.1029	0.90	3.06	3.82	3.21	0.37
273.25	21.10	0.0072	0.0017	0.1088	0.89	6.14	4.72	2.84	0.35
283.15	1.97	0.0011	0.0002	0.0814	0.92	7.51	1.03	5.34	0.43
283.15	5.66	0.0027	0.0005	0.0900	0.91	5.36	0.12	5.03	0.50
283.15	9.42	0.0039	0.0008	0.0973	0.90	6.75	1.73	5.27	0.58
283.15	13.38	0.0048	0.0011	0.1038	0.90	7.41	4.48	4.75	0.56
283.15	16.98	0.0053	0.0013	0.1085	0.89	6.44	4.38	4.35	0.54
283.15	20.89	0.0057	0.0015	0.1125	0.89	8.15	2.51	4.22	0.55
303.05	2.08	0.0009	0.0002	0.1029	0.90	1.23	3.89	2.29	0.49
303.05	5.65	0.0021	0.0004	0.1083	0.89	7.03	4.73	1.83	0.32
303.05	9.49	0.0031	0.0007	0.1136	0.89	2.70	6.12	0.99	0.20
303.05	13.33	0.0038	0.0009	0.1175	0.88	4.18	4.71	0.23	0.09
303.05	17.32	0.0043	0.0011	0.1209	0.88	3.91	1.35	0.17	0.07
303.05	20.93	0.0047	0.0013	0.1231	0.88	4.22	1.01	0.05	0.05

Table S22 VLE data for NaCl concentration of 10 wt. % predicted by VPT

Temperature (K)	Pressure (MPa)	Predictions Made by VPT (Mole Fraction)				Relative Deviation (%)			
		Aqueous Phase		Vapor Phase		Aqueous Phase		Vapor Phase	
		CO_2	N_2	CO_2	N_2	CO_2	N_2	CO_2	N_2
273.25	2.00	0.0013	0.0002	0.0844	0.9153	0.69	0.00	0.36	0.00
273.25	5.59	0.0032	0.0004	0.0935	0.9064	1.70	0.73	1.19	0.14
273.25	9.42	0.0047	0.0006	0.1009	0.8990	0.52	0.49	0.40	0.06
273.25	13.26	0.0056	0.0008	0.1075	0.8924	0.67	0.01	0.09	0.00
273.25	17.12	0.0062	0.0010	0.1127	0.8873	1.76	0.54	0.37	0.04
273.25	21.08	0.0066	0.0012	0.1166	0.8834	1.24	0.12	0.13	0.01
283.15	2.02	0.0010	0.0001	0.0916	0.9078	5.34	0.63	2.89	0.23
283.15	5.72	0.0026	0.0004	0.0998	0.9000	4.33	0.07	1.83	0.18
283.15	9.49	0.0037	0.0006	0.1066	0.8932	5.98	0.44	2.00	0.22
283.15	13.49	0.0046	0.0008	0.1127	0.8871	4.33	1.32	2.46	0.30
283.15	17.09	0.0051	0.0009	0.1167	0.8832	3.73	0.53	2.43	0.31
283.15	20.93	0.0054	0.0011	0.1201	0.8798	5.44	1.35	2.28	0.30
303.05	1.98	0.0007	0.0001	0.1053	0.8925	9.26	9.91	2.97	0.12
303.05	5.64	0.0018	0.0003	0.1117	0.8874	7.45	3.10	1.68	0.12
303.05	9.51	0.0026	0.0005	0.1162	0.8832	9.34	4.61	2.11	0.22
303.05	13.44	0.0032	0.0007	0.1202	0.8793	8.55	8.71	1.63	0.17
303.05	17.20	0.0037	0.0008	0.1228	0.8768	6.75	6.11	1.69	0.19
303.05	21.11	0.0039	0.0010	0.1251	0.8745	9.94	6.88	1.60	0.19

Table S23 VLE data for NaCl concentration of 15 wt. % predicted by VPT

Temperature (K)	Pressure (MPa)	Predictions Made by VPT (Mole Fraction)				Relative Deviation (%)			
		Aqueous Phase		Vapor Phase		Aqueous Phase		Vapor Phase	
		CO_2	N_2	CO_2	N_2	CO_2	N_2	CO_2	N_2
273.25	1.99	0.0011	0.0001	0.0870	0.9130	4.07	1.14	7.75	0.81
273.25	5.76	0.0028	0.0003	0.0958	0.9041	7.52	2.44	5.74	0.64
273.25	9.50	0.0038	0.0004	0.1033	0.8966	8.34	4.04	4.72	0.56
273.25	13.36	0.0046	0.0006	0.1100	0.8899	9.69	5.46	3.63	0.46
273.25	17.66	0.0051	0.0007	0.1155	0.8844	8.70	4.58	3.40	0.45
273.25	21.56	0.0053	0.0008	0.1193	0.8806	9.93	5.29	3.34	0.46
283.15	1.98	0.0008	0.0001	0.0940	0.9054	9.78	2.32	7.84	0.82
283.15	5.74	0.0021	0.0003	0.1029	0.8969	8.24	0.77	5.07	0.59
283.15	9.58	0.0031	0.0004	0.1094	0.8904	8.48	0.15	3.58	0.44
283.15	13.41	0.0037	0.0006	0.1147	0.8851	7.88	0.83	2.60	0.33
283.15	17.24	0.0041	0.0007	0.1188	0.8811	6.10	0.86	2.75	0.37
283.15	21.60	0.0043	0.0008	0.1222	0.8776	7.11	1.10	2.81	0.39
303.05	2.07	0.0006	0.0001	0.1105	0.8875	7.44	5.99	4.02	0.30
303.05	5.81	0.0016	0.0003	0.1148	0.8844	4.69	5.72	3.13	0.33
303.05	9.59	0.0023	0.0004	0.1188	0.8806	3.48	1.35	1.81	0.18
303.05	13.43	0.0028	0.0005	0.1221	0.8774	0.21	1.37	0.80	0.06
303.05	17.20	0.0032	0.0007	0.1247	0.8749	3.01	2.82	0.50	0.02
303.05	21.28	0.0035	0.0008	0.1268	0.8729	8.16	5.13	0.46	0.02

Predictions of PC-SAFT

Table S24 VLE data for NaCl concentration of 5 wt. % predicted by PC-SAFT

Temperature (K)	Pressure (MPa)	Predictions Made by PC-SAFT (Mole Fraction)				Relative Deviation (%)			
		Aqueous Phase		Vapor Phase		Aqueous Phase		Vapor Phase	
		CO_2	N_2	CO_2	N_2	CO_2	N_2	CO_2	N_2
273.25	1.96	0.0013	0.0002	0.0745	0.9252	0.21	13.76	1.38	0.15
273.25	5.52	0.0032	0.0005	0.0834	0.9165	1.57	11.08	1.11	0.11
273.25	9.31	0.0047	0.0008	0.0920	0.9079	0.89	11.69	0.40	0.05
273.25	13.43	0.0058	0.0011	0.1004	0.8996	0.90	11.34	0.28	0.04
273.25	17.08	0.0064	0.0013	0.1062	0.8937	2.35	11.97	0.12	0.00
273.25	21.10	0.0068	0.0016	0.1120	0.8879	0.49	12.07	0.04	0.01
283.15	1.97	0.0011	0.0002	0.0837	0.9156	3.32	11.30	2.60	0.17
283.15	5.66	0.0027	0.0005	0.0922	0.9075	4.62	12.85	2.77	0.26
283.15	9.42	0.0039	0.0007	0.0996	0.9003	6.62	11.37	3.10	0.33
283.15	13.38	0.0048	0.0010	0.1063	0.8935	6.94	12.22	2.49	0.29
283.15	16.98	0.0053	0.0012	0.1111	0.8887	5.84	11.54	2.02	0.24
283.15	20.89	0.0057	0.0014	0.1153	0.8846	7.21	10.29	1.88	0.23
303.05	2.08	0.0008	0.0002	0.1052	0.8927	4.53	10.60	4.60	0.75
303.05	5.65	0.0019	0.0004	0.1106	0.8886	0.19	11.31	3.99	0.57
303.05	9.49	0.0029	0.0006	0.1159	0.8835	1.84	12.09	3.11	0.46
303.05	13.33	0.0036	0.0008	0.1200	0.8795	0.08	12.19	2.40	0.38
303.05	17.32	0.0041	0.0010	0.1235	0.8760	1.90	10.76	2.37	0.38
303.05	20.93	0.0044	0.0012	0.1258	0.8738	1.88	10.04	2.26	0.37

Table S25 VLE data for NaCl concentration of 10 wt. % predicted by PC-SAFT

Temperature (K)	Pressure (MPa)	Predictions Made by PC-SAFT (Mole Fraction)				Relative Deviation (%)			
		Aqueous Phase		Vapor Phase		Aqueous Phase		Vapor Phase	
		CO_2	N_2	CO_2	N_2	CO_2	N_2	CO_2	N_2
273.25	2.00	0.0013	0.0001	0.0876	0.9121	4.52	10.74	3.34	0.34
273.25	5.59	0.0031	0.0004	0.0962	0.9037	6.94	8.87	4.12	0.43
273.25	9.42	0.0044	0.0006	0.1036	0.8963	6.65	6.33	3.07	0.35
273.25	13.26	0.0052	0.0008	0.1103	0.8896	6.87	6.67	2.50	0.31
273.25	17.12	0.0056	0.0009	0.1155	0.8844	7.30	8.44	2.17	0.29
273.25	21.08	0.0059	0.0010	0.1194	0.8805	8.97	11.40	2.32	0.32
283.15	2.02	0.0010	0.0001	0.0936	0.9057	1.02	10.41	0.69	0.00
283.15	5.72	0.0025	0.0003	0.1017	0.8981	0.25	10.35	0.02	0.03
283.15	9.49	0.0035	0.0005	0.1086	0.8912	0.32	10.61	0.20	0.00
283.15	13.49	0.0042	0.0007	0.1148	0.8850	2.81	10.78	0.61	0.06
283.15	17.09	0.0046	0.0008	0.1189	0.8809	4.77	12.39	0.53	0.06
283.15	20.93	0.0049	0.0009	0.1224	0.8775	4.54	12.50	0.38	0.04
303.05	1.98	0.0007	0.0001	0.1075	0.8903	7.63	14.84	0.94	0.13
303.05	5.64	0.0017	0.0003	0.1139	0.8853	0.30	12.89	0.22	0.12
303.05	9.51	0.0024	0.0004	0.1185	0.8810	0.67	10.03	0.19	0.04
303.05	13.44	0.0029	0.0006	0.1226	0.8769	1.94	6.56	0.35	0.10
303.05	17.20	0.0033	0.0007	0.1253	0.8743	5.28	9.03	0.35	0.10
303.05	21.11	0.0035	0.0008	0.1277	0.8719	2.78	9.27	0.45	0.11

Table S26 VLE data for NaCl concentration of 15 wt. % predicted by PC-SAFT

Temperature (K)	Pressure (MPa)	Predictions Made by PC-SAFT (Mole Fraction)				Relative Deviation (%)			
		Aqueous Phase		Vapor Phase		Aqueous Phase		Vapor Phase	
		CO_2	N_2	CO_2	N_2	CO_2	N_2	CO_2	N_2
273.25	1.99	0.0011	0.0001	0.0913	0.9084	5.35	11.07	3.23	0.30
273.25	5.76	0.0027	0.0003	0.0999	0.8999	3.46	11.36	1.68	0.18
273.25	9.50	0.0037	0.0004	0.1073	0.8926	5.26	10.14	1.04	0.12
273.25	13.36	0.0043	0.0005	0.1140	0.8859	4.01	11.75	0.15	0.01
273.25	17.66	0.0047	0.0006	0.1194	0.8805	0.34	11.41	0.15	0.01
273.25	21.56	0.0049	0.0007	0.1231	0.8769	1.27	12.60	0.32	0.04
283.15	1.98	0.0008	0.0001	0.0972	0.9022	9.98	10.22	4.66	0.46
283.15	5.74	0.0021	0.0002	0.1058	0.8939	7.23	11.82	2.33	0.26
283.15	9.58	0.0030	0.0004	0.1124	0.8874	6.05	11.50	0.97	0.10
283.15	13.41	0.0036	0.0005	0.1178	0.8821	3.78	11.73	0.02	0.01
283.15	17.24	0.0039	0.0006	0.1219	0.8780	0.77	12.75	0.23	0.02
283.15	21.60	0.0041	0.0007	0.1253	0.8746	1.78	12.71	0.39	0.04
303.05	2.07	0.0006	0.0001	0.1132	0.8848	5.54	11.03	1.67	0.01
303.05	5.81	0.0014	0.0002	0.1175	0.8817	4.54	10.90	0.86	0.02
303.05	9.59	0.0021	0.0004	0.1216	0.8779	7.15	10.25	0.46	0.13
303.05	13.43	0.0025	0.0005	0.1250	0.8746	9.99	11.62	1.49	0.26
303.05	17.20	0.0028	0.0006	0.1275	0.8721	8.16	10.96	1.80	0.31
303.05	21.28	0.0030	0.0007	0.1297	0.8700	6.49	10.85	1.82	0.31

GC measurements

A gas chromatograph (Varian 3600, Agilent Technologies) was employed for compositional analysis of the samples collected from the measurement vessel by the capillary sampler. The carrier gas for all the measurements was research-grade Helium (purity 99.9995 vol. % supplied by BOC Ltd) and the detector type was Thermal Conductivity Detector (TCD) which measures the variations in the thermal conductivity of the effluent gas from the GC column (Packed Column supplied by Restek) and compares it against that of the carrier gas (Helium) reference flow. For each point, the CG column temperature was set at 323 K for 10 minutes during which three samples taken by the sampler were injected; then, the temperature ramped up to 378 K for 1 minute at the rate of 323 K/min in order to vaporize the content of the column.

The CG was calibrated to achieve an accurate quantification of the proportion of each component of the sample at any instant. Known volumes of pure compounds (N_2, CO_2) were injected into the GC in order to find their signature chromatograms, retention times, and peak area. Thereafter, to obtain the calibration correlations, the moles of each compound at different volumes (in mole/m^3) were plotted versus their corresponding peak areas. Table S27 summarizes the correlation types and coefficients:

Table S27 Calibration correlation type and coefficients of GC for N_2 and CO_2

Compound	Correlation Type	Correlation Coefficients	R^2
CO_2	Linear, $y = ax$	$a = 2.8199 \times 10^{-11}$	0.9997
N_2		$a = 3.006 \times 10^{-11}$	0.9992

The calibration equations were then used for estimation of the relative amount of their corresponding components in the vapor phase. When summed together, the proportion of each individual component in the vapor phase could be estimated.

Appendix B for Chapter 3

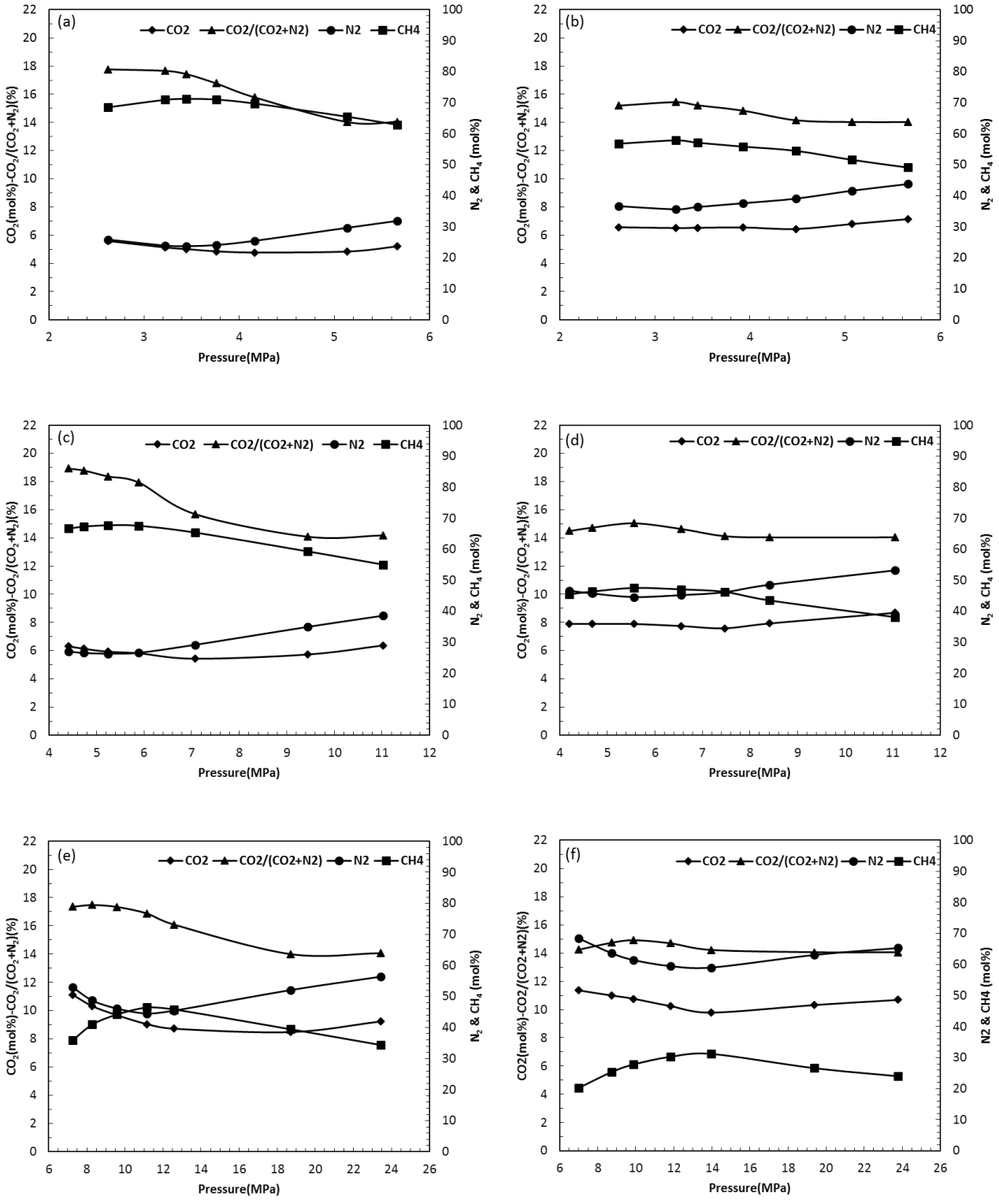

Figure 1 Variation in the system composition change during the stepwise depressurization. (a)-(f) for Experiments 1-6. System composition is made up of all gases in the water, hydrate and gas phases, were calculated using mass balance and measurement of the removed gas at end of each depressurization stage.

Appendix C for Chapter 5

Sand Characterization

Table S1 Mineralogical composition of 8 samples from Fife sand analysed using X-ray diffraction: As can be seen it is mainly consist of four types of minerals; quartz, microcline, calcite, and kaolinite.

Sample	Quartz /%	Microcline /%	Calcite /%	Kaolinite /%
1	100	Trace	0	0
2	97	3	0	0
3	97	3	0	Trace
4	97	3	0	Trace
5	97	3	Trace	Trace
6	97	3	0	Trace
7	97	3	Trace	Trace
8	97	3	0	Trace

Table S2 Particle size distribution for the silica sand determined by using a Malvern Mastersizer (MS1000) which measures the particle size distribution based on the principle of laser scattering.

Size/ µm	Ratio/mass%	Size/ µm	Ratio/mass%	Size/µm	Ratio / mass %	Size/µm	Ratio/mass%	Size/µm	Ratio/mass%
600	0.9	166	3.0	46.2	0.3	12.8	0.1	3.55	0.0
544	1.2	151	2.1	41.8	0.2	11.6	0.1	3.22	0.0
493	1.9	137	1.5	37.9	0.2	10.5	0.1	2.92	0.0
446	3.3	124	1.3	34.3	0.2	9.52	0.0	2.64	0.0
404	5.2	112	1.0	31.1	0.1	8.63	0.0	2.39	0.0
366	7.6	102	0.8	28.2	0.1	7.82	0.0	2.17	0.0
332	10.2	92.1	0.7	25.5	0.1	7.08	0.0	1.97	0.1
301	12.0	83.4	0.6	23.1	0.1	6.42	0.0	1.78	0.1
273	12.6	75.6	0.5	21	0.1	4.82	0.0	1.61	0.1
247	11.3	68.5	0.5	19	0.1	5.27	0.0	1.46	0.1
224	8.2	62.1	0.4	17.2	0.1	4.77	0.0	1.32	0.1
203	5.7	56.2	0.4	15.6	0.1	4.33	0.0	1.2	0.1
184	4.1	50.9	0.3	14.1	0.1	3.92	0.0		
Mass medium = 256.54 µm				Specific surface area = 0.0236 m^2/g					

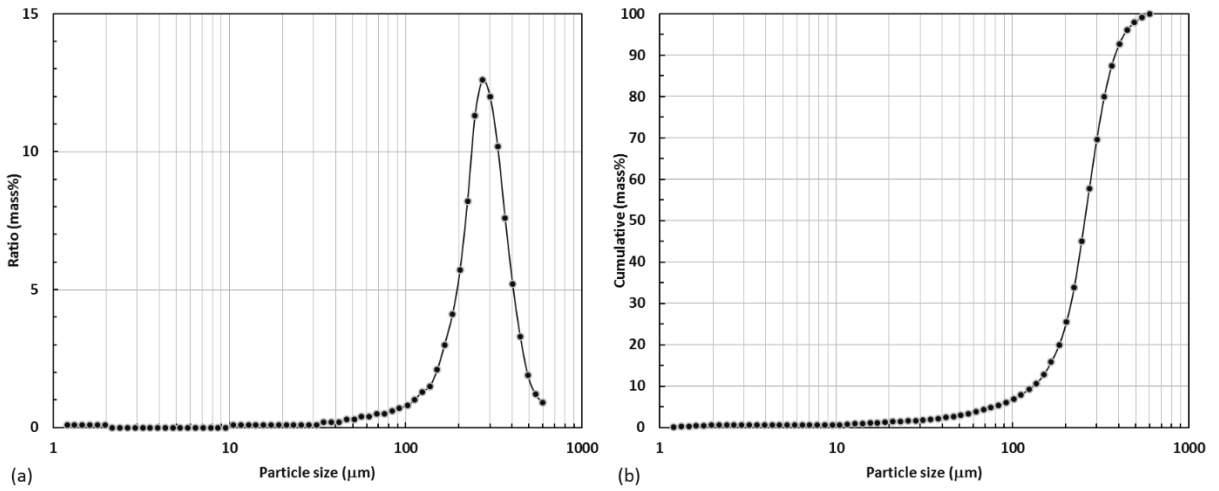

Figure S1 Particle size distributions of the sand determined by using the Malvern Mastersize.

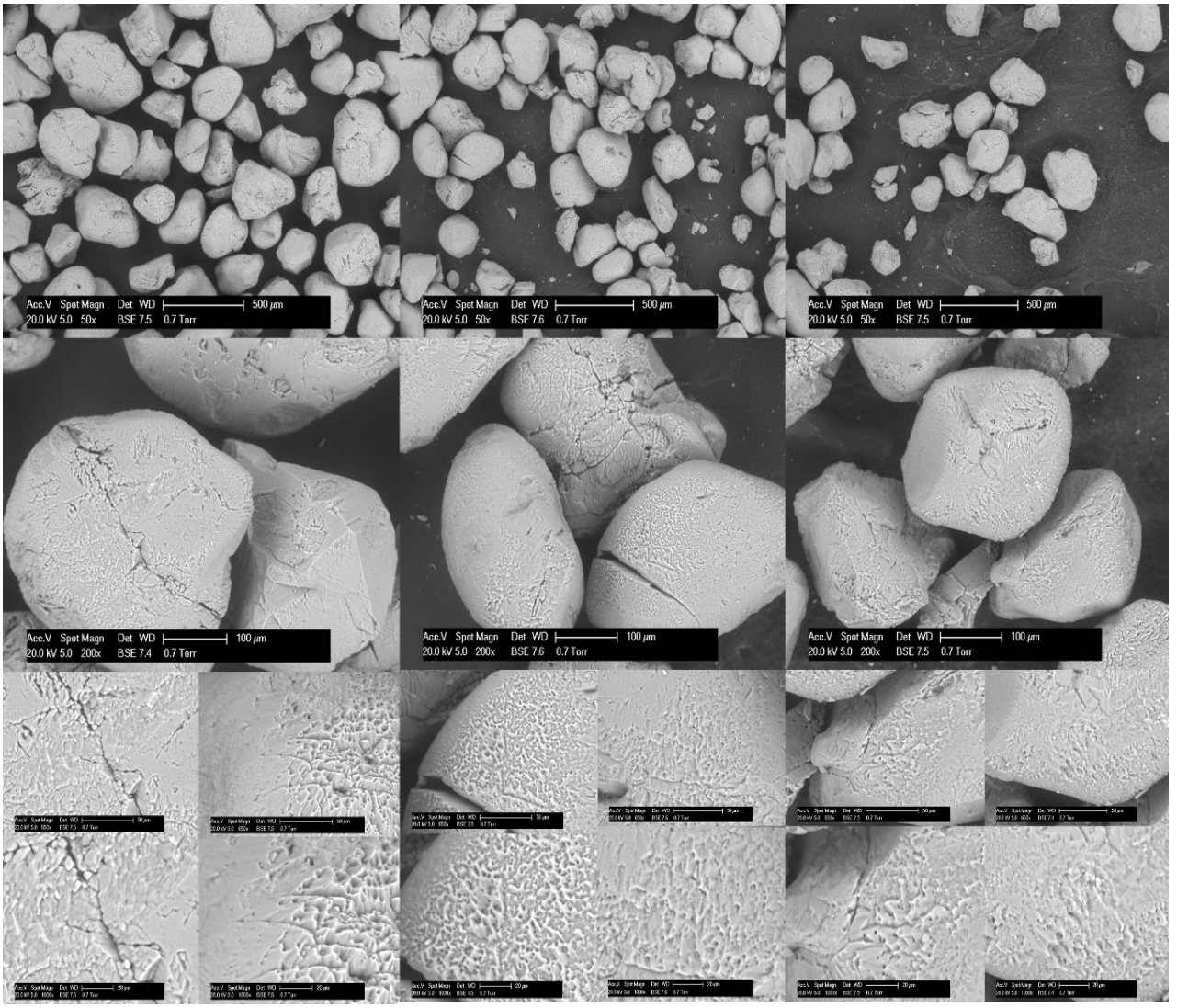

Figure S2 ESEM micrographs of the sands obtained by using a FEI Quanta 650 FEG SEM, with a back scattered electron (BSE) imaging detector.

Table S3 Density, Young's modulus, and Poisson's ratio of Fife silica sand.

Density	r =	2.64		g/cm3
Young' modulus	E =	19.98 - 24.86		GPa
Poisson's ratio	g =	0.12-0.17		

More Detailed Results

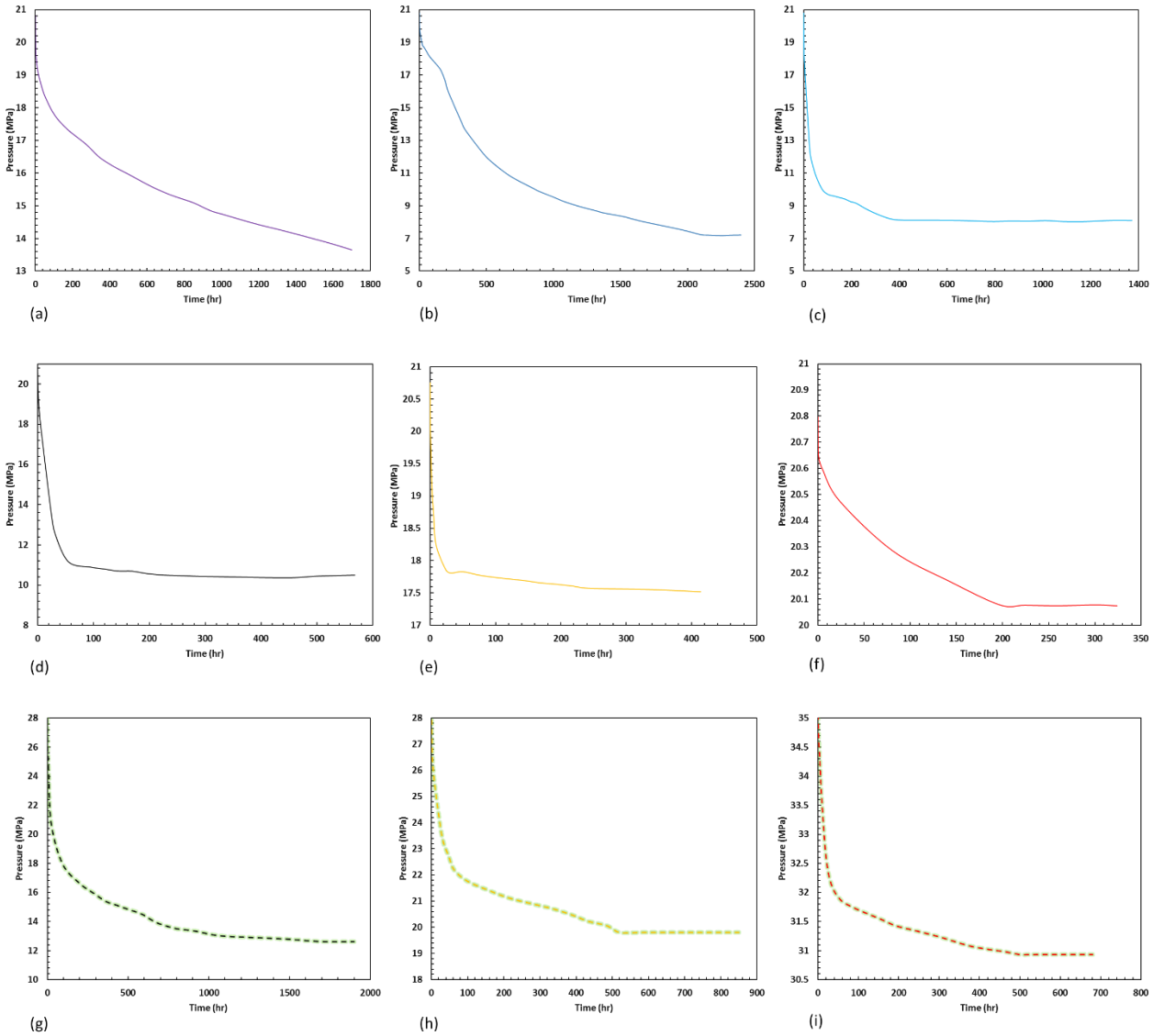

Figure S3 Detailed Pressure Changes after flue gas injection (a)-(i) for Exp1-9.

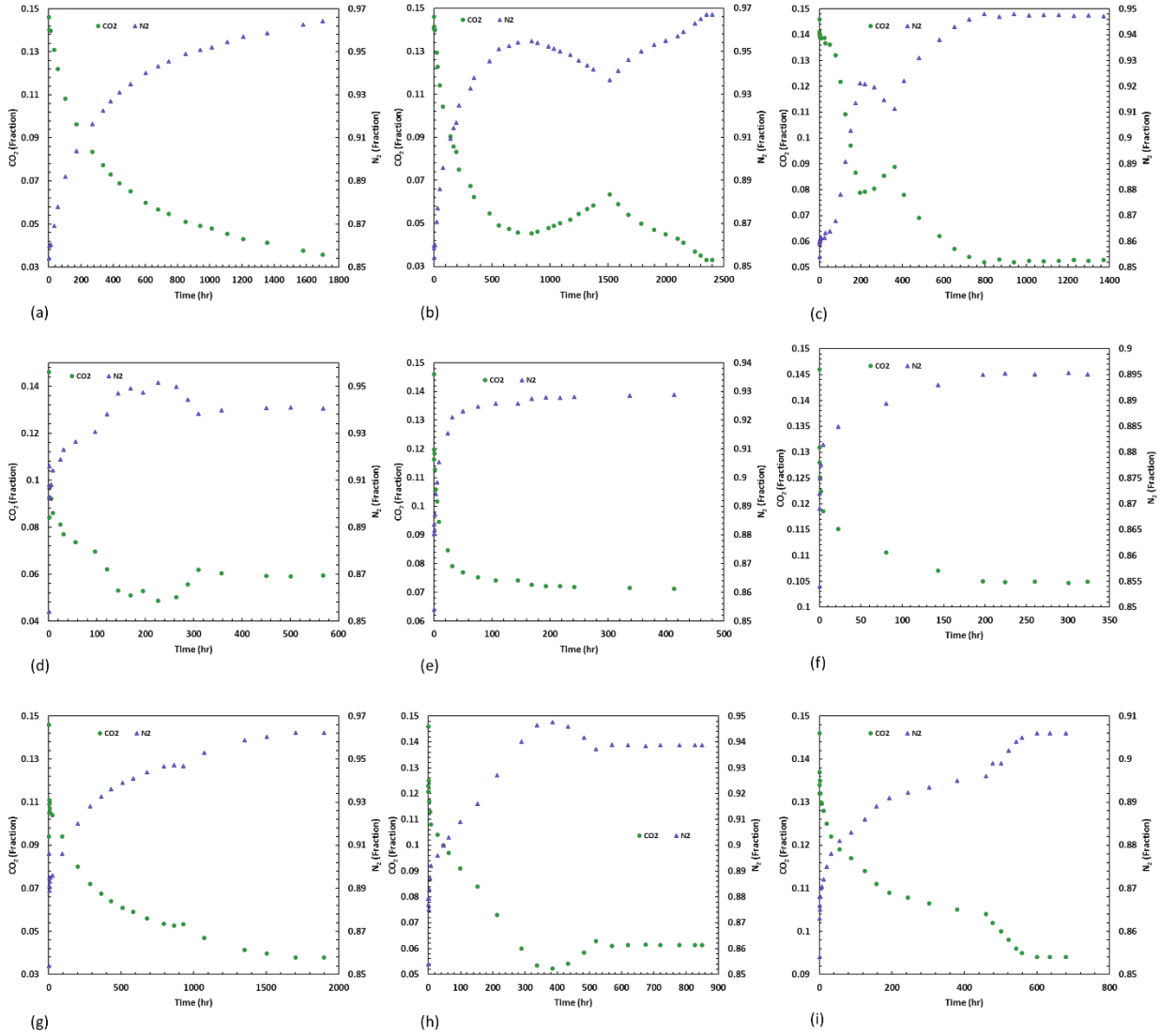

Figure S4 Detailed Changes in CO2 and N2 concentration in the gas phase after flue gas injection (a)-(i) for Exp1-9.

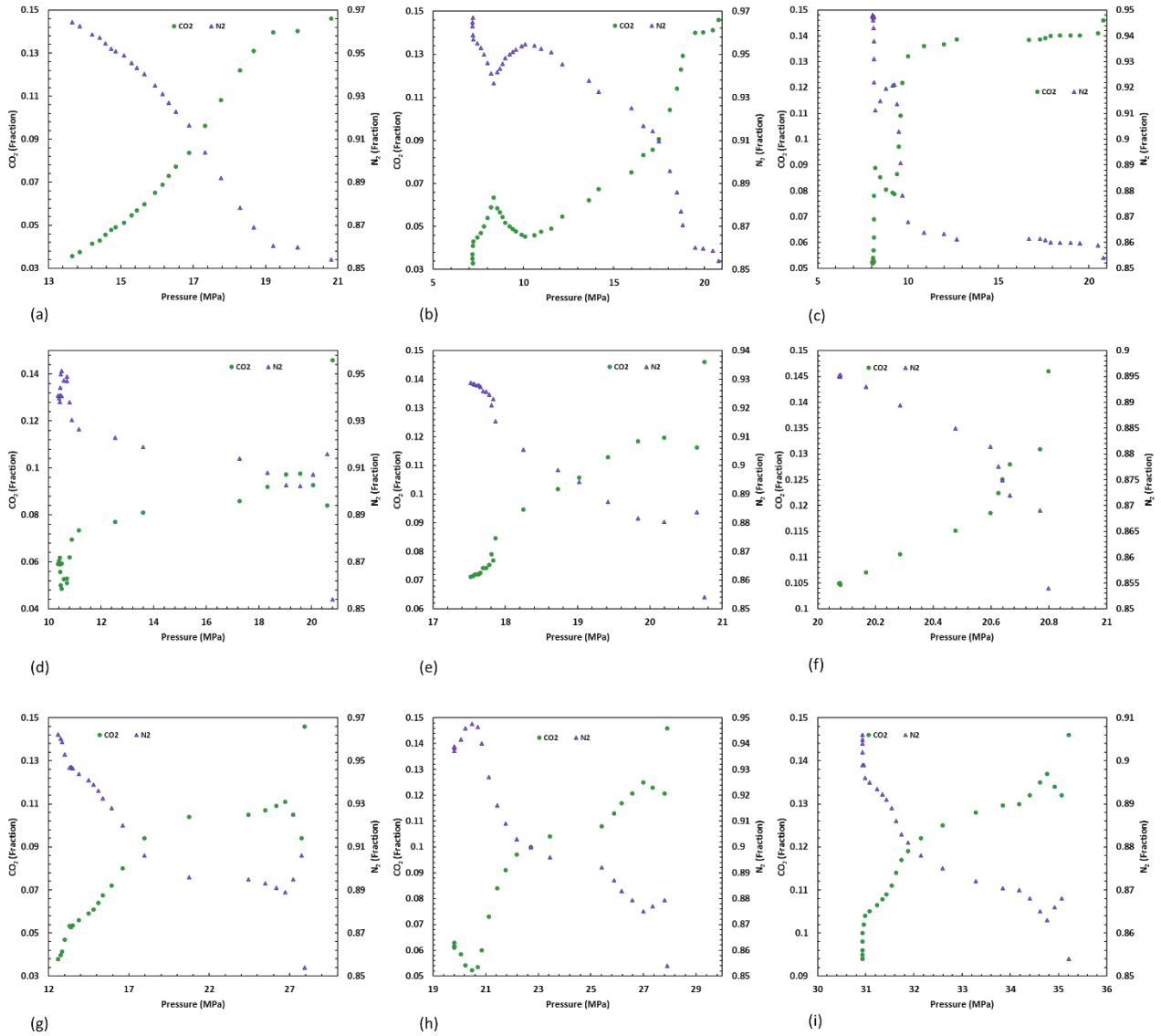

Figure S5 Detailed changes in CO2 and N2 concentration in the gas phase versus pressure after flue gas injection (a)-(i) for Exp1-9.

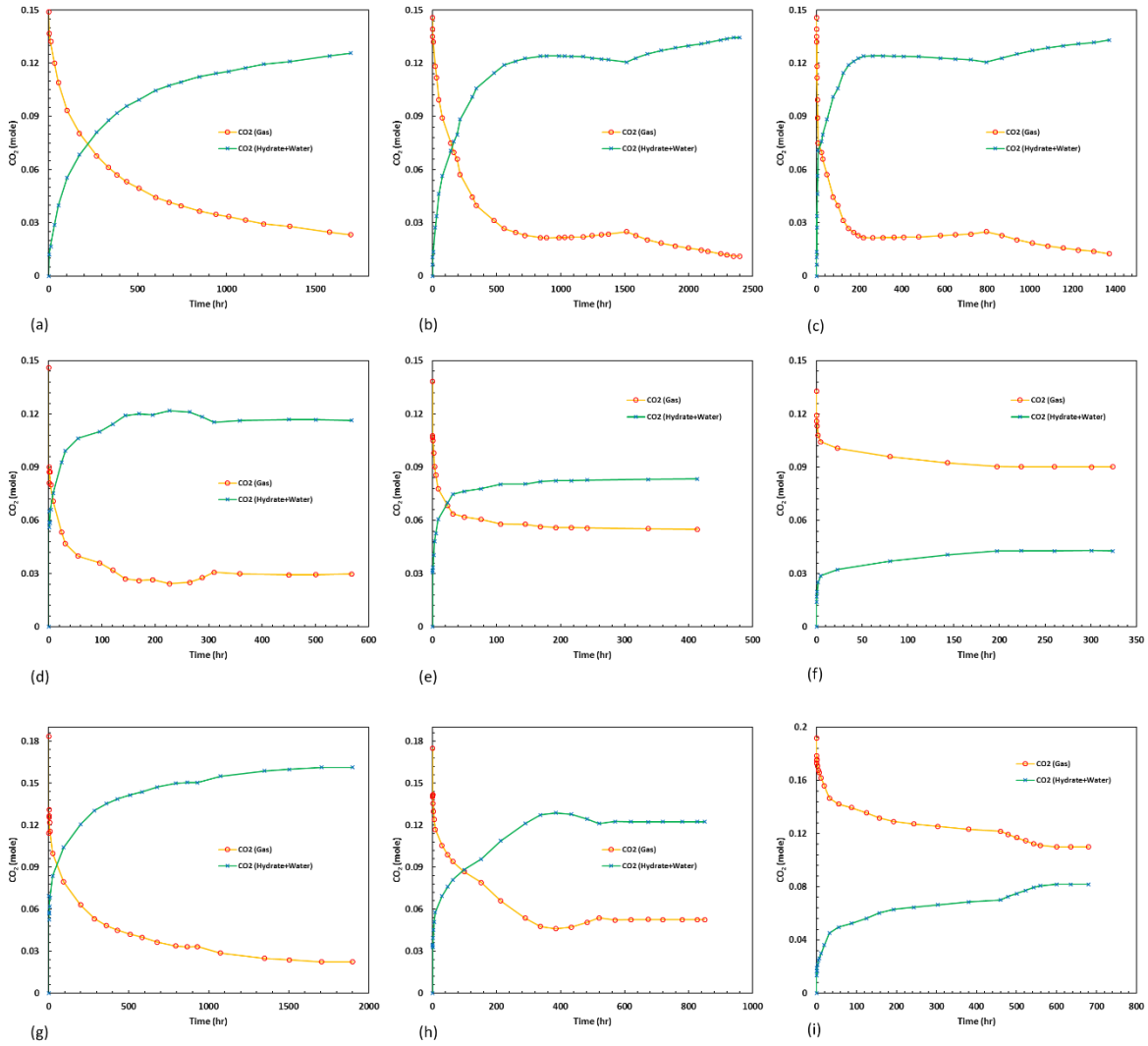

Figure S6 Quantities of CO2 moles in the gas phase and Hydrate + Water phases versus time after flue gas injection (a)-(i) for Exp1-9. Thermodynamic behaviour of the fluid system at different pressures, temperatures and compositions were modelled using CPA equation of state for the non-solid phase, with the Peng-Robinson equation of state as the non-association part, and a modified van der Waals and Platteeuw method for the solid phase.

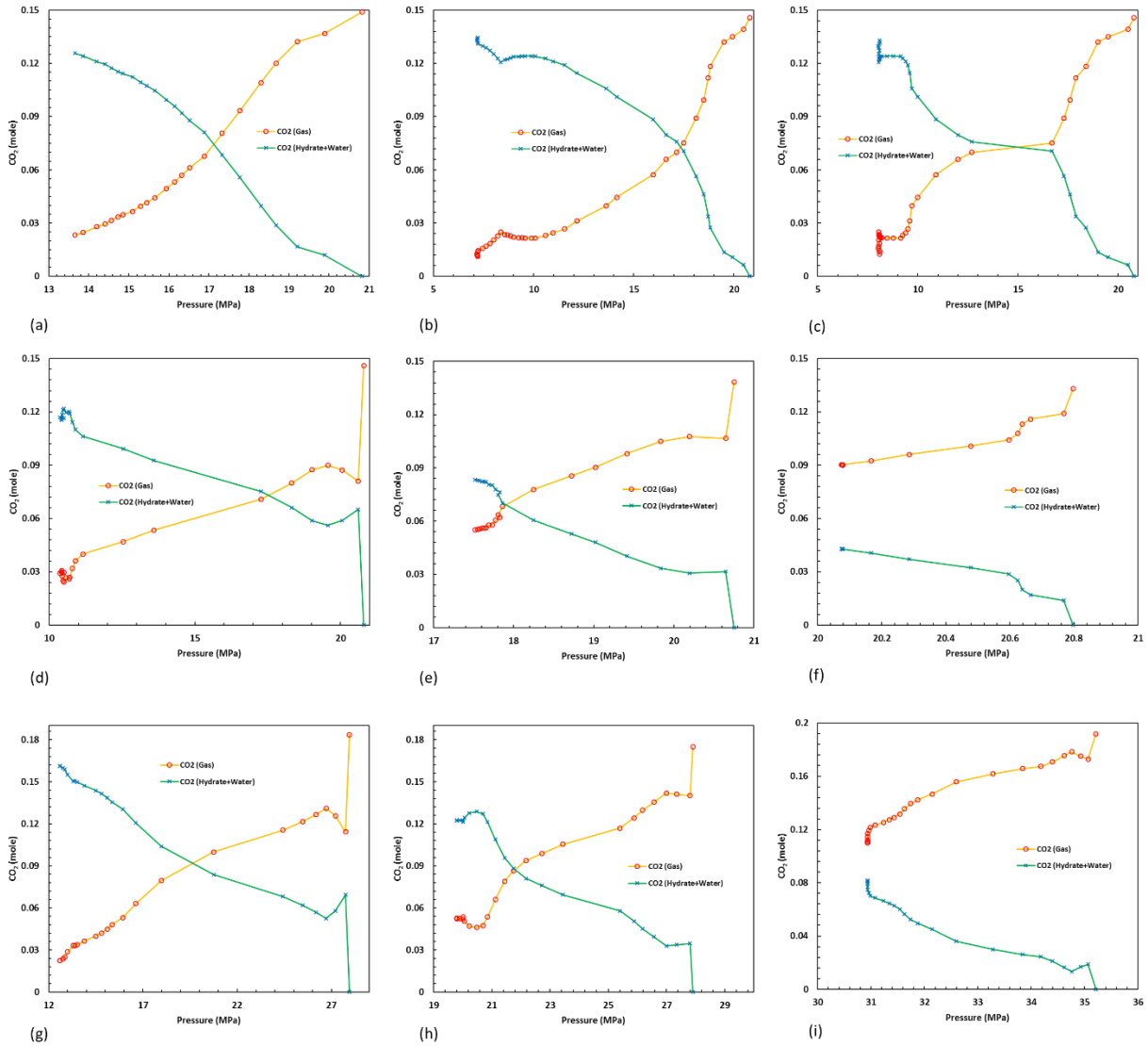

Figure S7 *Quantities of CO2 moles in the gas phase and Hydrate + Water phases versus pressure after flue gas injection (a)-(i) for Exp1-9.*

Table S4 *Detailed quantities of parameters determined for C-values calculation.*

Exp. No	1	2	3	4	5	6	7	8	9
Injected Gas(mol)	1.0198	0.9974	0.9761	1.0009	0.9476	0.9111	1.2574	1.1974	1.3137
Injected CO2(mol)	0.1489	0.1456	0.1425	0.1461	0.1383	0.1330	0.1836	0.1748	0.1918
Final CO2 in Gas(mol)	0.0232	0.0112	0.0198	0.0297	0.0550	0.0902	0.0223	0.0524	0.1099
Final CO2 in Hydrate+Water(mol)	0.1256	0.1344	0.1227	0.1164	0.0834	0.0428	0.1612	0.1224	0.0819
C-Value (%)	84.39	92.30	86.08	79.67	60.26	32.16	87.83	70.01	42.69

Appendix D for Chapter 6

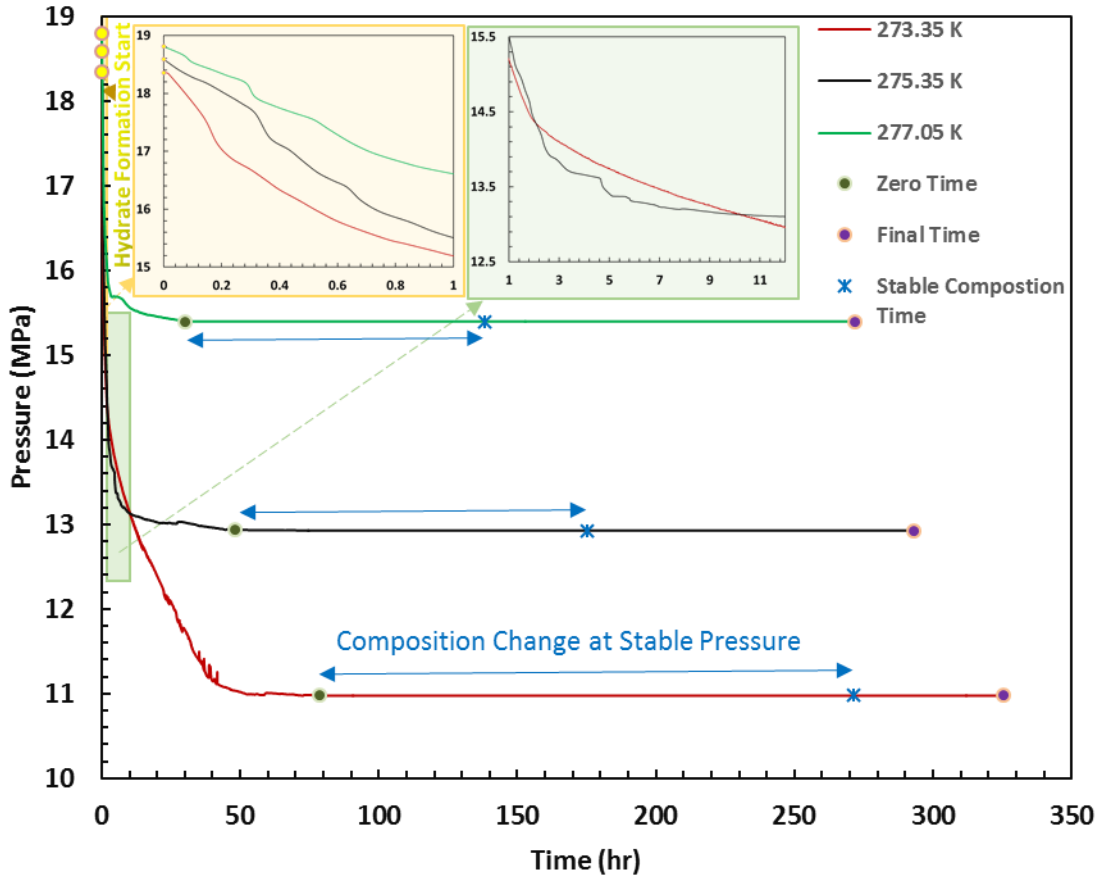

Figure S1 Detailed pressure-time profile after the onset of flue gas hydrate formation. Zero time corresponds to the moment the pressure just reached stable state; Final time corresponds to duration of the experiments from the beginning of hydrate formation; Stable Composition Time corresponds to the time when the gas composition just reached stable.

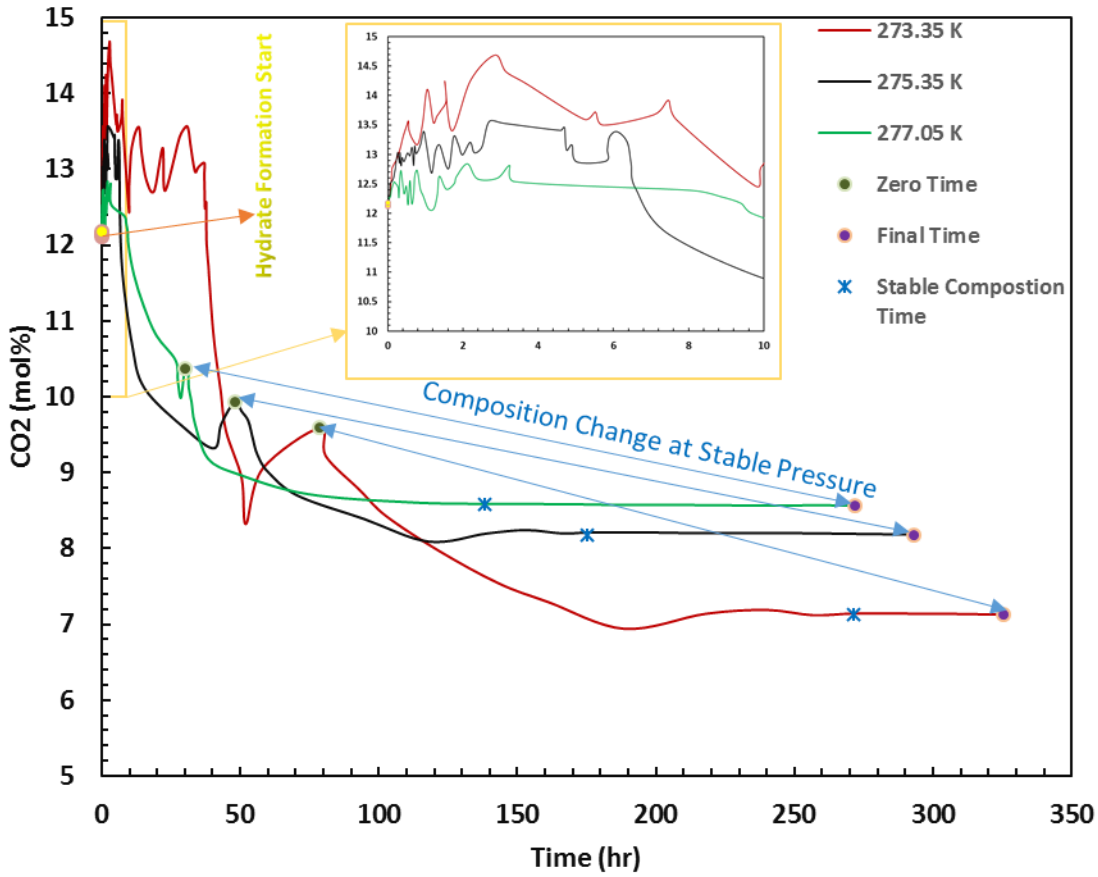

Figure S2 Detailed CO2 concentration in the gas phase versus time profile after the onset of flue gas hydrate formation. Zero time corresponds to the moment the pressure just reached stable state; Final time corresponds to duration of the experiments from the beginning of hydrate formation; Stable Composition Time corresponds to the time when the gas composition just reached stable.

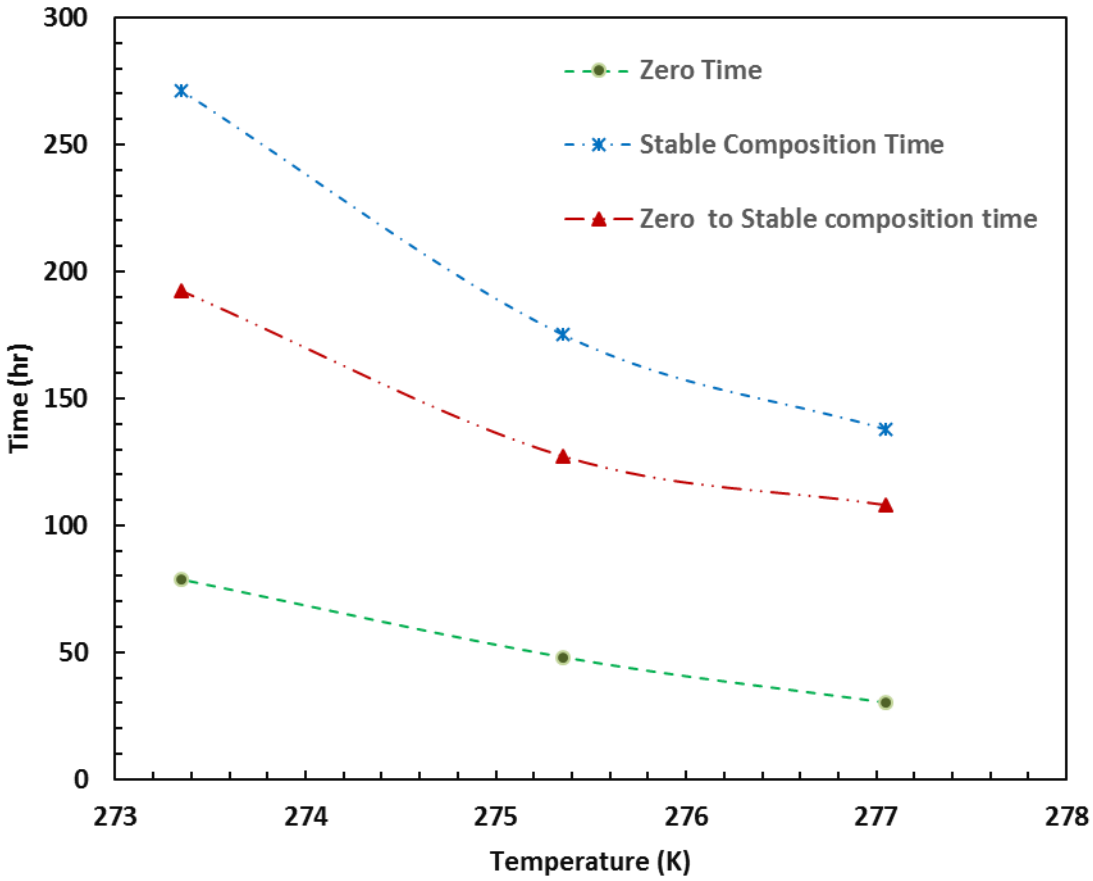

Figure S3 Time to reach the different stages during experiments. This figure shows the dependence of the CO2 capture kinetics on the system temperature. High experimental temperature will lead to short reaction time to complete the CO2 capture process.

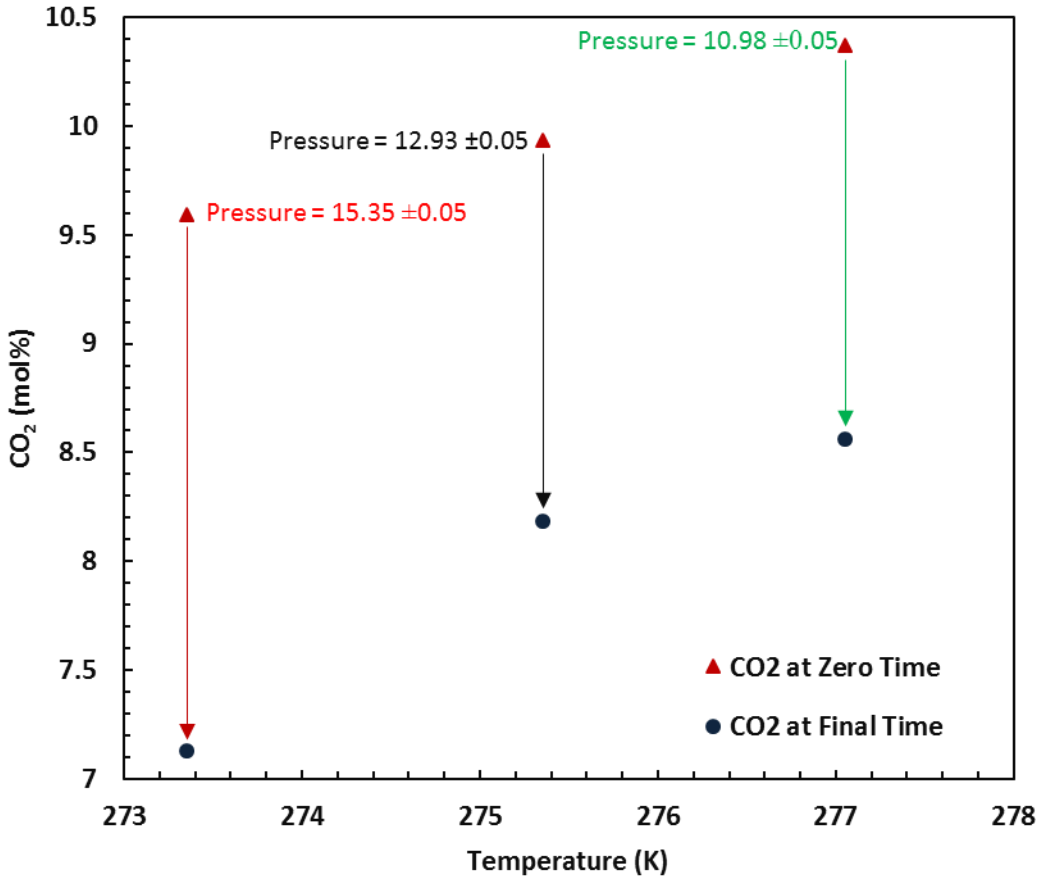

Figure S4 Evolution of CO2 concentration after reaching stable pressures. It can be seen that, after the system pressure became stable, there is still change in CO2 concentration.

Table S1 Summary of the determined experimental results

Temperature (K)	Zero Time (hr)	Stable composition Time (hr)	Zero to Stable composition Time (hr)	Stable Pressure (MPa)	CO_2 at Zero Time (mole%)	CO_2 at Final Time (mole%)
273.35	78.84	271.17	192.33	10.98±0.05	09.60	7.13
275.35	48.10	175.43	127.33	12.93±0.05	09.94	8.18
277.05	30.03	138.03	108.00	15.35±0.05	10.37	8.56